University of Kent

Natural Sciences Division

School of Physical Sciences

Synthesis and study of potential fluorescent sensors and steps towards understanding a new class of SSAs

By

Sena Ozturk

Thesis for the Master of Science by Research
October 2021

Abstract

This thesis reports the synthesis of four receptors designed to be potential fluorescent sensors for anions. The binding of these receptors to a series of anions were studied in the organic solvent DMSO; following this, a series of studies on the fluorimeter were conducted to assess their sensing potential. This thesis also reports the study of two SSAs and their neutral counterparts previously synthesised by Tjorge Neumann (University of Kiel). The self-associative properties of the four compounds were studied in the solution state to discern any structure specific activity, and assess their potential as a new class of SSAs.

Contents

Publications not related to this work:

"The phospholipid membrane compositions of bacterial cells, cancer cell lines and biological samples from cancer patients" K. L. F. Hilton, C. Manwani, J. E. Boles, L. J. White, S. Ozturk, M. D. Garrett and J. R. Hiscock, *Chem. Sci.*, 2021.

Acknowledgments

There are number of people I would like to thank for making it possible to have come as far as I have. First, and foremost, I would like to thank my family for their unyielding love and support. Their eternal encouragement in my pursuit of knowledge goes further back than I can remember. I would to thank my supervisor, Dr. Jennifer Hiscock, for her guidance, patience, and faith in me as a scientist and a student. She is all I could have asked for in a supervisor, and I am eternally grateful for everything she has given me and taught me. I would like to extend my gratitude to my colleagues in the laboratory for never failing to answer my questions, and their help in shaping my chemist's intuition – with a special thanks to Rebecca J Ellaby for incepting part of my project, for training me, and helping me at every turn. Last but not least, I would like to thank my friends, and my bandmates in Splinterface, for their love and upkeep of my morale during this year.

Abbreviations

Å	Angstrom
ADP	Adenosine diphosphate
ATP	Adenosine triphosphate
ArH	Aromatic proton
ArC	Aromatic carbon
$^{13}C\{^{1}H\}$	Proton decoupled Carbon NMR
CAHB	Charge assisted hydrogen bond
CD	Cyclodextrin
$CHCl_3$	Chloroform
CMC	Critical micelle concentration
CoEK	Co-operative equal K
D	Diffusion coefficient
d	Doublet (NMR)
DCB	Dynamic covalent bonds
DCM	Dichloromethane
d_H	Hydrodynamic diameter
DLS	Dynamic light scattering
DMSO	Dimethylsulfoxide
DMSO-d_6	Deuterated dimethylsulfoxide

DOSY	Diffusion ordered NMR spectroscopy
EK	Dimerization/equal K
EM	Electromagnetic
EtOAc	Ethyl acetate
EtOH	Ethanol
g	grams
GFP	Green fluorescent protein
HBA	Hydrogen bond acceptor
HBD	Hydrogen bond donor
HRMS	High resolution mass spectrometry
hv	Energy of a photon
J	Joules
J	Coupling constant
K	Kelvin
K_a	Association constant
K_{dim}	Dimerization constant
K_e	Equal constant
K_{sv}	Stern-Volmer constant
m	Multiplet (NMR)
m/z	Mass to charge ratio

MeCN	Acetonitrile
MeOH	Methanol
mol	Mole(s)
MS	Mass spectrometry
mV	millivolts
m/z	Mass to charge ratio
NAD	Nicotinamide adenine dinucleotide
nm	Nanometres
NMR	Nuclear magnetic resonance
OBz	Benzoate
OLED	Organic light emitting diode
pH	Power of hydrogen
PEO	Poly(ethylene oxide)
PDB	Protein data bank
PDI	Polydispersity index
pm	picometers
ppm	parts per million (NMR)
q	Quartet (NMR)
qNMR	Quantitative NMR
R	alkyl groups

RAHB	Resonance assisted hydrogen bonds
s	singlet (NMR)
S_0	Ground state
S_n	Excited state
SA	Supra-amphiphile
SLS	Sodium lauryl sulphate
SSA	Supramolecular self-associating amphiphile
t	triplet (NMR)
TBA	Tetrabutylammonium
THF	Tetrahydrofuran
TFA	trifluoroacetic acid
UV	Ultraviolet
XRD	X-ray diffraction
Φ_f	Quantum yield (fluorescence)

1. Introduction

1.1. History of supramolecular chemistry

The term “supramolecular”- compiled of the prefix ‘supra’ derived from the Latin meaning ‘beyond’, and ‘molecular’ referring to one or more chemical components - was coined by Jean-Marie Lehn in 1969.[1] These interactions transcend beyond a molecular ‘boundary’ and act between molecules - known as non-covalent interactions. The study of supramolecular chemistry was trail-blazed by 1987 Nobel prize winners Charles Pedersen,[2] Donald Cram,[3] and Jean-Marie Lehn,[4] and gathered the attention of chemists, biologists, and material scientists. The key component of their award-winning research was the study of the structure-specific nature of the interactions. These interactions show high selectivity and have allowed the world of science to mimic and utilise the non-covalent intermolecular forces of the natural world. These necessary higher-order complexes in nature can be formed as a result of hydrogen bonds, van der Waals forces, electrostatic interactions, and π-donor-π-acceptor interactions.[5] Applying these principles within research has allowed for steps towards valuable applications such as catalysis,[6] drug-delivery,[7] chemosensors,[8,9] materials,[10] and even in the use of some household items such as adhesives for example.[11]

Before an understanding of these reversible forces were developed, molecular study dominated chemical research. The foundation of modern molecular chemistry began to form shape with Friedrich Wöhler in 1828 via his successful synthesis of urea crystals in an inorganic reaction; this ultimately disproved ‘vital’ force theory (Scheme 1). Vital force theory was an outdated notion introduced by Paracelsus (1490-1541) and reinforced by Berzelius in 1809 that organic compounds were fuelled by a vital principle and could only be created by a ‘vital’ or ‘spiritual’ force and never created from inorganic components.[12]

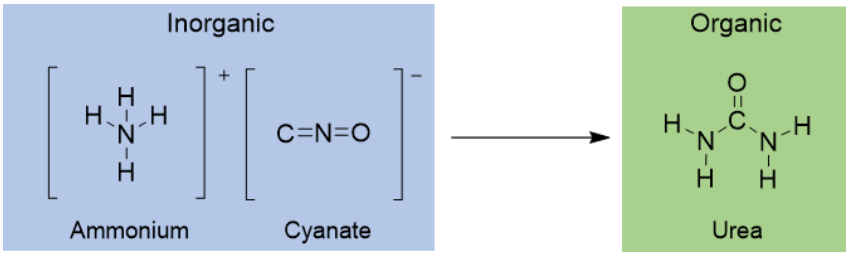

Scheme 1 – The formation of urea, an organic compound, from ammonium and cyanate, inorganic compounds; disproving vital force theory.

However, that was not the case. Despite the term only being coined in 1969, the face of supramolecular chemistry began to form when Johannes Diderik van der Waals initially proposed the existence of 'intermolecular forces' also called Van der Waals forces.[13] Followed shortly by Emil Fisher's hypothesis of the 'lock and key' principle, which contributed towards the understanding of non-covalent interactions produced between enzyme-substrate complexes.[14] His hypothesis incepted what is now engulfing host-guest chemistry (Figure 1).[15] Essentially laying the groundwork for the science used in modern pharmaceuticals.[16,17]

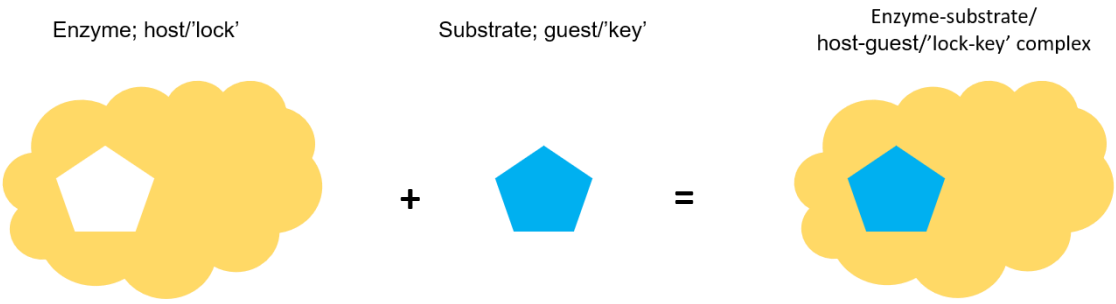

Figure 1 – A simplified illustration of Emil Fisher's 'lock and key' principle; also referred to as host-guest formation.

In current day, supramolecular chemistry continues to grow and evolve, even facilitating a second Nobel prize in this area of Chemistry in 2016 to co-award-winners Jean-Pierre Sauvage, Sir J. Fraser Stoddart and Bernard Feringa.[18] Where their research in molecular machines and rotaxanes proved that supramolecular complexes could be utilised to act as an electrochemically triggered motor.[19,20] Many naturally occurring phenomena would not be possible without the existence of this array of non-covalent interactions; which provide the foundation for a variety of research fields.

1.2. Non-covalent interactions

Valency is dictated by the power an element has to displace or combine a hydrogen atom. 'Covalency' however refers to the number of bonds an atom is able to form with another atom. A covalent interaction is the sharing of electron density between one or more atoms. Gilbert N. Lewis (1875-1946) published a paper in 1916 where 'Lewis' theory' was created and soon used as a world-known representation of a chemical bond as a pair of electrons being shared between to atoms (Figure 2).[21] This representation is commonly known as a 'dot and cross' diagram.

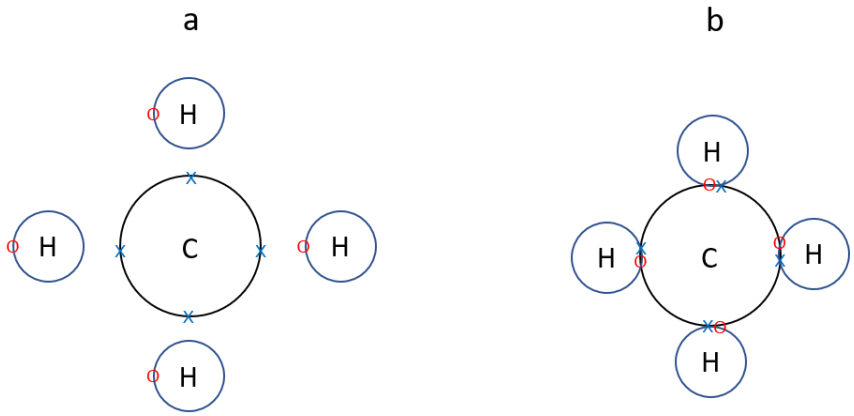

Figure 2 - Depiction of a Lewis dot and cross diagram (b) of a methane molecule, where the crosses represent valence electrons of the carbon atom, and the dots represent the valence electrons of the hydrogen atoms.

It wasn't until Tom Moore and Thomas Winmill utilised the 'lock and key' principle, and hypothesised the hydrogen bond in 1912,[22] little was known about the significance of this non-covalent interaction and its importance in holding biological life together. However, more research was necessary to prove that hydrogen-bonds differed from dipole interactions. Latimer and Rodebush were able to prove the existence of hydrogen bonds in a 1920 publication where they questioned the underlying principles of Lewis theory (which they referred to as "*first principle of molecular structure*").[23] They explored how the degree of polarity between two atoms is dependent on the differences of electronegativities. With atoms of two differing

electron affinities and complementary net charges, the electron is thought to be not 'shared' but passed on from one species to another to form a weak ionic interaction. The paper discusses the variation of polarity in different compounds and studies the unique nature of hydrogen associating in certain molecules, namely water as a result of a different kind of dipole.[23] A dipole is formed when a bond or a molecule having opposing relative charges on either end; hydrogen bonds specifically form between highly electronegative atoms (oxygen and nitrogen) and electropositive hydrogens (Figure 3).

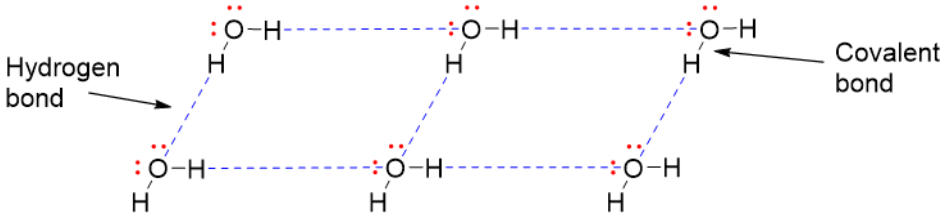

Figure 3 - An example of hydrogen bonding between water molecules; δ+ hydrogen atoms, hydrogen bonding to the lone pair on electronegative oxygen atoms.

As Figure 3 shows, hydrogen-bonding utilises an optimised 180° bond angle in water, as opposed to having a 'bent' geometry. This is particularly true of single donor systems; when multiple hydrogen bond donors (HBD), or hydrogen bond acceptors (HBA) are introduced, a variety of trifurcated geometries are adopted.[24] Hydrogen bonds where a linear geometry is formed are the strongest due to the directionality of hydrogen bonding. Hydrogen bonds are generally long (> 1.5 Å); in comparison to covalent bonds (1.2 - 1.5 Å).[25] The overall strength of a hydrogen bond is determined by the electronegative HBA and electropositive HBD. This HBA/HBD interaction is observed in all facets of nature.

Non-covalent interactions, despite being generally weaker than a covalent bond (100-1500 kJ mol^{-1}),[21] are fundamental in facilitating nature and life. Besides hydrogen-bonding, and Van der vaals forces, the term 'non-covalent' interactions also encompass dipole-dipole interactions, ion-dipole interactions, and ion-ion interactions (Figure 4). Van Der Waals forces, which are of the weakest, are electrostatic interactions which can be induced by surrounding

molecules due to random fluctuations of electron density. Though these interactions are weaker than covalent bonds, (Table 1), these 'weak' interactions are vital in nature.

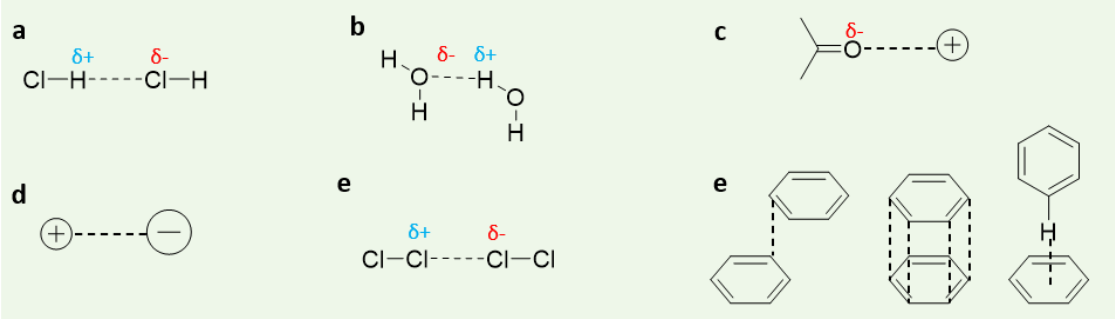

Figure 4 - Types of non-covalent interaction a. dipole-dipole; b. hydrogen bonding; c. ion-dipole; d. ion-ion; e. Van der Waals; e. π-π stacking- (left to right) face-to-face slip/edge-to-edge, face-to-face, edge-to-face.

As the Table 1 shows, the strength of a covalent bond can range from 100 to 1500 kJ mol^{-1}, and the strength of a hydrogen bond can reach up to 120 kJ mol^{-1}. This is due to the partial covalent character of hydrogen-bonding; particularly in structures which possess one of negatively charged assisted hydrogen bonds (- CAHB), positively charged hydrogen bonds (+ CAHB), or resonance assisted hydrogen bonds (RAHB).[26]

Table 1 - Strengths of different types of bonding/interaction and their descriptions.

Bonding/Interaction type	**Description**	**Energy/ kJ mol^{-1}**
Covalent bond	Sharing of an electron pair between atoms.[21]	100-1500
Dipole-dipole interaction (**4a**)	Weakest dipole interaction formed by the attraction of one dipole to another.[27]	5 – 50
Hydrogen bond (**4b**)	Form between hydrogen bond donor (HBD) and hydrogen bond acceptor (HBA) groups, and display both covalent and non-covalent character.[28,29]	4 - 165
Ion-dipole (**4c**)	Created between dipoles and charged ions.[30]	50 - 200
Ion-ion (**4d**)	Closest in strength to that of a covalent bond.[31–33]	10 – 350
Van der Waals (**4e**)	A weak electrostatic interaction caused by polarisation of electron clouds.[27]	<5

π-π (**4f**)	A result of the delocalised electrons in conjugated systems; π-π stacking can occur face-face, edge-edge, and offset.[34]	0 - 50

A good example of non-covalent interactions found in nature that is crucial is within proteins, and (DNA) deoxyribonucleic acid; which was discovered by James Watson, Francis Crick, and Rosalind Franklin in 1953.[35] The building blocks of proteins begin as amino acids - which when combined via a peptide bond, form a protein. These bonds are classified as the 'primary structure' of a protein (Figure 5).[36]

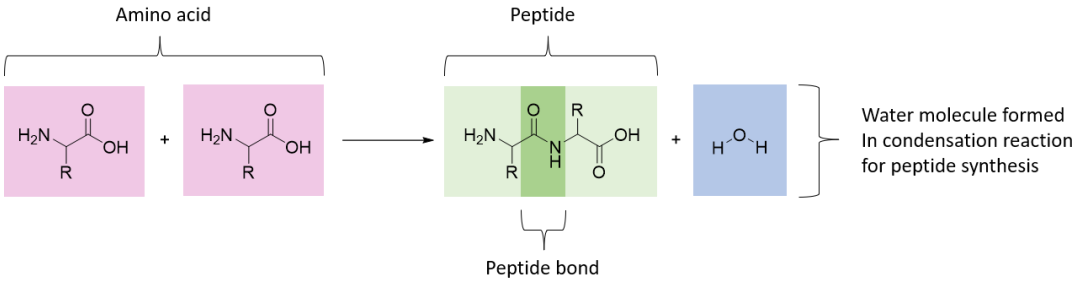

Figure 5 - Showing peptide synthesis in a condensation reaction; whereby the nature of the R group can provide a variety of properties; polar, non-polar, acidic, basic, and aromatic.[36]

The secondary structure of protein is one of three conformations; β-pleated sheets, α-helices and β-turns/coils (Figures 6 b and c); this is dictated by the sequence of amino acids in the primary structure, and formed as a result of self-assembly of the primary structure. The secondary structure is held together with hydrogen bonding formed between peptide bonds and other hydrogen bonding sites which may be present, providing rigidity to the structure.[37]

Beyond this point, a tertiary structure forms, where non-covalent interactions and disulfide bridges between R groups bring together amino acids that are not directly joined to one another; this produces the three-dimensional structure of the protein. The structure is stabilised by internal hydrophobic interactions created between the external hydrogen bond, the ionic bond interactions, the non-polar amino acid side chains, and the hydrophobic effected caused by the aqueous conditions of the cell.[38] A quaternary structure can form via various

covalent and non-covalent interactions if a particular protein has multiple peptide chains or co-factors (Figure 6 e). As such, non-covalent interactions are mandatory to stabilise these larger, macromolecular, structures compiled of nucleotides and proteins.[5]

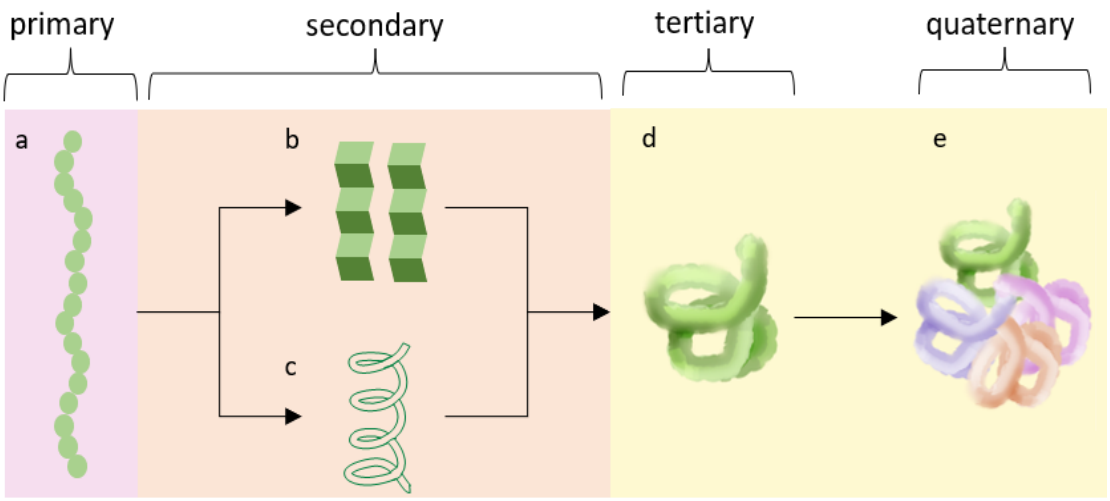

Figure 6 - Simplified depiction of the various layers of structure for a protein; a) primary structure produced by a sequence of amino acids; b) an example of a secondary structure, β-pleated sheets; c) another example of a secondary structure, α-helices; d) tertiary structure- the completed peptide; e) quaternary structure; the final conformation.[38]

The nitrogenous bases present in a sequence within DNA will determine the hydrogen bonding formed between the peptides; there are four nucleobases found in DNA; adenosine (A), thymine (T), cytosine (C), and guanine (G). The nucleobase combinations are A-T where two hydrogen bonds will form, and G-C; where three hydrogen bonds will form. Therefore, a higher abundance of the G-C combination will result in a more stable structure; this is due to hydrogen bonds being additive, and thus also results in an increase in melting point. [39]

1.3. Host-guest binding

1.3.1. What is it?

Host-guest chemistry is a branch of supramolecular chemistry which refers to complexes which consist of two species held together by non-covalent interactions; most commonly hydrogen bonding. The larger molecule is regarded as the host, and the smaller as the guest. Although the first enzyme to be observed and published was diastase (Figure 7) by French chemists Anselme Payen and Jean-François Persoz in 1833,[40] humans have been unknowingly using enzyme catalysis since as far back as 7000 BC to ferment sugars into alcohol.[41] In 1836, Berzelius introduced the first concept of a catalyst – a chemical which facilitated a reaction without undergoing any permanent changes, he then hypothesised that enzymes were biological catalysts.[42]

1

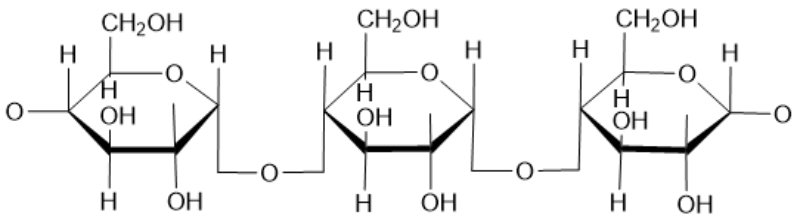

Figure 7 - Structure of diastase extracted from malt solution; although in modern day diastase refers to any α-, β-, or γ-amylase (all of which are hydrolases) that can break down carbohydrates.[40]

The selectivity of host-guest complexes is the fundamental backbone of biocatalysis, although not as simple as the Emil Fisher's 'lock and key' principle proposed in 1894, Koshland's 'induced fit' model proposed in 1958 provided a better explanation on enzymatic catalysis (Figure 8).[43]

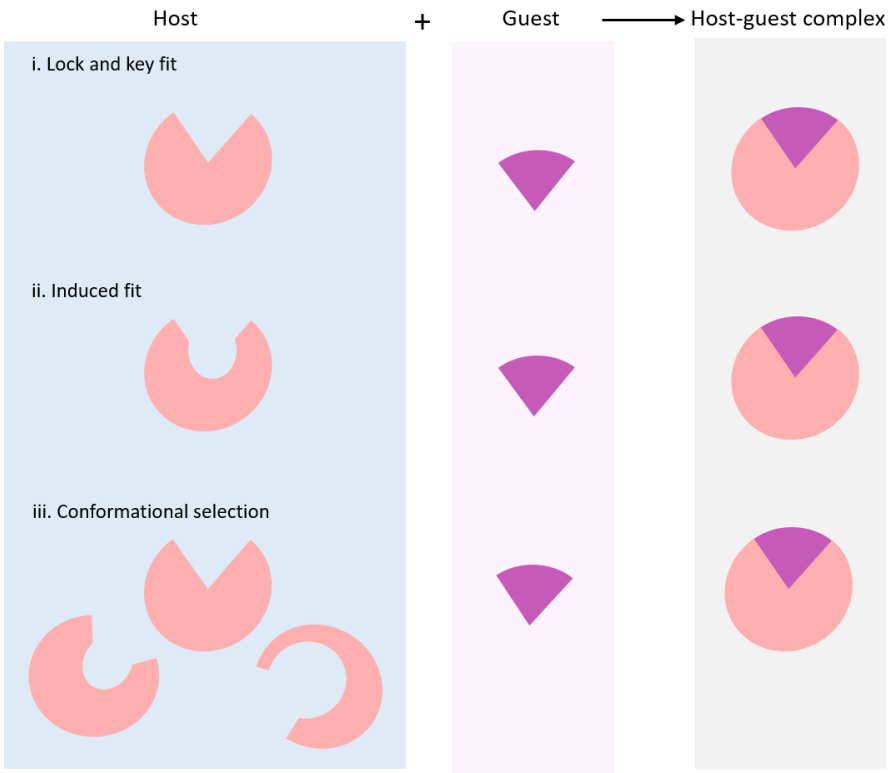

Figure 8 - Schematic diagrams of the three different binding models for host-guest complexation; i. lock and key fit; ii. Induced fit; and iii. Conformational selection.

The induced fit accounts for the conformational changes which take place on the protein (host) during the binding process to a guest species. The model is supported by the vast number of structures on the Protein Data Bank (PDB)[44] which were observed to have ligands buried within the protein-binding sites – which suggested that these ligands may be engulfed by the binding-site residues once the initial binding event has passed.[45] However, this didn't cover the whole story; the induced fit theory left many conformational changes (such as domain rearrangements, backbone collective motions, and disorder-to-order transitions) for highly flexible proteins unaccounted for. Giving rise to the 'conformational-selection' model, introduced in 1999, which suggested that the unbound protein would fluctuate between different conformational states with occupancy probabilities in corelation to the relative free energies; according to the Boltzmann distribution.[46,47] Only certain conformations would be able to bind to the guest species, where an encounter with a matching substrate was hypothesized to shift the distribution of energy to one of these states to allow for binding.[48] The main

difference between the 'induced-fit', and the 'conformational-selection' models is whether or not the holo structure exists before the binding event (Figure 8).

There are multiple steps to enzymatic catalysis – but all begin with the formation of a highly selective host-guest complex. These complexes form at very high rates and frequently result in an equilibrium of its components forming in solution (Scheme 2). Which is then followed by covalent bonds being formed and then broken before decomplexation begins.[49]

Scheme 2 – Formation of non-covalent (HG) host-guest complex, from (H) host, and (G) guest, in an equilibrium process where the association constant is given by $K_{ass.}$

There are three major modes of host-guest binding which are differentiated from one another by the nature of the receptor involved; anionic, cationic, and neutral receptors.

1.3.2. Anion receptors

The foundation of all tangible things is created by atoms - which are comprised of protons, neutrons and electrons. These three quantum particles produce a fundamental unity. Atoms with a greater number of electrons than protons – which are anions, are present throughout the natural world. Serving a number of necessary purposes; nitrates and phosphates are crucial for plant health and growth, [50,51] as well as cell membrane function – where chloride anions maintain an electrochemical gradient across cell membranes in order to control water content of mucous membranes. Which is just one example of why anions are particularly important, as the absence of chloride anions and thus an abnormal mucus membrane results in the genetic disease cystic fibrosis.[52,53] Anions can also be crucial to many important enzyme-substrate complexes in our bodies, as well as "energy currency" in living systems as adenosine diphosphate (ADP) and adenosine triphosphate (ATP).[54]

Unfortunately, there are a number of obstacles that are faced when designing an anion receptor due to some characteristics of anions;

- Anions can be protonated in low pH conditions, there can be difficulty when designing protonated anion receptors.
- The formal negative charge on an anion results in a larger radius than that of analogous isoelectric cations. This results in a lower charge-to-radius ratio and makes for a poorer fit, for example the ionic radius of F^- is 119 pm whereas Li^+ is 90 pm.[55]
- There is also a wide variety of geometries across different anions; this means that when designing a receptor it must be specifically optimised to a complementary anion-receptor binding (e.g., as seen in Figure 9 single atom anions such as Cl^- and F^- are spherical, whereas linear geometries are observed in anions like CN^-, and trigonal planar geometries in HCO_3^- and NO_3^-).[56]
- Taking solvent effects into consideration is also important as strong interactions form between both the anion and the free receptor; creating strong competition over any recognition forces between the counterparts.[57]
- Anion pairing can also unfortunately be out-competed by stronger directional interactions such as hydrogen bonding; which is able to conform to an optimal angle of 180° in order to interact with a given anion's geometry.

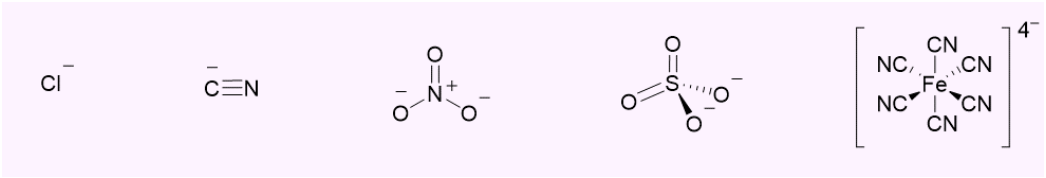

Figure 9 – Examples of anions with different geometries; (left to right) Cl^- spherical, CN^- linear, NO_3^{2-} trigonal planar, SO_4^{2-} tetrahedral, and $Fe(CN)_6^{4-}$ octahedral.

The first reported example of successful anion binding to an anion receptor was by Simmons and Park in 1968.[58] Whereby a tripodal ammonium bridged design was found to bind to chloride anions in 50 % trifluoroacetic acid (TFA) solution, with a binding constant of 4 M^{-1}. It wasn't until later in 1975 that the crystal structure of this complex was confirmed by Marsh and co-workers; the x-ray crystallography did not provide the full structure of the interaction however it did reveal that the hydrogen atoms on the ammonium were pointing towards the interior of the 'capsule' when bound to a chloride anion (Figure 10).[59,60]

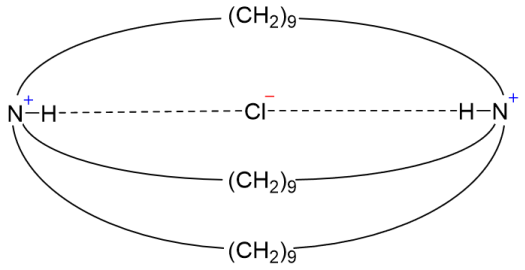

Figure 10 - A simplified diagram showing the tripodal ammonium bridge of the receptor binding to a chloride anion.[60]

Since then, anion receptor chemistry has continued to grow, developing into two main categories of synthetic anion receptors; ones that utilise metals in their motif and those who do not. The non-metallic category of anion receptors can be further subcategorised into systems that are neutral, and systems that are charged. The first instance of a neutral anion receptor was a hydrogen bonding amide-based receptor synthesised by Pascal and co-workers in 1986 which in DMSO-d_6 (deuterated dimethyl sulfoxide) was found to bind to fluoride utilising the tripodal capsule motif in Figure 11.[61]

2

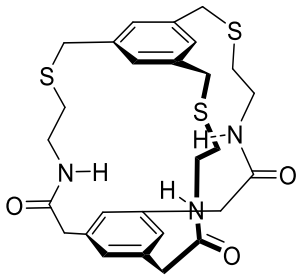

Figure 11 - Structure of the first macrocyclic neutral anion receptor; 2,25,28-trioxo3,16,29-triaza-6,19,32-trithia[7.7.7](1,3,5)cyclophane synthesised by Pascal and co-workers.[61]

The original design trail blazed a path for further studies on neutral-bond-donor receptors by research groups such as Reinhoudt and co-workers,[62] Smith and Davis and co-workers,[63,64] up to Crabtree and co-workers in 1997 developing a variety of anion receptors.[65] Gale and co-workers eventually began incorporating a more rigid scaffold into the design of the receptors based on the isophthalamide unit in 2007.[66] This allowed for pre-organisation of the receptor, and increase anion affinity through decreasing flexibility. Ghosh and co-workers contributed numerous receptors to the field, utilising motifs ranging from 1,3,5-trimethyl-2,4,6-triaminobenzene scaffolds (which included three amide NH bond donor groups), to bistripodal and amide-based receptors.[67–69]

Commonly hydrogen bonds are employed for anion binding motifs due to their directional nature; allowing for differentiation between anionic species that have different geometries.[70] Therefore, utilisation of groups with NH-like hydrogen donating properties; such as amine, amide, urea, pyrrole, and indole neutral groups, as well as ammonium, guanidiums, and imidazolium-based charged groups have dominated anionic sensing chemistry.[71] Amidepyridinium-based anion receptors, although less researched, were reported by Steed and co-workers in 2002. The series of fluorescent chemosensors reported combined the hydrogen donating properties of the neutral amide group and acidic C–H at the pyridinium ring, which when combined together, allowed for anion sensing. The structures were described as 'Venus flytrap' hosts due to the geometries produced when they bind via a three-hydrogen bonding 'arm' motif (Figure 12).

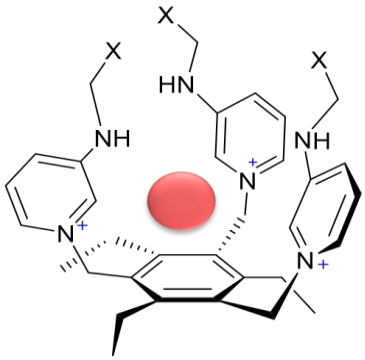

Figure 12 - General structure of the series of 'Venus flytrap' anion receptors synthesised by Steed and co-workers; the red sphere represents the location of an anion when binding.[72]

The receptors were measured for their affinities with a series of simple inorganic anions. Upon measuring, **3a** had a selective affinity for Br^- with a binding association of 850 M^{-1}, whereas **3b** showed an association with a constant of 13800 M^{-1} for Br^-, and 467 M^{-1} for NO_3^-, and 10500 M^{-1} for $CH_3CO_3^-$.[72] Receptors **3a** and **3b** were expected to bind to anions in a chelating 'cone' conformation (akin to what's shown in Figure 12) by utilising the strong hydrogen donor functionalities on the receptor 'arms', and/or via weak interactions with the pyridinium *ortho* CH groups. In anion receptor chemistry, the geometry of these hosts facilitates pre-organisation into the binding 'cone' geometry as it is more energetically favourable due to the steric preference for the alternation around the hexa- substituted core of the receptor scaffold.[73]

3

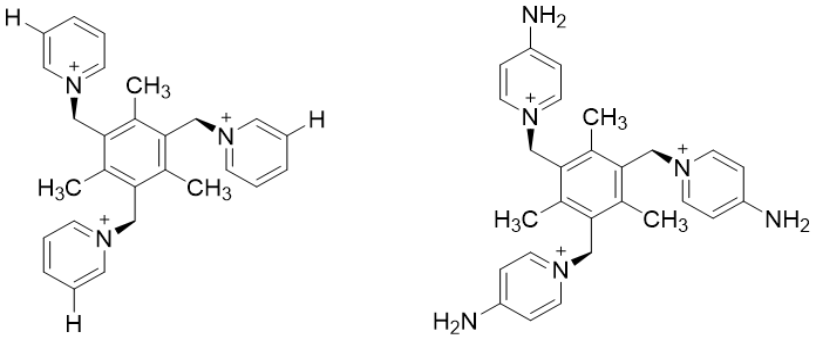

a **b**

Figure 13 - Structures of two of the receptors synthesised by Steed and co-workers.[72]

These flexible podand receptors differ from typical, more rigid cyclic structures as their flexibility can cause them to display rapid complexation/decomplexation kinetics and undergo significant conformational change on binding. These properties of flexible receptors have often been utilised in molecular switches and switchable sensing device chemistry.[74,75]

In 2008 Gong and co-workers used cyclohexane as the scaffold for the receptor, which allowed for use of its axial sites for amide substituents. Inherently facilitating the convergence of the hydrogen bonding array. This preorganised the NH HBD groups for coordination with the anion. The anthracene substituted analogue for the receptor **4** (Figure 14) can act as a fluorescent chemosensor for dihydrogen phosphate as there was selectivity to this anion when compared to all over TBA salts which were examined in a MeCN (90 %) and MeOH (10 %) solution. In this solvent a 505 nm excimer emission was observed when the sample was irradiated at 368 nm.[76]

4

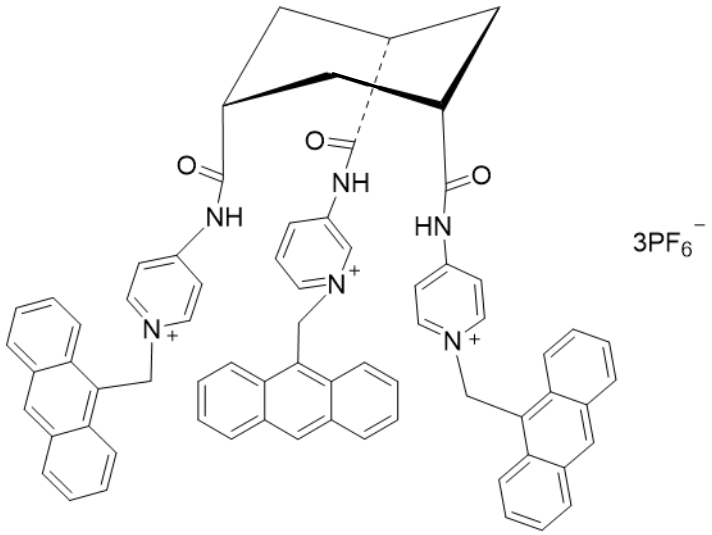

Figure 14 - Structure of the chemosensor designed by Gong and co-workers; A novel amidepyridinium-based tripodal fluorescent chemosensor for phosphate ion.[76]

Research into the selectivity of pyridine-2,6-dicarboxamide receptors was explored in 2010, and the affinity and selectivity of the receptors were measured for various analogues which incorporated positive charges into their structures. Two of the receptors synthesised **5b** and **5c** were dicationic analogues of the neutral receptor **5a** (Figure 15).[77] The stability of the

constants of the receptors were determined in CD_3CN via ^1H NMR analysis, and the association constants observed are shown in Table 2. The neutral pyridine-dicarboxamide **5a** receptor was found to show no interaction or binding with chloride and weak binding with acetate (log *K* = 0.7). However, when **5b** was observed, the receptor showed binding to chloride (log *K* = 4.3), and to bromide (log *K* = 3.27) with no interaction observed for iodide anions. Compound **5c** showed a lot more promise and was studied with a greater variety of anions, displaying association to chloride (log *K* = 5.85), bromide (log *K* = 5.40), iodide (log *K* = 3.80), nitrate (log *K* =4.40). The increased affinity of the dicationic receptor **5c** for the anions may be attributed to the methylation of thepyridines which causes a very strong acidification of amide groups; as typical pK_a values of amides are generally around 15, methylation of the pyridine group was found to increase the acidity of NH-donor groups up to 10 orders of magnitude. Ultimately making **5c** a better anion receptor with greater potential to form a host:guest complex in comparison to **5a** and **5b**.

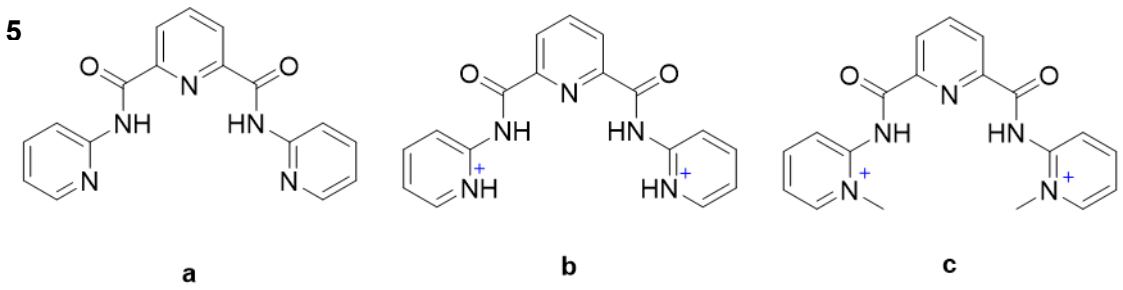

Figure 15 - Showing the structures of some of the N,N' -bis(pyridyl)-2,6- pyridine-dicarboxamide anion receptors synthesised by Yatsimirsky and co-workers.[77]

Anion	**5a**	**5b**	**5c**
Cl^-	0.7(2)	4.3(1)	5.85(9)
Br^-		3.27(9)	5.40(8)
I^-		*b*	3.80(8)
AcO^-	*b*		
NO_3^-			4.40(6)

Table 2 – Showing association constants (log *K* / M^{-1}) of receptors **5a, 5b, 5c** with anions in MeCN at 298 K.[77]

[a]The values in the parentheses are the standard errors of the data in the last significant digit.

[b]No interaction observed from the ^1H NMR titration data. Blanks represent no experiment conducted for the given receptor-anion pairing.

1.3.3. Supramolecular complexes

Molecular recognition is a key piece in both host-guest chemistry, and self-assembly. The key difference between the two is that once a host-guest complex is formed, the host or receptor is no longer an 'active' structure; reactions and changes to the structure no longer occur while complexed. Whereas within self-assembly driven synthesis, the supramolecular complex formed generally remains somewhat 'active' to carry out functions. Self-assembly is commonly observed in biological processes, of which are governed by innumerable non-covalent interactions.[78] Thus, the design of self-assembling systems which can partake in precise non-covalent interactions has proven difficult. A good example of a self-assembling biological supramolecular complex observed in nature is haemoglobin. This protein-based complex is essential to life, its components work together flawlessly to transport oxygen throughout our bodies. Its brilliant design facilitates an increasing affinity for oxygen with each subsequent addition due to the unique conformational changes which take place upon binding to each unit.[79,80] Haemoglobin is formed by four globular protein subunits, each of which are tightly

associated with a haem group (Figure 16), crucial to oxygen transport as the iron ion is the site of binding.

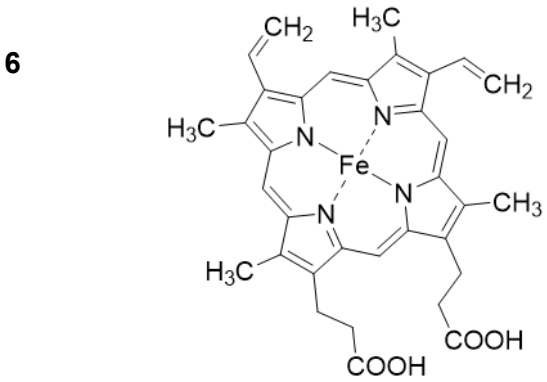

Figure 16 - Structure of the haem group in haemoglobin.

The birth of supramolecular host-guest chemistry began with crown ethers by Pendersen in 1988,[81] followed by cryptates by Lehn,[58] and spherand by Cram[82] (Figure 17). These molecules were all able to bind with metallic cations (such as K^+, Li^+ and other small spherical cations).

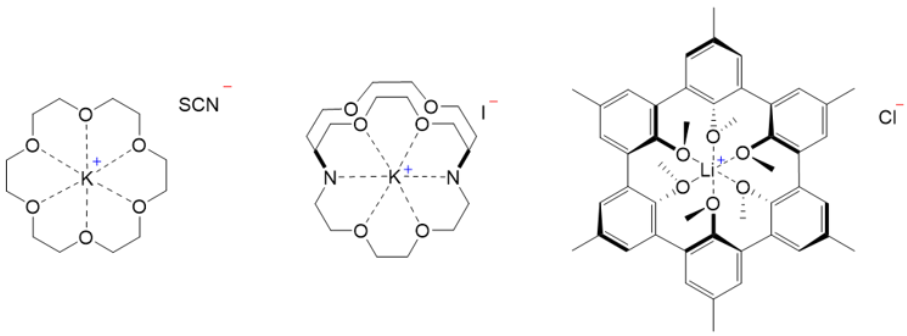

Figure 17 - Series of early supramolecular host guest complexes by Charles Penderson; Crown ether (**7**), Jean-Marie Lehn; cryptate (**8**), and Donald Cram; spherand (**9**).[58,81,82]

However, the incorporation of larger, more complex macrocyclic receptors into the field of receptor chemistry, only began to evolve in the late 1990s - combining both traditional host-guest chemistry and self-assembly chemistry. This new direction provided more promise as macrocyclic receptors have been found to form much needed, more stable complexes when binding to anions, due to increased thermodynamic stability; provided by what is known as the

'macrocyclic effect'.[83,84] The cyclic structure allows for the receptor to be more rigid; which can increase anion selectivity as the receptor will be less flexible to anions which are not an optimal 'fit' or those that are slightly larger than the binding site cavity. However, there are some exceptions where rigid structures had been previously used - which include the bicyclic cyclophane (which was found to selectively bind to dihydrogen phosphate)[85] and calix[4]pyrrole (which utilises four HBDs to bind to fluoride and spherical anions alike).[86]

Although initially used in cationic receptor chemistry, supramolecular anion receptor cryptates have also been reported by Lehn; dubbed as '*Spherical Anion Cryptates'* due to their high affinity for spherical anions of suitable size. The tetra-protonated forms of these structures (Figure 18) form macrotricyclic anion cryptates with halide anions held in a tetrahedral array of hydrogen bonds located inside of the spherical cavity of the ligand.[58] Cryptates **10a** and **10b** were observed to have higher stability constants (log K_s) for chloride anions, both much greater than 4.0. Cryptate **10c** however, had log K_s below 1.7 for chloride and bromide; suggesting that the incorporation of the methyl group at the amide in **10c** is a contributing factor to decreased anion-binding.

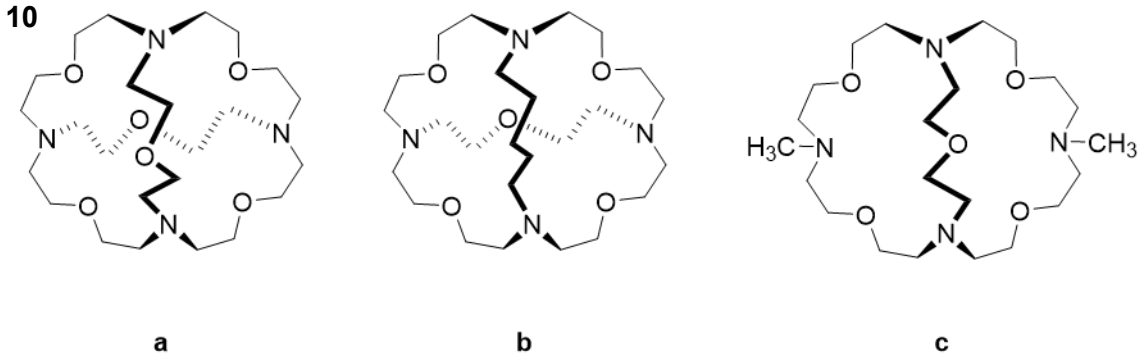

Figure 18 - Structures of cryptates that were tetra-protonated to form spherical anion receptor cryptates.[58]

The studies of these cryptates (prior to tetra-deprotonation) revealed that elongation of the macrotricycle bridges increased cavity size and selection for larger cations, and thus, the same could be assumed of the spherical anion receptor analogues.[58] Larger cavity sizes in

cryptands have been shown to display affinity for larger anions,[87] and a publication in 2001 was able to show selectivity for dinegative oxoanionic guests (such as CrO_4^{2-}) over mononegative oxoanionic guests when larger, protonated azacryptate hosts were used.[88]

A good example of the macrocyclic effect being utilised was in a study by Hamilton and Choi in 2000;[89] where the binding constants were tested using ^1H NMR studies on various different anions from TBA salts. Their Job plot analysis indicated a 1:1 binding stoichiometry with the tosylate anion with one of their novel receptors **11**. The binding took place through the contribution of the central aryl protons and amide protons, where the aryl protons of the anion showed a ≈ 0.3 ppm upfield shift upon binding which was presumed to be a result of the ring current effect of the macrocycle. More complicated binding modes with 1:1 and 1:2 (macrocycle:anion) models were formed with spherical halide, planar nitrate, and tetrahedral sulfate and dihydrogen phosphate anions.[89] All of the anions that compound **11** was found to bind to, have a more 'even' distribution of charge; ultimately facilitating the formation of sandwich complexes with two equivalences of macrocycles. Iodide was found to have a much higher affinity than chloride, the partial selectivity held accountable for the greater charge density and size of iodine as the binding site is large and rigid.[89]

11

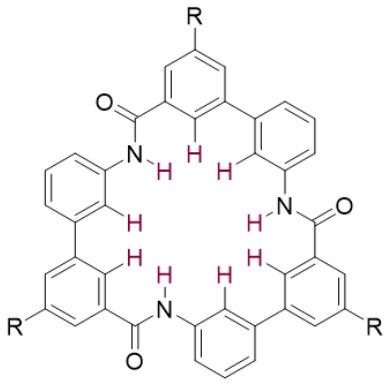

Figure 19 - Structure of Hamilton and Choi's macrocyclic receptor, with aryl protons and amide protons involved in binding highlighted in purple.[89]

1.4. Amphiphiles and Supra-amphiphiles

1.4.1. Amphiphiles

The term 'amphiphile' translates to 'both-loving'; in this case referring to displaying hydrophilic (water-loving) and hydrophobic (water-hating) behaviour. Which also can be referred to as lipophobic (fat-hating), and lipophilic (fat-loving). This is achieved by the molecule possessing both a polar or anionic group covalently bound together - which is the hydrophilic terminal of the molecule, as well as an apolar hydrocarbon group with a chain length greater than four carbons – forming the hydrophobic terminal of the molecule; however aromatic rings and fluorinated groups[90] can also be used as they are also sufficiently hydrophobic.[91,92] There are a variety of amphiphiles, which are dependent on the type of hydrophilic group it possesses; the hydrophilic group can be anionic, cationic, zwitterionic, or non-ionic (neutral) (Figure 20).[93]

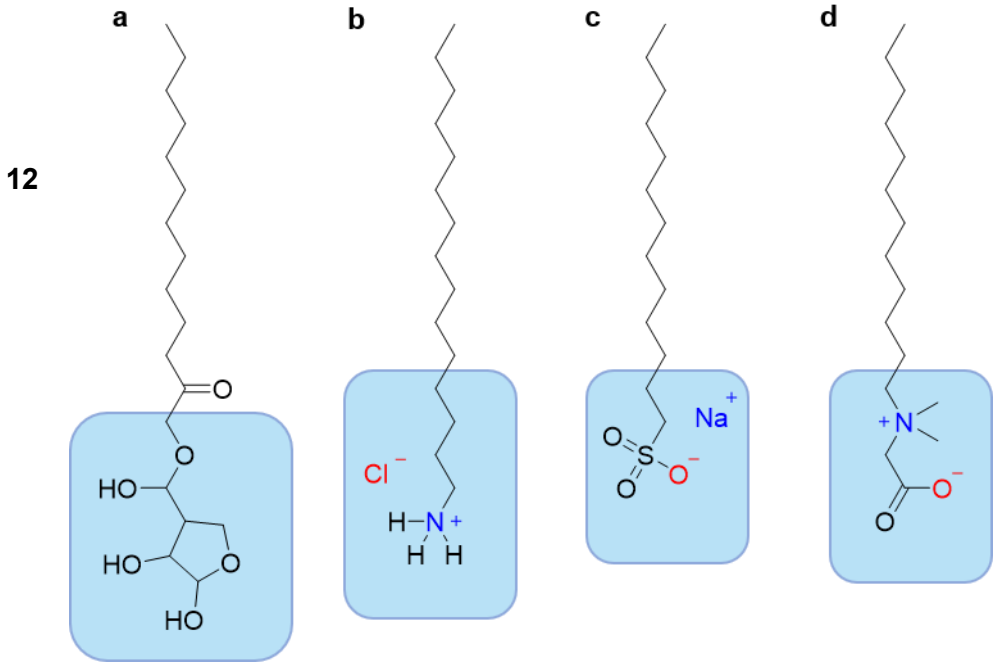

Figure 20 - Examples of different kinds of amphiphilic molecules with the hydrophilic headgroups highlighted in blue - a. neutral (non-ionic); b. cationic; c. anionic; d. zwitterionic.

Due to their structure, amphiphiles display a strong affinity towards both polar and non-polar solvents; ethers, esters, and hydrophobic hydrocarbons. The possession of 'both-loving'

moieties allows for self-assembly; where the structures formed use molecules as building blocks - as opposed to atomic units. This unique bottom-up approach provides limitless possibilities for the construction of new materials.[94] Cationic amphiphiles like pentadecane-1-aminium (**12b**), have a positive head which commonly is an amine group, or an ammonium ion, along with a counter-anion.[95] Anionic amphiphiles such as sodium lauryl sulfate (SLS, **12c**), often possess moieties such as carboxylates, sulphates, sulphonates, and phosphates as anionic head groups, and a corelating non-amphiphilic counter cation.[96] Whereas the zwitterionic amphiphiles possess both a negatively charged and positively charged moiety, like (carboxylatomethyl)dodecyldimethylammonium (**12d**), and although most commonly their hydrophobic component is a hydrocarbon chain, some variations can also include aromatic rings, and trifluoromethyl functional groups instead.[97,98]

The ability of amphiphiles to self-associate can allow for solvent dependent macromolecular structures to form - which are a result of a series of 'preferential' interactions taking place in the solution state - akin to water droplets forming to minimise surface tension. In nature, this self-assembly is observed in many morphologies; which include lipid bilayers, micelles, reverse micelles, and vesicles (Figure 21).[99,100] The difference between a micelle and a reverse micelle is dependent on the solvent environment. In a non-polar solvent, the non-polar tails of the amphiphile face outwards while the polar groups are faced inwards; becoming encapsulated to avoid the unfavourable interaction; in an aqueous solvent the exact opposite occurs, forming a micelle. This is true of more linear amphiphiles which contain only one lipophilic hydrocarbon chain - however a multi-tail topology would result in the favoured formation of a bilayer.[101] As such, the properties of these 'self-assembled' structures are dependent on the architecture of the amphiphiles.

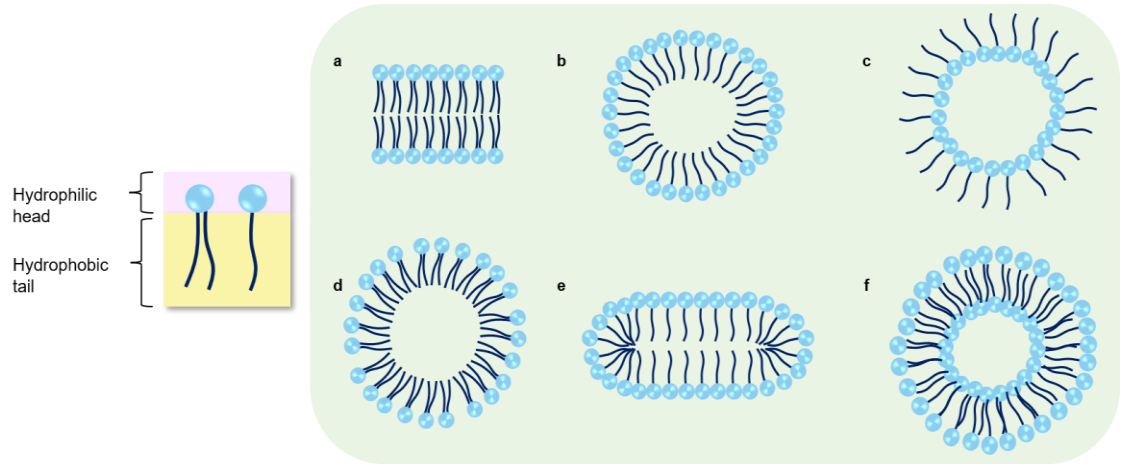

Figure 21 - Simplified representation of different amphiphilic structures of monolayer and bilayer systems formed in solution – a. bilayer; b. spherical micelle (single hydrocarbon chain); c. reverse micelle; d. spherical micelle (multiple hydrocarbon chain); e. cylindrical; f. vesicle (liposome).

When compared to low molecular weight amphiphiles, polymeric amphiphiles were found to have greater stability and offered more structural diversity, with the larger size of the self-assemblies providing capacity for guest molecules.[102] The aggregation of low molecular weight amphiphiles are dependent on the equilibrium between aggregated and non-aggregated molecules in the solution. These self-assemblies are relatively dynamic, however with polymeric amphiphiles - their increased self-assembly stability is provided by stronger interactions, and the resulting 'entanglement' of the polymer chains.[102] Ultimately, this circumvention of quick molecular exchange has resulted in applications in drug delivery and templated synthesis of nanomaterials.[103,104]

1.4.2. Examples of amphiphiles

Amphiphiles are the stars of many biological functions as they provide basis for self-assembly of protein folding,[105,106] nucleic acid assembly and tertiary structure,[107] ribosomes,[108] microtubules, and phospholipid membranes.[109] The amphiphilic structure of the phospholipid bilayer found in nature is critical to living organisms as it contributes to a majority of the make-up of a cell membrane.[110] These bilayer structures are able to form when amphiphiles have more than one hydrocarbon chain which make it unfavourable to form a contained micelle due to its

bulky size.[111] Natural phospholipids are a class of amphiphilic molecules, which tend to consist of one hydrophilic head, and two hydrophobic tails - and such, when dispersed in water, their polar groups turn towards the surrounding aqueous solution and their lipophilic chains turn towards the inside; thus favouring the formation of bilayers when aggregating (as illustrated in Figure 21 **a**).

Adjusting this structure to have two head groups linked to the same alkyl chain has made it possible to produce a Bolaform amphiphile (Figure 22) - a type of thermo resistant bilayer commonly found in the membranes of thermophilic bacteria.[112,113] Another unique class of amphiphiles - the gemini-form amphiphile, in which two headgroups are attached to the middle of the alkyl chain, are able to aggregate at very low concentrations; which has instigated a lot of research in their usage as molecular carriers.[114]

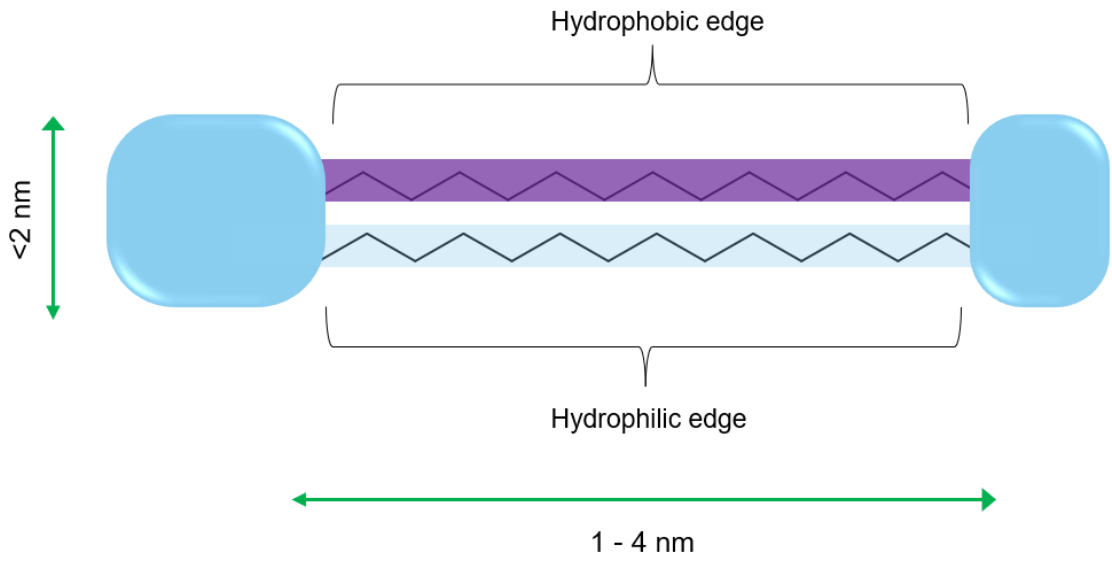

Figure 22 - General structure of a bolaamphiphile; with the blue sections representing the hydrophilic components, and the purple representing the hydrophobic component.[112]

Another well-known example of amphiphiles are modern-day cleaning products; surfactants.[115] The name evolving from the self-explanatory term 'surface-active-agent' coined in 1950.[116] These molecules are able to adhere to the interface of a surface (water-air for example), and induce a decrease of interfacial tension via adsorption.[116] Surfactants always

possess a hydrophobic region but can have anionic, cationic, zwitterionic, and non-ionic hydrophilic heads. SLS is a common anionic surfactant which is water-soluble at room temperature and has been commonly used within pharmaceuticals as its amphiphilic behaviour allows for antimicrobial activity to take place. The detergent increases solubility of a variety of chemical species, and disrupts aggregates therefore it has become a key class of compounds which are used to disorganise phospholipid bilayers and solubilise proteins.[117] With studies extending to even the exploration of an SLS composite material for the development of sterilized and non-infectious contact lenses.[118] Various other uses and research applications utilising the amphiphile motif also include drug delivery,[119,120] antidepressants,[121] β-blockers,[122] nano-devices,[123,124] and template synthesis.[125]

1.4.3. Supra-amphiphiles

Supramolecular chemists have utilised the amphiphile motif for the formation of supramolecular structures using non-covalent interactions in order to self-assemble.[126,127] Fabrication via non-covalent interactions results in the formation of reversible complexes. Complex formations are often aided by one of the following; hydrogen bonds,[128] π-π stacking,[129] electrostatic interactions,[130] charge-transfer interactions,[131,132] host-guest recognition,[133] the presence of imine bonds,[134] and boronic ester bonds (Figure 23).[135] As such construction of supra-amphiphiles (SA) can be classified by the leading driving force involved; however, this does not mean that only one driving force is being utilised, as multiple driving forces will collectively contribute for the formation of SAs.[127] The desired functional groups can be attached to supramolecular amphiphiles by using various noncovalent interactions; which is much simpler than tackling the complexities that covalent synthesis presents; which come with traditional amphiphiles preparation.[136]

13

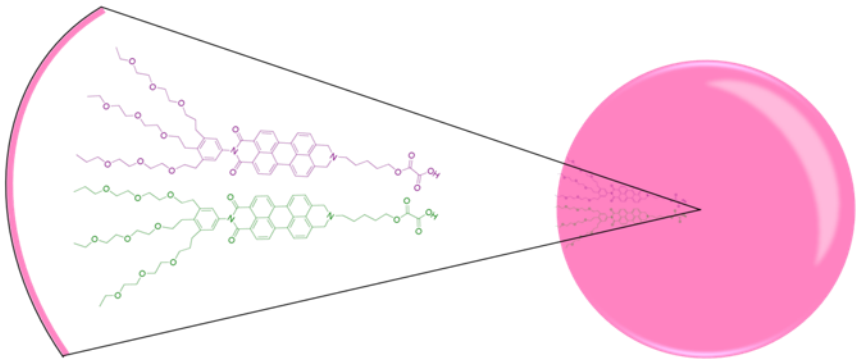

14

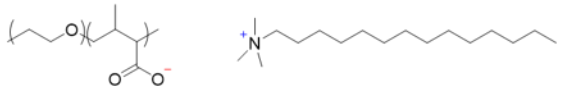

15

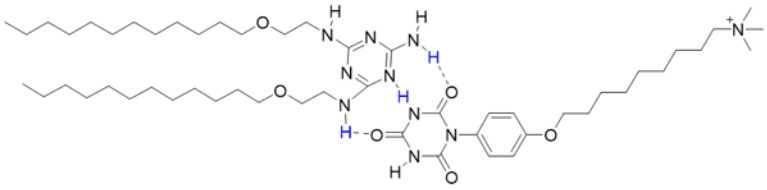

Figure 23 - Examples of SAs utilising various fabrication methods for non-covalent assembly: 13. π-π stacking;[129] 14. Electrostatic;[137] and 15. Hydrogen bonding.[127]

Some examples of SA fabrication for each of the different major non-covalent interactions are as follows:

- *Hydrogen Bonding*- In 1993, Kunitake and Kimizuka substituted melamines and isocyanuric acid derivatives to be used as molecular building blocks and introduced to utilisation of hydrogen bonding for SA fabrication.[138]
- *Host-guest recognition*- In 2003, Zhang et al. used cyclodextrin (CD) as a host to form inclusion complexes with guest components; such as aliphatic molecules or azobenzene.[127]
- *Metal-ligand coordination*- Schubert et al. in 2002, showed that metal-ligand coordination can be used as a linker to form amphiphilic polymers. Metal-ligand coordination, despite being much stronger than most intermolecular interactions, is reversible; which allows it to function as a form of supramolecular bond.[139]

- *Electrostatic attraction*- Block ionomer, 'surfactant complexes', can be formed with various single-tail cationic surfactants with the hydrophilic di-block copolymer of poly(ethylene oxide) (PEO), and poly (sodium methacrylate) As this complex forms due to electrostatic attraction; as caused by the ionic head group on the surfactant binding to polyion segments - it may be considered a form of SA. The PEO chains behave as stabilizers for the insoluble components in aqueous solution, resulting in micelle-like aggregation.[137] An example of this is also demonstrated in Figure 23.
- *Charge-transfer interactions* - The self-assembled complex of 1-(11-oxo-11-pyren-1-ylmethoxy) undecyl)pyridinium bromide and ethane-1,2-diyl bis(3,5-dinitrobenzoate), utilises the charge transfer between electron donors and acceptors; which, in aqueous solution, forms vesicular aggregats.[131]
- *π-π interactions*- In 2007, Wurthner utilised perylene bisimides to fabricate SAs, after successfully synthesising PBI moiety containing, dumbbell-shaped and wedge-shaped amphiphiles; and when mixed together, the amphiphiles were found to co-assemble to form an SA; forming vesicular structures via the new π- stacking parameters.[140] An example of this is also demonstrated in Figure 23.
- *Coiled-coil peptide interactions*- Utilise a variety of different intermolecular interactions that naturally take place within some specific peptide sequences; these complexes form due to this "coiled-coil" peptide interaction. A 2008 study explored the use of this motif to connect proteins and hydrophilic polymers.[141]

Being able to fine-tune these interactions provides a way for scientists to adjust amphiphilicity; allowing for control over both self-assembly and disassembly processes.[132] Supra-amphiphiles are also able to associate through 'dynamic' covalent bonds (DCBs); for example imine and disulphide- which due to its conditional reversibility can also be treated as a non-covalent interaction.[142] As such, the dynamic and reversible nature of the noncovalent interactions also provides gateway for chemists to create stimuli responsive supramolecules.[103]

Zhang et al have successfully utilised DCBs for fabrication, using two benzoic imine bonds to connect two bolaform amphiphiles together to form a series of supra-amphiphiles with an "H" shape (Figure 24), these were found to aggregate to form micelles at very low concentrations. The newly studied "H" shape of the SA provided greater stability than their conventional amphiphiles counterparts also formed by imine bonds.[143] This type of SA is fabricated via a DCB as increasing the pH of the solution results in assembly, and decreasing the pH causes 'disassembly' of the dynamic imine bond in **16a**; and thus, aggregates in basic conditions. The benzoic imine bonds utilised by Zhang et al provide a simple, well-defined structure, and pH responsiveness when in water; making it one of the most useful dynamic covalent bonds for fabricating SAs. These characteristics unsurprisingly attracted many research groups to further study SA topologies designed about benzoic imine bonds since they were first reported in 2009.[143–146]

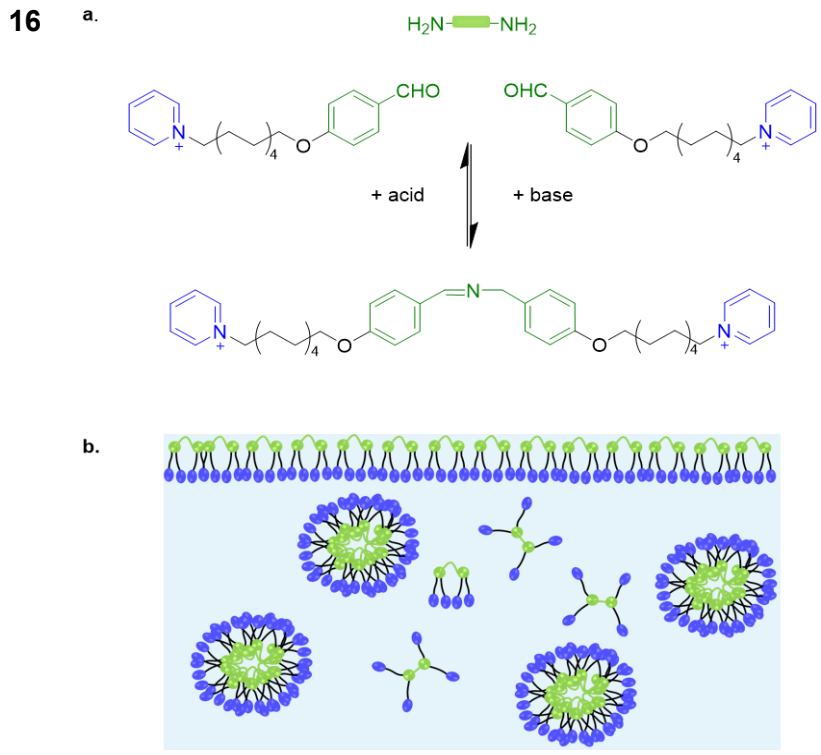

Figure 24 - Structures shown in **a** hydrolyse in basic conditions to form two bolaform amphiphiles; which combine together to form supra-amphiphiles with a "H" shape, **b** shows self-association structures formed in low concentrations inside water and at the water-air interface.[145]

Faustino et al have developed monomeric and dimeric surfactants (Figure 25) with the hopes of creating new biocompatible and biodegradable surfactants;[147] the anionic urea-based dimeric (gemini) surfactants derived from the amino acids are a particular area of interest as they hold potential to be a new class of antimicrobial, drug delivery, and transfection agents.[144,148,149] The study of compounds from this family of surfactants were shown to exhibit critical micelle concentrations (CMC) which were competitive with other more traditional carboxylate surfactants like sodium dodecanoate.[150] This was attributed to the hydrogen bonding properties of the urea functionality; these surfactants have increased acidity of the NHs and thus make it more favourable to self-assemble to form aggregates through HBA/HBD interactions.

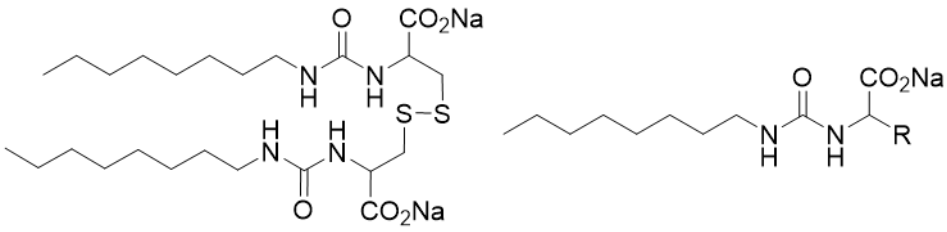

17 **18**

Figure 25 - Structures of the anionic urea-based surfactant derived from cysteine **17** and its monomeric counterpart **18** (Where R = CH_2SH; $CH_2CH_2SCH_3$; or CH_2SO_3Na).[147]

In 2016, Hiscock et al studied the self-associating properties of amphiphiles with modified sulfonate-urea salts and found that some of the amphiphilic salts showed promise for further study by displaying antimicrobial activity.[151] The general structure of the SSA can be seen in Figure 26, where the hydrophobic region contains R groups which can be finetuned to change the acidity of the amines. Research into SSAs with 'frustrated' systems (Figure 26) was conducted; as they possess the ability to adopt a variety of self-associative hydrogen bonding modes – but only one binding mode at a time, which is dependent on the environment and species present. An example is seen in Figure 27, an SSA which was found to form hydrogen-bonded complexes with halide anions, with affinities increasing with basicity; fluoride > chloride

> bromide. A series of ^{1}H NMR titrations with these anions showed a downfield change in chemical shift/peak broadening of the NH signals of resonances corresponding to the urea moiety. Hiscock et al found that in DMSO, the addition of competitive HBD compounds, or anionic guest species played a significant role in which binding mode dominated and thus the nanostructure formed.[151]

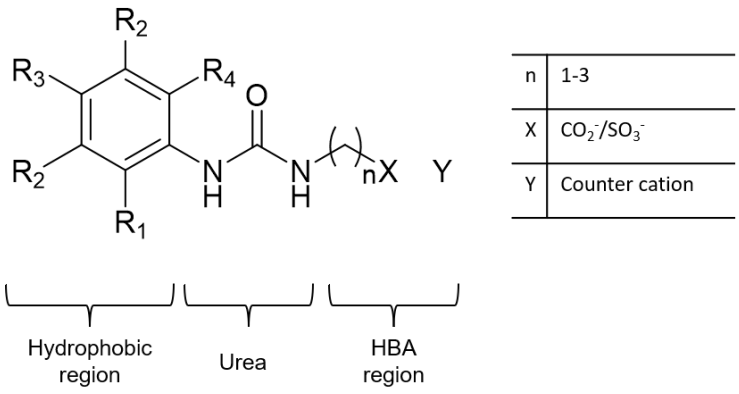

n	1-3
X	CO_2^-/SO_3^-
Y	Counter cation

Figure 26 - General structure of a frustrated self-associating amphiphilic system, first reported by Hiscock et al.[151]

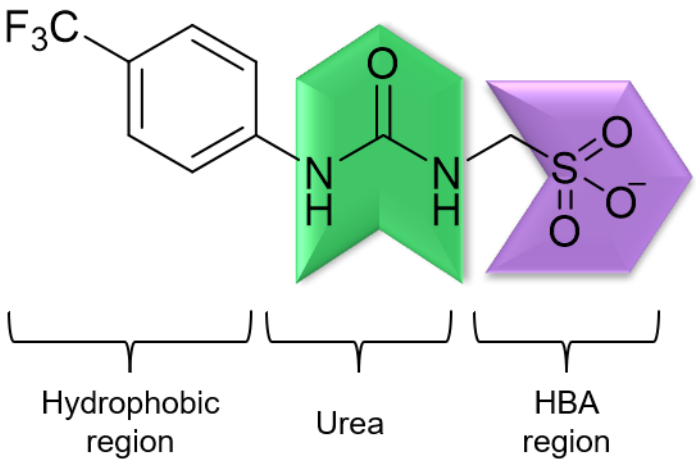

Figure 27 - Structure of TBA sulfonate urea salt, the structure of the TBA counter cation has been omitted for clarity. [151]

These amphiphiles are described as 'frustrated' structures, with four possible self-associative hydrogen bonding modes – which are unable to co-exist. Thus, the form of self-association which dominates and takes over is dependent on the balance of each respective

binding mode; ultimately influencing self-association and nanostructure formation. A general depiction of the two different categories of binding modes (urea-urea, and anion-urea) are show on Figure 28. For this class of SAs self-association can occur either via urea-anion or urea-urea hydrogen bonding. When binding takes place via a urea-urea motif; either a dimer or tape structure is formed, and when the binding is urea-anion; an *anti*-stacking or *syn*-stacking structure is formed. Utilising the self-associating nature of these molecules have made it possible for this class of compounds to form larger, supramolecular structures.[152]

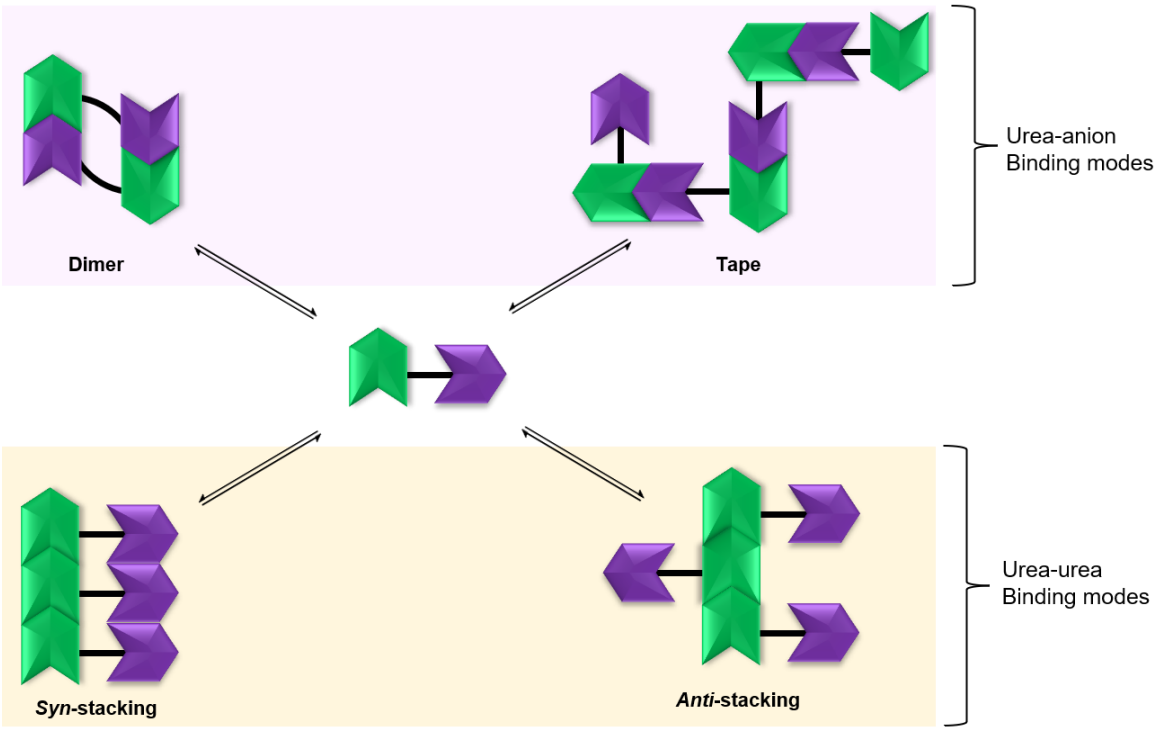

Figure 28 - Simplified diagram of the Urea-anion and Urea-urea binding modes displayed in amphiphiles utilising sulfonate-urea salt motifs.[151,152]

Amphiphiles designed with the inclusion of hydrophobic aromatic rings, and electron withdrawing/donating groups such as an amide or nitro group were also developed.[153] A part of this unique take on amphiphiles also involved the exchange of the urea moiety for a thiourea moiety. Self-association of low molecular weight amphiphiles were found to take place through hydrogen bonding,[154] the urea moiety on the amphiphile was found to be the hydrogen-bonding site.[155]

Overviewing the variations of supra-amphiphile topology so far published include; bola-forms (as discussed above),[112] multi-chain head-to-tail; where multiple tails can be present on either just one or both components of the amphiphile,[156] and polymeric supra-amphiphiles (which either utilise dynamic covalency or non-covalent interactions to hold two or more polymeric groups).[157] In 2019, research in polymeric amphiphiles provided useful headway for applications within cancer therapy, nanocarriers, and a new kind of surfactant.[158] It is difficult to imagine the potential of research yet to come regarding this versatile class of compounds; however, a small fraction can begin in this project understanding a new class of bi-pyridine incorporated SSAs.

1.5. Research project aims and objectives

1.5.1. Project aims

- To synthesise and study potential fluorescent sensors.
- To study the behaviour of a new class of SSAs synthesised by Dr Anna McConnel and Tjorge Neumann.

1.5.2. Objectives

1. To synthesise and characterise a set of potential fluorescent sensors **35**-**38** (Figure 40)
2. To carry out binding association studies on **35**-**38** to investigate anion binding selectivity through both ^{1}H NMR titration techniques and fluorescence titrations.
3. To further study compounds **35**-**38** and assess whether or not any selective binding influences fluorescence intensity.
4. To discern the self-associative properties of **39**-**42**.

2. Fluorescent pincer receptors

2.1. Introduction to fluorescence

Fluorescence, is best described as the emission of light caused as a result of light or electromagnetic (EM) radiation absorption by a material; with the resulting emission possessing a longer wavelength than that of the incident radiation. As such, it is defined as a form of luminescence; spontaneous light emission that is not caused by heat - "cold light" or "weak glow" from the Latin.[159] The etymology of the term 'fluorescence' can be tracked back to its use by the physicist Sir George G. Stokes, in 1852 he published a paper "*On the change of refrangibility of light*".[160] Where he described the "*property of glowing in ultraviolet light*" as he first observed the phenomenon by fluorspar (fluorine) and uranium glass, and combined it with an analogy of phosphorescence. In this publication, he also established the first rule of luminescence known as 'Stokes rule' - stating that the wavelength of luminescence is always longer than the wavelength of exciting radiation.[160] The molecule-specific change in wavelength - lowering of energy - observed from incident light to emitted/scattered light is named after him as the 'Stokes shift'. There are three categories of luminescence: chemiluminescence; a reaction triggered glow, fluorescence and phosphorescence; which are both triggered by light.

Simply by description, both radiative processes, fluorescence and phosphorescence sound fairly similar, as they are both types of photoluminescence (light triggered luminescence) however there is a distinct observable difference separating the two phenomena - the time it takes for emission and its duration. Phosphorescent materials are able to store the energy absorbed; delaying its release and producing an afterglow. When the initial radiation causes the molecule to go from a lower energy, ground state, to an excited state (sometimes a portion of this energy can be lost to non-radiative processes - such as collisions), as a result the molecule attains a lower vibrational energetic level. Upon return to its ground state, a photon of lower energy (longer wavelength) to the initial radiation is emitted. The average lifetime of the excited

state of fluorescent molecules is 10^{-8} seconds when it is undisturbed by collisions.[161] However, certain molecules can have an increased duration in a metastable excited state; this metastable state creates the emission delay; and thus, the difference between fluorescence and phosphorescence.[162] In the case of a higher energy photon being emitted, it is referred as 'anti-stokes radiation' but is fairly uncommon.[163] To better understand what is happening on a quantum scale, the Jablonski diagram (Figure 29) can be used.[164]

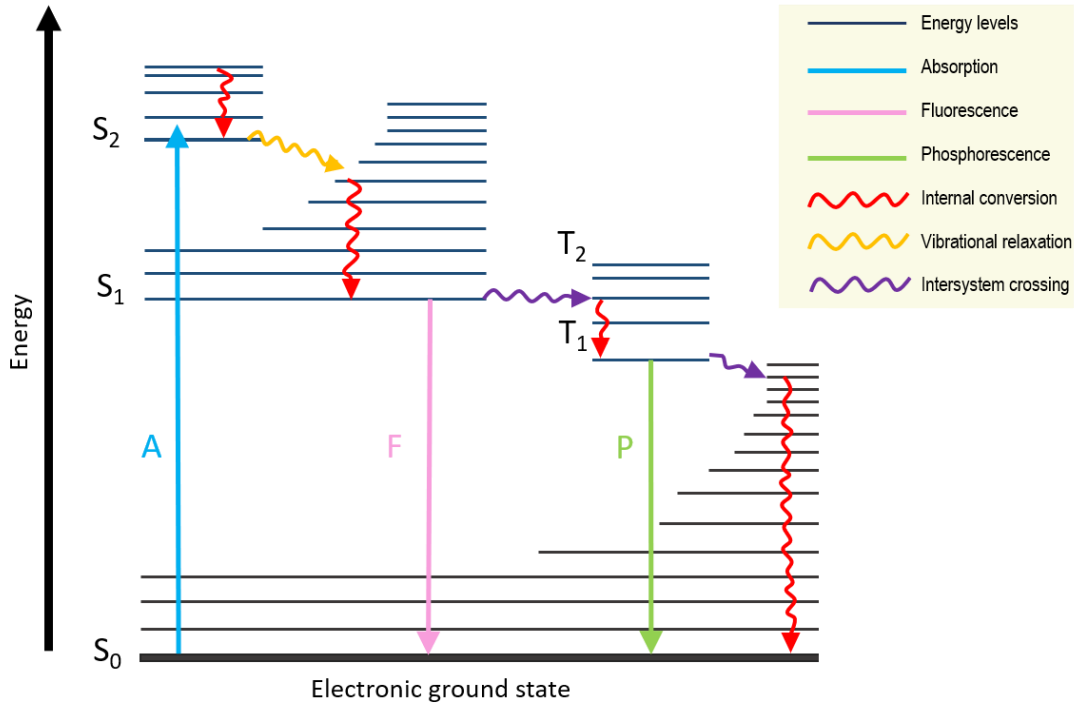

Figure 29 - A typical Jablonski diagram showing absorption (A) of a photon, exciting an electron from the ground state to a singlet state (S_2), with two modes of relaxation being displayed resulting in either 1. Fluorescence (F), or 2. Phosphorescence (P).

Fluorescence is described by a spin-allowed radiative transition between two states of the same multiplicity, as seen in Figure 29. Phosphorescence however, is a spin-forbidden radiative transition as it is between two states of different multiplicity. Commonly the energy of each respective photon released is notarised as follows – hv_f for fluorescence, and hv_p for phosphorescence, and is given by the formula seen in Equation 1.

$$E = hf = \frac{hc}{\lambda}$$

Equation 1 - Einstein's equation can be used to calculate the energy, E, of a photon. Where h; Planck's constant (6.63×10^{-34} Js), f; frequency of photon, c; speed of light in a vacuum (3×10^{8} ms^{-1}), and λ; lambda representing the wavelength of the photon in metres (m).

To understand to contributing factors for the phosphorescence and fluorescence, understanding the processes noted below is important;

Photoexcitation - The molecule absorbs light radiation; resulting in electronic excitation. This occurs via a molecule-bound electron absorbing the incident photon, taking it instantaneously (~ 10^{-15} sec) from a ground state (S_0) to an excited state (S_n). These excited states are unstable, and the electron is bound to relax back down to its ground state; energy may be dissipated via non-radiative processes.

Vibrational relaxation – A rapid non-radiative transition; lasting between 10^{-12} to 10^{-10} sec. This is a process by which the energy of vibrational relaxation is lost as heat to neighbouring molecules. This can be scripted as relaxation from higher vibrational levels (v = n) to a vibrationless state (v = 0); generally, the excited molecule will decay to the lowest vibrational level of the lowest excited state (usually the ground state).[165]

Internal conversion - Slightly faster than vibrational relaxation, 10^{-14} to 10^{-11} sec, internal conversion is also a non-radiative transition. Where a transition takes place from one electronically excited state (S_{n+1}) into a vibrational state of the same energetic level but with a lower excited state (S_n). This transition does not result in any dissipation of energy.

As the same electronic transitions are iterated from excitation to emission, the spectra of both events tend to resemble reflections of one another; often noted as the 'mirror image rule' of fluorescence (Figure 30).[166]

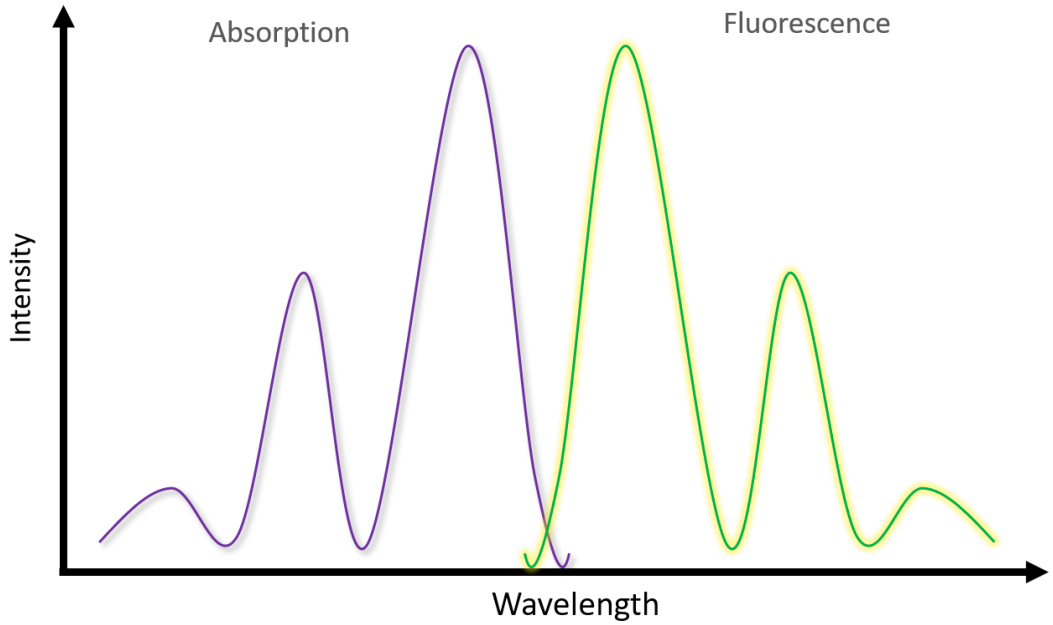

Figure 30 – A visual of the 'mirror-image rule', where the intensities and patterns are the same for both the absorption and fluorescence as wavelength increases (energy of photon decreases).

An electron in an excited state can dissipate all the initial energy absorbed solely through vibrational relaxation and internal conversion; leaving no energy for photon emission. The molecule will not fluoresce or phosphoresce in this case, and thus, the probability that these radiative effects will occur versus the probability of non-radiative relaxation gives us the quantum yield of a fluorophore - and allows for estimation on how brightly the molecule will shine.[167] The quantum yield of a fluorophore can be defined by the ratio of photons emitted to absorbed (Scheme 3).[168]

$$\Phi_f = \frac{Photons\ emitted}{photons\ absorbed}$$

Scheme 3 – Equation for fluorescence quantum yield, Φ_f, given by the ratio of photons emitted to photons absorbed.

However, it is slightly more complicated than this. The single quantum yield for fluorescence of a fluorophore can also be defined as the rate of photon emission events over the sum of rate constants of all de-excitation events. The full scope of these de-excitation pathways for the fluorophore will go beyond just the paths involving fluorescence emission. Of which, each pathway has an associated quantum yield between 0 and 1; with the sum of all paths' quantum yields being 1. The other differences in the other de-excitation pathways can be observed by measurement of the heat emitted, and differences in emitted photon energy.[169]

There are many families of fluorescent compounds, most often, fluorophores will have highly conjugated polycyclic systems; providing essential delocalised electrons to jump up a band to stabilise energy absorbed from incident light. Some common examples of fluorophores are seen in Figure 31.[170–173]

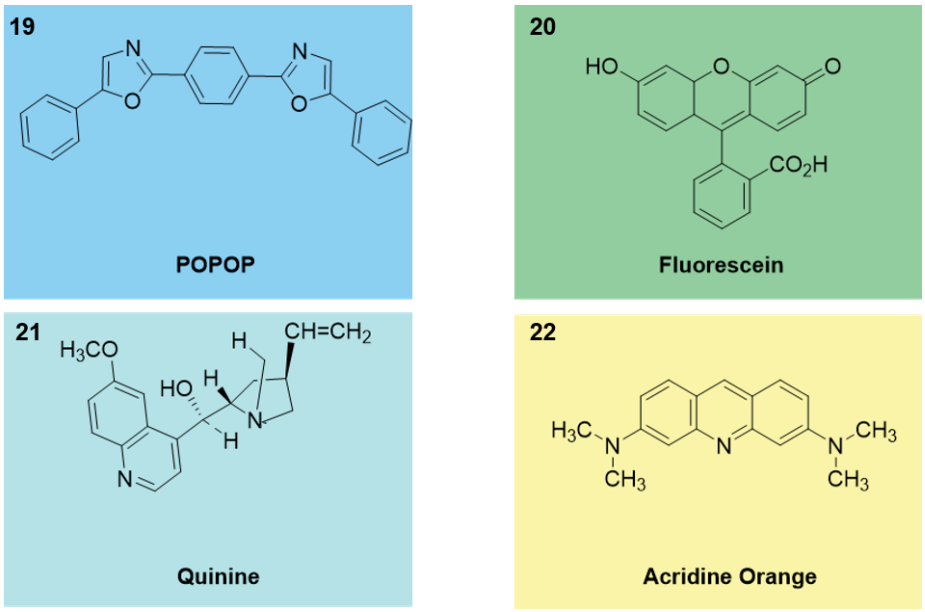

Figure 31 - Structures of various fluorophores with their corresponding colours of fluorescence. **19**; 1,4-bis(5-phenyloxazol-2-yl) benzene is used as a wavelength shifter,[173] **20**; used as a fluorescent tracer,[170] **21**; used as malaria medication and as a fluorescence standard,[172] and **22**; used for cell-cycle studies due to its ability to permeate cell membranes.[171]

2.1.2. Examples of fluorescence applications

Since its discovery, fluorescence has provided groundwork for a variety of applications; from simple lighting to a variety of sensors and uses for biologists and chemists alike;[174–176] the presence of fluorescent functionalities allows for non-destructive monitoring, analysis and sensing. This is particularly useful in bio-applications and application within the medical field. Autofluorescence is an intrinsic fluorescence already present in many proteins and small molecules inside cells presented when excited with ultraviolet (UV) light;[177] well-known examples include tryptophan, chlorophyll, nicotinamide adenine dinucleotide (NAD) (Figure 32),[178] and green fluorescent protein (GFP) (Figure 33).

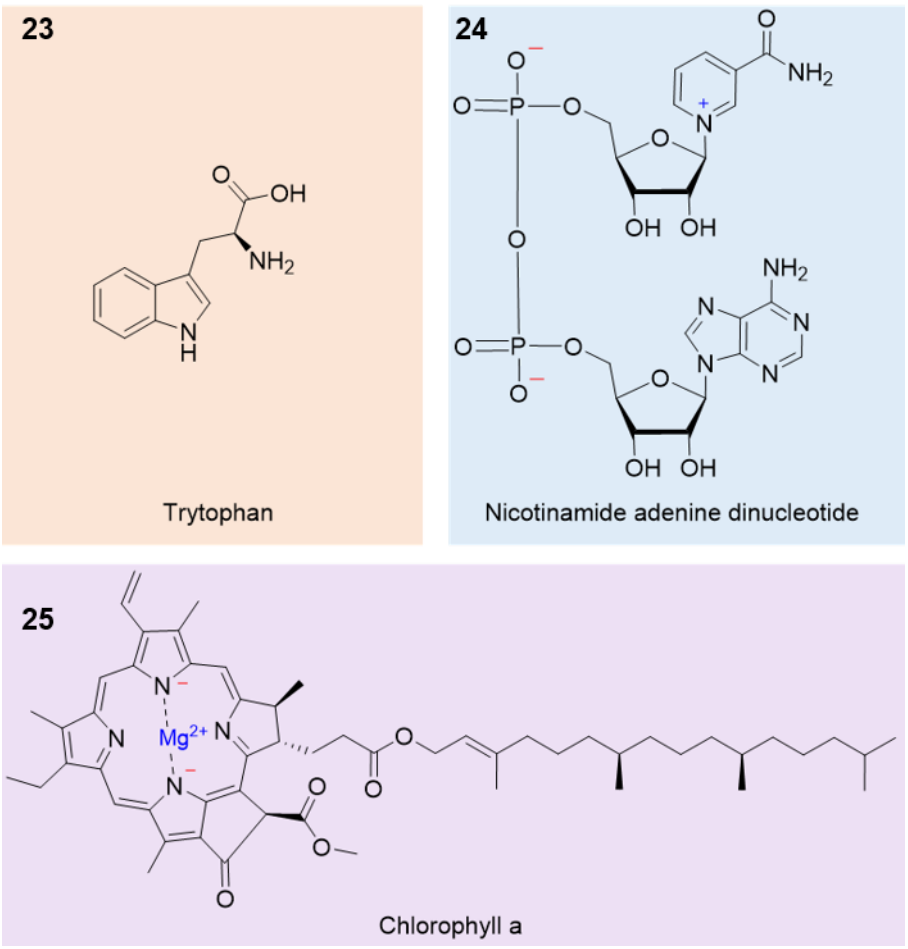

Figure 32 - Structures of autofluorescent compounds tryptophan **23**, (NAD) nicotinamide adenine dinucleotide **24**, and chlorophyll a **25**.[179]

GFP was first extracted and purified from the jellyfish Aequorea Victoria in 1962 by Shimomura et al;[180] this protein was later also found to be present in a variety of corals, sea anemones, and other aquatic organisms.[181] The aequorin was found to interact with Ca^{2+} ions, to induce a blue glow - which would result in a shift towards green when a portion of the luminescent energy was transferred to the GFP.[182] It wasn't until later in 1992 when the greater potential of GFP began to emerge - where Prasher et al reported the cloning and nucleotide sequence of the fluorescent gene.[183] With further studies from various groups, eventually the derivative of the GFP in which the cofactors specific to the jellyfish for fluorescence was no longer necessary.[184,185] These developments found that the GFP could fluoresce when it folded at room temperature.

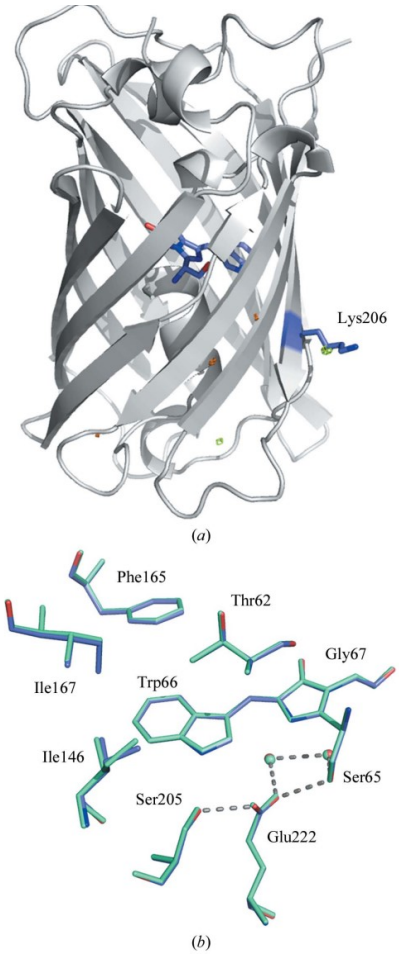

Figure 33 - Structure of a GFP variant; mTurquoise (a) with tryptophan-based chromophore shown in blue. Material reproduced with permission of the International Union of Crystallography, according to the terms and conditions of use of material published by the International Union of Crystallography.[181]

GFP and other fluorescent proteins alike can be attached to other proteins. A unique use of GFP is as a 'reporter gene', where the protein can be attached to a host to measure toxicity levels of various chemicals in a given environment;[186] this is particularly useful as the addition of GFP was found to have no effect on the host's cellular environment, this also meant that no stains, ATP, or cofactors were necessary for measuring such toxicity levels. A study by Song, Kim, and Seo in 2016 found that in GFP bound cells, there was a significant decrease in cellular density and fluorescence as levels of pollutants in the environment were increased.[187]

Similarly, zebrafish with expressive GFP was also used to study nanoparticle toxicity back in 2012 too.[188]

Fluorescence microscopy is a tool widely utilised by geologists too, for example to study coal, where traces of autofluorescent substances were indicative of the presence of impurities.[189] Geologists also use fluorescence microscopy to study the thermal maturity of a sample; assessing the number of changes caused in organic matter within rock layers due to heat.[190]

Zhujun and Seitz in 1983 published a study on creating fluorescent sensors for pH ranges (6.5 to 8.5 pH). The sensor was prepared by using an anion-exchange membrane to immobilize the trisodium salt of 8-hydroxyl-1,3,6-pyrene trisulfonic acid. Rapid deprotonation of the sensor occurred when electronically excited; and with both the acidic and basic counterparts of the sensor being fluorescent, pH values between 6 and 9 were able to be quantified in corelation to the ratio of fluorescence intensity at selective wavelengths for each counterpart of the sensor.[191]

These examples are just the tip of the iceberg for fluorescent sensor applications; with studies in selective glucose sensing,[192] drug sensing such as cocaine,[193] sensing lead (Pb^{2+}) in living cells,[194,195] other toxic heavy metal sensors,[195–200] and countless other applications.[201]

Common families of well-studied organic fluorophores include; azobenzene, cyanine, pyrene, coumarin, and many others (Figure 34).[202] Many organic fluorophore motifs are found in fluorescent dyes- also referred to as reactive dyes or fluorophores; they differ from fluorescent proteins as they provide higher photostability and shine brighter, they also do not require time to mature.

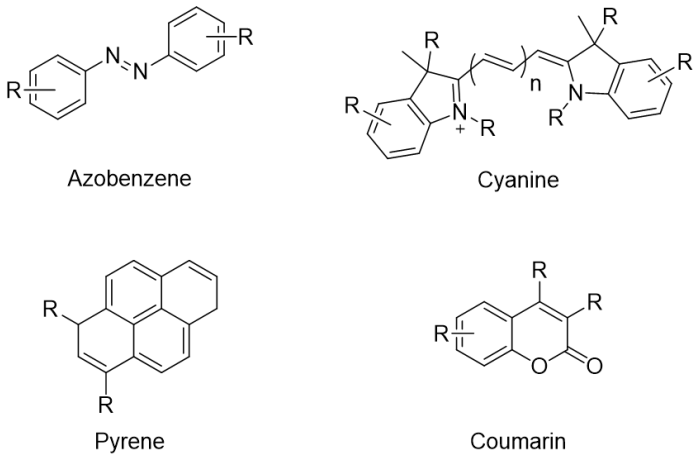

Figure 34 – Examples of common families of fluorophores: azobenzene, cyanine; (where n = 1-3) pyrene; and coumarin.[203]

Fluorescent dyes are often used by biologists by creating antibody conjugates or peptide tags to target a protein; but due to this process requiring the fixation of the cell being studied, any dynamic aspects of the cell cannot be observed.[204] Fluorescent dyes, such as Rhodamine WT (Figure 35), have been used previously to track and monitor the movement of water and solutes in rivers and groundwater; with the earliest record of such use dating back to 1877, this method has since been used to also monitor water-quality in corelation to hurricanes, floods, and algal blooms.[205]

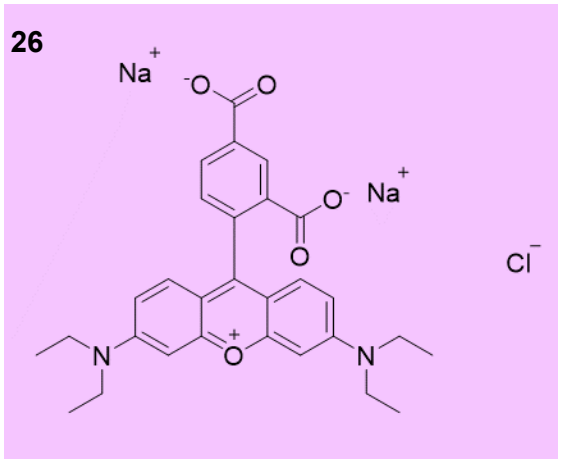

Figure 35 – Structure of rhodamine WT; with its corresponding colour of fluorescence in the background.[205]

Up to over 50 years ago, the fluorescent dye resazurin was commonly used to monitor bacterial and yeast contamination (as well as semen quality); known as the 'resazurin reduction

test'; where the blue nonfluorescent dye is reduced to a highly fluorescent pink derivative - which can also be further reduced to an uncoloured and nonfluorescent derivative (Scheme 4).[206]

UK scientists, O'Brien, Wilson, Orton, and Pognan have investigated the use of Alamar blue, **27a**, to measure mammalian cell cytotoxicity. This was particularly useful as the dye did not harm the cells. They found that a weaker fluorescent signal was produced in dying cells.[206] Biologists have also used the fluorescent dye thioflavin T to examine amyloid fibrils in vitro; where it's absence would result in weak fluorescence and vice versa.[207]

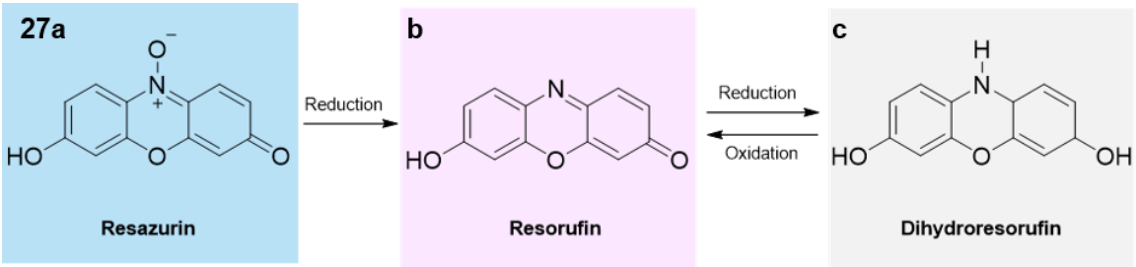

Scheme 4 – Showing reduction of weakly fluorescent resazurin **27a**, to highly fluorescent resorufin **27b**, finally to non-fluorescent dihydroresorufin **27c**.[206]

As different fluorescent dyes can have different dependency factors; researchers have even utilised temperature dependent fluorescence intensity to measure temperature of microfluidic systems.[208] Notably, collagen also displays temperature dependent fluorescence which has been used as a molecular probe.[209] Fluorescent dyes are also often used in organic light-emitting diodes (OLEDs), common compound derivatives include perylene, quinacridone, and rubrene.[210]

2.2. Pincer receptors

Although in modern chemistry a pincer ligand is generally categorised as 'a chelator that binds to three adjacent coplanar sites on the metal centre' (Figure 36)[211] these highly researched class of compounds can also utilise a pyridine-2,6-dicarboxamide motif for selective detection of cations. A number of fluorescent arene and pyridine-2,6-dicarboxamide-based chelating pincer receptors have already been developed by Gupta and co-workers as selective cation detectors; with their anthracene-based receptor showing particularly high selectivity for Fe(II) and Fe(III) ions (Figure 37).[212,213]

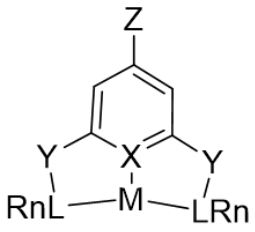

Figure 36 – General structure of a traditional pincer ligand: typically, X = C,N; Y = $(CH_2)_n$, O, NH; L = P,N,O; Z = Halogen, R, RO.

Pincer **28** displayed a significant emission at 440 nm in several solvents (including THF, MeOH, and MeCN). In THF, various metals ions were aliquoted up to 10 equivalents to asses effect on fluorescence of receptor; Fe^{2+} and Fe^{3+} showed selectivity and fluorescence quenching over all the other ions tested – Na^{+}, Mg^{2+}, Ca^{2+}, Cr^{3+}, Mn^{2+}, Mn^{3+}, Co^{2+}, $Ni^{2+,}$ Cu^{2+}, Zn^{2+}, Hg^{2+}, Cd^{2+}, and Pb^{2+}. In order to further assess the competitiveness for the iron cations, Gupta and co-workers conducted a series of binding studies in THF, finding that none of the metal ions tested were able to effectively interfere with the binding with Fe^{2+} and Fe^{3+} ions; confirming that even in the presence of different ions, **28** was still a selective sensor for Fe ions. The Stern-Volmer constant (K_{SV}) was 4.94 x 10^3 for Fe(II) with a detection limit of 11.27 µM, and 1.48 x 10^4 for Fe(III) with a detection limit of 5.56 µM. When **28** was binding to Fe^{3+} a 1:1 stoichiometry was reported.[213]

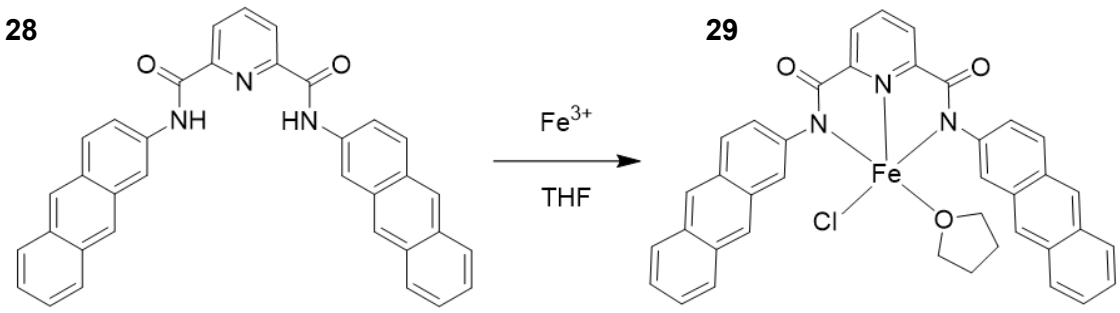

Figure 37 – Structure of one of the fluorescent detectors for cations Fe^{3+} and Fe^{2+} **28**, and fluorescent inactive pincer ligand **29** when bound to Fe^{3+} in THF developed by Gupta and co-workers.[213]

As the field further developed and grew, the potential of pincers as anion sensors began to emerge. Today, amide-based receptors can be seen in anion sensing, extraction, and transport.[214–216] Often these pincers will be meta-substituted with hydrogen bond donating groups, like amines, ureas and thioureas, and indoles to extend the chelating site. Following the studies of Crabtree[217] and Smith[218] on the inclusion of indole and biindole groups for high anion affinity and selectivity; The works of Jeong and co-workers[219] and Sessler and co-workers[220] on 2,6-dicarboxamidopyridine skeleta for receptors – both concepts were merged later on in 2007.[221]

A series of fluorescent group containing anion receptors were successfully synthesised by Gale and co-workers; among which included highly selective fluoride anion receptors **30** and **31**.[221–223] The two receptors were found to favour fluoride over other putative anion guests (such as acetate, dihydrogen phosphate, chloride, benzoate) after a series of binding studies were performed. A stability constant of 1360 M^{-1} for the binding of **31** to fluoride in a 1:1 binding model; and stability constants of K_1 = 940 M^{-1}, and K_2 = 21 M^{-1} in a 1:2 (receptor:anion) binding model was observed for **30**. Although analysis of the crystal structure revealed that both receptors adopted a 'twisted' conformation when bound to fluoride, **30** was found to have slightly longer hydrogen bonds to fluoride as well as a short interaction between the isophthalamide CH group in position 2 of the central aromatic ring.[220]

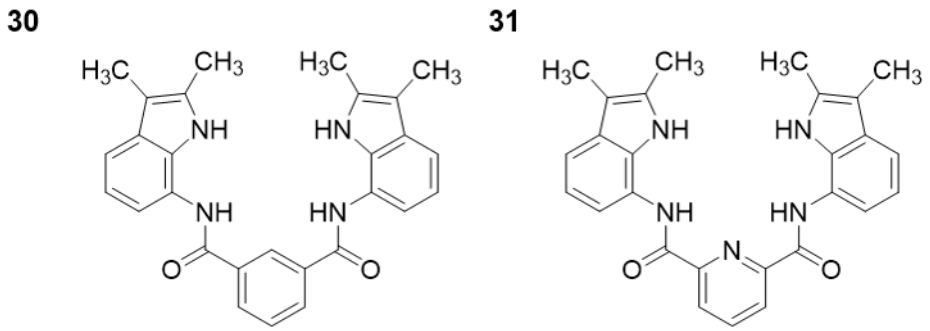

Figure 38 – Structures of the receptors synthesised by Gale and co-workers.[221]

Yatsimirsky and co-workers have also developed a range amide-based fluorescent receptors for sensing of anions in water of which the N-methylated quinolinium groups were found to show high affinity towards small ions and neutral guests such as ureas and amides, and other receptors showed high selectivity to pyrophosphate and nucleotides (Figure 39).[77]

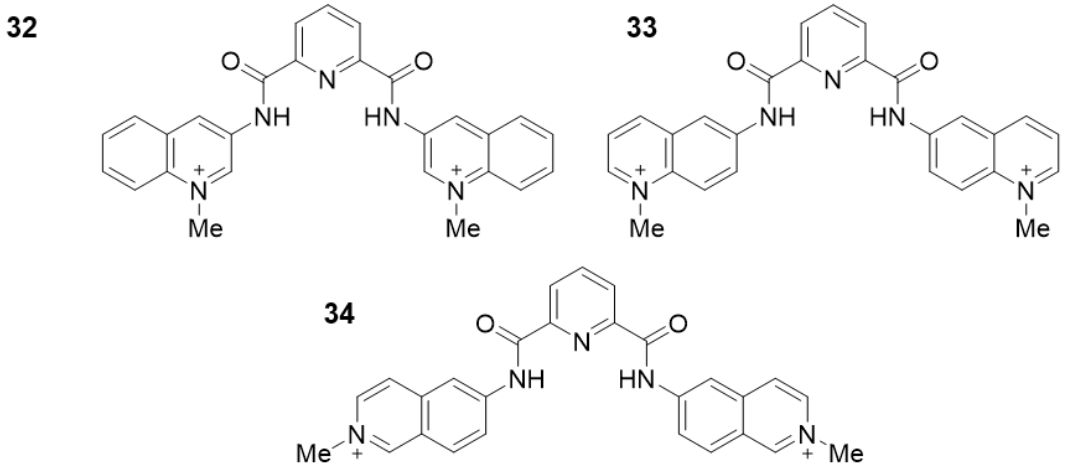

Figure 39 – Structures of pyridine-2,6-dicarboxamide based sensors with N-methylated quinolinium groups.[77]

Different positions of the N-methylated groups were used in order to observe the effect on binding these variations electronics posed. Upon analysis of crystal structures of the receptors, the counter-ion binding of **32** was found to involve multiple short contacts/H-bonds with N–H and C–H donors, whereas **33** showed only use of N-H donors, and **32** appeared to include, in the cleft between the amide groups a cluster of 3 water molecules – where the counter-ions were bound. By observing the chemical structures of these receptors, some of these findings should be of no surprise; **32** anion-binding utilises both the dicationic nature of

the receptor as well as reinforcing hydrogen bonding; and **34** anion-binding is dominated by its dicationicity as it is a stronger interaction, and being further from the 'cavity', ultimately outcompeting the N–H and C–H donors. Significant fluorescence quenching was observed by both **32** and **33** by binding to acetate, halide, pyrophosphate and nucleotide anions, as well as minor quenching in the fluorescence of **34** with these anions.[77]

In 2013, Bowman and co-workers produced a series of six palladium pincer complexes, including synthesis of the NNN pincer **36** (Figure 40), and researched as a detector for (CEES) 2-chloroethyl ethyl sulfide – a simulant for the chemical warfare agent sulfur mustard. [224]

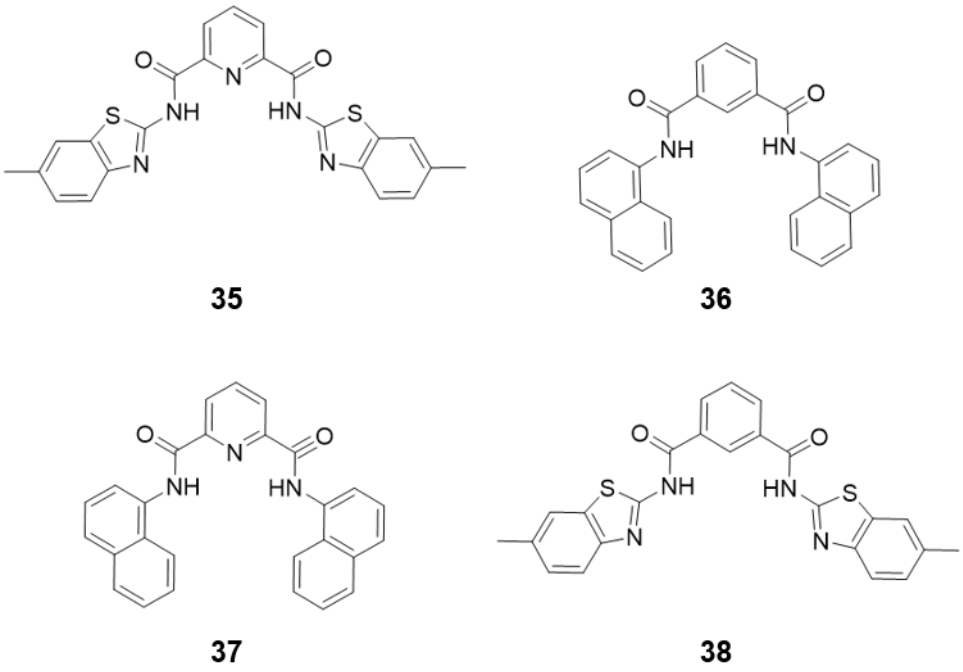

Figure 40 – Receptors **35-38**, utilising NCN and NNN scaffolds and fluorescent R groups.

Here-in, inspired by the works of Gupta and co-workers,[213] as well as Bowman and co-workers,[224] fluorescent pincers (**35-38**) were synthesised in the hopes of further merging anion pincer receptor chemistry and fluorescent sensing chemistry. The receptors synthesised have varying amide substituents - the incorporation of the larger aromatic systems was to increase steric hinderance and electronic interactions; in order to encourage size-related anion binding events – and thus anion size-related selectivity. To incorporate fluorescent sensing potential, commonly used fluorescent, aromatic moieties were chosen as R groups. The inclusion of both

pyridine-2,6-dicarboxamide and isophenyl-dicarboxamide was to test the effects of the pyridine nitrogen on anion binding selectivity and fluorescence, if any. A series of studies were carried out to discern whether or not the receptors showed selectivity for any anions, and whether or not the changes in electron distribution created by these binding events affected the fluorescence of the naphthalene and benzothiazole groups. To ensure that any potential changes in fluorescence activity were driven by binding events, ^{1}H NMR deprotonation studies were also carried out to follow shifts in ppm of peaks of HBDs or protons near the binding cavity, as well as titrations on the fluorimeter to follow fluorescence intensity.

2.3. Solution state studies

For all of the tests carried out on receptors **35-38**, the chosen solvent was DMSO and DMSO-d_6 aliquoted with 0.5 % water; to maintain water content of the hygroscopic solvent throughout experiments. This solvent was chosen for a number of reasons - due to solubility limitations in most organic solvents, availability of deuterated solvent, interference with expected ^{1}H NMR peaks, and the introduction of a competitive species into the environment; to increase validity of any data on observed binding selectivity. The following solution state studies utilise ^{1}H NMR titrations to observe effects on the amide NH and aryl protons on the potential binding site, and also utilise fluorimeter titrations to test for sensor potential with any of the anions studied.

2.3.1. Deprotonation studies

For this project it was important to carry out a series of studies pertaining to both NMR and fluorimeter studies to investigate whether or not the deprotonation of the amide groups were the cause of changes in chemical shift or changes in fluorescence intensity. For this purpose, TBA OH^- was aliquoted into a solution of the receptor and observed up to six guest equivalences. If the data shows that when deprotonated these qualities of the receptor remain

unchanged, then changes in chemical shift during ^{1}H NMR titrations, and changes in fluorescence intensity in adding guest anions are better supported to be as a result of a binding event.

In the deprotonation of **35** (Figure 41), at 2.5 OH^- guest equivalences, the NH peak observed at 13.55 ppm disappears, and the peaks observed in the aromatic region (highlighted in the blue box) were found to shift an overall of 0.32 ppm upfield. This effect can be expected to be caused by the receptor going from a neutral species to a dianionic species; resulting in a shift in electron distribution in the structure away from the electron-donating nitrogen atom on the pyridine ring. Similarly, the NH peak in **36** is also observed to disappear (Figure 42), but instead of an upfield shift of the aromatic protons (highlighted in the blue box), a downfield shift of 0.14 ppm was found from the data presented. There are a number of factors to consider as to why this may be happening; but to view the whole picture, examining the deprotonation stack of **37** in Figure 43 is essential. Receptor **37** was found to show an upfield shift of 0.12 ppm at 5 equivalences of TBA OH^- added. The two compounds only differ by one atom – the presence of an N-H on the core of the receptor between the fluorescent substituents, or the presence of a C-H. Some factors which may be contributing to the difference in the direction of signal shift may be due to the electronic effects caused by the differences in electronegativity between the two atoms - carbon being less electronegative (Pauling scale 2.55) than nitrogen (3.04); posing a difference of electron redistribution the hydrogen bond on the carbon; making the scaffold a little less accessible or creating more steric as the molecule becomes dicationic, or maybe the presence of hindrance.

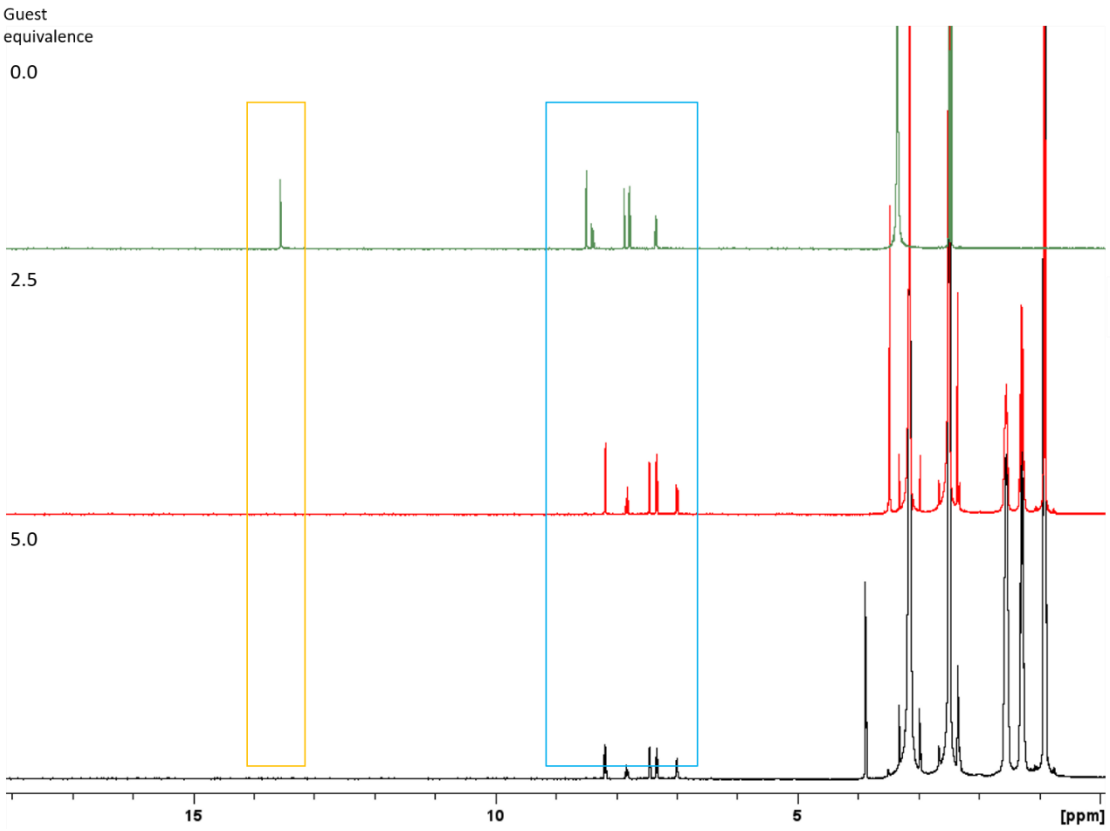

Figure 41 - Enlarged ^{1}H NMR stack plot of compound **35** in a DMSO-d_6 0.5 % H_2O solution. TBA OH^- in MeOH solution was titrated in, guest equivalences stated on the left. NH region is highlighted in yellow, and the aromatic region is highlighted in blue.

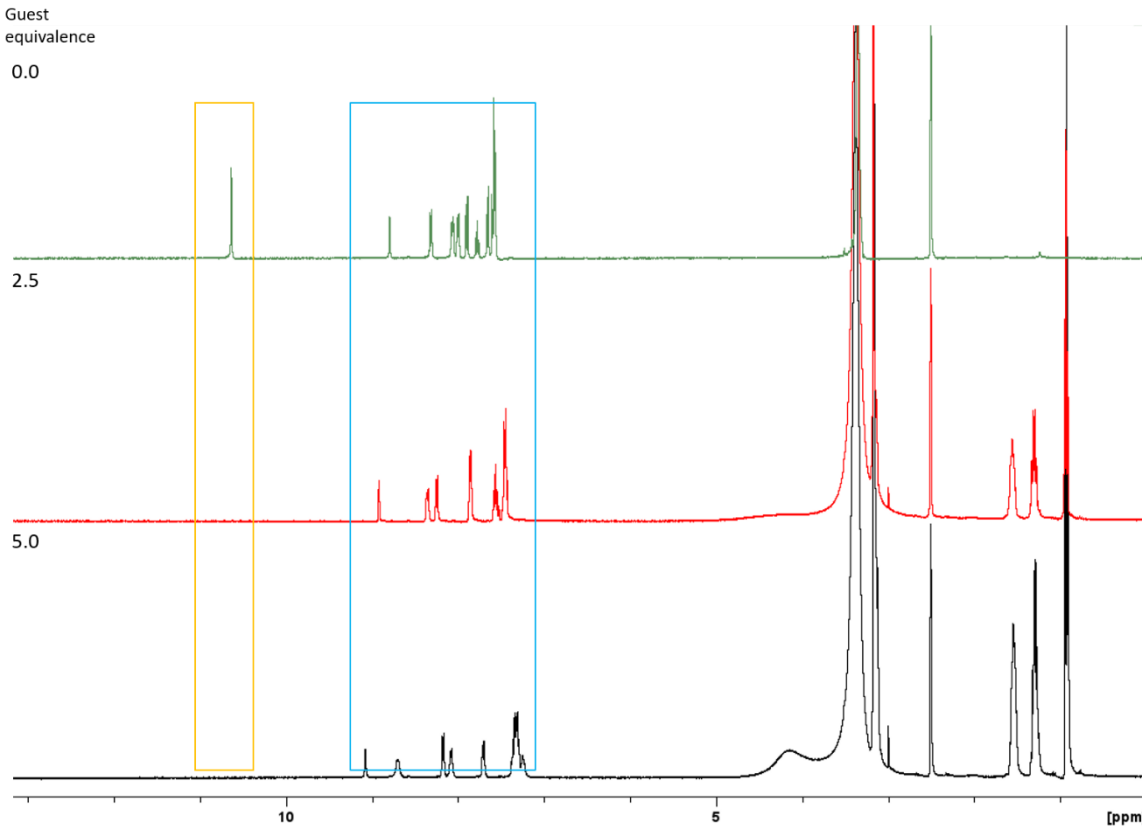

Figure 42 - Enlarged ^{1}H NMR stack plot of compound **36** in a DMSO-d_6 0.5 % H_2O solution. TBA OH^- in MeOH solution was titrated in, guest equivalences stated on the left. NH region is highlighted in yellow, and the aromatic region is highlighted in blue.

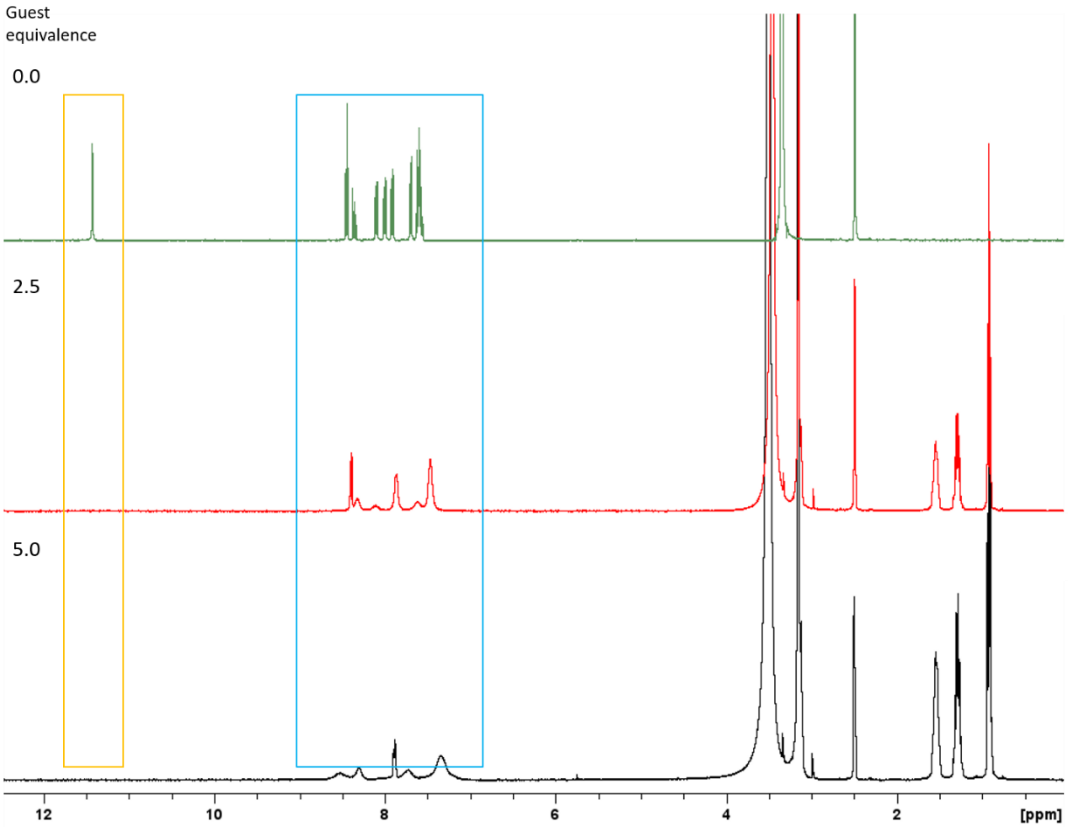

Figure 43 - Enlarged ^{1}H NMR stack plot of compound **37** in a DMSO-d_6 0.5 % H_2O solution. TBA OH^- in MeOH solution was titrated in, guest equivalences stated on the left. NH region is highlighted in yellow, and the aromatic region is highlighted in blue.

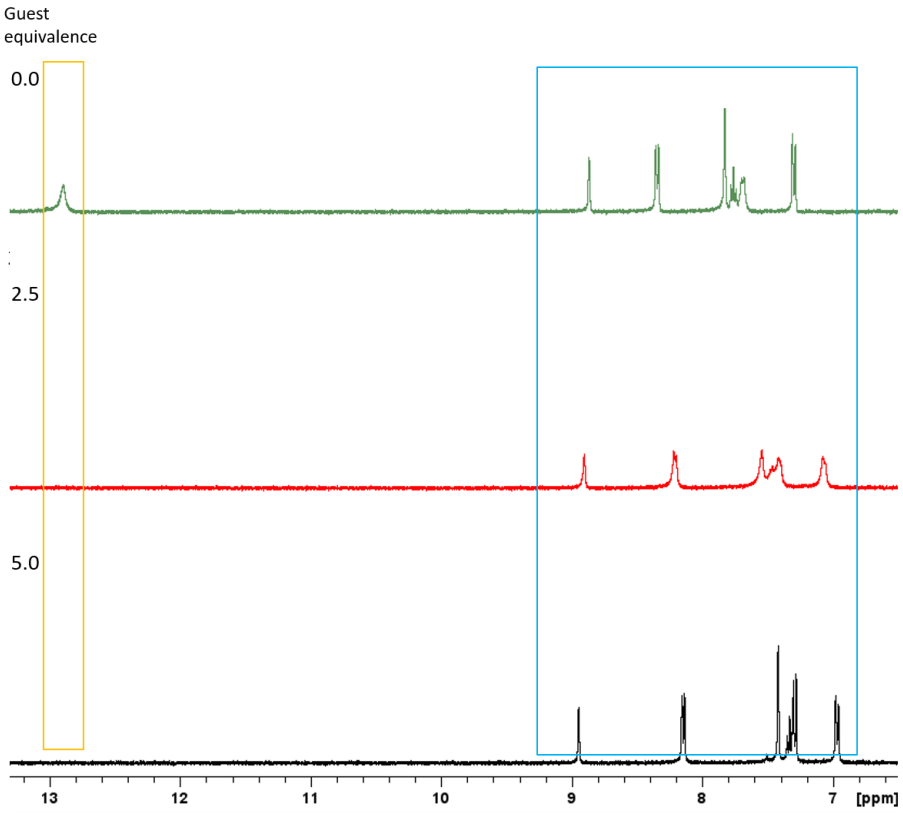

Figure 44 - Enlarged ^{1}H NMR stack plot of compound **38** in a DMSO-d_6 /0.5 % H_2O solution. TBA OH^- in MeOH solution was titrated in, guest equivalences stated on the left. NH region is highlighted in yellow, and the aromatic region is highlighted in blue.

It's important to note that the data was collected in increments of 2.5 guest equivalences, but the full deprotonation of the amide groups would be expected to be observed at 2.0 guest equivalences.

Referencing back to Figure 41 for the stack plot of **35**, we can also compare this data to that of **38** shown in Figure 44. As expected, the NH peak diseappears upon addition of 2.5 guest equivalences, but the aryl protons observed in the blue box move up field 1.02 ppm, whereas **35** showed a change in chemical shift of 0.12 ppm upfield. The disparity in the data collected from the two benzothiazole containing receptors, is much smaller than that of the the two naphthalene contaning receptors – however this still confirms that undoubtedly there still is an effect, even if minor, of replacing the N with the C-H in the scaffold. The cause of this, again, may be due to variances in electronegativity – but also the nature of the benzothiazole

substituent, the N-C-S may be stabilising the new dicationic structure. Given that the deprotonation event is expected to be complete for both amides, Figure 45 shows a slight plateau in the increase of fluorescence intensity at 2 equivalences – albeit minor. However, the continuation of the steady incline suggests that these may be due to other interactions taking place witht the guest species, especially past the point of deprotonation of **35**. The fluorescence intensity deprotonation graph for compounds **37** and **38** have been omitted due to the overall in fluorescence instensity obersved being < 10, approaching a highly miniscule and sensitive scale.

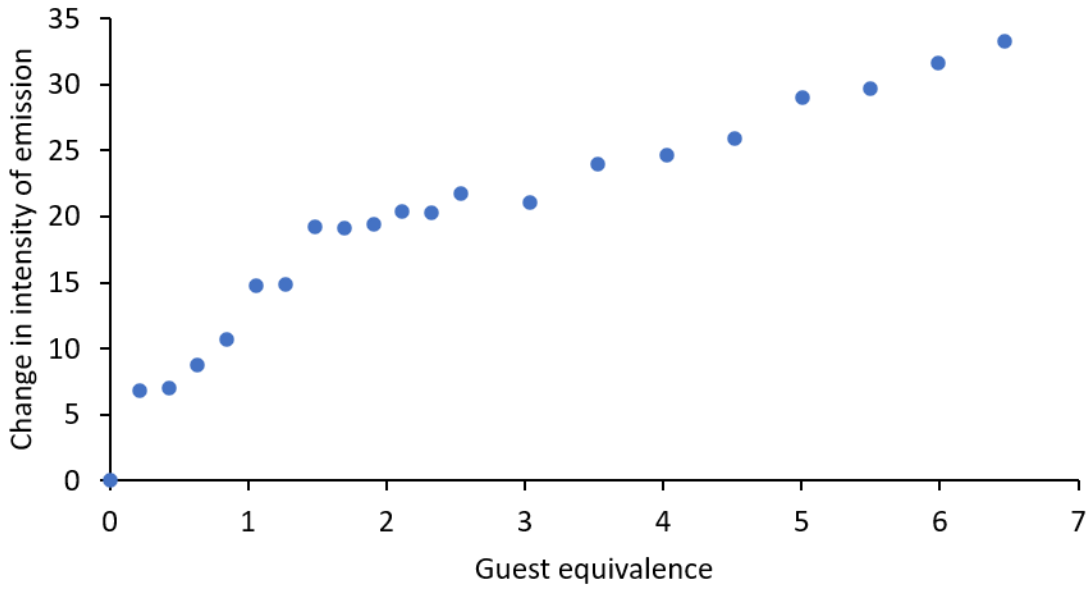

Figure 45 - Graph showing change in intensity of emission at 400 nm of **35** upon the addition of TBA OH^- in DMSO /0.5 % H_2O solution at 298 K.

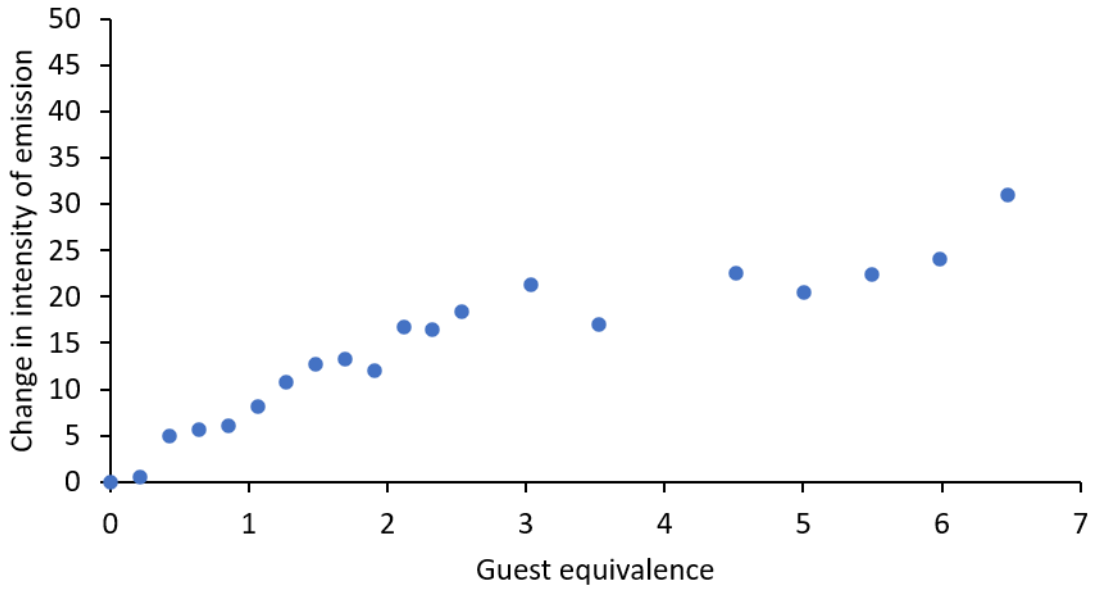

Figure 46 - Graph showing change in intensity of emission at 340 nm of **36** upon the addition of TBA OH^- in DMSO /0.5 % H_2O solution at 298 K.

Due to the scale of increase in fluorescence intensity in Figures 45 and 46 for receptors **35** and **36** respectively, being almost equally as small as the omitted results, there's no way to define a definitive cause of this change in fluorescence. However, what can be concluded, is that no significant change of fluorescence occurs in these receptors upon deprotonation.

2.3.2. Anion binding studies

A series of anions were selected to be tested for binding with receptors **35-38**, the guest species as a TBA salt (0.075 M) were titrated into a solution of the receptor (0.005 M). The chosen anions (benzoate, dihydrogen phosphate, sulphate, hydrogen sulphate, and chloride) covered a range of geometries, anion sizes, and charge densities to provide a better general understanding for what type of anion the receptors may exhibit binding selectivity towards.

2.3.3. ^{1}H NMR titrations

In order to better establish the strength of host-guest complexes in a solution of DMSO/0.5 % H_2O at 298 K, a series of ^{1}H NMR titrations were conducted with the receptors. The amide protons and aryl protons were followed via the change in chemical shift in the ^{1}H NMR spectra collected upon each subsequent addition of guest species to the receptors. The changes

in chemical shift collected from the spectra were input to Bindfit v0.5 (http://app.supramolecular.org/bindfit/) to calculate association constants;[225] testing for 1:1, 1:2, and 2:1 (host:guest) binding isotherms. This was done to provide a guide for identifying binding stoichiometry, and to alleviate the problems that may be faced with the use of Job plots to provide similar information. Receptor **35** showed great promise as a selective anion receptor for dihydrogen phosphate (Table 3), with a moderate 1:1 association constant of 24 M^{-1} (± 8 %), derived from aryl protons as a proxy for the NH peak signal which was not visible after the first addition due to peak broadening into the baseline.

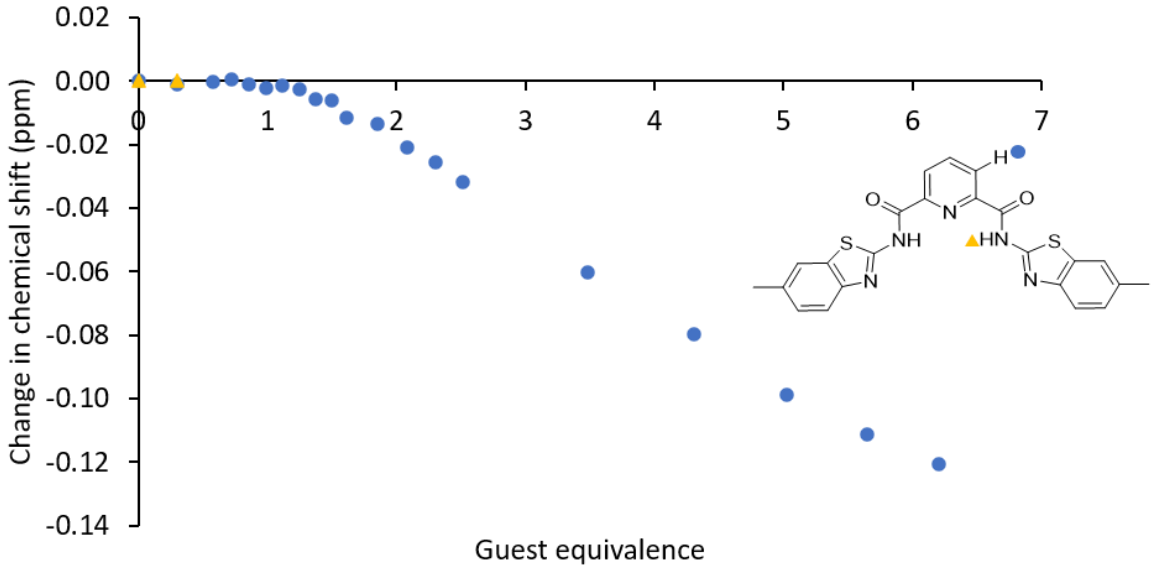

Figure 47 - Change in chemical shift for the NH and CH resonances of **35** (host) upon the addition of TBA dihydrogen phosphate (guest) in DMSO-d_6/0.5 % H_2O at 298 K. The 1:1 binding association derived from the ArH change in chemical shift, K_{ass} = 23.74 M^{-1} ± 7.94 %.

Upon the addition of TBA dihydrogen phosphate, **36**, has a weak 1:1 binding association constant of 10 M^{-1} ± 4 % when derived from the change in chemical shift of NH, and an association of 9 M^{-1} ± 9 % when derived from change in chemical shift of an aryl CH on the scaffold (Figure 48). When comparing the data sets between the addition of dihydrogen phosphate, the scale of the axis is important; to assess the extent of the effect of anion binding on either receptor. Receptor **37** showed selectivity when binding to hydrogen sulfate anion in a

1:1 binding event with an association constant of 57 M^{-1} (± 9 %) derived from the change in chemical shift of the amide protons (Figure 49).

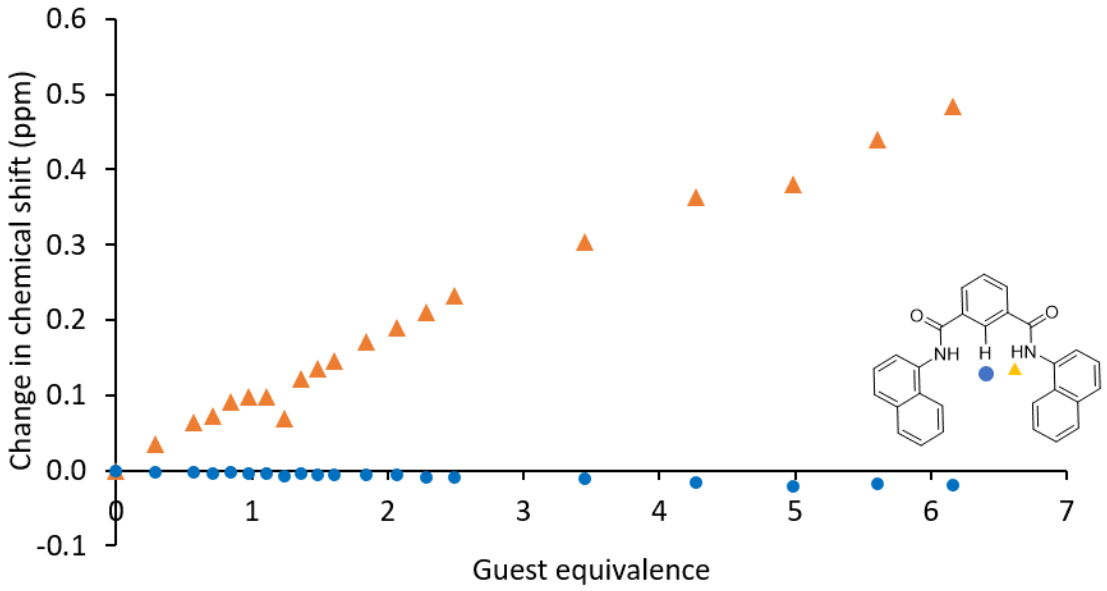

Figure 48 - Change in chemical shift for the NH and CH resonances of **36** (host) upon the addition of TBA dihydrogen phosphate (guest) in DMSO-d_6/0.5 % H_2O at 298 K. The 1:1 association constant derived from the NH change in chemical shift, K_{ass} = 9.58 M^{-1} ± 3.56 %, and the ArH change in chemical shift K_{ass} = 9.22 M^{-1} ± 9.31 %.

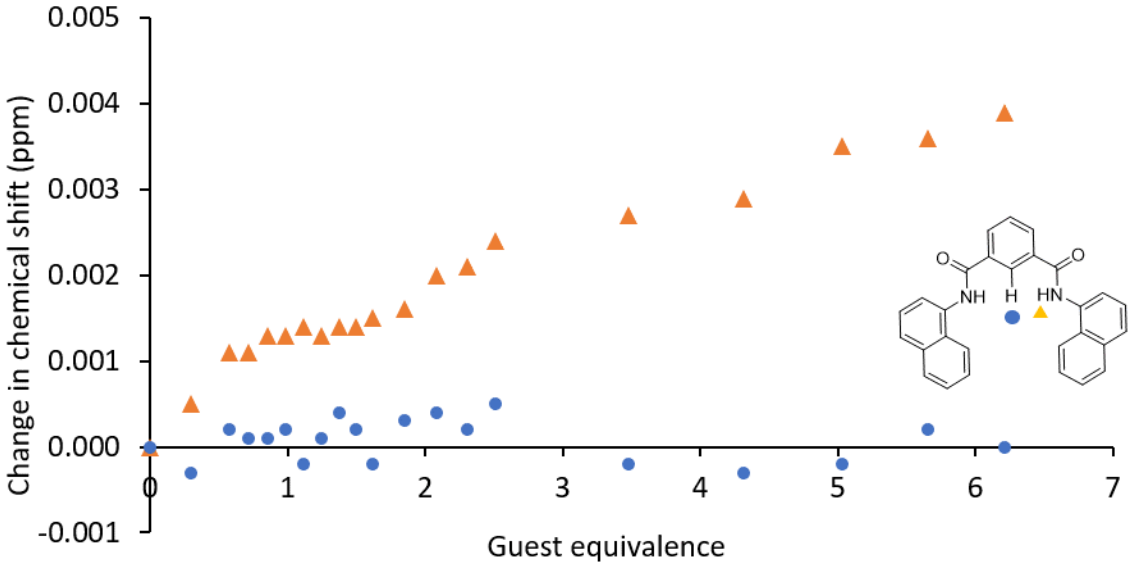

Figure 49 - Change in chemical shift for the NH and CH resonances of **37** (host) upon the addition of TBA hydrogen sulphate (guest) in DMSO-d_6/0.5 % H_2O at 298 K. The 1:1 binding association constant derived from the NH change in chemical shift, K_{ass} = 56.75 M^{-1} ± 8.68 %.

As the binding motif was expected to utilise the pyridinium in the NNN scaffolds of **35** and **36**, it was no surprise when the NCN scaffold receptor **36** showed no indication of strongly binding to any of the anions, however receptor **38** was found to bind to benzoate with a 1:1 binding association of 207 M^{-1} (8 %) derived from the change in chemical shift of the aryl protons (Figure 50).

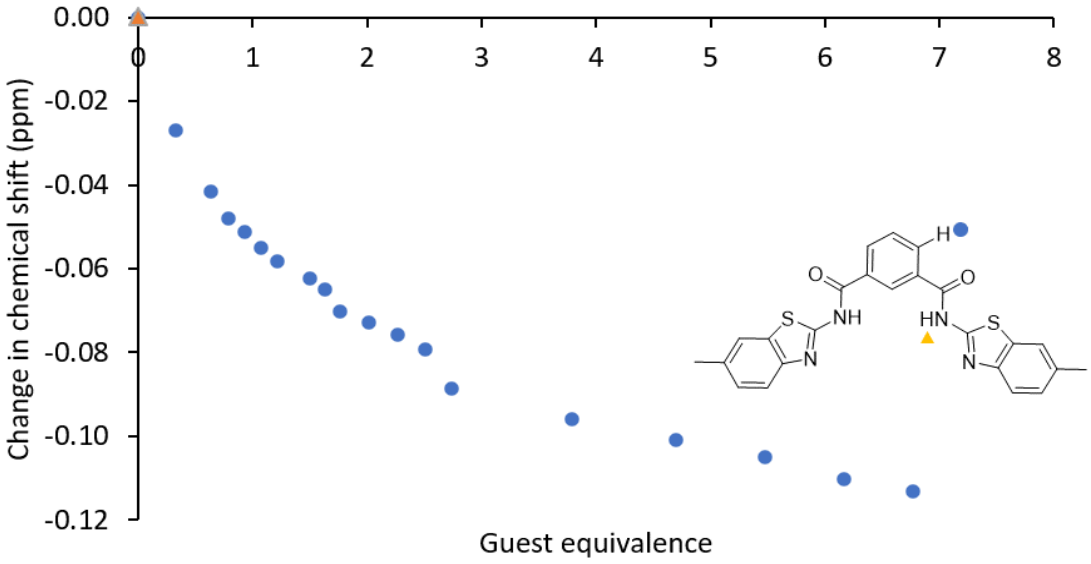

Figure 50 - Change in chemical shift for the NH and CH resonances of **38** (host) upon the addition of TBA benzoate (guest) in DMSO-d_6/0.5 % H_2O at 298 K. Due to peak broadening, the chemical shift for the NH resonance could not be followed accurately. The 1:1 binding association derived from the ArH change in chemical shift, K_{ass} = 206.53 M^{-1} ± 8.41 %.

Furthermore, receptor **38** also showed 2:1 (host:guest) binding with an association of K_{11} 107 M^{-1} (± 9 %) and K_{21} = 217 M^{-1} (± 4 %) with sulphate anion (Figure 51), while also showing weak binding to phosphate anions in a 1:1 binding isotherm and association constant of 18 M^{-1} (± 3 %) derived from the change in chemical shift of the amide protons (Figure 52). Not only were these results unexpected, they also were the highest association constants from these experiments; although **38** didn't exhibit selectivity to a specific anion, it displayed interesting

behaviour, and perhaps potential to be further fine-tuned and redesigned for encourage selectivity.

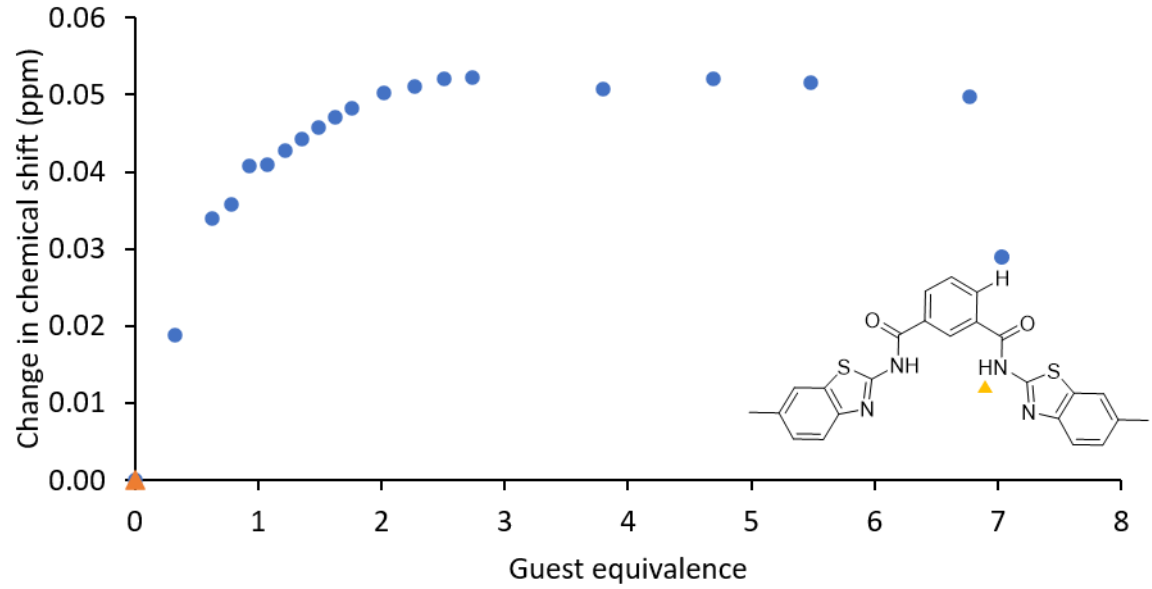

Figure 51 - Change in chemical shift for the NH and CH resonances of **38** (host) upon the addition of TBA sulphate (guest) in DMSO-d_6/0.5 % H_2O at 298 K. Due to peak broadening, the chemical shift for the NH resonance could not be followed accurately. The 2:1 (host:guest) binding association derived from the ArH change in chemical shift, K_{11} = 107.37 M^{-1} ± 9.18 %, and K_{21} = 217.23 M^{-1} ± 3.57 %.

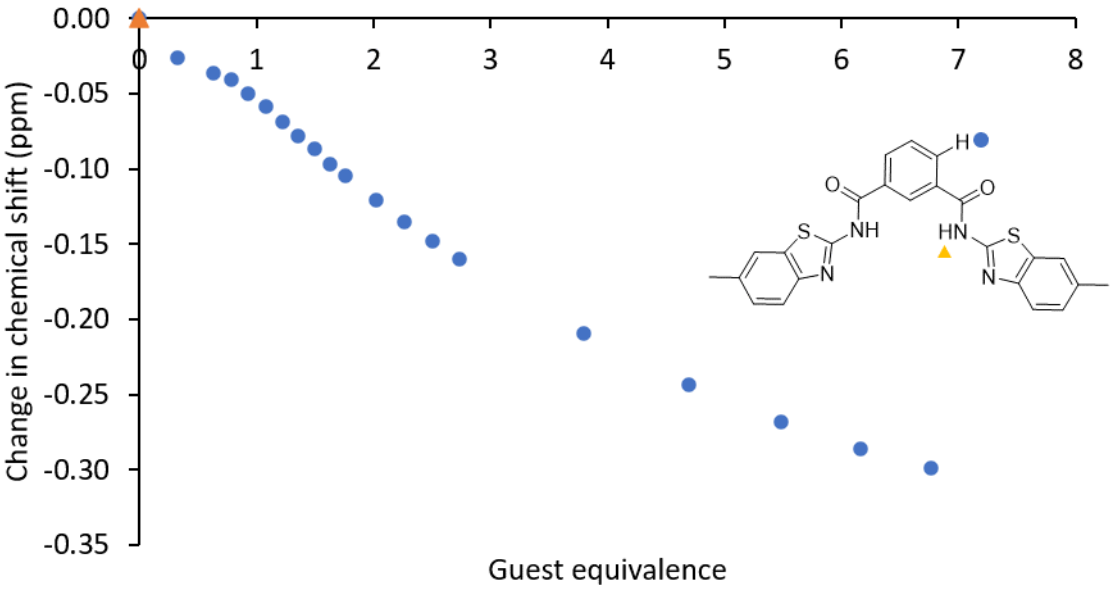

Figure 52 – Change in chemical shift for the NH and CH resonances of **38** (host) upon the addition of TBA dihydrogen phosphate (guest) in DMSO-d_6/0.5 % H_2O at 298 K. Due to peak broadening, the chemical shift for the NH resonance could not be followed accurately. The 1:1 binding association derived from the ArH change in chemical shift, K_{ass} = 17.75 M^{-1} ± 2.59 %.

A summary of all of the ^{1}H NMR titration experiments carried out can be seen in Table 3. When viewing the bigger picture, and treating them as a comparable data set, a number of things can be inferred. As it is possible to compare each the effects of each fluorescent R group (the naphthalene and benzothiazole moieties), as well as the effects of incorporating an aryl or a pyridine ring to the core of the scaffold. Whereas **35** incorporates an NNN scaffold, which would be expected to further facilitate anion binding – weaker binding associations were observed than its NCN counterpart receptor **38**. Albeit, more selectivity was observed; suggesting that the incorporation of the nitrogen atom in the ring may discourage stronger binding, but encourage selectivity. The data sets for **36** and **37** may also be compared in a similar manner; observing both equally low association constants, but a wider range of anion responses in the NCN counterpart of the naphthalene duo. As this is true of both pairs, it may be assumed that NCN scaffolds may be better at accepting a range of anions than their NNN counterparts. Graphs of each receptor with all guest species can be found in the appendix (S32-35) for a visual comparison of magnitudes for changes in chemical shift.

Table 3 – Data for binding association constants, K_{ass}, of **35**-**38** with various anions; calculated from ^{1}H NMR titration data in DMSO-d_6/0.5 % at 298 K.

Anion	**35**	**36**	**37**	**38**
Benzoate	<10 [a]	<10 [a]	<10 [a]	206.53[a]
Sulphate	*b*	*b*	*b*	K_{11} 107.37[a], K_{21} 217.23[a]
Dihydrogen phosphate	23.74 [a]	<10 [a]	*b*	17.75[a]
Hydrogen sulphate	*b*	<10 [a]	*b*	*b*
Chloride	*b*	<10 [a]	<10 [a]	*b*

*[a] represents error for the given association constant is < ± 10 %, [b] represents that no binding could not be fitted; as the change in chemical shift was below the limitations for the NMR machine, or the percentage error was too great. For all association constants presented here, all fit a binding isotherm of 1:1, with the exception of the **38** binding associations to sulphate which fits a 2:1 (host:guest) binding isotherm.*

The general behaviour of **38** seen with anion selectivity is quite broad; as increases in fluorescence intensity later discussed in 2.3.4. (Table 4) are observed upon the addition of hydrogen sulphate, and benzoate anions – despite no observable association taking place with hydrogen sulphate. The receptor also produced strong association constants with sulphate

anions in a 2:1 (host:guest) binding isotherm; although further study would be necessary to confirm the arrangement of this association. A likely theory for this is both host species 'twisting' and facing each other's binding sites (like two crocodile mouths) with the anion stuck in the middle (Figure 53); this behaviour may be specific to SO_4^{2-} due to its higher charge-to-size ratio, and its dicationic nature. The benzothiazole substituents are also more linear than the naphthalene groups, perhaps causing more steric hinderance and preventing a suitable conformation forming for this mode of binding to occur in **36**.

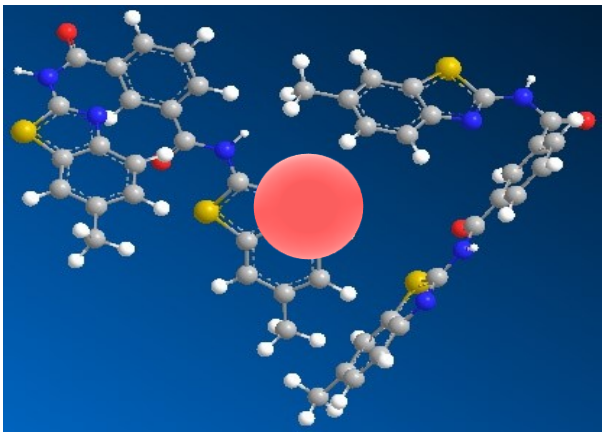

Figure 53 – Hypothesised 2:1 (host:guest) binding of **38**, with the SO_4^{2-} anion represented by the red sphere.

2.3.4. Fluorimeter titrations

The fluorescence of a compound, if observed to be affected by non-covalent interactions in the solution state with anions, can be utilised to create sensors. Sensing chemistry is particularly sought out and useful as it can help in identifying toxic compounds, or can be used to follow the progress of reactions and biological processes.[9,187,194,197,208] In order to complete these experiments, an optimal concentration of receptor in a non-fluorescent solvent was required. As the fluorimeter is a highly sensitive instrument, serial dilution studies were carried out using an ultraviolet-visible light (UV-Vis) spectrophotometer in order to obtain a concentration with an output of < 0.1 absorption. The optimal concentration was

found to be 0.01 mM of host species, a 4.2 mM solution of guest was aliquoted in increasing increments up to 7 equivalences of host. These experiments were also carried out in DMSO/0.5 % H_2O to provide comparable data sets with NMR titration studies.

Table 4 – Overview of the log of binding association constants, log K_{ass}, of **35**-**38** with various anions; calculated from changes in fluorescence intensity in DMSO/0.5 % H_2O at 298 K.

Anion	**35**	**36**	**37**	**38**
Benzoate	6.3 (± 14 %)	5.6 (± 14 %)	*b*	5.0 (± 20 %)
Sulphate	4.7 [a]	*b*	*b*	*b*
Dihydrogen phosphate	4.6 [a]	*b*	*b*	*b*
Hydrogen sulphate	*b*	*b*	*b*	2.2 (± 14 %)
Chloride	*b*	*b*	*b*	*b*

[a]represents error for the given association constant is < ± 10 %, [b] represents that no binding could not be fitted; as the change in intensity of emission was too low. For all association constants presented here, all fit a binding isotherm of 1:1.

In the scope of the project, changes in fluorescence corelating to specific anion binding events were desirable (Table 3), however such behaviour of the receptors was not observed. Receptor **35** showed high selectivity to dihydrogen phosphate anions, but also showed a large increase in fluorescence intensity upon the addition of TBA benzoate, TBA sulphate, and TBA dihydrogen phosphate (Figures 54-56). The titrations carried out with TBA hydrogen sulfate, and TBA chloride displayed no discernible increase in fluorescence intensity; much like that observed in the deprotonation of **35**. Taking this into consideration, the data shown in Figures 54-56, despite not being able to fit to any binding isotherms in the ^{1}H NMR titration experiments, may be indicative of an anion specific interaction as it does not follow the trend seen in its deprotonation. A possible cause in the changes in fluorescence is perhaps due to receptor-receptor interactions which were not able to be facilitated without the presence of anions in the solution to compete with the DMSO. The magnitude of the increases in fluorescence intensity of **35** with these three anions, as well as the association constants produced, can be easier visualised looking at the summary in Table 4. Graphs of each receptor with all guest species can

also be found in the appendix (S56-59) for a visual comparison of magnitudes for changes in intensity of emission.

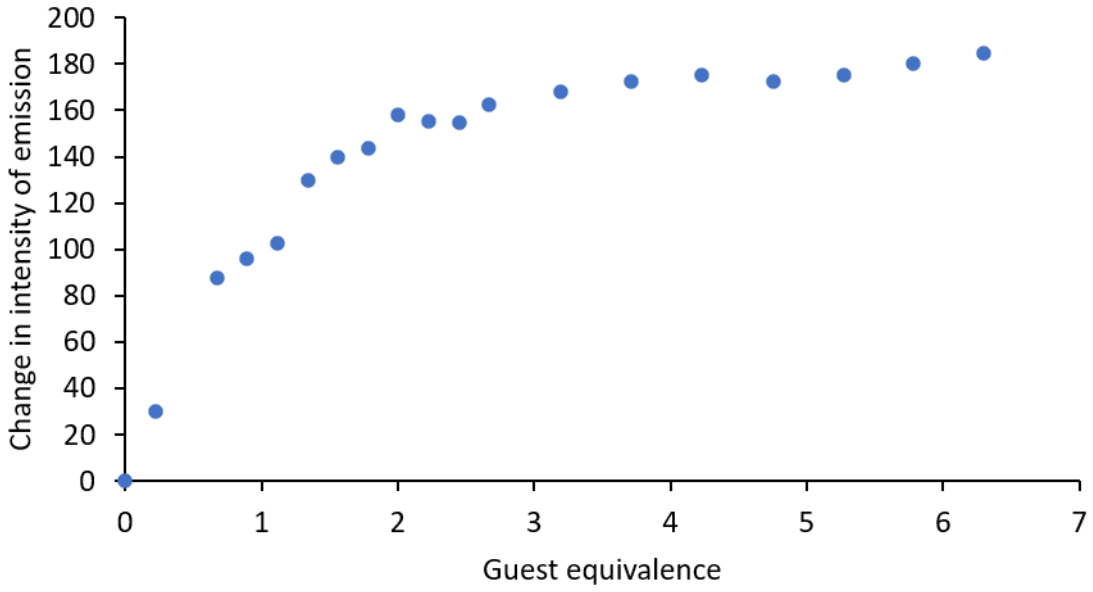

Figure 54 - Change in emission intensity at 400 nm of **35** (host) upon the addition of TBA benzoate (guest) in DMSO/0.5 % H_2O at 298 K. The 1:1 binding association derived from the change in intensity of emission at 400 nm, K_{ass} = 1958476.59 M^{-1} ± 13.75 %.

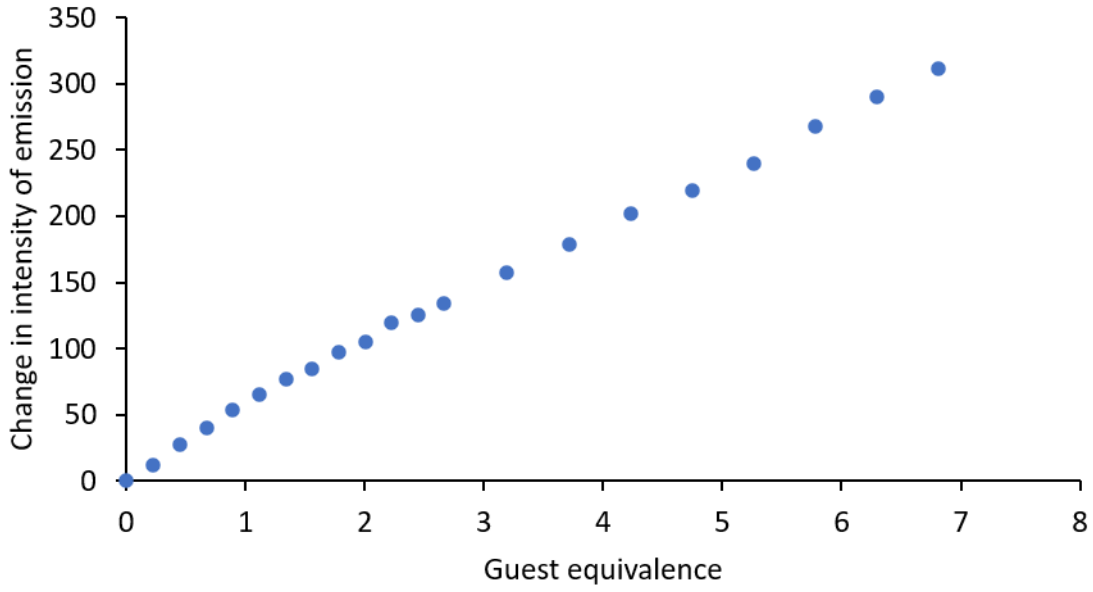

Figure 55 - Change in intensity of emission at 400 nm of **35** (host) upon the addition of TBA sulphate (guest) in DMSO/0.5 % H_2O at 298 K. The 1:1 binding association derived from the change in intensity of emission at 400 nm, K_{ass} = 45836.02 M^{-1} ± 1.51 %.

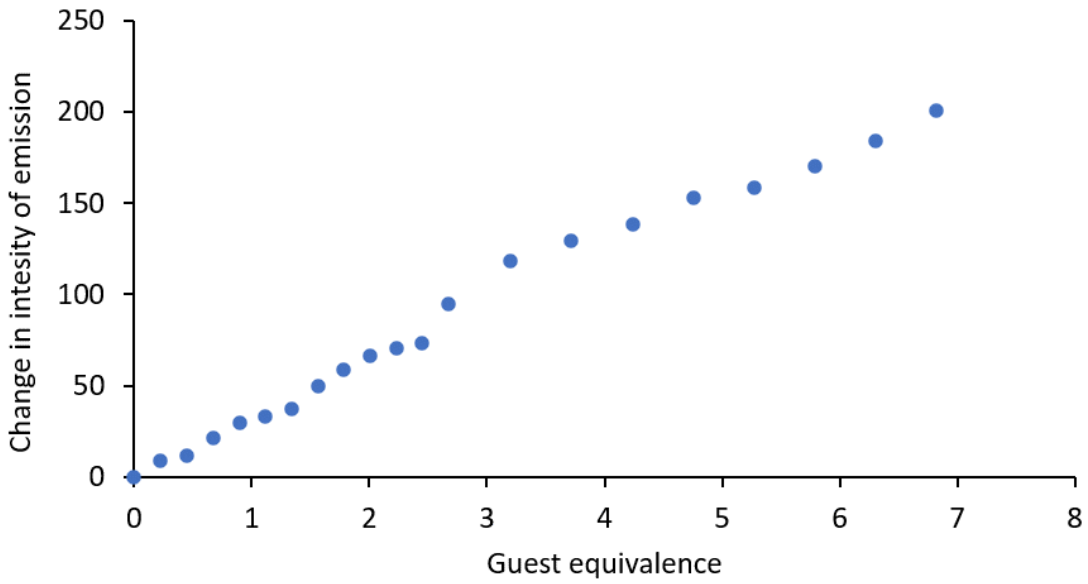

Figure 56 - Change in intensity of emission at 400 nm of **35** (host) upon the addition of TBA dihydrogen phosphate (guest) in DMSO/0.5 % H_2O at 298 K. The 1:1 binding association derived from the change in intensity of emission at 400 nm, K_{ass} = 35670.05 M^{-1} ± 3.58 %.

Receptor **35** shows binding selectivity and affinity towards phosphate anions, however not selectivity in its fluorescent activity. And thus, it is unclear whether or not the binding of the phosphate anion is corelated to the shift in fluorescence intensity, or if these results are caused by other interactions which may be taking place in the solvent upon the introduction of certain anions; it is likely that the TBA introduced with the guest may also be contributing to a change in behaviour. The smallest anions used, chloride, and hydrogen sulphate were the only anions which did not result in an increase of fluorescence intensity, and thus it can be assumed that more favourable solvent-anion interactions may have been more dominant and favourable. Paired with its (albeit) weak binding to benzoate, **36** shows promise as a benzoate anion sensor (Figure 57), as it was the only anion which produced a large increase in intensity of emission; and produced a resultant 1:1 binding association of 3.7 x 10^5 M^{-1} with an error of ± 14 %. Normally, an error this high would invalidate the results of the experiment, however when observing Figure 57, it is clear that there is an observable trend and significant increase in the fluorescence intensity – this percentage error can most likely be held accountable to human error in the earlier guest equivalence plots. Receptor **37** showed essentially no significant increase in fluorescence intensity with any of the anions (simply fluctuations of intensity below

40 were observed), or a correlation with the ^{1}H NMR anion titration data, although further studies with the inclusion of different anions may change this verdict.

Receptor **38**, showed a slight increase in fluorescence with the addition of TBA benzoate (Figure 58), yielding a very high 1:1 binding association constant of 9 x 10^{3} M^{-1}, with a considerably high percentage error of ± 19.7 % - the high error may be a result of the small scale of the change; and thus, small deviations from the trendline may be caused by sensitivity of the instrument. Compound **38** also showed an increase in intensity with the addition of TBA hydrogen sulphate (Figure 59) – which was shown to have no binding association with the receptor. That being said, the trend in the change in intensity seen here (Figure 59), may be indicative of a more complicated interaction, as a certain concentration of guest addition is required to effect a change to the change in fluorescence intensity. This ultimately may suggest that a receptor-receptor interaction may have been taking place, which is more favourable than binding to the hydrogen sulphate anion at low guest concentrations.

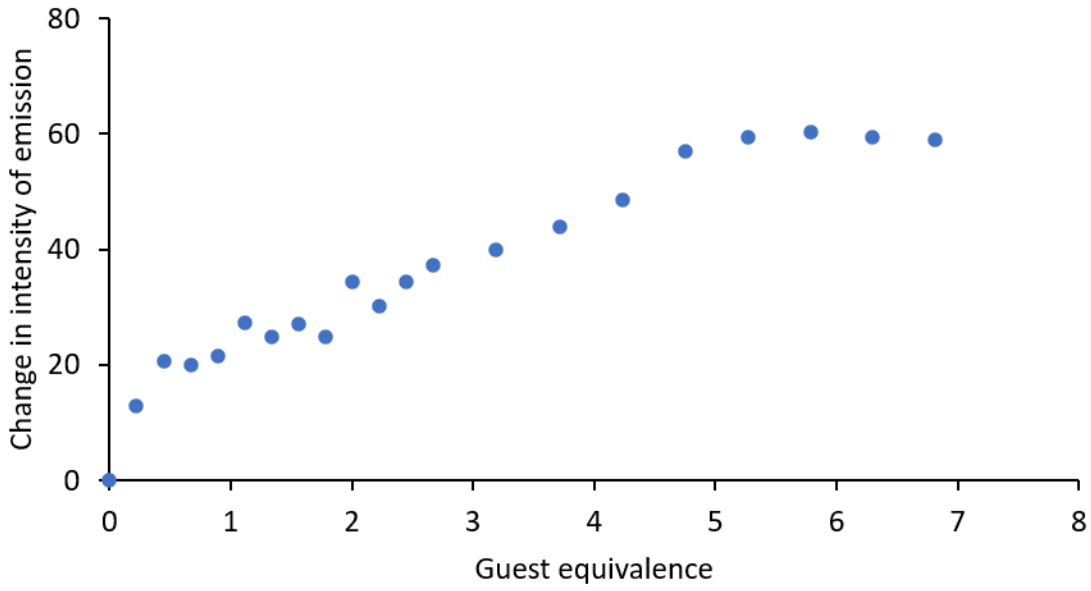

Figure 57 - Change in emission at 340 nm of **36** (host) upon the addition of TBA OBz (guest) in DMSO/0.5 % H_2O at 298 K. This data could not be fitted to a 1:1, 2:1 or 1:2 binding isotherm with a reliable percentage error (however, a 1:1 binding association of 366945.27 M^{-1} was obtained with an error of ± 14 %).

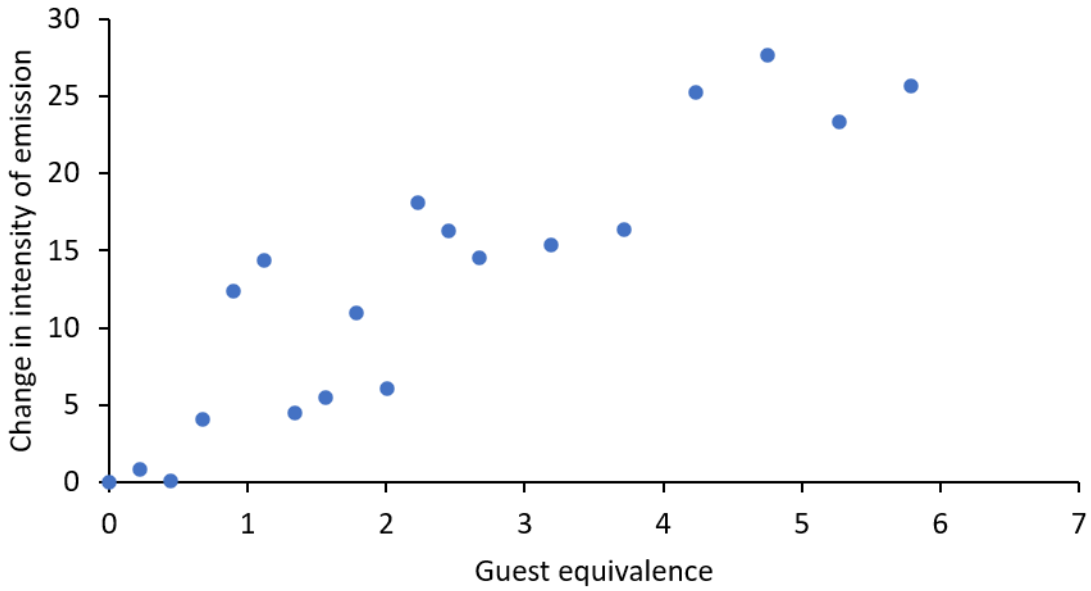

Figure 58 - Change in emission at 346 nm of **38** (host) upon the addition of TBA benzoate (guest) in DMSO/0.5 % H_2O at 298 K. This data could not be fitted to a 1:1, 2:1 or 1:2 with a reliable percentage error (however, a 1:1 binding association of 89089.29 M^{-1} was obtained with an error of ± 19.73 %).

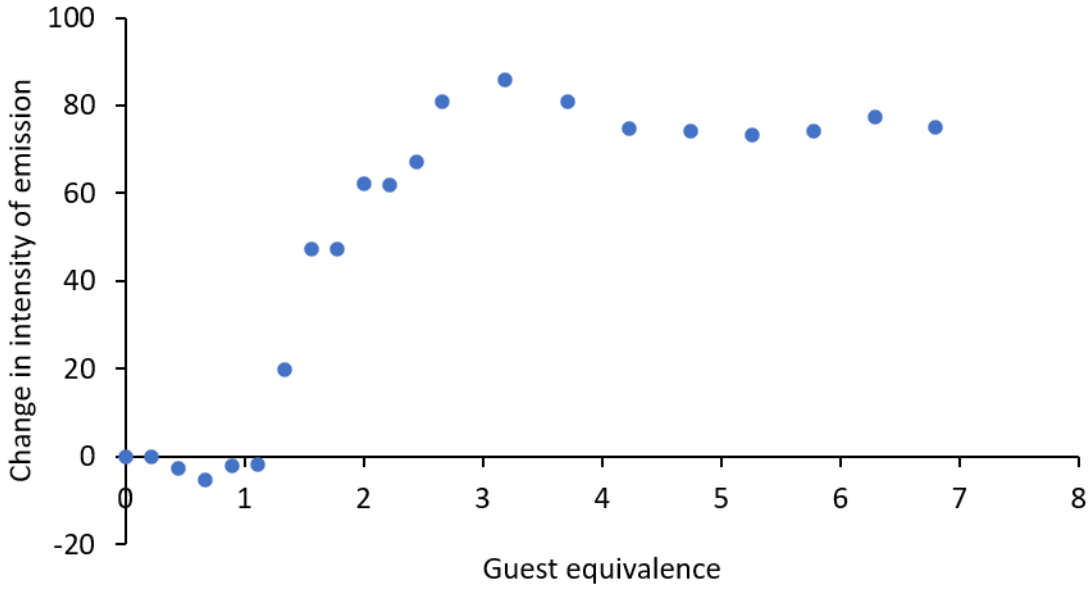

Figure 59 – Change in emission at 346 nm of **38** (host) upon the addition of TBA hydrogen sulphate (guest) in DMSO at 298 K. This data could not be fitted to a 1:1, 2:1 or 1:2 binding isotherm.

Looking overview of the binding associations of all the fluorimeter studies pursued with compounds **35** – **38** (Table 4), the data suggests that the inclusion of the naphthalene moiety

does not produce strong sensor potential with either NNN or NCN scaffolds due to low binding selectivity, and that the benzothiazole group possesses a lot more potential with both scaffolds for fluorescent responses. The largest association constant observed in this experiment, log 6.29 M^{-1} (Figure 54) was for receptor **35** which produced very large axis scale for change in fluorescence intensity for all three of the anions which produced association constants. Especially when compared to the scales of **38** – where both are sub-100 scales. Suggesting that the incorporation of a phenyl ring instead of a pyridine ring has encouraged stronger fluorescent responses in the presence of benzoate, sulphate, and dihydrogen phosphate anions.

Although **35** has displayed selectivity for dihydrogen phosphate (Table 3), the changes in fluorescence of **35** with the chosen anions were observed where necessarily binding was not (Table 4 and 5). The selectivity of **35** to $H_2PO_4^-$ over HSO_4^- and SO_4^{2-} cannot be attributed to differences in geometry as all anions adopt a tetrahedral shape; and thus, other defining qualities of these anions must be the cause. Atomic size, and electronic factors may be the cause of this; dihydrogen phosphate is also mono-anionic like hydrogen sulphate; however, the phosphate anion has a line of symmetry down the middle, creating a more localised negative charge on the oxygen; this is not the case for hydrogen sulphate. The sulphate anion may have been unfavoured due to it being a di-anionic species. Looking at Table 3, we could also infer that spherical anions, such as chloride are unlikely to bind to **35**, and so the receptor may be able to be further developed into selective binding to lesser researched anions, and due to its strong fluorescent responses may have potential as a sensor.

Table 5 – Simplified summary of the effects of the addition of various anions to **35**-**38** when studied via fluorimeter titrations in DMSO/0.5 % at 298 K. Where ↑, represents an increase in fluorescence intensity, and —, shows no noticeable increase or an increase below 20.

Anion	**35**	**36**	**37**	**38**
Benzoate	↑	↑	—	↑
Sulphate	↑	—	—	—
Dihydrogen phosphate	↑	—	—	—
Hydrogen sulphate	—	—	—	↑
Chloride	—	—	—	—

Receptor **36**, displayed very weak binding to multiple anions as seen in Table 3, however it is the only compound which exhibited a selective increase in fluorescence. This could prove as a potential sensor for benzoate anions, as despite binding weakly, it may still be able to be used for sensing – the maximum increase in fluorescence intensity was 60 for benzoate, whereas all other anions were sub-20. This provides some information on the behaviour of this receptor – especially when the behaviour of **37** is also taken into consideration. The two compounds are discerned simply by the incorporation of NNN or NCN on the receptor's skeleton near the potential binding site. And so, the data presented definitively shows that the C-H bond is crucial to the selective increase in intensity; but not essential to its ability to bind to the anion.

The structure with the least promise in fluorescent sensing application was **37**, which showed no anion selectivity for effects on fluorescence intensity, and no strong affinity for any particular anion. When comparing the data of **36** and **37**, although more investigation is required, the very weak binding of the two compounds to chloride and benzoate may lead to the assumption that both utilise a similar mechanism via the dicarboxamide and naphthalene moiety influence for these two anions. But as for the binding observed for hydrogen sulphate and dihydrogen phosphate; these are specific only to **36**; so, despite having no influence on the fluorescence whether or not a pyridine ring is incorporated; it does have an influence on the binding. Further analysis of crystals may provide better insight into the varying architectures of both receptors when binding. The largest association constant is observed for **38** with the benzoate anion, followed by sulphate. The data suggests that shifts in fluorescent behaviour may favour the C-H inclusive binding sites of **36** and **38**. This may infer that selectivity towards benzoate is more dependent on core of the structure; and the affinity for it is influenced by the R group of the dicarboxamide group. Undeniably, the incorporation of benzothiazole shows a very large increase in the association constant (K_{ass} = 206.53 M^{-1} for **38**, and <10 M^{-1} for **36**). A possible cause of this effect may be the electron-withdrawing nature of the functionality; causing the amide protons to increase in acidity and promote anion binding further. It can also

be noted that none of the guest species tested resulted in a quenching of fluorescence for the receptors, suggesting that on/off sensor potential may not be very high – but increases in fluorescence, or fluorescence wavelength (and thus, colour) are possible.

2.4. Conclusions

After investigating the receptors presented in Figure 40, it can be concluded that despite binding to anions being observed in most host species, for the use of these compounds as fluorescent anion sensors further fine-tuning is required. The most promising receptor, **35** displayed selectivity for dihydrogen phosphate in binding, however when testing the changes in fluorescence of **35** (Table 3) - increases in intensity were observed where binding was not (Table 4). Receptor **36** also shows promise as a benzoate anion fluorescent sensor, despite it showing weak binding to multiple anions, the positive fluorescent response was only observed with benzoate (Table 5).

3. A new class of Supramolecular Self-associating Amphiphiles

3.1. Introduction

Observing the self-association of SSAs requires multiple methods of analysis; within the solid, and solution state, and also within the gas phase. Due to the complexity of these association interactions, chemists must observe the behaviour of their compounds via a range of methods to gain a better understanding of the associations that are taking place. A general guide is illustrated in Figure 60 for an optimised order for carrying out a number of studies for the characterisation of these systems.

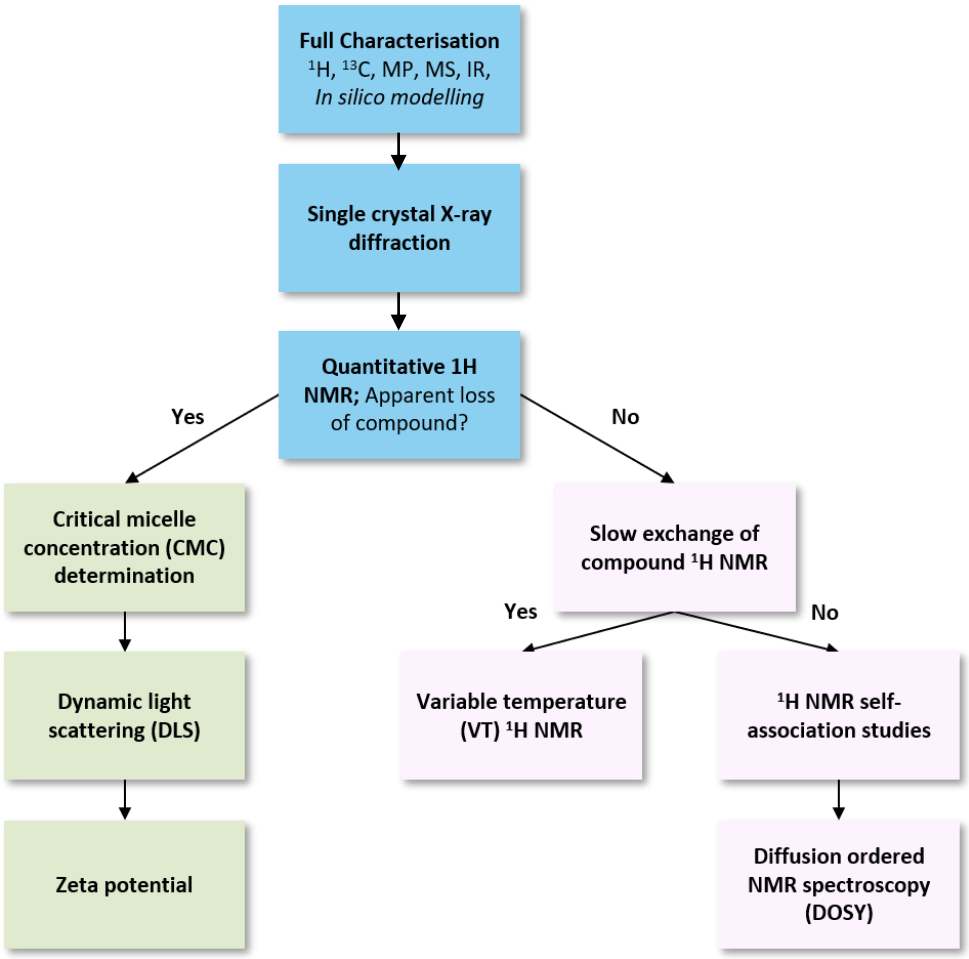

Figure 60 – Flowchart of techniques used in SSA characterisation.

Following the flowchart shown in Figure 60, as a part of the full characterisation of an SSA, it is general practice to use X-ray diffraction to analyse a single crystal. This a very useful,

non-destructive method which produces information on the crystalline structure of the self-associating binding modes present in the solid state of SSAs.[226] There are a number of different binding modes accessible to SSAs (Figure 28), whereby they are able to interact via urea-rea or anion-urea motifs. It is important to investigate both solid state, solution state, and gas phase molecular interactions; single crystal x-ray diffraction simply uncovers the behaviour of the SSA when influenced by crystal packing forces, and so the information is still limited; this method provides smaller-scaled, detailed information – however it leaves out information on bulk characterisation (which XRD powder diffraction would be able to provide). Moving into the solution state, association studies allow for an understanding on the effects of introducing in solvent-solute interactions.[151,152,227] This is a crucial part in assessing SSA behaviour as these interactions can influence self-association events, and any resultant aggregate formation processes. The intermolecular forces which occur between the solvents and the solute compete with those occurring between the solute molecules. The hydrogen bonded self-associated complexes formed as a result need to be disrupted in order for the formation of hydrogen bonded self-associated complexes to take place. This is particularly true when solvents such as DMSO or water are used due to increased hydrogen bonding interactions with HBA or HBD groups.

Quantitative ^{1}H NMR (qNMR) allows for the quantification of NMR active components in the solution state – and whether or not any aggregates the SSAs form exhibit solid-like properties – such as the large structures tumbling slowly in the solution; results in these larger aggregates not being observable in using solution state NMR.[92,228] Assessing whether or not there is an 'apparent loss of compound' in this experiment provides insight into what percentage of the compounds may be forming such aggregates in the solution state. These results lead to a decision to be made; if there is no observable "loss" of signal, then determining self-association constants is the next step. As we have confirmed that we observe the whole of the compound in solution, NMR is utilised as it is sensitive to weak and non-covalent interactions,[229] dilution

studies can be performed to monitor changes in chemical shift at the site of interaction, which are indicative of non-covalent interactions taking place. For example, hydrogen bonding can be observed as the shift in ppm of ^{1}H signals (ranging up to 5 ppm)[230,231] and π-π interactions through ^{1}H chemical shifts of CHs in quinacridone derivatives.[232] Thus, the data collected from a dilution study can be used to calculate an association constant by fitting the changes in chemical shift to a binding isotherm. This method, is then often followed by a diffusion ordered spectroscopy (DOSY); an NMR technique which allows for calculation of the size of these aggregates found to be forming in solution from the previous pseudo 1D experiment.

Taking the left leg of the (Figure 60) flowchart however, instructs us to next use critical micelle concentrations (CMC) determination. This is because if there is no apparent 'loss' of signal is observed in the ^{1}H qNMR studies, it suggests either ^{1}H NMR visible self-assembly is occurring (such as micelle formation), or no self-association is occurring at all. The CMC is defined as the concentration of a surfactant-like structure, at which surface tension does not continue to decrease with increasing concentration,[233] and above which any extra addition of compound will form larger self-associated structures within the bulk of the solution (micelles, reverse micelles, vesicles, aggregations.[234,235] The size of these structures is determined through Dynamic Light Scattering (DLS) and the stability of these aggregates are studied using Zeta potential studied.

This new class of SSAs is still in its infancy, the study of compounds **40** and **42** (Figure 61) in accordance with the flowchart in Figure 60 is a crucial step towards understanding their behaviour and thus their potential for applications. The inclusion of structures **39** and **41** in this study allows for determination of structure activity relationships in order to study the role of the sulfonate group in self-association. The compounds possess more HBD groups than HBA groups, resulting in a more 'frustrated' structure. The thiourea functionality increases acidity of the NH groups, and is a commonly exploited moiety in supramolecular chemistry; for cage formations,

potential self-association, and formation of extended supramolecular structures.[10,27,79,236,237] The presence of the carbon triple bond in compounds **41** and **42**, restricts bond rotation and increases the rigidity of the structures. As **39** and **41** are a more hydrophobic, and neutral species, their self-associating behaviour would be expected to be weaker in comparison to the sulphate containing, more amphiphilic SSAs **40** and **42**. Herein, solution state studies of the neutral SSAs **39** and **40**, and their anionic counterparts **40** and **42** follow.

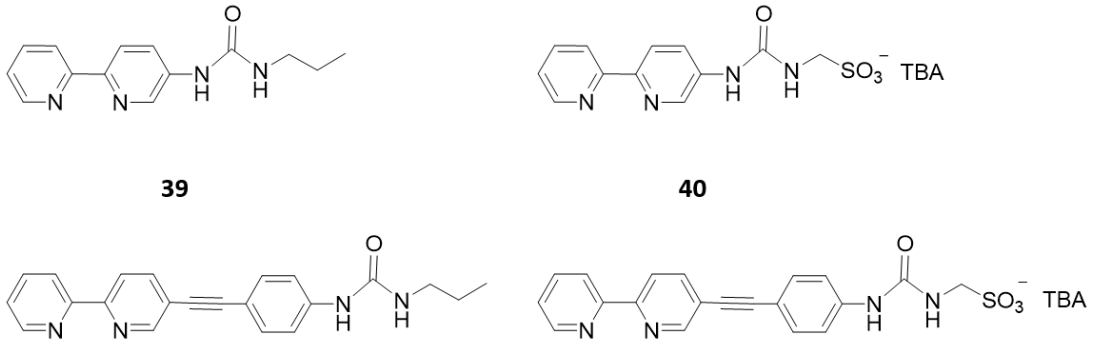

39 **40**

41 **42**

Figure 61 – Chemical structures of SSAs **40** and **42**, and their comparative analogues **39** and **41** as synthesised by Jorge Newmann.

3.2. Self-association in the solution state

Solution state studies are a key piece to understanding an SSA, it provides a deeper insight into self-association in the presence of solvent-solute interactions. The introduction of these interactions into a study, allows for aggregates, micelles, or inverse micelles to form as a result of self-association events. The resulting intermolecular forces between the solute and solvents generates competition between solute molecules; this produces solvent-solute hydrogen bonded self-associated complexes. Generally, SSAs have been observed to form dimers in DMSO, and spherical aggregates in EtOH:H_2O 1:19.[92,151] The EtOH:H_2O combination is

used to increase solubility of the SSAs upon addition of 5 % EtOH, and to produce comparable data with previously published data on solution state studies of other SSAs.[7,94,238]

3.2.1. Quantitative ^{1}H NMR studies

Quantitative NMR (qNMR) is a technique used in order to quantify the concentrations of the molecular components that are NMR active in the solution state. In order to do this, an internal standard must be used to maintain a reference for a constant concentration. The internal standard used changes with the deuterated solvent being used; DMSO-d_6 is doped with 1 % DCM, and D_2O is doped with 5 % EtOH. The standards were chosen in consideration with miscibility, presence of NMR active nuclei, and whether or not the signal of the standard can be easily observed. With SSAs, the peaks often do not interfere with the standard, as the chemical shifts of the aromatic bi-pyridine (7-9 ppm), and the thiourea (0-4 ppm) in the compounds are in different regions. The experiment was carried out by increasing relaxation time (T_1) to 60 seconds, increasing accuracy by allowing time for the entire signal of all nuclei to be detected. This is important as different conditions and factors can influence relaxation times of different nuclei.

This data can thus be used to comparatively integrate the signal of the standard against the anionic and cationic components of the SSA. The percentage of apparent loss is then calculated using the molar ratio of compound to internal standard (Equation 2), then subtracted from the expected integration value.

$$\frac{1.42\ mg}{256.31\ gmol^{-1}} = \ 0.0556\ mmol \qquad \frac{0.08\ mmol}{0.0556\ mmol} = \ 1.44\ \times 2 = \ 2.88$$

Equation 2 - In DMSO-d_6, millimoles of **39** calculated (0.0556 mM, 0.5 mL), the ratio of DCM (0.08 mM) to **39** is 1.44 per proton, but as DCM has two protons, the peak at 5.75 ppm integrates for 2.88.

Using the qNMR of **39** as an example (Figure 62), it shows an integral of 2.8698 for DCM at 5.72 ppm; 2.8698/2.88*100 = 99.65 % NMR active percentage. Therefore, 100 – 99.65 = 0.35

% apparent 'loss' is observed; this value can be considered as 0 % loss. The calculated value, 2.88, signifies the expected integration for two protons of the DCM standard which can then be used to calculate the difference between the expected integral and real integral of the compound.

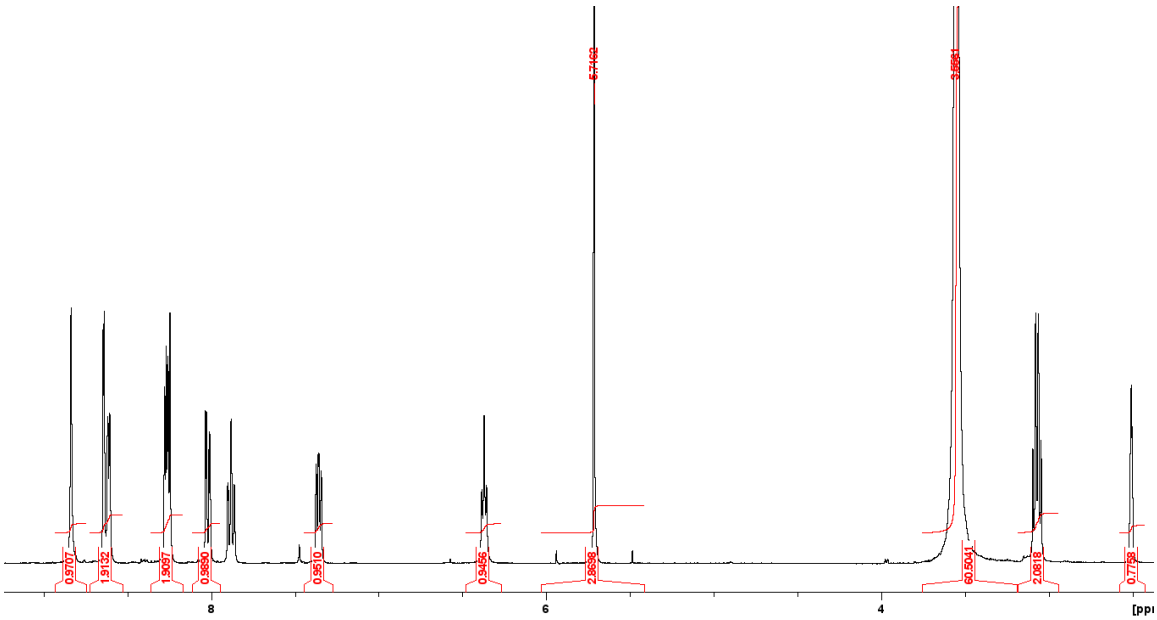

Figure 62 - ^{1}H NMR spectrum (d_1 = 60 s) of compound **39** (112 mM) in DMSO-d_6/1.0 % DCM. Comparative integration indicates 0.35 % of **39** has become NMR silent.

As seen below in Table 6, in DMSO-d_6 the neutral compound **39**, showed a small percentage loss of components at 0.35 % (Figure 62), its anionic counterpart, **40**, showed a 3.95 % loss of signal (Figure 63). These values can be dubbed as no apparent percentage "*loss*" of signal as they are below a significant and reliable range (anything below 5 % apparent "loss"), this indicates that no large aggregates are present in the doped DMSO-d_6 solution. SSA **41** showed 25.45 % loss of signal, strongly suggesting the formation of large aggregates (Figure 64). Unexpectedly, the more amphiphilic anionic counterpart, SSA **42**, showed no apparent loss of compound (Figure 65).

Table 6 - Overview of ^{1}H qNMR study results, values given in % represent the component of the compound that has become NMR silent. SSAs were at concentrations of 112 mM in DMSO-d_6, and 11.2 in D_2O, with the exceptions of **39** (0.55 mM) and **42** (0.43 mM) due to solubility issues.

Compound	DMSO-d_6 1% DCM (%)			D_2O 5 % EtOH (%)		
	Neutral	Anionic	Cationic	Neutral	Anionic	Cationic
39	0.4	-	-	0.0	-	-
40	-	4.0	2.0	-	0.0	0.0
41	25.5	-	-	*a*	-	-
42	-	0.0	0.0	-	60.0	30.1

'a' indicates that the experiment was not conducted, and the dashes represent the data not being applicable due to the neutral or anionic nature of the compound.

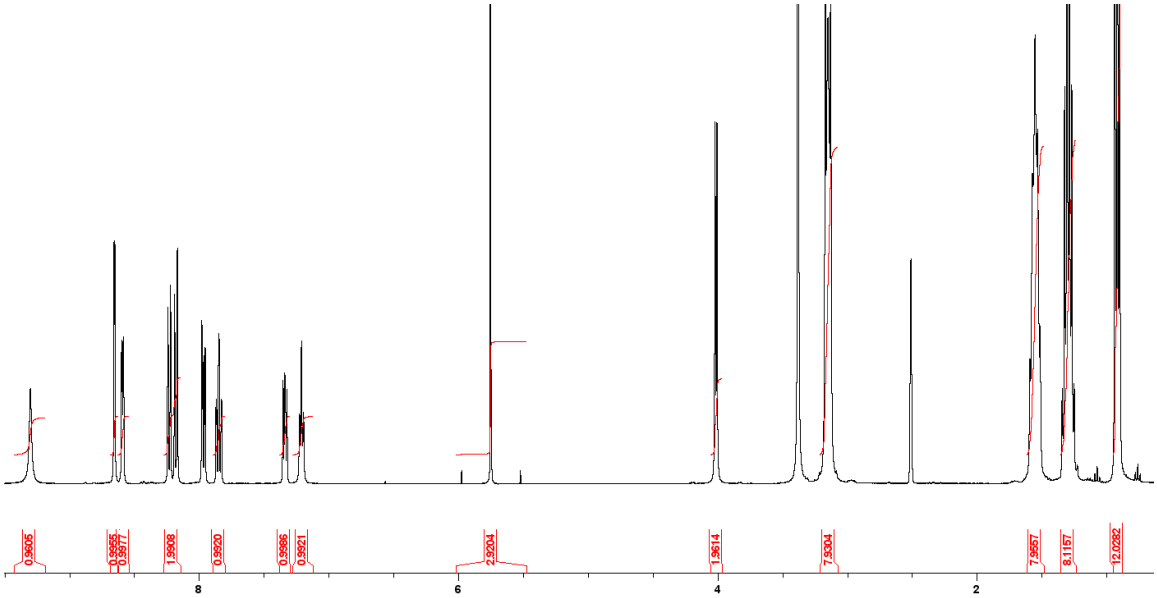

Figure 63 - ^{1}H NMR spectrum (d_1 = 60 s) of compound **40** (112 mM) in DMSO-d_6/1.0 % DCM. Comparative integration indicates 3.95 % of the anionic component, and 2.0 % of the cationic component **40** has become NMR silent.

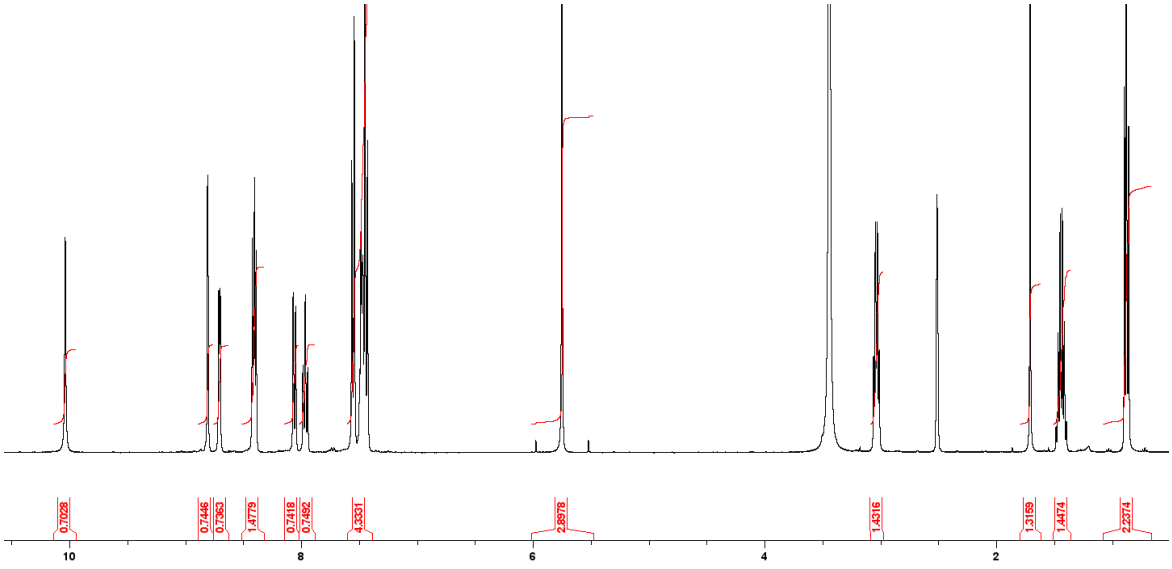

Figure 64 - ^{1}H NMR spectrum (d_1 = 60 s) of compound **41** (112 mM) in DMSO-d_6/1.0 % DCM. Comparative integration indicates 24.5 % of **41** has become NMR silent.

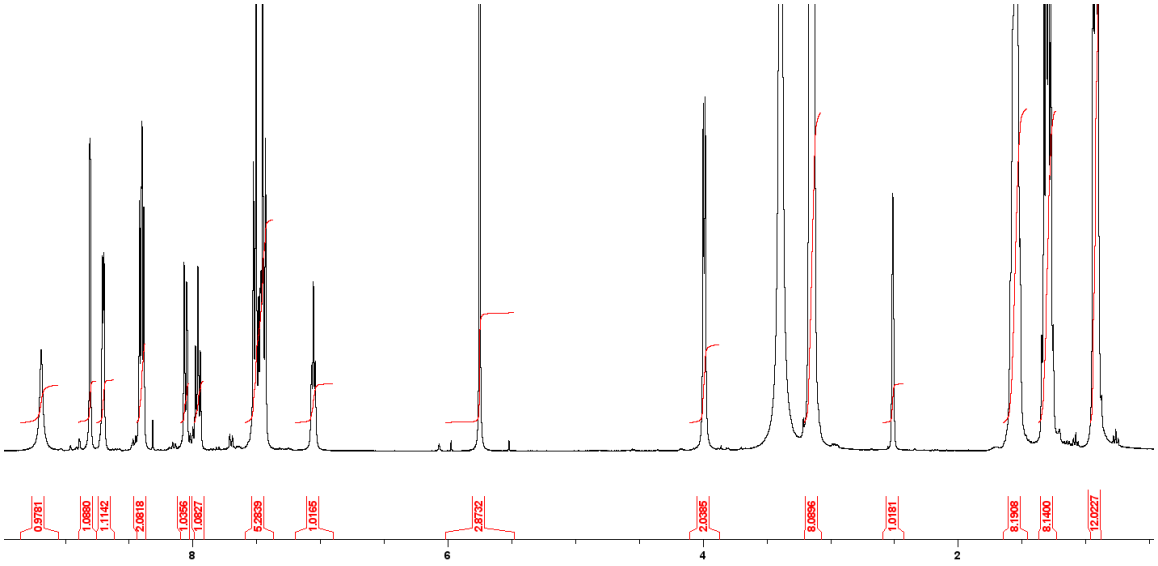

Figure 65 - ^{1}H NMR spectrum (d_1 = 60 s) of compound **42** (112 mM) in DMSO-d_6/1.0 % DCM. Comparative integration indicates none of the anionic component or cationic component of **42** has become NMR silent.

However, in D_2O, many issues were encountered regarding solubilities of the SSAs, even when the allotted volume of EtOH for doping was added to the sample first - which was done in order to aid in breaking intermolecular interactions in the solid state. However, no matter how dilute, **41** could not be dissolved, and so qNMR was not able to be carried out for this sample. Although SSA **38** and **42** also displayed poor solubility, when sufficiently diluted, the experiment was able to be conducted.

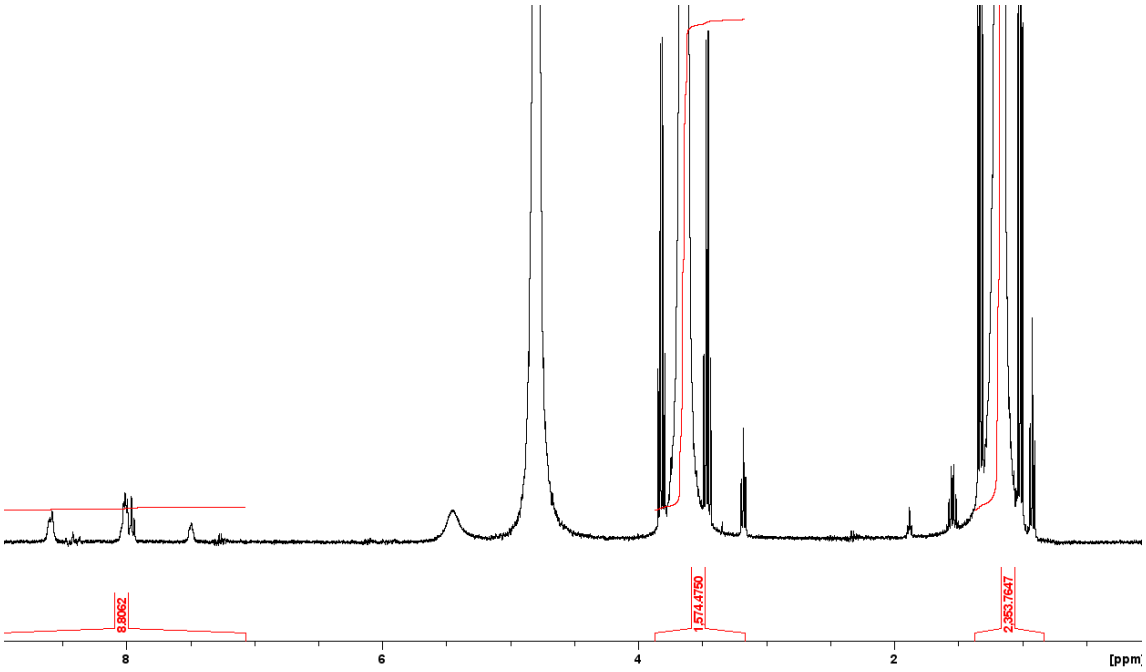

Figure 66 - ^{1}H NMR spectrum (d_1 = 60 s) of compound **39** (0.55 mM) in D_2O/5.0 % EtOH. Comparative integration indicates none of **39** has become NMR silent.

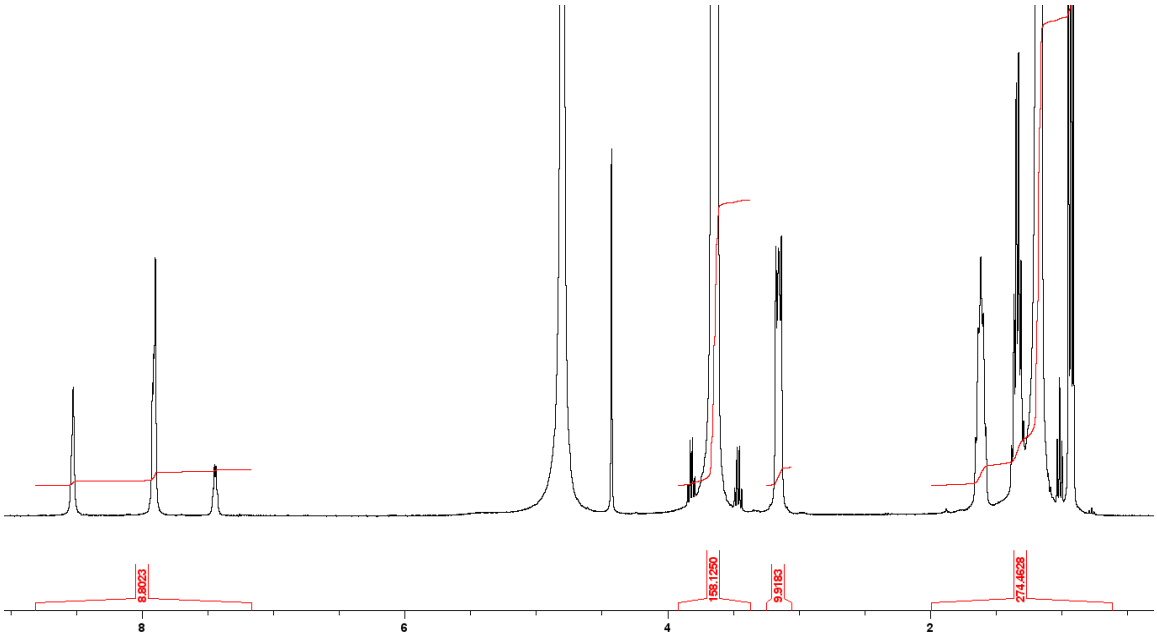

Figure 67 - ^{1}H NMR spectrum (d_1 = 60 s) of compound **40** (5.44 mM) in D_2O/5.0 % EtOH. Comparative integration indicates none of the anionic component of **40** has become NMR silent.

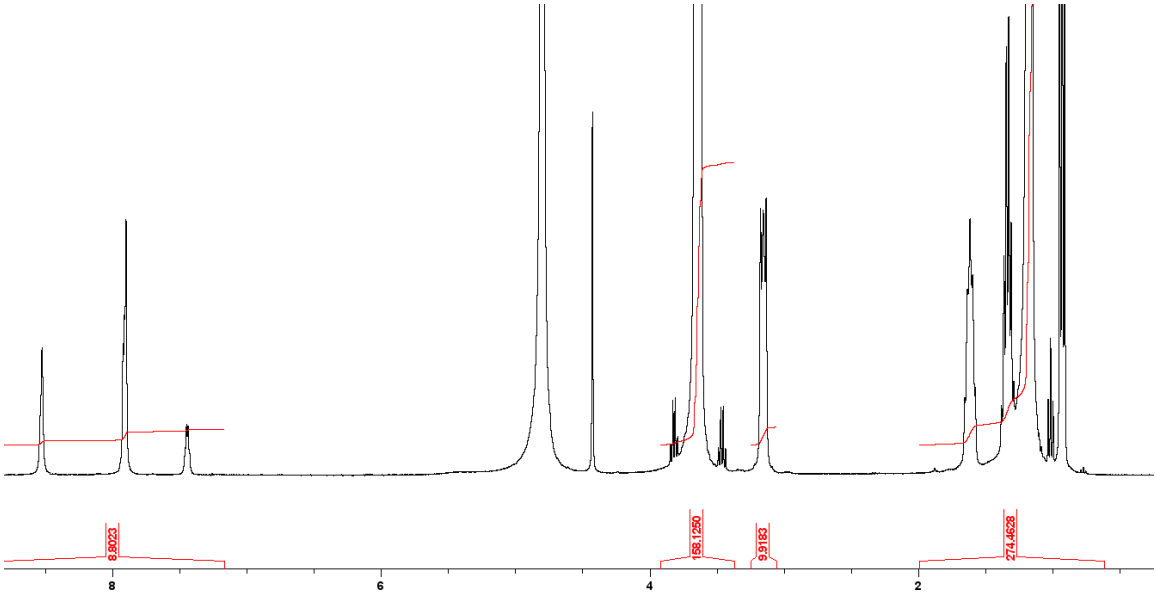

Figure 68 – ^{1}H NMR spectrum (d_1 = 60 s) of compound **42** (0.43 mM) in D_2O/5.0 % EtOH. Comparative integration indicates 59.6 % of the anionic component and 30.1 % of the cationic component of **42** has become NMR silent.

Further examining the data in Table 6, **41** shows the largest percentage of compound that has become NMR silent in doped DMSO-d_6/0.5 % H_2O; suggesting that larger aggregates with solid-like properties may be forming in the solution. When comparing it to its anionic counterpart, **42**, which showed no apparent 'loss' of components, this data becomes a bit more interesting – a structure activity relationship is being observed, not only is the neutral compound more likely to be self-associating in DMSO-d_6/0.5 % H_2O, it also showed decreased solubility in the doped D_2O. Larger self-assemblies would be expected to form with the anionic SSAs like **42** due to their potential to form anion-assisted hydrogen bonds, however this assumption is only supported by the data produced by **39** and **40** in the DMSO-d_6/0.5 % H_2O solvent system; showing that this small change in structure has facilitated up to 10 times more loss of signal; suggesting the formation of larger aggregates. Following this data, we would also expect **39**, **40**, and **42** to all have smaller hydrodynamic diameter values in DMSO; as later discussed and seen in 3.2.2.

3.2.2. ^{1}H NMR DOSY studies

The ^{1}H NMR DOSY experiment separates the signals of each molecule according to their diffusion coefficients. As each different molecule in a solution will register with a difference diffusion coefficient, it allows for mixtures with multiple compounds to be analysed.[239] Supramolecular chemists use this value in order to calculate the hydrodynamic diameter of a component by using the Stokes-Einstein equation (Equation 3).[240]

$$d_{\mathrm{H}} = \frac{k_B T}{3\pi\eta D}$$

Equation 3 – Stokes-Einstein equation, showing the calculation of hydrodynamic diameter (m), d_H, where k_B is the Boltzmann constant (1.38 x 10^{-23} $m^2kg^{-2}K^{-1}$); T is temperature (K); η is solvent viscosity ($kgm^{-1}s^{-1}$); and D is the diffusion coefficient (m^2s^{-1}).

Although this is very useful information regarding the size of the molecule, the value calculated is not completely accurate. The Stokes-Einstein equation assumes that the molecule is 'spherical', and thus these values are just estimations of the hydrodynamic diameter. Variations in SSA topology and association type can affect the size of the molecule, as seen in Figure 69.

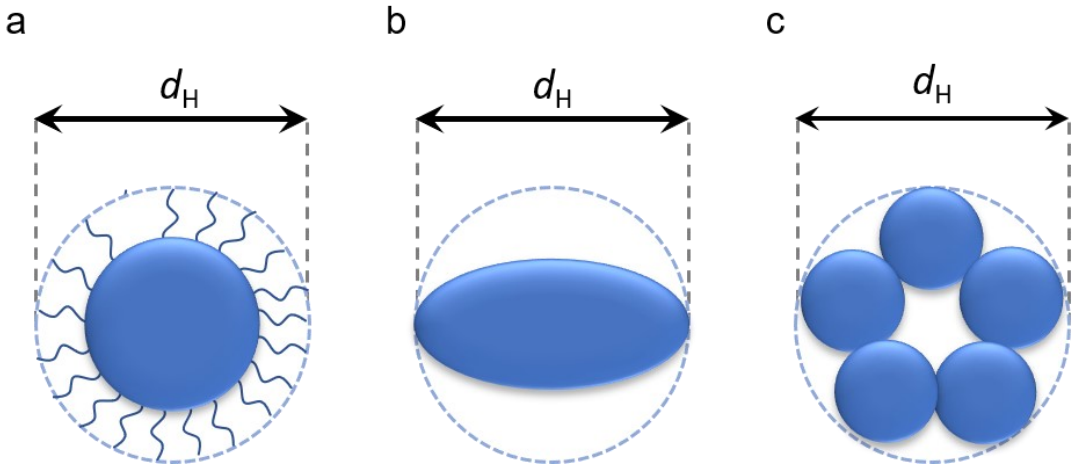

Figure 69 - Examples of the limitations that using the Stokes-Einstein equation to calculate hydrodynamic diameter (d_H) presents; a) A large molecule with tails, where the d_H value includes the tails; b) a non-spherical molecule, where the d_H value only provides information on one dimension of it; c) A unit of multiple molecules together, but d_H assumes the collective size of them.

An example of a calculation for the d_H for a molecule, in this case **39**, using the data in Figure 68 is as follows:

$$d_{\mathrm{H}} = \frac{(1.38 \times 10^{-23}) \times 298}{3 \times \pi \times 0.00199 \times (2.09 \times 10^{-10})} = 1.05\ nm$$

Equation 4 – An example of the calculation of d_H, using **39** as an example; where D is calculated by the average of the diffusion coefficients provided by the DOSY experiment data in Figure 68, the value viscosity value for DMSO is used, and the diffusion coefficients are taken from the data presented from the DOSY data table (Table 8).

The same calculation seen in Equation 4 is used to calculate the anionic and cationic components of **40** and **42**; where the D value used is an average of the diffusion coefficients for each respective set of peaks. For example, looking at Table 9, peaks 11-14 are seen to correspond to the cationic TBA component of **40**, and so the averages of these values are used.

Table 7 - An overview of the hydrodynamic diameters (nm), d_H, calculated for **39** – **42** in DMSO-d_6/0.5 % H_2O at 298 K.

Compound	d_H (nm)		
	Neutral	Anionic	Cationic
39	1.05	-	-
40	-	*1.46*	*1.24*
41	*a*	-	-
42	-	1.46	1.23

'a' indicates that the experiment was not conducted, and the dashes represent the data not being applicable due to the neutral or anionic nature of the compound.

Looking at the data in Table 7, we can observe how variations in the structure of the base compounds, **39**, affects the size of the hydrodynamic diameter. The neutral structure on its own, appears to have the smallest diameter of 1.05 nm; this result expected as **39** is a neutral, more hydrophobic species which lacks the anion-assisted hydrogen bonding potential which **40** and **42** possess. This data may suggest the formation of dimers as they are smaller ordered species; this may be further supported by the ^{1}H NMR dilution study data, seen in Table 8, where the dimerization association constant of 0.61 M^{-1}. However, this constant is fairly small. Unfortunately, data was not able to be collected for **41** due to poor solubility in the solvent, and

so the effects of simply incorporating a triple bond to the base neutral structure cannot be fully explored. However, we can compare both **40** and **42**, which have shown to have very similar values for calculated d_H and as these values are not very high, especially in comparison to **39** which showed no evidence of larger self-assembly in the qNMR experiment, it can be inferred that lower-order self-associated structures have formed. This set of data also suggests that the presence of the triple bond in **42** does not produce a significant difference in the d_H size, as this is the only difference between the two compounds. The main effect expected by the introduction of a triple bond to this structure was increased rigidity/decrease in bond rotation between the bi-pyridine and the urea. And so, it can be assumed, that increasing rigidity of this class of SSAs does not affect the d_H value; or if it does, the effect is very small. Investigating the hydrodynamic diameter of **41**, would have been a particular area of interest as it also showed the greatest percentage decrease in signal in DMSO; strongly suggesting the formation of larger, NMR-inactive structures.

The data from the DOSY studies also supports that the anionic and cationic components of **40** and **42** are not strongly associated in the solution state as the diffusion constants (Table 9 and Table 10) are different for both components; the qNMR data (Table 6) further supports this as it also shows different values for signal loss for both components of the compounds.

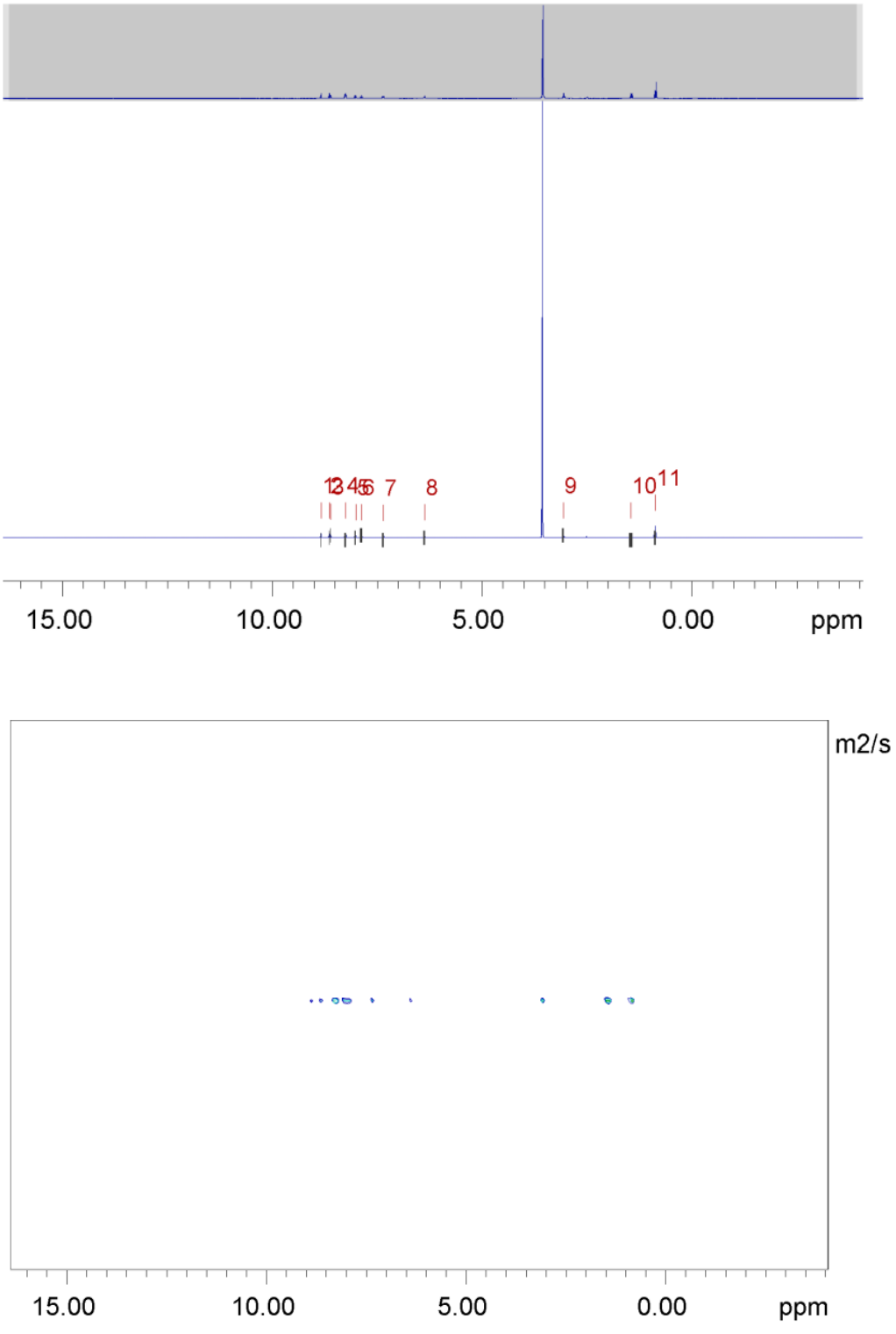

Figure 70 - ^{1}H DOSY NMR of compound **39** (111.2 mM) in DMSO-d_6 conducted at 298 K.

Peak name	F2 [ppm]	Io	error	D [m2/s]	error
1	8.838	9.45e+07	3147	2.09e-10	1.530e-14
2	8.639	1.10e+08	2784	2.08e-10	1.161e-14
3	8.610	1.14e+08	3499	2.09e-10	1.414e-14
4	8.258	2.49e+08	4768	2.09e-10	8.833e-15
5	8.017	1.28e+08	4602	2.09e-10	1.656e-14
6	7.879	1.31e+08	5434	2.09e-10	1.903e-14
7	7.357	1.27e+08	4829	2.09e-10	1.756e-14
8	6.372	1.04e+08	4622	2.09e-10	2.038e-14
9	3.069	2.62e+08	5829	2.09e-10	1.025e-14
10	1.454	2.75e+08	7742	2.08e-10	1.291e-14
11	0.873	3.91e+08	5232	2.09e-10	6.141e-15

Table 8 - ^{1}H DOSY NMR spectrum of the compound **39** (111.2 mM) in DMSO-d_6 at 298 K and a table reporting the diffusion constants calculated for each peak used to determine the solvation sphere diameter (d_H = 1.05 nm).

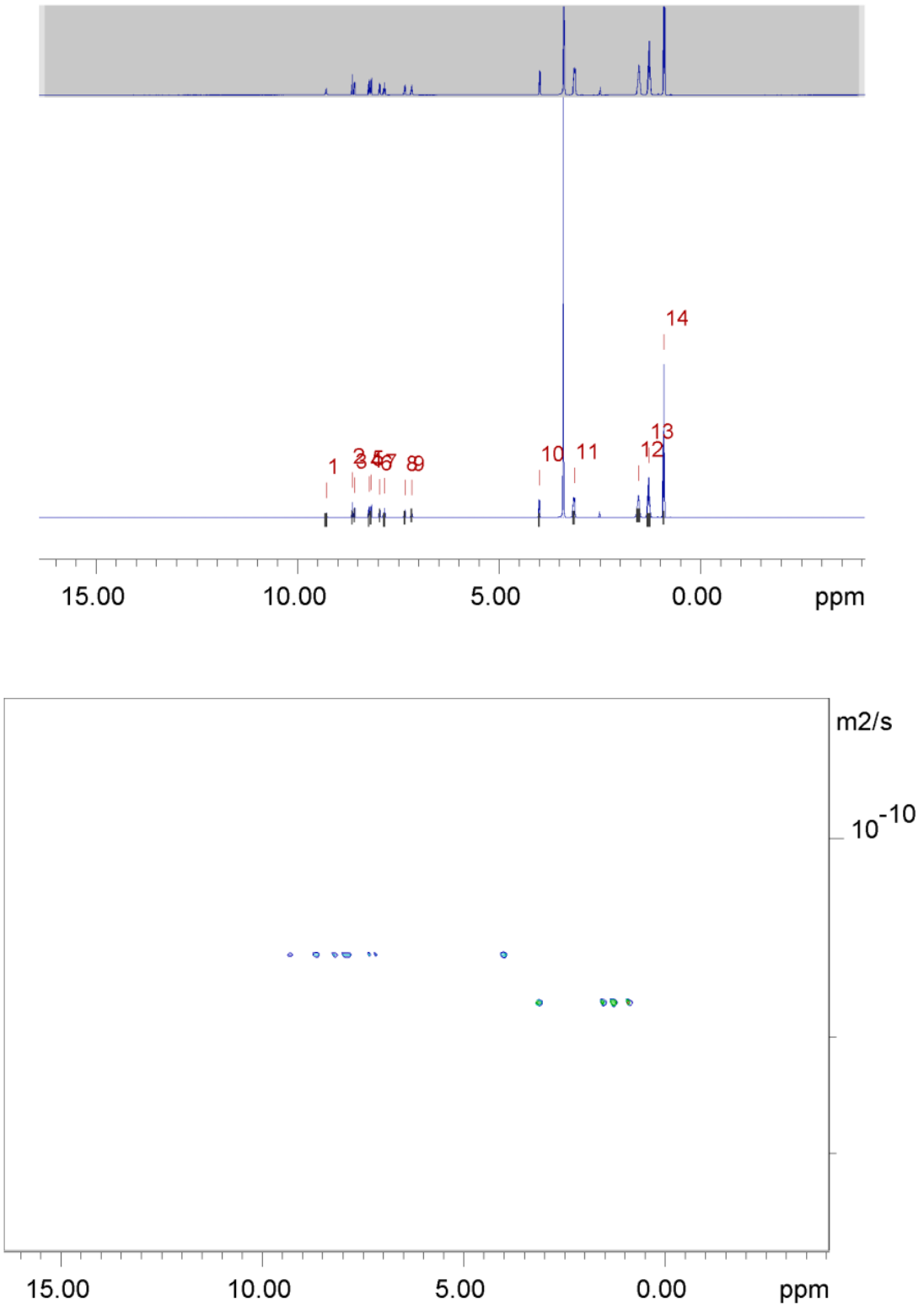

Figure 71 - ^{1}H DOSY NMR of compound **40** (112 mM) in DMSO-d_6 conducted at 298 K. Anionic component is highlighted in blue, TBA counter cation highlighted in green.

Peak name	F2 [ppm]	Io	error	D [m2/s]	error
1	9.293	4.40e+08	4.132e+04	1.50e-10	3.042e-14
2	8.649	6.75e+08	2.828e+04	1.50e-10	1.354e-14
3	8.591	6.44e+08	2.684e+04	1.50e-10	1.346e-14
4	8.230	6.27e+08	2.683e+04	1.50e-10	1.382e-14
5	8.180	6.32e+08	2.774e+04	1.51e-10	1.426e-14
6	7.964	6.36e+08	2.829e+04	1.50e-10	1.438e-14
7	7.849	6.50e+08	3.344e+04	1.50e-10	1.664e-14
8	7.340	6.64e+08	3.171e+04	1.50e-10	1.546e-14
9	7.172	5.16e+08	3.182e+04	1.50e-10	1.995e-14
10	4.007	1.12e+09	2.784e+04	1.50e-10	8.056e-15
11	3.146	3.05e+09	3.718e+04	1.77e-10	4.597e-15
12	1.549	3.77e+09	4.707e+04	1.78e-10	4.722e-15
13	1.293	4.90e+09	4.791e+04	1.78e-10	3.698e-15
14	0.916	7.93e+09	3.437e+04	1.78e-10	1.642e-15

Table 9 - ^{1}H DOSY NMR spectrum of the compound **40** (112 mM) in DMSO-d_6 at 298 K and a table reporting the diffusion constants calculated for each peak used to determine the solvation sphere diameter of the anionic component of **40** (d_H = 1.46 nm), and of the cationic component of **40** (d_H = 1.23) nm Peaks 1 - 10 correspond to the anionic component of **40** while peaks 11 - 14 correspond to the cationic component of **40**.

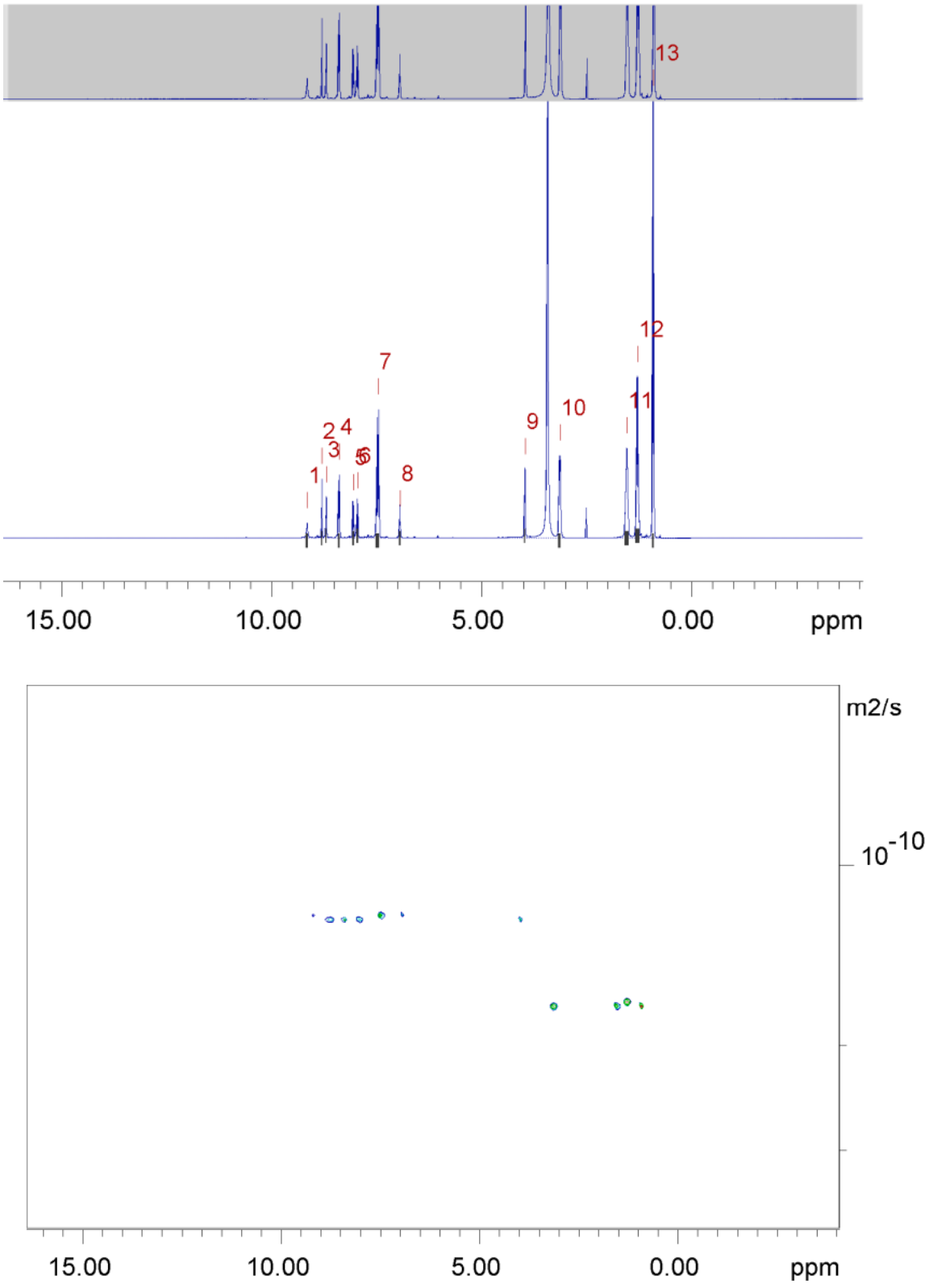

Figure 72 - ^{1}H DOSY NMR of compound **42** (112 mM) in DMSO-d_6 conducted at 298 K. Anionic component is highlighted in blue, TBA counter cation highlighted in green.

Peak name	F2 [ppm]	Io	error	D [m2/s]	error
1	9.158	5.42e+08	6.174e+04	1.22e-10	3.026e-14
2	8.805	8.17e+08	3.776e+04	1.23e-10	1.237e-14
3	8.700	9.93e+08	4.529e+04	1.23e-10	1.221e-14
4	8.397	2.07e+09	6.183e+04	1.23e-10	7.989e-15
5	8.060	9.75e+08	5.474e+04	1.23e-10	1.498e-14
6	7.959	1.11e+09	6.332e+04	1.24e-10	1.530e-14
7	7.473	5.38e+09	8.222e+04	1.23e-10	4.070e-15
8	6.951	8.11e+08	5.776e+04	1.22e-10	1.891e-14
9	3.972	1.54e+09	4.531e+04	1.24e-10	7.860e-15
10	3.142	4.66e+09	7.477e+04	1.71e-10	5.813e-15
11	1.549	5.89e+09	9.450e+04	1.71e-10	5.800e-15
12	1.296	7.85e+09	9.836e+04	1.70e-10	4.523e-15
13	0.919	1.26e+10	6.844e+04	1.71e-10	1.963e-15

Table 10 - ^{1}H DOSY NMR spectrum of the compound **42** (112 mM) in DMSO-d_6 at 298 K and a table reporting the diffusion constants calculated for each peak used to determine the solvation sphere diameter of the anionic component of **41** (d_H = 1.78 nm), and of the cationic component of **8** (d_H = 1.28) nm Peaks 1 - 9 correspond to the anionic component of **42** while peaks 10 - 13 correspond to the cationic component of **42**.

3.2.3. ^{1}H NMR self-association studies

As shown in Figure 60, if there is no "*loss*" of signal in the ^{1}H qNMR experiment observed, the next step is to determine self-association constants using ^{1}H NMR self-association studies. During these studies the sample is diluted through the step-by-step addition of solvent to study any hydrogen-bonded self-association events which may be occurring in solution. As DMSO-d_6 is highly hygroscopic, an aliquot of H_2O was added to minimise changes in H_2O concentration to ensure that the samples of the study were able to produce comparable data. The ^{1}H NMR is a very useful tool in understanding the behaviour of SSAs as it provides a method to monitor weak and non-covalent interactions.[241] Any hydrogen bonds that may form between the HBD of the urea functionality's NHs, and the HBAs on the SSAs can be monitored by these ^{1}H NMR dilution studies. To calculate any binding constants, the data collected was fitted to the both the Co-operative equal K (CoEK) model and the dimerization/Equal K (EK) model using Bindfit.[225] Both of these binding isotherms however present a common limitation; any aggregates formed are assumed to be singular component one-dimensional homogenous aggregates.[237] The EK model assumes that all association events are constant throughout the

data, and the CoEK model assumes that the first association event observed has a different association constant to any subsequent events.[242]

The results these of dilution studies allow us to estimate the strength of any hydrogen bond formation which is to be observed as the concentration of the SSA increases, the NHs protons shift are seen to shift downfield. Kumar *et al*. proposed that the bigger the chemical shift, the greater the strength of the bond being formed.[243]

Hiscock *et al*. have observed that the ethyl linker between the urea and sulfonate group causes the SSA to cyclise and form an intermolecular hydrogen bond to form a six membered ring in the crystal structure.[227] And so, as suspected by their previous data for analogous compounds, it can be hypothesised that **40** and **42** may exhibit a similar type of cyclisation; although, a five membered is less stable the extent of ring-strain is not great enough to rule out this hypothesis entirely (Figure 73). This theory may be further supported by the DOSY data previously seen in Table 7, as there is no evidence of anion-cation interactions observed due to their diffusion coefficients being very different.

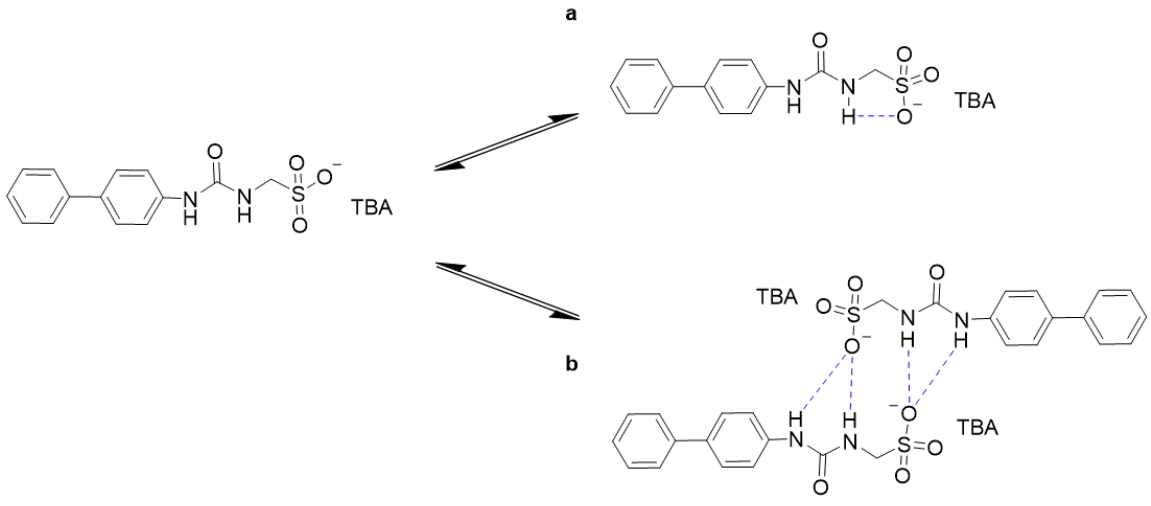

Figure 73 - An analogous example of the hypothesised self-association theorised for previous analogous compounds that may be observed in **40** and **42**. a) Compound **40** forms an intermolecular bond to form a 5 membered ring; or b) compound **40** dimerises which is more of SSAs.[92,151,152]

Table 11 – Overview of self-association constants (M^{-1}) calculated for **39** – **42**, in DMSO-d_6 0.5 % H_2O solution at 298 K. Constants were obtained for EK and CoEK models using Bindfit v0.5.[225] through the input of ^1H NMR dilution study data following NH resonances.

Compound	EK model (M^{-1})		CoEK model (M^{-1})		
	K_e	K_{dim}	K_e	K_{dim}	**ρ**
39	0.61 (± 8 %)	0.30 (± 4 %)	10.13 (± 24 %)	5.06 (± 12 %)	0.26 (± 71 %)
40	4.91 (± 1 %)	2.45 (± 1 %)	15.63 (± 2 %)	7.81 (± 1 %)	0.39 (± 7 %)
41	*a*	*a*	*a*	*a*	*a*
42	2.34 (± 2 %)	1.17 (± 1 %)	9.31 (± 5 %)	4.66 (± 2 %)	0.42 (± 12 %)

Where 'a' represents the experiment not being completed as a loss of compound was observed in the qNMR.

As seen in Table 11, the dilution study of compound **39** showed that using the EK model, there is a weak dimerization constant, K_{dim} 0.30 M^{-1} (± 4 %); when comparing the percentage errors of these values between the two models, (especially with an error of ± 71 % for the **ρ** value seen in the CoEK model) the EK model is the most appropriate model for this compound. That being said, however, we can conclude that there is no real self-association occurring here; the self-association constants produced using this model are very low and below a threshold of significance. The overall downfield change in chemical shift (0.018 ppm) is also very small; and the trend of the data is almost completely linear (Figure 74). This all supports the theory that the less amphiphilic neutral structure would be less capable at self-associating. Comparing **39** to its anionic counterpart **40** further supports this theory; where the data is fit to either model, the association constants calculated are higher and errors are much lower (Table 11). When comparing the results from both association models – it is difficult to discern which model is better suited; as both yield very small percentage errors. The association constants of K_e 15.63 M^{-1} (± 2 %), and K_{dim} 7.81 M^{-1} (± 1 %), with a ρ value of 0.39 (± 7 %) in the CoEK model, may be further supported with the greater overall downfield shift in chemical shift (0.6 ppm) – not only indicating self-association, but a much stronger hydrogen bond formation than **39**. Despite the EK model having slightly lower percentage errors, when considering that the trendline of the

data is also clearly a curve (Figure 75), it may be reasonable to rely on the model with the higher constant output. The K_{dim} constant being 50 % of the K_e constant suggests dimerization of **40**, which is commonly observed behaviour by other SSAs when in DMSO.[7,94] Both sets of data for **39** and **42** (Figure 74 and Figure 76) display little to no curvature – further supporting the low, negligible constants calculated for compounds **39** and **42** with both association models. Despite the higher constants being obtained for **42** using the CoEK model, the error is greater than 10 % for ρ, and when compared with the incredibly small errors using the EK model, the smaller constants calculated become more reliable – these values suggest a very small level of dimerization.

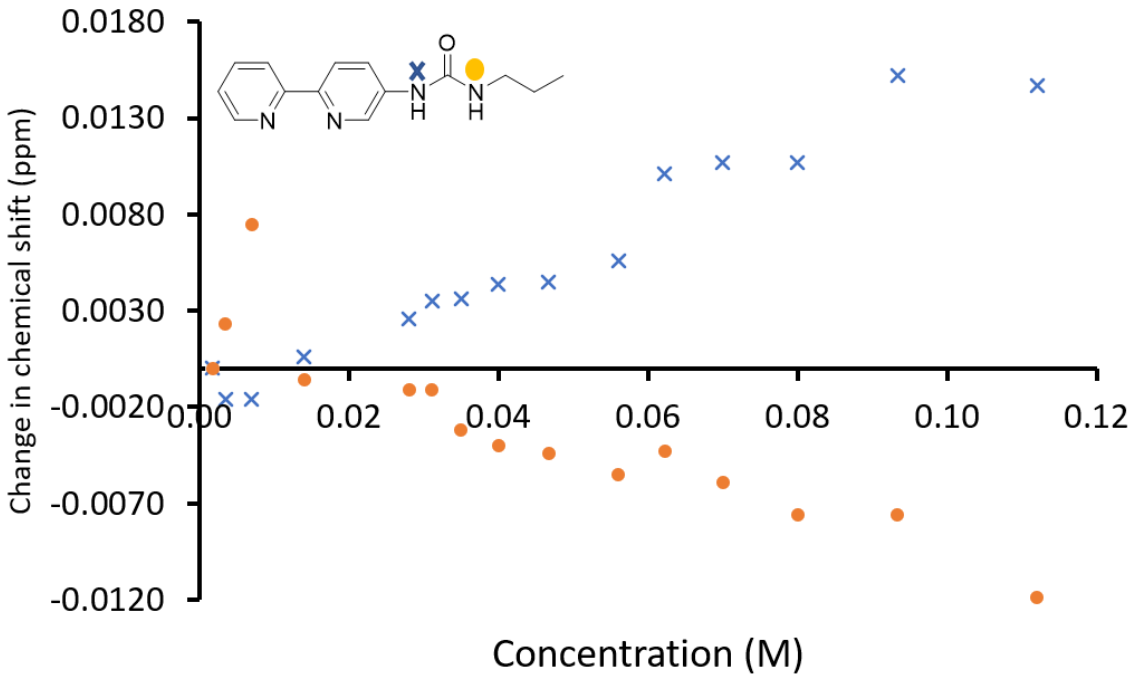

Figure 74 - Graph illustrating the ^{1}H NMR change in chemical shift of urea NH resonances with increasing concentrations of compound **39** in DMSO-d_6/0.5 % H_2O solution (298 K).

Observing the trends in the changes in chemical shift on each graph can further help us understand if self-association via hydrogen bonding is taking place too. When analysing the trend for **39** (Figure 74), the two NH protons can be seen to have a mirroring effect; with the proton closest to the bipyridine showing a downfield change, and the proton next to the aliphatic carbon chain showing an upfield change in chemical shift. This indicates that whatever

is taking place in solution which is producing an opposite effect on either side of the urea moiety; for example, de-shielding is likely occurring about the NH next to the bipyridine; causing a down-shift change. Using aforementioned hypothesis by Hiscock et al. [227] it may be hypothesised **42** may exhibit a similar type of cyclisation; although a five membered is less stable, the ring extent of ring-strain is not great enough the rule out this hypothesis entirely.[244,245] As the ^{1}H NMR dilution study for **42** did not produce a reliable self-association result; the change in chemical shift may be due to this.

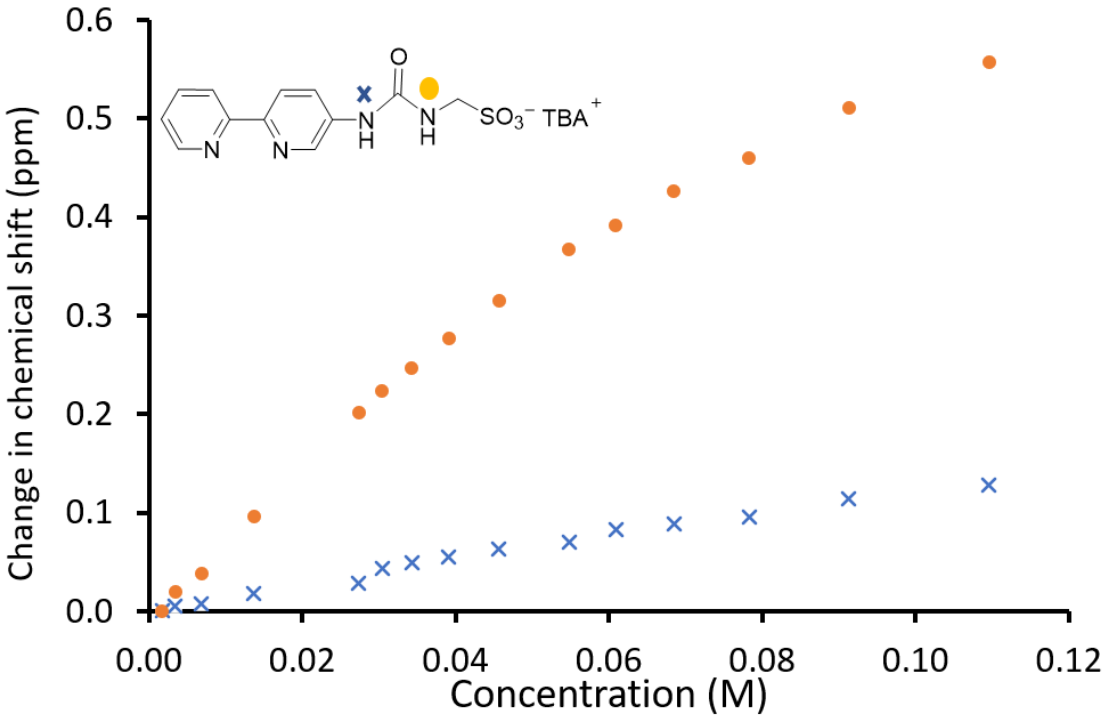

Figure 75 - Graph illustrating the ^{1}H NMR change in chemical shift of urea NH resonances with increasing concentrations of compound **40** in DMSO-d_6/0.5 % H_2O solution (298 K).

Looking at the bigger picture, when piecing in the data obtained from the qNMR experiments (Table 6) and from the DOSY experiments (Table 7) with the dilution studies (Table 11), the data comes together to further confirm the presence of lower order self-association of **40** in DMSO. As the dilution studies support the presence of hydrogen-bonded dimers and trimers, the d_H values show evidence of the anionic and cationic components not being strongly associated in the solution state, and qNMR showed no loss of components, ruling out the presence of higher-order self-assemblies. In the same manner, the data also supports the

absence of higher-order self-assemblies for **39**,**40**,**42**, and little to no evidence of lower-order structures such as dimers of **39** and **40**.

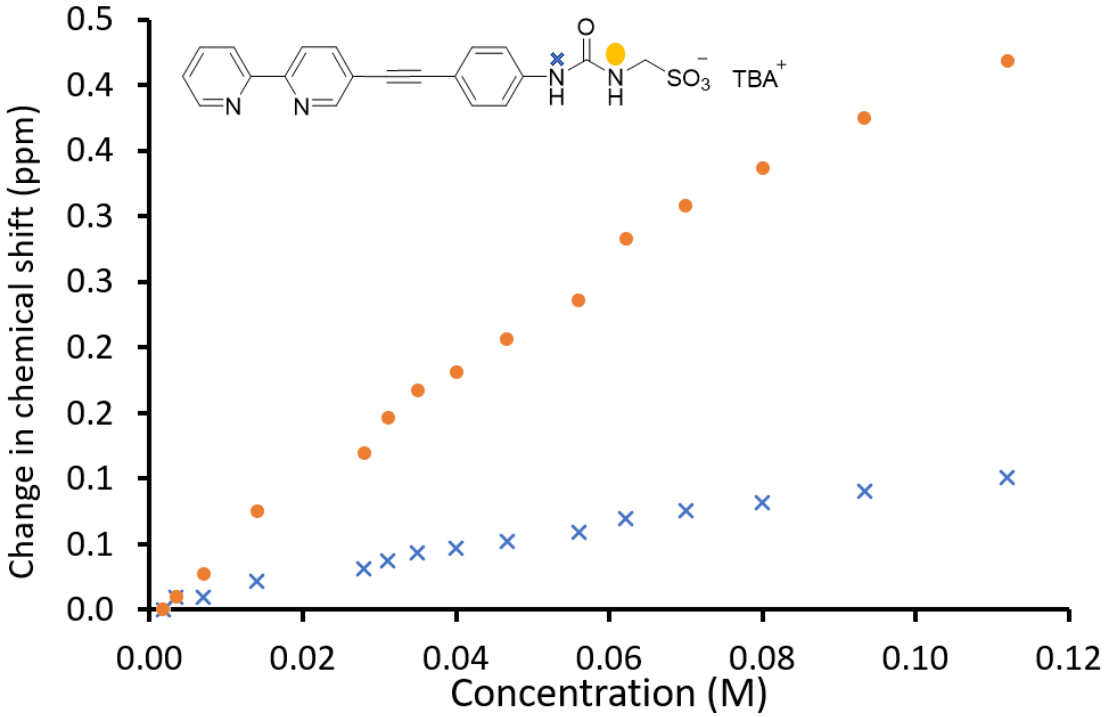

Figure 76 - Graph illustrating the ^{1}H NMR down-field change in chemical shift of urea NH resonances with increasing concentrations of compound **42** in DMSO-d_6/0.5 % H_2O solution (298 K).

3.2.4. Tensiometry and CMC determination

As stated previously the CMC of a compound is defined as the concentration barrier of a given surfactant at which micelles will form once exceeded. Thus, is may also be defined as the concentration at which surface tension does not continue to decrease with increasing concentration of a surfactant-like compound. Beyond this concentration, larger, self-associated structures begin to form in the bulk of the solution (such as micelle, reverse micelle, and vesicle aggregates) as illustrated in Figure 77. The decrease in surface tension is caused as a result of the interface becoming saturated.

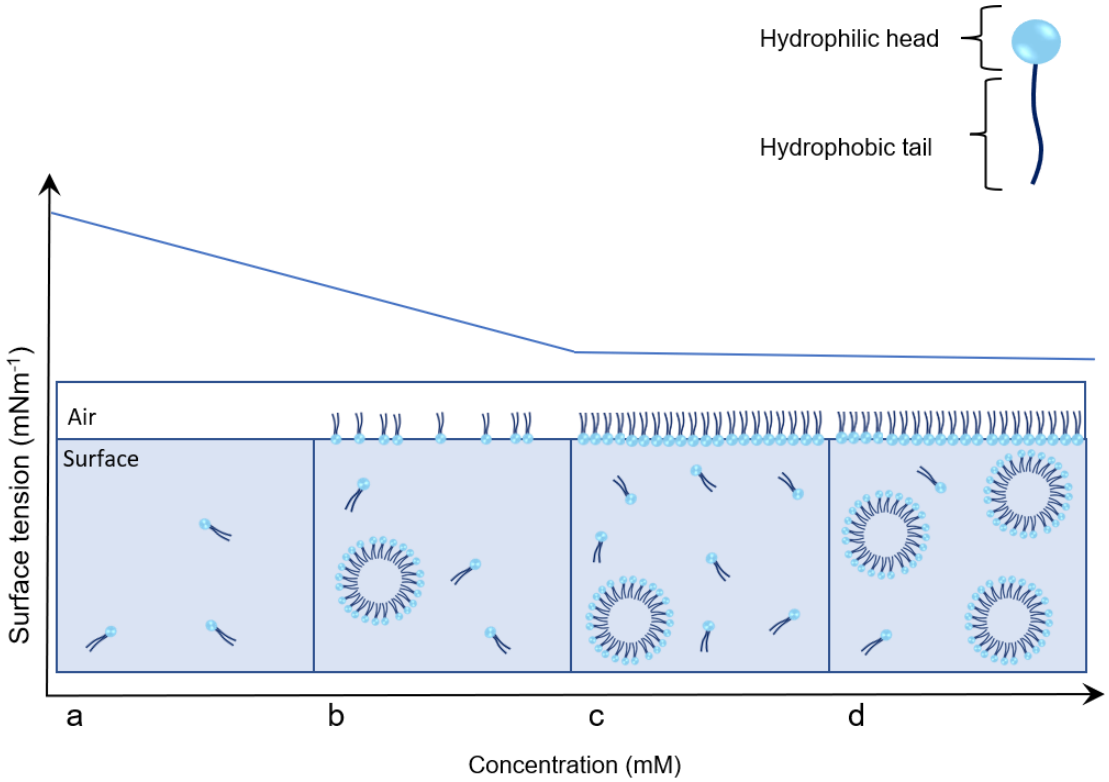

Figure 77 - The initial determination of CMC by Williams et al.[235] Where a) at a low concentration, no self-assembly is observed; b) Surfactants begin aggregating at the air-water interface, and some self-assembly is observed; c) Surface becomes saturated, forming a bi-layer and surface tension stops decreasing; d) Micelle formation is facilitated.

In order to determine CMC, the pendant drop method in EtOH:H_2O 1:19 was used, and the averages of these values (n=3) of surface tension for each concentration were plotted. Due to solubility limits of **41**, and **42**, the maximum concentration for these studies were chosen in relation to the maximum saturation in the solvent system. The CMC for **40** was calculated to be 27.96 mM at a surface tension of 43.86 mNm^{-1} (Figure 79). The CMC for other reported SSAs

have commonly found to be anywhere between 8-200 mM with surface tensions ranging 34-42 mNm^{-1}, a comparable data point from a published anionic SSA with thiourea group, and phenyl ring with a trifluoromethyl group had a CMC of 24.1 mM and surface tension of 34.35 mNm^{-1}. [238] Looking at this data, we can make some assumptions about **40**. The data suggests that the changes in the structure of **40** (namely, the inclusion of the bi-pyridine) doesn't introduce a unique value for CMC, but shows a slightly higher surface tension for this ballpark of CMC value. This may be worth noting as out of 50 compounds observed in this study, only this structure produced similar results as compound **40**.

Table 12 - An overview of CMC calculations for **39** – **42** in an EtOH:H_2O 1:19 mixture at 298 K.

Compound	CMC / mM	Surface tension/ mNm^{-1}
39	*a*	*a*
40	27.96	43.86
41	*a*	*a*
42	*a*	*a*

'a' indicates that a CMC value was not found, suggesting the absence of surfactant-like properties for the structure.

Investigating the compounds studied here (**39**-**42**), and mainly comparing **39** and **40**, it is clear that the introduction of the anionic sulfonate group assists in solubility; via the introduction of anion assisted hydrogen bonding. Comparing **41** and **42**, we can see that no CMC value was able to be calculated, and major solubility limits resulted in extremely dilute concentrations being used; suggesting that the introduction of the triple bond – and so the increased rigidity of the structure, may also affect solubility and micelle formation in EtOH:H_2O 1:19.

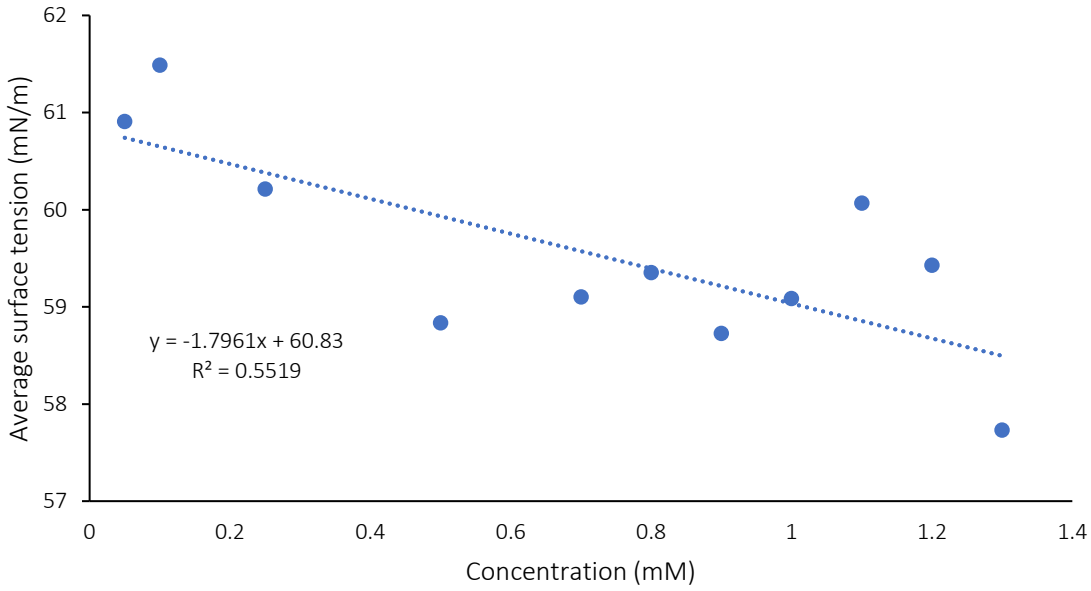

Figure 78 - Calculation of CMC for compound **39** in an EtOH:H_2O 1:19 mixture using surface tension measurements, here this shows no CMC value could be attained, suggesting no surfactant properties for this structure.

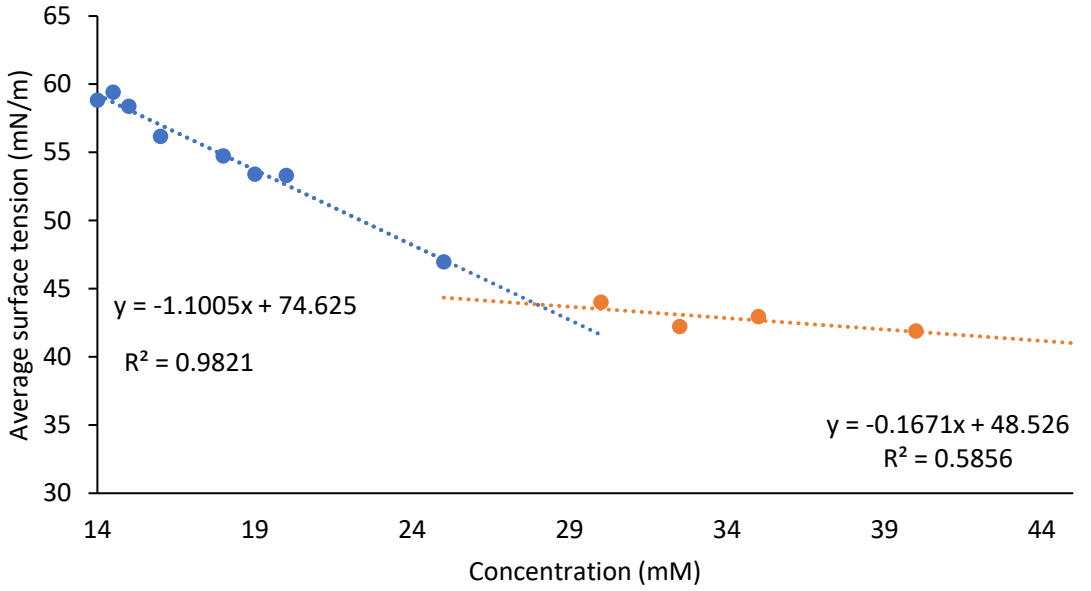

Figure 79 - Calculation of CMC (27.96 mM at 43.86 mNm^{-1}) for compound **40** in an EtOH:H_2O 1:19 mixture using surface tension measurements, suggesting surfactant properties for this structure.

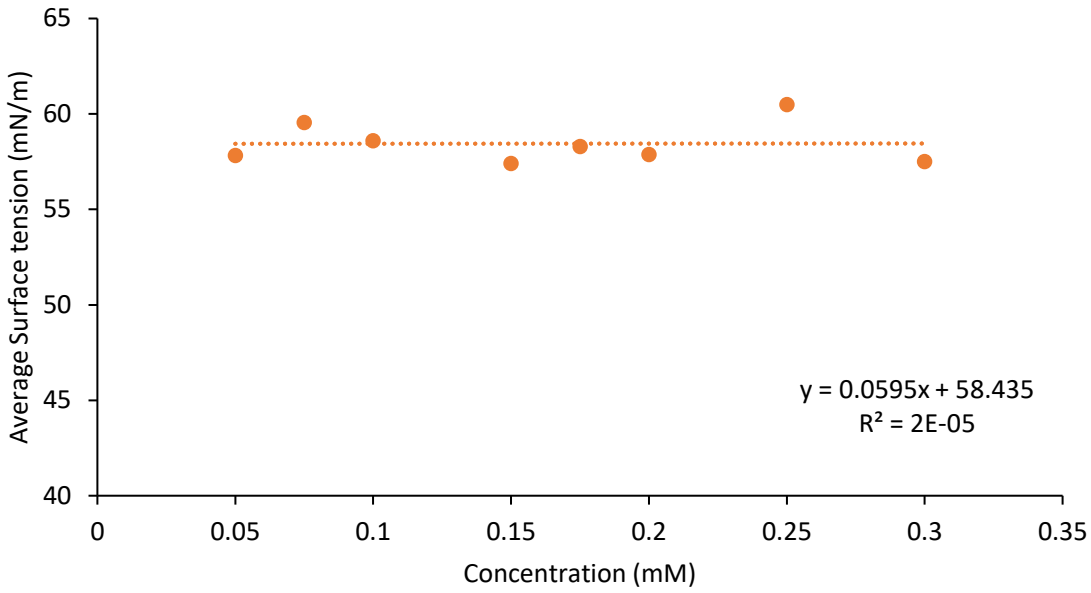

Figure 80 - Calculation of CMC for compound **41** in an EtOH:H_2O 1:19 mixture using surface tension measurements, here this shows no CMC value could be attained, suggesting no surfactant properties for this structure..

Another small factor to note is that when comparing **41** and **42**, the introduction of the sulfonate group appears to have not affected the general surface tension with both sets of data fluctuating around 58 mNm^{-1}.

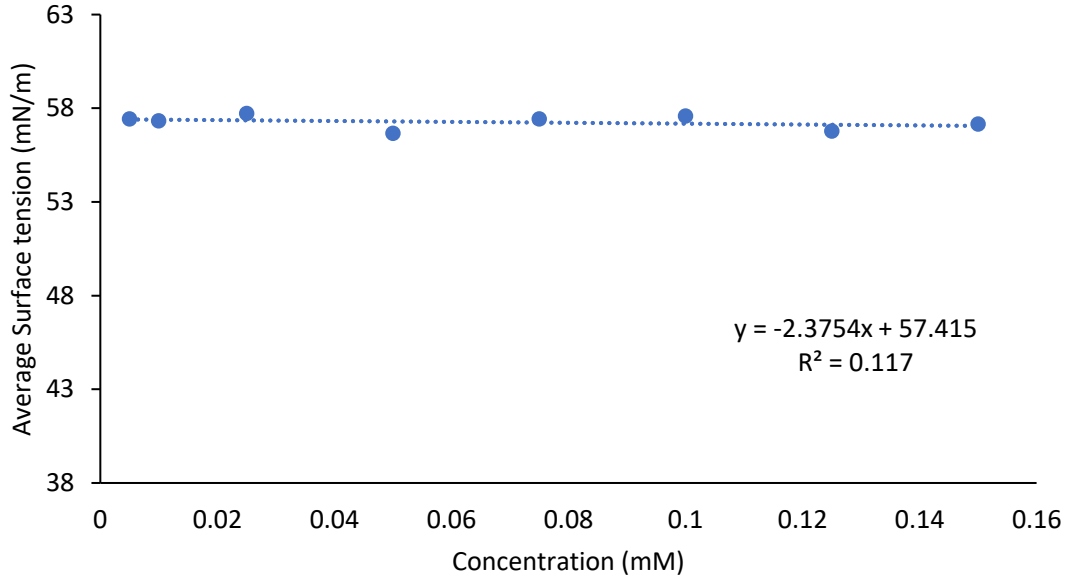

Figure 81 - Calculation of CMC for compound **42** in an EtOH:H_2O 1:19 mixture using surface tension measurements, here this shows no CMC value could be attained, suggesting no surfactant properties for this structure..

3.2.5. Dynamic light scattering studies

When an apparent 'loss' of signal is observed in the ^{1}H qNMR results, it can be assumed, that larger aggregates with solid-like properties may be forming; inhibiting them from being detected via ^{1}H NMR analysis. Thus, DLS studies are carried out to determine the size of the aggregates in solution (Figure 60).

DLS is a simple but extremely helpful technique regularly used by chemists and biologists for the detection of aggregates formed in solution by macromolecules. This technique utilises the Brownian motion of dispersed particles; which results in constant energy transfer between particles due to constant collisions.[246] Due to the conservation of energy, the motion of the larger molecules will differ when compared to the motion of smaller molecules. And such, when these particles are irradiated with visible monochromatic light, the intensities of the resultant scattered light fluctuate as the distances between particles continuously change. When recorded over a period of time, these intensities can be analysed to determine the diffusion coefficient (D) and through the use of the Stokes-Einstein equation, the hydrodynamic diameter (d_H) can be calculated (Equation 3); therefore, as with that of the ^{1}H DOSY NMR experiments, this method also assumes structures are spherical (Figure 69). This method is crucial for the study of larger diameters of high-order species, as it possess size limits from 1 – 1000 nm.[247]

The DLS experiment produces graphs of intensity distributions which are weighted by size – and as the refractive indexes of the compounds are currently unknown, we cannot produce data relating to number, which is typically used in this experiment, instead we can consider the polydispersity (PDI) of the molecules/aggregates. A larger PDI value indicates that a larger range of size are observed among the molecules/aggregates. Three different types of light scattering occur; which possess variations in dependency of the angle of the incident laser and the size of the particle (Figure 82).

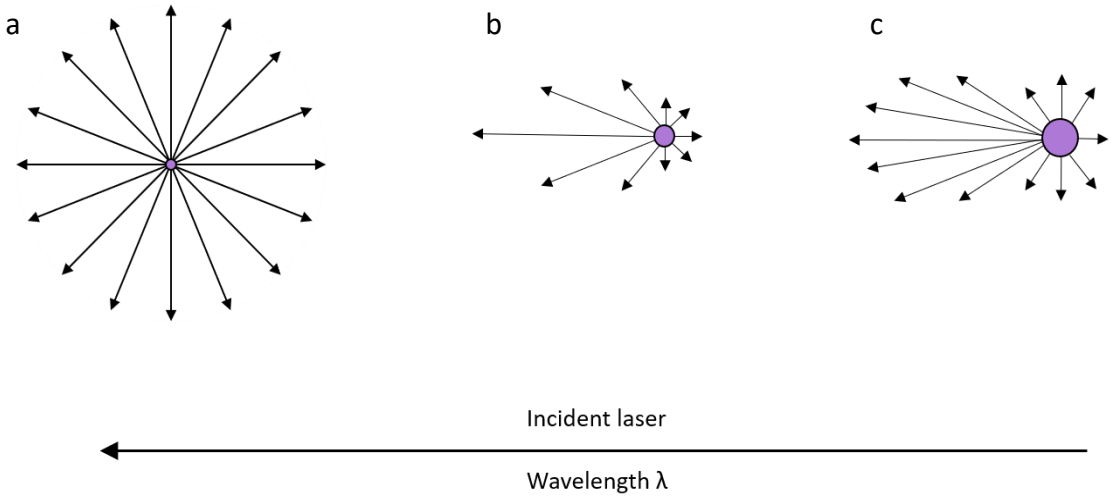

Figure 82 – Illustration of the differences between the two types of scatters – Rayleigh and Mie scattering. a) Rayleigh scattering, which is not angle-dependent, b) Mie scattering, which is angle dependent, c) Mie scattering, angle-dependence which increases with particle size.[248]

A DLS study is expected to be performed on the structures which showed percentage 'loss' of signal; looking at Table 5, the data shows that compounds **40** and **41** may be forming larger aggregates. The 0.35 % loss for **39**, is fairly low, however a DLS study was still carried out. Unfortunately, due to limitations with sample availability, **40** was not able to be studied via DLS for either solvent system. Furthermore, compounds **39**, **41**, and **42** are insoluble at the desired concentrations in order to produce comparable data in EtOH:H_2O 1:19, however the results attained in DMSO are detailed in Table 13.

Table 13 – Overview of DLS data for **39**-**42** in DMSO at 111.2 mM, where average intensity of particle size distribution is calculated from 10 DLS runs. Samples were prepared by heating to 40 °C and cooling to 25 °C. Error = standard error of the mean and given to 1 dp.

Compound	PDI (%)	Peak maxima (nm)
39	34.42 (± 1 %)	3216.95 (± 1633)
40	*a*	*a*
41	374.19 (± 171 %)	719.70 (± 33)
42[b]	27.35 (± 1 %)	1351.90 (± 35)

Where 'a' represents the experiment not being able to be completed, and 'b' represents a sample which did not require a DLS study due to 0 % 'loss' of signal in DMSO-d_6 during the ^{1}H qNMR studies.

Although the data on hand is limited, we can still investigate extended aggregate formation in **39** and **41** at 111.2 mM in DMSO. The PDI of **39** is 34.42 %, suggesting that we may be able to hypothesise the presence of a variety of macrostructures in the solution, as the error for this PDI is very low, however the standard error for the peak maxima is extremely high, substantially affecting the determination of the size of these particles; as there is a larger spread of data, a larger error is observed. Looking at the graphs for this experiment adds worth to these values, Figure 83 shows that the particle diameters around 260 nm are abundant, and most likely the best estimate for the structures this compound may be forming; however much larger diameters are also seen – suggesting higher order self-assembly may be taking place, the larger error for this experiment can also be attributed to the wider spread of data; the largest structures observed can be assumed to be an amalgamation of these larger structures. Dilution studies of **39**, also showed no evidence of low-order hydrogen-bonded self-assembly, however, the small d_H value, coupled with a qNMR percentage loss of virtually 0 %, the presence of a high-order species is also not evident. This indicates that this compound does not undertake any observable self-association under the conditions used.

The data produced for **41**, shows a very high standard error of ± 171 % for the PDI, perhaps ruling out the validity of this data, however looking at the particle size distribution (Figure 84), it is clear that **41** forms large aggregates with particle diameters near 720 nm; suggesting that self-association in this solvent system may be possible for this neutral species. The data produced for this compound is very limited, as a number of the experiments were not conducted for this compound; although it is worth noting that a considerably high apparent percentage loss of signal of 25.5 % (Table 6) was observed in DMSO-d_6/0.5 %; which had previously hinted the formation of larger NMR-silent structures forming in this solvent system.

Looking at **42** (Figure 85), however, we can still infer that the d_H values seen are very large; ranging up to 47735 nm, which is indicative of a much larger higher-order self-assembly

in solution coming together to form a large amalgamation. This also is supported by the highest percentage loss of signal being observed for this SSA; it is also supported by the fairly low dimerization association constants calculated from the dilution studies, and the DOSY data producing a much lower d_H value; as the higher-order species are NMR silent.

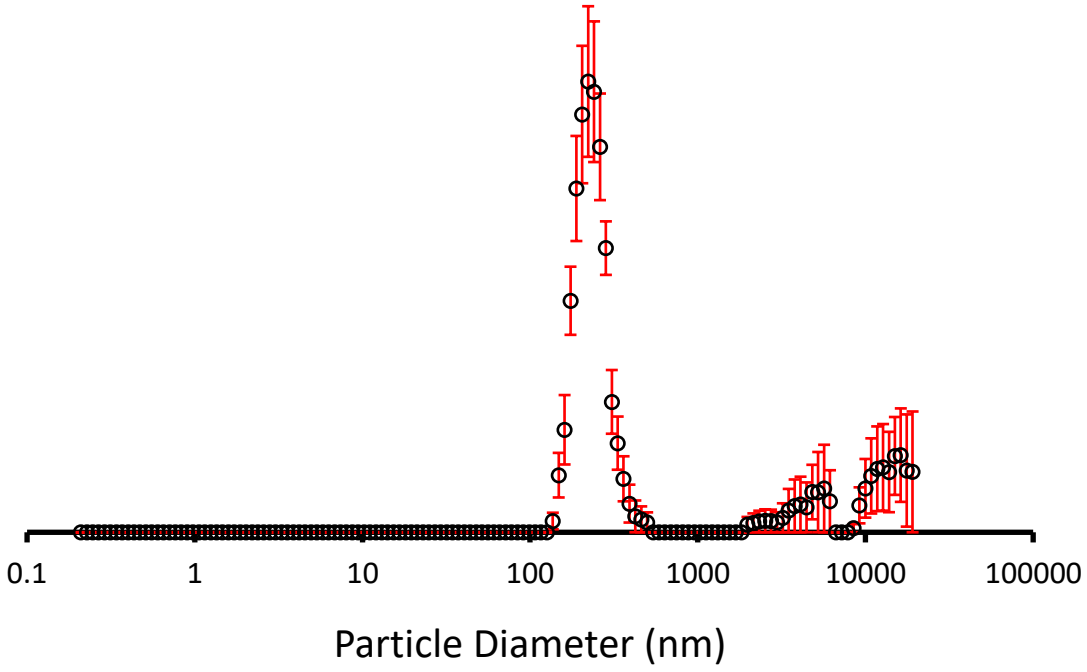

Figure 83 - The average intensity particle size distribution calculated (261 nm) using 10 DLS runs for compound **39** (111.2 mM) in DMSO/0.5 % H_2O solution at 298 K.

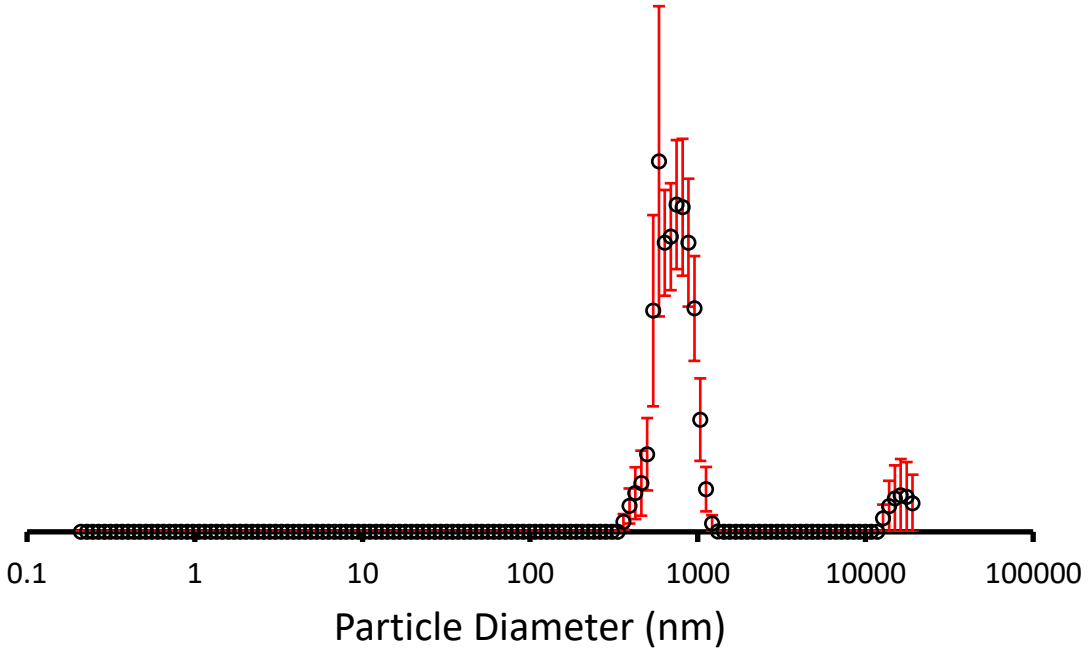

Figure 84 - The average intensity particle size distribution calculated (720 nm) using 10 DLS runs for compound **41** (111.2 mM) in DMSO/0.5 % H_2O solution at 298 K.

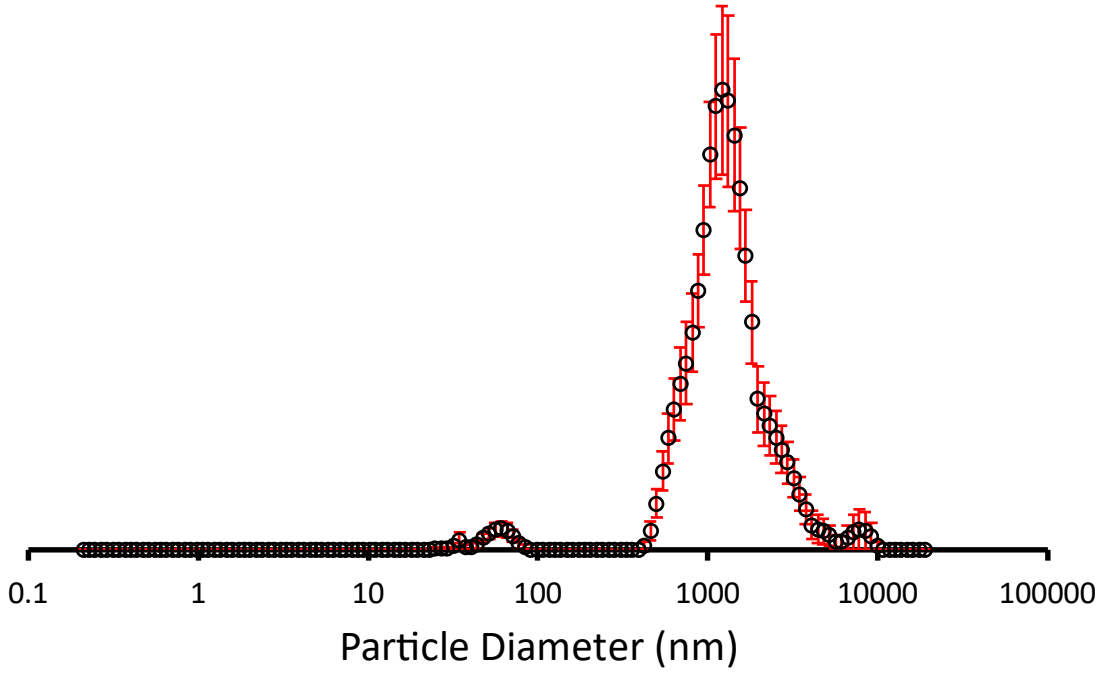

Figure 85 - The average intensity particle size distribution calculated (1216 nm) using 10 DLS runs for compound **42** (111.2 mM) in DMSO/0.5 % H_2O solution at 298 K.

3.2.6. Zeta potential studies

Zeta potential, also referred to as "*electrokinetic potential*", defines the potential of a colloid particle moving through an electrical field.[249] Zeta potential can be used to discern the stability of a colloid particle or aggregation in solution. To put it simply, when values between -30 mV and +30 mV are output, the structure is considered unstable, if there is an output extending this range – either lower than - 30 mV or greater than + 30 mV, this then signifies that the structure is moderately stable or very stable.[250] This experiment cannot be performed using DMSO/0.5% H_2O as a solvent system, as it will react with the zeta cell when a current is passed through (deeming the cell unusable), and so only an aqueous solvent, a EtOH:H_2O 1:19 mixture, is used. However, this introduces hard limitations to the experiments which can be carried out on compounds **39**-**42**, as they are mostly insoluble in this solvent system; and unable to produce solutions of the desired concentrations for this experiment. The only compound which readily dissolves in this solvent system is **42**, however **42** did not have an observable CMC in this solvent system, and so without surfactant-like properties being observed in a EtOH:H_2O 1:19 mixture stable aggregate formation would be expected to be unlikely.

The mean zeta potential for **42** however, is -56.95 mV (Figure 86), signifying that the assemblies formed by this compound in EtOH:H_2O 1:19 are very stable; this stability refers to any high-order larger self-assembly taking place. We can assume that this is self-assembly independent of anion-cation interactions as the DOSY for this compound showed different diffusion constants for both components in solution; however, that study is in a DMSO/0.5 % H_2O solution, and so this may not be necessarily reflect the self-association in a EtOH:H_2O 1:19 mixture.

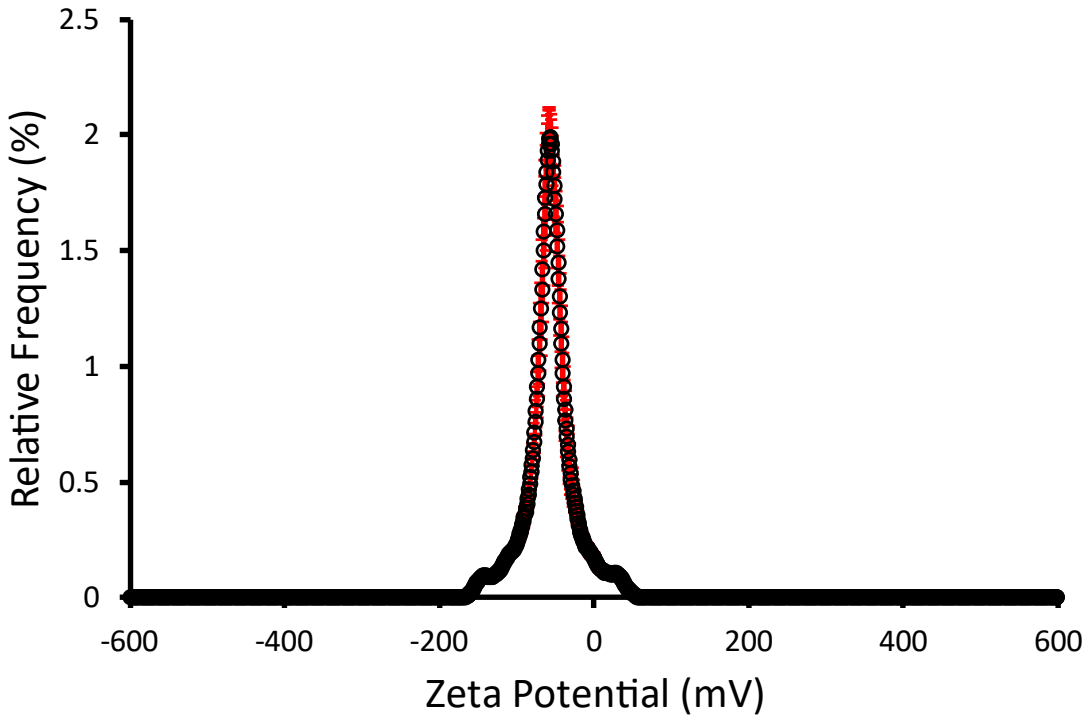

Figure 86 - The average zeta potential distribution calculated using 10 runs for compound **42** (0.56 mM) in EtOH:H_2O (1:19) solution at 298 K. Average measurement value - 56.95 mV.

3.3. Conclusion

Here, the physicochemical properties of the four compounds (**39**-**42**) have been described. The comparison of the results for the SSAs **40** and **42** show that the inclusion of a triple bond produces many different structure activity relationships; namely regarding CMC, solubility, and different responses in different solvent systems. SSA **42** shows more evidence of higher-order structures forming in D_2O/5 % EtOH solution from the qNMR studies, without any loss in DMSO-d_6 – whereas **40** shows no evidence of larger assembly in either solvent system, but has displayed surfactant-like behaviour in D_2O/5 % EtOH with a CMC calculated at 27.96 mM. Further study into these compounds is required; namely the solid-state studies, in order to further investigate the self-assembly these two SSAs are capable of.

4. Future work

1. Single crystal XRD to be performed on all compounds **35**-**38** and **39**-**41**.
2. As receptors **35**, **36** and **38** showed promise as sensors, adjustments to their structure with additional methyl groups on the fluorescent moieties to try and encourage further selectivity.
3. To investigate a wider range of anions with receptors **35**, **36** and **38** to further validate their anion selectivity.
4. Single crystal XRD is desirable for any binding events observed by receptors **35**, **36** and **38** with anions to understand the stoichiometry and conformation of the events.
5. Sample limitations of SSA **40** prevented some studies from being completed; DLS and zeta potential, to complete these experiments to have a comparable data set against both the neutral counterpart **39**, and the SSA **42**.

5. Experimental

5.1. Experimental methods

General remarks: All reactions were performed under slight positive pressure of nitrogen using oven dried glassware. NMR spectra were determined using a Bruker AV II or NEO 400 MHz spectrometer with chemical shifts reported in parts per million (ppm) and calibrated to the centre of the solvent peak set. Herein: br = broad; s = singlet; d = doublet; t = triplet; q = quartet, sept = septet and; m = multiplet. All solvents and starting materials were purchased from commercial sources or chemical stores where available and, used as purchased unless stated otherwise. The melting point for each compound was determined using Stuart SMP10 melting point apparatus.

Proton NMR titration method: A solution of receptor **35-38** (1.5 mL, 0.005 M) was initially prepared in DMSO-d_6 0.5 %. water. Of this solution 0.5 mL was placed in an NMR tube. The remaining 1 mL of the receptor solution was used to prepare a 0.075 M solution of the guest (**5-9**). The guest-receptor stock solution was titrated into the NMR tube and a ^{1}H NMR was taken before/after each subsequent addition of the stock solution.

Fluorimeter titration method: A solution of receptor **35-38** (5 mL, 0.01 mM) was prepared in DMSO/0.5 % H_2O, of which 2.5 mL was transferred into the cuvette. Peak maxima intensity of the receptor was followed as a solution made up of the remaining 2.5 mL and 4.2 mM of the guest was added. A total of 20 additions used to create a solution of 1:7 (host:guest) solution.

Association constant and self-association determination: Bindfit v0.5 (http://app.supramolecular.org/bindfit/)[225] was used to calculate all of the association constants. All data relating to the calculation of the association constants can be accessed online, through the links given for each association event.

Mass spectrometry: Initially 1 mg of each compound was dissolved in 1 mL of methanol, this was then further diluted before undergoing analysis. Then 10 µL of each sample was injected directly into a flow of 10 mM ammonium acetate in 95 % water (flow rate = 0.02 mL/min).

Tensiometry Studies: All samples were prepared in an EtOH:H_2O (1:19) solution. All samples were prepared through serial dilution of the most concentrated sample; the addition of the EtOH was done first to help with solubility. Three surface tension measurements were obtained for each sample at a given concentration; for each measurement 10 seconds were recorded at an average of 14 frames per second using the pendant drop method. The average of the all the values from the three measurements were plotted to calculate the critical micelle concentration (CMC).

DLS studies: All solvents used (DMSO) were filtered to remove any particulates that may interfere with results. The samples were not diluted as the experiments able to be conducted only pertained to DMSO. All samples were heated to 313 K then allowed to cool back to 298 K to facilitate an annealing process, allowing for each sample to reach a thermodynamic minimum. A series of 10 runs were recorded for each sample at 298 K.

Zeta potential studies: All solvents used (EtOH:H_2O 1:19) were filtered to remove any particulates that may interfere with the results. All samples were heated to 313 K then allowed to cool back to 298 K to facilitate an annealing process, allowing for each sample to reach a thermodynamic minimum. The resultant zeta potential value produced is an average of the number of experiments conducted at 298 K.

5.2. Synthesis

Compound 35: Pyridine-2,6-dicarbonyl dichloride (0.25 g, 1.23 mmol) was added to a 0°C solution of 6-methylbenzothiazol-2-amine (0.46 g, 2.46 mmol) in dichloromethane (25 mL). The mixture was left to slowly warm up to room temperature during an overnight stir. The precipitate was collected, washed with methanol and then dried to give a final product of a yellow solid (0.31 g, 0.67 mmol) in a yield of 54.2 %. ^{1}H NMR: (400 MHz, 298 k, DMSO-d_6): δ: 2.46 (s, 6H), 7.35 (dd, J_1 = 8.34 Hz, J_2 = 1.34 Hz, 2H), 7.87 (s, 2H), 7.79 (d, J = 8.21 Hz, 2H), 8.39 (m, 1H), 8.50 (d, J = 7.76 Hz, 2H), 13.55 (s, 2NH); ^{13}C{^{1}H} NMR (100 MHz, 298 K, DMSO-d_6): δ: 21.1 (CH_3), 120.9 (ArCH), 121.7 (ArCH), 127.2 (ArCH), 128.0 (ArCH), 132.8 (ArC), 134.1 (ArC), 140.7 (ArC), 147.4 (ArCH), 148.3 (ArC), 157.8 (NCS), 163.3 (NC=O). FT-IR: ν˜ = (cm^{-1}): 3248.13 (N-H stretch), 1689.64 (C=O stretch), 1273.02 (C-N stretch); MP.: >200° C; HRMS ($C_{23}H_{16}N_5O_2S_2$)$^-$ (ESI$^-$): m/z: act: 432.2766, [M]$^-$ cal: 432.0511 [M]$^-$.

Compound 36: Isophthaloyl dichloride (0.51 g, 2.46 mmol) was added to a solution of 1-aminonapthalene (0.72 g, 4.93 mmol) in pyridine (15 mL). The mixture was stirred under nitrogen at 60 °C reflux overnight. The precipitate was filtered and washed over with water to yield a white solid (0.68 g, 1.63 mmol) in a yield of 66.3 %. ^{1}H NMR (400 MHz, 298 k, DMSO-d_6): δ: 7.60 (m, 8H), 7.77 (m, 1H), 7.89 (d, J = 8.10 Hz, 2H), 8.03 (m, 4H), 3.32 (d, J_1 = 7.61 Hz, J_2 = 1.34, 2H), 8.79 (s, 2NH); ^{13}C{^{1}H} NMR (100 MHz, 333 K, DMSO-d_6): δ: 123.9 (ArCH), 124.3 (ArCH), 126.1 (ArCH), 126.5 (ArCH), 126.6 (ArCH), 126.9 (ArCH), 127.9 (ArCH), 128.6 (ArCH), 129.2 (ArCH), 129.6 (ArCH), 131.3 (ArC), 134.2 (ArC), 134.3 (ArC), 135.3 (ArC), 166.3 2(NC=O). FT-IR: ν˜ = (cm^{-1}): 3207.6 (N-H stretch), 1672.3 (C=O stretch); MP.: >200 °C; HRMS ($C_{28}H_{19}N_2O_2$)$^-$ (ESI$^-$): m/z: act: 414.0060, [M]$^-$ cal: 416.1525 [M]$^-$.

Compound 37: Pyridine-2,6-dicarbonyl dichloride (0.25 g, 1.23 mmol) was added to a 0°C solution of 1-aminonaphthalene (0.35 g, 2.46 mmol) in dichloromethane (25 mL). The mixture was left to slowly warm up to room temperature during an overnight stir.196 The

precipitate was collected, washed with excess dichloromethane, saturated $NaCO_3$ aq. and water, then was left to dry to yield a white solid product (0.267 g, 0.64 mmol) in a yield of 52.1 %. 1H NMR (400 MHz, 298 k, DMSO-d_6): δ: 7.67 (m, 8H), 7.92 (d, J = 8.09 Hz, 2H), 8.01 (dd, J_1 = 7.91 Hz, J_2 = 1.38 Hz, 2H), 8.11 (dd, J_1 = 8.12 Hz, J_2 = 0.94 Hz, 2H), 8.37 (dd, J_1 = 6.88 Hz, J_2 = 1.66 Hz, 1H), 8.46, (d, 2H), 11.44 (d, 2H); this NMR spectra was found to match previously published values.[224]

Compound 38: Isophthaloyl dichloride (0.82 g, 4.0 mmol) was added to a solution of amino-benzothiazole (1.32 g, 8 mmol) in pyridine (20 mL). The mixture was refluxed overnight under N_2 at 110°C. The precipitate (side product) was filtered off, and water was added as an antisolvent to crash out the product from the filtrate. Once filtered, the compound was purified using column chromatography (95% EtOAc, 5% MeOH), and recrystallised from DMSO in a yield of 12.8 %. 1H NMR (400 MHz, 298 k, DMSO-d_6): δ: 2.45 (s, 6H), 7.30 (d, J = 8.34 Hz, 2H), 7.70 (d, J = 7.22 Hz, 2H), 7.76 (t, J = 7.78 Hz, 1H), 7.84 (s, 2H), 8.35 (d, J = 7.78 Hz, 2H), 8.88 (s, 1H), 12.89 (s, 2NH); $^{13}C\{^1H\}$ NMR (100 MHz, 298 K, DMSO-d_6): δ: 21.3 (CH_3), 120.9 (ArCH), 121.7 (ArCH), 127.2 (ArCH), 128.1 (ArCH), 132.7 (ArCH), 134.1 (ArC), 137.9 (ArCH), 137.6 (ArCH), 140.7 (ArC), 148.3 (ArCH), 157.6 (NCS), 163.3 (NC=O). FT-IR: $\tilde{\nu}$ = (cm^{-1}): 3130.5 (N-H stretch), 1658.8 (C=O stretch); MP.: >200 °C; HRMS $(C_{24}H_{17}N_5O_2S_2)^-$ (ESI^-): m/z: act: 459.2793, $[M]^-$ cal: 459.0871 $[M]^-$.

6. References

1 J. M. Lehn, *Angew. Chemie Int. Ed*., 1990, **29**, 1304-1319.

2 R. M. Izatt, *Chem. Soc. Rev.*, 2017, **46**, 2380–2384.

3 D. J. Cram, *Angew. Chemie Int. Ed*., 1988, **27**, 1021-1027.

4 J. M. Lehn, *Acc. Chem. Res*., 1978, **11**, 49–57.

5 J. Černý and P. Hobza, *Phys. Chem. Chem. Phys*., 2007, **9**, 5291.

6 P. Ballester, P. W. N. M. van Leeuwen and A. Vidal, in *Comprehensive Inorganic Chemistry II*, Elsevier, 2013.

7 L. J. White, J. E. Boles, K. L. F. Hilton, R. J. Ellaby and J. R. Hiscock, *Molecules*, 2020, **25**, 4126

8 M. Cardona, K. Farrugia and D. C. Magri, *Xjenza Online*, 2013, 34–41.

9 J. K. Tusa and H. He, *J. Mater. Chem*., 2005, **15**, 2640.

10 D. B. Amabilino, D. K. Smith and J. W. Steed, *Chem. Soc. Rev*., 2017, **46**, 2404–2420.

11 U. C. Meier and C. Detellier, *J. Phys. Chem. A*, 1999, **103**, 9204–9210.

12 Kinne-Saffran and R. K. H. Kinne, *Am. J. Nephrol*., 1999, **19**, 290–294.

13 J. S. Rowlinson, *Nature.*, 1973, **244**, 414–417.

14 D. E. Koshland, *Angew. Chem. Int. Ed. Engl*., 1995, **33**, 2375–2378.

15 Host-Guest Chemistry on JSTOR, https://www.jstor.org/stable/1737191, (accessed August 12, 2021).

16 U. Boas and P. M. H. Heegaard, *Chem. Soc. Rev.*, 2004, **33**, 43–63.

17 T. Higashi, K. Motoyama and H. Arima, *J. Pharm. Soc. Japan*, 2019, **139**, 175–183.

18 J. C. Barnes and C. A. Mirkin, *Proc. Natl. Acad. Sci.*, 2017, **114**, 620–625.

19 A. Livoreil, C. O. Dietrich-Buchecker and J. P. Sauvage, *J. Am. Chem. Soc.*, 1994, **116**, 9399–9400.

20 R. A. Bissell, E. Córdova, A. E. Kaifer and J. F. Stoddart, *Nature*, 1994, **369**, 133–137.

21 G. N. Lewis, *J. Am. Chem. Soc*., 1916, **38**, 762–785.

22 T. S. Moore and T. F. Winmill, *J. Chem. Soc., Trans*., 1912, **101**, 1635–1676.

23 W. M. Latimer and W. H. Rodebush, *J. Am. Chem. Soc*., 1920, **42**, 1419–1433.

24 J.W. Steed, D.R. Turner and K. Wallace, *Core Concepts in Supramolecular Chemistry and Nanochemistry: From Supramolecules to Nanotechnology*, West Sussex, UK, 2007.

25 J. Emsley, *Chem. Soc. Rev*., 1980, **9**, 91-124.

26 G. Gilli and P. Gilli, *J. Mol. Structure*, 2000, **552**, 1–15.

27 J. W. Steed, J. L. Atwood, *Supramolecular Chemistry*, Wiley, Chichester, 2000

28 P. Dapporto, P. Paoli and S. Roelens, *J. Org. Chem*., 2001, **66**, 4930–4933

29 G. Ono, A. Izuoka, T. Sugawara and Y. Sugawara, *J. Mater. Chem*., 1998, **8**, 1703–1709.

30 A. Eisenberg and M. Hara, *Polym. Eng. Sci*., 1984, **24**, 1306–1311.

31 D. A. Dougherty, *Acc. Chem. Res*., 2012, **46**, 885–893.

32 B. L. Schottel, H. T. Chifotides and K. R. Dunbar, *Chem. Soc. Rev*., 2008, **37**, 68–83.

33 *Modern Electrochemistry 1*, 2002, Springer, Boston, MA, 225–359.

34 M. L. Waters, *Current Opinion in Chem. Biology*, 2002, **6**, 736–741.

35 J. D. Watson and F. H. C. Crick, *Nature*, 1953, **171**, 737–738.

36 C. A. Hunter, *Angew. Chem. Int. Ed*., 2004, **43**, 5310–5324.

37 R. E. Hubbard and M. Kamran Haider, in *Encyclopedia of Life Sciences*, John Wiley & Sons, Ltd, Chichester, UK, 2010.

38 C. O. Mackenzie, J. Zhou and G. Grigoryan, *Proc. Natl. Acad. Sci*., 2016, **113**, 7438–7447.

39 P. Yakovchuk, *Nucleic Acids Res.*, 2006, **34**, 564–574.

40 E. F. Armstrong, *Nature*, 1933, **131**, 535–537.

41 P. E. McGovern, J. Zhang, J. Tang, Z. Zhang, G. R. Hall, R. A. Moreau, A. Nunez, E. D. Butrym, M. P. Richards, C. -s. Wang, G. Cheng, Z. Zhao and C. Wang, *Proc. Natl. Acad. Sci*., 2004, **101**, 17593–17598.

42 J. N. Armor, *Catalysis Today*, 2011, **163**, 3–9

43 D. E. Koshland, *Proc. Natl. Acad. Sci*., 1958, **44**, 98–104

44 H. M. Berman, *Nucleic Acids Res.*, 2000, **28**, 235–242.

45 S. J. Teague, *Nat. Rev. Drug Discov.*, 2003, **2**, 527–541.

46 C. J. Tsai, S. Kumar, B. Ma and R. Nussinov, *Protein Sci.*, 1999, **8**, 1181–1190.

47 B. Ma, S. Kumar, C.-J. Tsai and R. Nussinov, *Protein Eng., Des. Sel*., 1999, **12**, 713–720.

48 C. Yan and X. Zou, in *Comp. Med. Chem. III*, Elsevier, 2017.

49 M. Arroyo, I. de la Mata, J.-L. García and J.-L. Barredo, *Biotechnology of Microbial Enzymes*, Elsevier, 2017, 451–473.

50 C. R. Frink, P. E. Waggoner and J. H. Ausubel, *Proc. Natl. Acad. Sci*., 1999, **96**, 1175–1180.

51 P. J. Thorburn, J. S. Biggs, K. L. Weier and B. A. Keating, *Agriculture, Eco. Env.*, 2003, **94**, 49–58.

52 C. Cossu, M. Fiore, D. Baroni, V. Capurro, E. Caci, M. Garcia-Valverde, R. Quesada and O. Moran, *Front. Pharmacol*., 2018, **9**.

53 P. Linsdell, *Exp. Phys*., 2005, **91**, 123–129.

54 H. Nury, C. Dahout-Gonzalez, V. Trézéguet, G. Lauquin, G. Brandolin and E. Pebay-Peyroula, *FEBS Letters.*, 2005, **579**, 6031–6036.

55 M. Rahm, R. Hoffmann and N. W. Ashcroft, *Chem. Eur. J*., 2016, **22**, 14625–14632.

56 S. R. Gadre and I. H. Shrivastava, *J. Chem. Phys*., 1991, **94**, 4384–4390.

57 F. Sommer, Y. Marcus and S. Kubik, *ACS Omega*, 2017, **2**, 3669–3680

58 J. M. Lehn, in *Chemistry for the Welfare of Mankind*, Elsevier, 1979.

59 R. A. Bell, G. G. Christoph, F. R. Fronczek and R. E. Marsh, *Science*, 1975, **190**, 151–152.

60 J. R. Hiscock, PhD thesis, University of Southampton, 2010.

61 R. A. Pascal Jr., J. Spergel and D. Van Engen, *Tetrahedron Lett.*, 1986, **27**, 4099–4102.

62 S. Valiyaveettil, J. F. J. Engbersen, W. Verboom and D. N. Reinhoudt, *Angew. Chem. Int. Ed. Engl*., 1993, **32**, 900–901.

63 S. K. Berezin and J. T. Davis, *J. Am. Chem. Soc*., 2009, **131**, 2458–2459.

64 K. J. Winstanley, S. J. Allen and D. K. Smith, *Chem. Commun*., 2009, 4299.

65 K. Kavallieratos, S. R. de Gala, D. J. Austin and R. H. Crabtree, *J. Am. Chem. Soc*., 1997, **119**, 2325–2326.

66 P. V. Santacroce, J. T. Davis, M. E. Light, P. A. Gale, J. C. Iglesias-Sánchez, P. Prados and R. Quesada, *J. Am. Chem. Soc*., 2007, **129**, 1886–1887.

67 M. Arunachalam and P. Ghosh, *Org. Lett*., 2009, **12**, 328–331.

68 M. Arunachalam and P. Ghosh, *Inorg. Chem*., 2009, **49**, 943–951.

69 M. Arunachalam and P. Ghosh, *Chem. Commun*., 2009, 5389.

70 P. A. Gale, S. E. García-Garrido and J. Garric, *Chem. Soc. Rev*., 2008, **37**, 151–190.

71 P. A. Gale, *Acc. Chem. Res*., 2006, **39**, 465–475.

72 L. O. Abouderbala, W. J. Belcher, M. G. Boutelle, P. J. Cragg, J. Dhaliwal, M. Fabre, J. W. Steed, D. R. Turner and K. J. Wallace, *Chem. Commun*., 2002, **4**, 358–359.

73 A. Metzger, V. M. Lynch and E. V. Anslyn, *Angew. Chem. Int. Ed. Engl*., 1997, **36**, 862–865.

74 L. O. Abouderbala, W. J. Belcher, M. G. Boutelle, P. J. Cragg, J. W. Steed, D. R. Turner and K. J. Wallace, *Proc. Natl. Acad. Sci*., 2002, **99**, 5001–5006.

75 K. J. Wallace, W. J. Belcher, D. R. Turner, K. F. Syed and J. W. Steed, *J. Am. Chem. Soc*., 2003, **125**, 9699–9715.

76 W. Gong and K. Hiratani, *Tetrahedron Lett*., 2008, **49**, 5655–5657.

77 A. Dorazco-González, H. Höpfl, F. Medrano and A. K. Yatsimirsky, *J. Org. Chem*., 2010, **75**, 2259–2273.

78 D. Philp and J. F. Stoddart, *Angew. Chem. Int. Ed. Engl*., 1996, **35**, 1154–1196.

79 D. S. Lawrence, T. Jiang and M. Levett, *Chem. Rev*., 1995, **95**, 2229–2260.

80 G. E. Schulz and R. H. Schirmer, *Angew. Chem*., 1984, **96**, 1003–1004.

81 C. J. Pedersen, *Science*, 1988, **241**, 536–540.

82 D. J. Cram and R. H. Bauer, *J. Am. Chem. Soc*., 1959, **81**, 5971–5977.

83 P. Gale, *Coord. Chem. Rev*., 2000, **199**, 181–233.

84 M. M. G. Antonisse and D. N. Reinhoudt, *Chem. Commun*., 1998, **4**, 443–448.

85 A. P. Bisson, V. M. Lynch, M.-K. C. Monahan and E. V. Anslyn, *Angew. Chem. Int. Ed. Engl*., 1997, **36**, 2340–2342.

86 P. A. Gale, J. L. Sessler, V. Král and V. Lynch, *J. Am. Chem. Soc*., 1996, **118**, 5140–5141.

87 C. A. Ilioudis, D. A. Tocher and J. W. Steed, *J. Am. Chem. Soc*., 2004, **126**, 12395–12402.

88 B. M. Maubert, J. Nelson, V. McKee, R. M. Town and I. Pál, *J. Chem. Soc., Dalton Trans*., 2001, 1395–1397.

89 K. Choi and A. D. Hamilton, *Angew. Chem., Int. Ed. Engl*, 2000, **120**, 2456–2457.

90 C. Biffinger, H. W. Kim and S. G. Dimagno, *ChemBioChem*, 2004, **5**, 622–627.

91 Amphiphile - an overview | ScienceDirect Topics, https://www.sciencedirect.com/topics/pharmacology-toxicology-and-pharmaceutical-science/amphiphile, (accessed August 19, 2021).

92 L. J. White, N. J. Wells, L. R. Blackholly, H. J. Shepherd, B. Wilson, G. P. Bustone, T. J. Runacres and J. R. Hiscock, *Chem. Sci*., 2017, **8**, 7620–7630.

93 D. Lombardo, M. A. Kiselev, S. Magazù and P. Calandra, *Adv. Condens. Matter Phys*., 2015, 1–22.

94 Supramolecular Self-associating Amphiphiles (SSAs) - Kent Academic Repository, https://kar.kent.ac.uk/88059/, (accessed September 28, 2021).

95 Y. Wang, H. Xu and X. Zhang, *Adv. Mater*., 2009, **21**, 2849–2864.

96 J. Boyle, Biochem. *Mol. Biol. Educ*., 2008, **36**, 317–318.

97 W.-R. Zhuang, Y. Wang, P.-F. Cui, L. Xing, J. Lee, D. Kim, H.-L. Jiang and Y.-K. Oh, *J. Controlled Release*, 2019, **294**, 311–326.

98 C. Wang, Z. Wang and X. Zhang, *Small*, 2011, **7**, 1379–1383.

99 Bradburn, Danielle, and Tom Bittinger, eds. *Micelles: Structural Biochemistry, Formation and Functions & Usage*. Nova Science Publishers, Incorporated, 2013.

100 N. Chaffey, *Ann. Bot.*, 2003, **91**, 401.

101 T. Kunitake and Y. Okahata, *J. Am. Chem. Soc.*, 2002, **99**, 3860–3861.

102 J. Nicolas, S. Mura, D. Brambilla, N. Mackiewicz and P. Couvreur, *Chem. Soc. Rev*., 2013, **42**, 1147–1235.

103 F. Yuen and K. C. Tam, *Soft Matter*, 2010, **6**, 4613-4630.

104 C. Alvarez-Lorenzo and A. Concheiro, *Chem. Commun*., 2014, **50**, 7743–7765.

105 A. L. Horwich, G. W. Farr and W. A. Fenton, *Chem. Rev*., 2006, **106**, 1917–1930.

106 C. A. Royer, *Chem. Rev*., 2006, **106**, 1769–1784.

107 W. W. Grabow and L. Jaeger, *Acc. Chem. Res*., 2014, **47**, 1871–1880.

108 J. B. Lee, J. Hong, D. K. Bonner, Z. Poon and P. T. Hammond, Nat. Matter, 2012, **11**, 316–322.

109 G. Yu, K. Jie and F. Huang, *Chem. Rev*., 2015, **115**, 7240–7303.

110 M. Aktas, M. Wessel, S. Hacker, S. Klüsener, J. Gleichenhagen and F. Narberhaus, *Eur. J. Cell Biol*., 2010, **89**, 888–894.

111 B. Alberts, A. Johnson, J. Lewis, M. Raff, K. Roberts and P. Walter, *Mol. Biol. Cell*, 2008, 1569–1588.

112 J. H. Fuhrhop and T. Wang, *Chem. Rev.*, 2004, **104**, 2901–2937.

113 A. Meister, M. Bastrop, S. Koschoreck, V. M. Garamus, T. Sinemus, G. Hempel, S. Drescher, B. Dobner, W. Richtering, K. Huber and A. Blume, *Langmuir*, 2007, **23**, 7715–7723.

114 F. M. Menger and C. A. Littau, *J. Am. Chem. Soc.*, 2002, **113**, 1451–1452.

115 S. M. Shaban, J. Kang and D. H. Kim, *Composites Comm*., 2020, **22**, 100537.

116 Rosen, Milton J., and Joy T. Kunjappu. *Surfactants and interfacial phenomena*, John Wiley & Sons, 2012, 600.

117 J. J. Kabara, D. M. Swieczkowski, A. J. Conley and J. P. Truant, *Antimicrob. Agents chemother.*, 1972, **2**, 23–28.

118 V. A. Karetsi, C. N. Banti, N. Kourkoumelis, C. Papachristodoulou, C. D. Stalikas, C. P. Raptopoulou, V. Psycharis, P. Zoumpoulakis, T. Mavromoustakos, I. Sainis and S. K. Hadjikakou, *Antibiotics*, 2019, **8**, 213.

119 G. T. Williams, C. J. E. Haynes, M. Fares, C. Caltagirone, J. R. Hiscock and P. A. Gale, *Chem. Soc. Rev*., 2021, **50**, 2737–2763.

120 A. Rösler, G. W. M. Vandermeulen and H.-A. Klok, *Adv. Drug Delivery Rev.*, 2012, **64**, 270–279.

121 S. K. Singh and N. Caram-Lelham, *J. Colloid Interface Sci.*, 1998, **203**, 430–446.

122 D. Attwood and S. P. Agarwal, *J. Pharm. Pharmacol.*, 2011, **31**, 392–395.

123 T. Shimizu, M. Masuda and H. Minamikawa, *Chem. Rev.*, 2005, **105**, 1401–1443.

124 P. K. Vemula and G. John, *Acc. Chem. Res.*, 2008, **41**, 769–782.

125 Q. Zhang, K. Ariga, A. Okabe and T. Aida, *J. Am. Chem. Soc.*, 2004, **126**, 988–989.

126 D. Lombardo, M. A. Kiselev, S. Magazù and P. Calandra, *Adv. Condensed Matter Phys*., 2015, 1–22.

127 X. Zhang and C. Wang, *Chem. Soc. Rev.*, 2010, **40**, 94–101.

128 P. Dapporto, P. Paoli and S. Roelens, *J. Org. Chem*., 2001, **66**, 4930–4933.

129 X. Zhang, Z. Chen and F. Würthner, *J. Am. Chem. Soc.*, 2007, **129**, 4886–4887.

130 C. Wang, Q. Chen, Z. Wang and X. Zhang, *Angew. Chem*., 2010, **122**, 8794–8797.

131 C. Wang, S. Yin, S. Chen, H. Xu, Z. Wang and X. Zhang, *Angew. Chem. Int. Ed*., 2008, **47**, 9049–9052.

132 K. Liu, Y. Yao, Y. Liu, C. Wang, Z. Li and X. Zhang, *Langmuir*, 2012, **28**, 10697–10702.

133 G. Yu, K. Jie and F. Huang, *Chem. Rev.*, 2015, **115**, 7240–7303.

134 C. B. Minkenberg, L. Florusse, R. Eelkema, G. J. M. Koper and J. H. van Esch, *J. Am. Chem. Soc*., 2009, **131**, 11274–11275.

135 X. Wu, X.-X. Chen, M. Zhang, Z. Li, P. A. Gale and Y.-B. Jiang, *Chem. Commun.*, 2016, **52**, 6981–6984.

136 C. Wang, Z. Wang and X. Zhang, *Small*, 2011, **7**, 1379–1383.

137 A. V. Kabanov, T. K. Bronich, V. A. Kabanov, K. Yu and A. Eisenberg, *J. Am. Chem. Soc*., 1998, **120**, 9941–9942.

138 N. Kimizuka, T. Kawasaki and T. Kunitake, *J. Am. Chem. Soc*., 1993, **115**, 4387–4388.

139 J. F. Gohy, B. G. G. Lohmeijer and U. S. Schubert, *Macromolecules*, 2002, **35**, 4560–4563.

140 X. Zhang, Z. Chen and F. Würthner, *J. Am. Chem. Soc*., 2007, **129**, 4886–4887.

141 H. R. Marsden, A. V. Korobko, E. N. M. van Leeuwen, E. M. Pouget, S. J. Veen, N. A. J. M. Sommerdijk and A. Kros, *J. Am. Chem. Soc*., 2008, **130**, 9386–9393.

142 A. Wilson, G. Gasparini and S. Matile, *Chem. Soc. Rev*., 2014, **43**, 1948–1962.

143 G. Wang, C. Wang, Z. Wang and X. Zhang, *Langmuir*, 2012, **28**, 14567–14572.

144 C. B. Minkenberg, F. Li, P. van Rijn, L. Florusse, J. Boekhoven, M. C. A. Stuart, G. J. M. Koper, R. Eelkema and J. H. van Esch, *Angew. Chem. Int. Ed*., 2011, **50**, 3421–3424.

145 C. Wang, G. Wang, Z. Wang and X. Zhang, *Chem. Eur. J*., 2011, **17**, 3322–3325.

146 R. Nguyen, E. Buhler and N. Giuseppone, *Macromolecules*, 2009, **42**, 5913–5915.

147 C. M. C. Faustino, A. R. T. Calado and L. Garcia-Rio, *J. Colloid Interface Sci*., 2010, 351, 472–477.

148 R. Zana, *J. Colloid Interface Sci*., 2002, **97**, 205–253.

149 M. C. Morán, A. Pinazo, L. Pérez, P. Clapés, M. Angelet, M. T. García, M. P. Vinardell and M. R. Infante, *Green Chem*., 2004, **6**, 233–240.

150 E. Blanco, A. González-Pérez, J. M. Ruso, R. Pedrido, G. Prieto and F. Sarmiento, *J. Colloid Interface Sci*., 2005, **288**, 247–260.

151 J. R. Hiscock, G. P. Bustone, B. Wilson, K. E. Belsey and L. R. Blackholly, *Soft Matter*, 2016, **12**, 4221–4228.

152 L. R. Blackholly, H. J. Shepherd and J. R. Hiscock, *CrystEngComm.*, 2016, **18**, 7021–7028.

153 S. N. Tyuleva, N. Allen, L. J. White, A. Pépés, H. J. Shepherd, P. J. Saines, R. J. Ellaby, D. P. Mulvihill and J. R. Hiscock, *Chem. Commun*., 2019, **55**, 95–98.

154 P. Foley, A. K. pour, E. S. Beach and J. B. Zimmerman, *Chem. Soc. Rev.*, 2012, **41**, 1499–1518.

155 F. Lortie, S. Boileau and L. Bouteiller, *Chem. Eur. J.*, 2003, **9**, 3008–3014.

156 C. Wang, Z. Wang and X. Zhang, *Acc. Chem. Res*., 2012, **45**, 608–618.

157 J. Zou, F. Tao and M. Jiang, *Langmuir*, 2007, **23**, 12791–12794.

158 Y. Chang, Y. Jiao, H. E. Symons, J.-F. Xu, C. F. J. Faul and X. Zhang, *Chem. Soc. Rev*., 2019, **48**, 989–1003.

159 D. R. Vij, *Luminescence of Solids*, Springer US, 2012.

160 George G. Stokes, *Phil. Trans. R. Soc*., 1852, **142**, 463–562.

161 S. C. Moldoveanu and V. David, in *Essentials in Modern HPLC Separations*, Elsevier, 2013.

162 G. N. Lewis and M. Kasha, *J. Am. Chem. Soc*., 1944, **66**, 2100–2116.

163 A. Jablonski, *Nature*, 1933, **131**, 839–840.

164 D. Frackowiak, *J. Photochem. Photobiol., B*, 1988, **2**, 399.

165 H. H. Jaffe and A. L. Miller, *J. Chem. Educ*., 1966, **43**, 469.

166 F. Torrens and G. Castellano, in *Molecular Chemistry and Biomolecular Engineering*, Apple Academic Press, 2019, 51–61.

167 J. B. Birks, *J. Res. Natl. Bur. Stand., Sect. A*, 1976, **80A**, 389.

168 M. E. Sommer, M. Elgeti, P. W. Hildebrand, M. Szczepek, K. P. Hofmann and P. Scheerer, *Membr. Proteins*, 2015, 563–608.

169 G. Hamilton and H. Sanabria, in *Spectroscopy and Dynamics of Single Molecules*, Elsevier, 2019.

170 Y. Pu, W. Wang, R. B. Dorshow and R. R. Alfano, *Energy Transfer Dynamics Between Target Contrast Agents and Prostate Cancer Cells Using Ultrafast Spectroscopy*, 2012, City University of New York.

171 I. Vermes and C. Haanen, Advances in Clinical Chemistry, 1994, **31**, 177–246.

172 R. F. Chen, *Anal. Biochem.*, 1967, **19**, 374–387.

173 M. S. Skorotetcky, O. V. Borshchev, N. M. Surin, Y. Odarchenko, S. A. Pisarev, S. M. Peregudova, K. W. Törnroos, D. Chernyshov, D. A. Ivanov and S. A. Ponomarenko, *Dyes and Pigments*, 2017, **141**, 128–136.

174 S. T. Hess, S. Huang, A. A. Heikal and W. W. Webb, *Biochem.*, 2001, **41**, 697–705.

175 M. T. Yaraki and Y. N. Tan, *Chem. Asian J.*, 2020, **15**, 3180–3208.

176 P. Mattei, *J. Pediatric Surgery*, 2021, **56**, 224–225.

177 F. Rost, in *Encyclopedia of Spectroscopy and Spectrometry*, Elsevier, 2017.

178 W. J. Y. A. Harden, *Proc. R. Soc. Lond. B*., 1906, **78**, 369–375.

179 O. Shimomura, F. H. Johnson and Y. Saiga, *J. Cell. Comp. Physiol*., 1962, **59**, 223–239.

180 D. von Stetten, M. Noirclerc-Savoye, J. Goedhart, T. W. J. Gadella Jr and A. Royant, *Acta Cryst Sect F*, 2012, **68**, 878–882.

181 H. Morise, O. Shimomura, F. H. Johnson and J. Winant, *Biochem*., 1974, **13**, 2656–2662.

182 D. C. Prasher, V. K. Eckenrode, W. W. Ward, F. G. Prendergast and M. J. Cormier, *Gene*, 1992, **111**, 229–233.

183 S. Inouye and F. I. Tsuji, *FEBS Lett.*, 1994, **341**, 277–280.

184 M. Chalfie, Y. Tu, G. Euskirchen, W. Ward and D. Prasher, *Science*, 1994, **263**, 802–805.

185 B.-E. Jugder, J. Welch, N. Braidy and C. P. Marquis, *PeerJ*, 2016, **4**, 2269.

186 Y. H. Song, C. S. Kim and J. H. Seo, *Korean J. Chem. Eng*., 2016, **33**, 1331–1336.

187 Y. Pan, A. Leifert, M. Graf, F. Schiefer, S. Thoröe-Boveleth, J. Broda, M. C. Halloran, H. Hollert, D. Laaf, U. Simon and W. Jahnen-Dechent, *Small*, 2012, **9**, 863–869.

188 J. C. Crelling, *J. Microscopy*, 1983, **132**, 251–266.

189 H. B. Lo, *Org. Geochem.*, 1987, **11**, 371–377.

190 Z. Zhujun and W. R. Seitz, *Analytica Chimica Acta*, 1984, **160**, 47–55.

191 T. D. James, K. R. A. S. Sandanayake and S. Shinkai, *Angew. Chem. Int. Ed. Engl*., 1994, **33**, 2207–2209.

192 M. N. Stojanovic, P. de Prada and D. W. Landry, *J. Am. Chem. Soc*., 2001, **123**, 4928–4931.

193 Q. He, E. W. Miller, A. P. Wong and C. J. Chang, *J. Am. Chem. Soc*., 2006, **128**, 9316–9317.

194 S. Deo and H. A. Godwin, *J. Am. Chem. Soc*., 1999, **122**, 174–175.

195 E. M. Nolan and S. J. Lippard, *J. Am. Chem. Soc*., 2003, **125**, 14270–14271.

196 T. Hirano, K. Kikuchi, Y. Urano, T. Higuchi and T. Nagano, *J. Am. Chem. Soc*., 2000, **122**, 12399–12400.

197 S. Yoon, E. W. Miller, Q. He, P. H. Do and C. J. Chang, *Angew. Chem*., 2007, **119**, 6778–6781.

198 T. Rasheed, M. Bilal, F. Nabeel, H. M. N. Iqbal, C. Li and Y. Zhou, *Sci. Total Environ*., 2018, **615**, 476–485.

199 Z. Xu, Y. Xiao, X. Qian, J. Cui and D. Cui, *Org. Lett*., 2005, **7**, 889–892.

200 S. T. Hess, S. Huang, A. A. Heikal and W. W. Webb, *Biochem.*, 2001, **41**, 697–705.

201 J. Liu, C. Liu and W. He, *COC*, 2013, **17**, 564–579.

202 J. R. Lakowicz, in *Principles of Fluorescence Spectroscopy*, Springer US, Boston, MA, 1999.

203 G. Süel, *Methods in Enzymology*, 2011, 275–293.

204 D. N. Myers, *Sep. Sci. Technol*., 2019, **11**, 219–283.

205 J. O'Brien, I. Wilson, T. Orton and F. Pognan, *Eur. J. Biochem.*, 2000, **267**, 5421–5426.

206 H. Naiki, K. Higuchi, M. Hosokawa and T. Takeda, *Anal. Biochem.*, 1989, **177**, 244–249.

207 D. Ross, M. Gaitan and L. E. Locascio, *Anal. Chem*., 2001, **73**, 4117–4123.

208 J. M. Menter, *Photochem. Photobiol. Sci*., 2006, **5**, 403.

209 Y. Sato, S. Ichinosawa and H. Kanai, IEEE J. *Select. Topics Quantum Electron*., 1998, **4**, 40–48.

210 G. Bauer and X. Hu, *Inorg. Chem. Front*., 2016, **3**, 741–765.

211 P. Kumar, S. Kaur, R. Gupta and K. Bowman-James, in *Pincer Compounds*, Elsevier, 2018, 295-325.

212 P. Kumar, V. Kumar and R. Gupta, *RSC Adv*., 2015, **5**, 97874–97882.

213 U. Manna and G. Das*, Coord. Chem. Rev.*, 2021, **427**, 213547.

214 S.-S. Sun, A. J. Lees and P. Y. Zavalij, *Inorg. Chem*., 2003, **42**, 3445–3453.

215 C. R. Bondy and S. J. Loeb, *Coord. Chem. Rev*., 2003, **240**, 77–99.

216 K. Kavallieratos, S. R. de Gala, D. J. Austin and R. H. Crabtree, *J. Am. Chem. Soc*., 1997, **119**, 2325–2326.

217 M. P. Hughes and B. D. Smith, *J. Org. Chem*., 1997, **62**, 4492–4499.

218 K. J. Chang, B.-N. Kang, M.-H. Lee and K.-S. Jeong, *J. Am. Chem. Soc*., 2005, **127**, 12214–12215.

219 J. L. Sessler, D.-G. Cho and V. Lynch, *J. Am. Chem. Soc*., 2006, **128**, 16518–16519.

220 G. W. Bates, P. A. Gale and M. E. Light, *Chem. Commun*., 2007, 2121–2123.

221 J. R. Hiscock, C. Caltagirone, M. E. Light, M. B. Hursthouse and P. A. Gale, *Org. Biomol. Chem*., 2009, **7**, 1781.

222 C. Caltagirone, P. A. Gale, J. R. Hiscock, S. J. Brooks, M. B. Hursthouse and M. E. Light, *Chem. Commun*., 2008, 3007-3009.

223 Q. Q. Wang, R. A. Begum, V. W. Day and K. Bowman-James, *J. Am. Chem. Soc*., 2013, **135**, 17193–17199.

224 J. P. Zhang, P.-Q. Liao, H.-L. Zhou, R.-B. Lin and X.-M. Chen, *Chem. Soc. Rev*., 2014, **43**, 5789–5814.

225 Bindfit supramolecular v0.5 http://app.supramolecular.org/bindfit/, (accessed September 2021).

226 L. J. White, S. N. Tyuleva, B. Wilson, H. J. Shepherd, K. K. L. Ng, S. J. Holder, E. R. Clark and J. R. Hiscock, *Chem. Eur. J*., 2018, **24**, 7761–7773.

227 S. K. Bharti and R. Roy*, TrAC Trends Anal. Chem.*, 2012, **35**, 5–26.

228 M. A. Nanny, J. M. Bortiatynski and P. G. Hatcher, *Environ. Sci. Technol*., 1997, **31**, 530–534.

229 M. H. Abraham, R. J. Abraham, J. Byrne and L. Griffiths, *J. Org. Chem*., 2006, **71**, 3389–3394.

230 G. A. Kumar and M. A. McAllister, *J. Org. Chem*., 1998, **63**, 6968–6972.

231 H. Sun, Y. Zhao, Z. Huang, Y. Wang and F. Li, *J. Phys. Chem. A*, 2008, **112**, 11382–11390.

232 Y. Hussein and M. Youssry, *Materials*, 2018, **11**, 688.

233 T. F. Tadros, *An Introduction to Surfactants*, DE GRUYTER, 2014.

234 R. J. Williams, J. N. Phillips and K. J. Mysels, *Trans. Faraday Soc*., 1955, **51**, 728–737.

235 N. Allen, L. J. White, J. E. Boles, G. T. Williams, D. F. Chu, R. J. Ellaby, H. J. Shepherd, K. K. L. Ng, L. R. Blackholly, B. Wilson, D. P. Mulvihill and J. R. Hiscock, *ChemMedChem.*, 2020, **15**, 2193–2205.

236 Y. Shrot and L. Frydman, *J. Magnet. Res.*, 2008, **195**, 226–231.

237 J. T. Edward, *J. Chem. Educ*., 1970, **47**, 261.

238 M. A. Nanny, J. M. Bortiatynski and P. G. Hatcher, *Environ. Sci. Technol*., 1997, **31**, 530–534.

239 L. K. S. von Krbek, C. A. Schalley and P. Thordarson, *Chem. Soc. Rev*., 2017, **46**, 2622–2637.

240 R. B. Martin, *Chem. Rev*., 1996, **96**, 3043–3064.

241 G. A. Kumar and M. A. McAllister, *J. Org. Chem*., 1998, **63**, 6968–6972.

242 A. Hinz, A. Schulz and A. Villinger, *Angew. Chem. Int. Ed*., 2015, **54**, 2776–2779.

243 H. C. Brown, J. H. Brewster and H. Shechter, *J. Am. Chem. Soc*., 1954, **76**, 467–474.

244 W. I. Goldburg, *Am. J. Phys*., 1999, **67**, 1152–1160.

245 A. R. Ferré-D'Amaré and S. K. Burley, *Structure*, 1994, **2**, 357–359.

246 Hahn, David W. "*Light scattering theory*." Department of Mechanical and Aerospace Engineering, University of Florida (2009).

247 M. Kaszuba, J. Corbett, F. M. Watson and A. Jones, *Phil. Trans. R. Soc. A*., 2010, **368**, 4439–4451.

248 J. D. Clogston and A. K. Patri, *Methods in Molecular Biology*, 2010, 63–70.

7. Appendix *Potential fluorescent sensors*

7.1. Tables of data

Table S14 – Data for binding association constants, K_{ass}, of **35**-**38** with various anions; calculated from ^{1}H NMR titration data in DMSO-d_6/0.5 % at 298 K.

Anion	**35**	**36**	**37**	**38**
Benzoate	<10 [a]	<10 [a]	<10 [a]	206.53[a]
Sulphate	*b*	*b*	*b*	K_{11} 107.37[a], K_{21} 217.23[a]
Dihydrogen phosphate	23.74 [a]	<10 [a]	*b*	17.75[a]
Hydrogen sulphate	*b*	<10 [a]	*b*	*b*
Chloride	*b*	<10 [a]	<10 [a]	*b*

*[a]represents error for the given association constant is < ± 10 %, [b] represents that no binding could not be fitted; as the change in chemical shift was below the limitations for the NMR machine, or the percentage error was too great. For all association constants presented here, all fit a binding isotherm of 1:1, with the exception of the **38** binding associations to sulphate which fits a 2:1 (host:guest) binding isotherm.*

Table S15 – Overview of the log of binding association constants, log K_{ass}, of **35**-**38** with various anions; calculated from changes in fluorescence intensity in DMSO/0.5 % H_2O at 298 K.

Anion	**35**	**36**	**37**	**38**
Benzoate	6.3 (± 14 %)	5.6 (± 14 %)	*b*	5.0 (± 20 %)
Sulphate	4.7 [a]	*b*	*b*	*b*
Dihydrogen phosphate	4.6 [a]	*b*	*b*	*b*
Hydrogen sulphate	*b*	*b*	*b*	2.2 (± 14 %)
Chloride	*b*	*b*	*b*	*b*

[a]represents error for the given association constant is < ± 10 %, [b] represents that no binding could not be fitted; as the change in intensity of emission was too low. For all association constants presented here, all fit a binding isotherm of 1:1.

Table S16 – Simplified summary of the effects of addition of various anions to **35**-**38** when studied via fluorimeter titrations in DMSO/0.5 % at 298 K. Where ↑, represents increase in fluorescence intensity, and —, shows no noticeable increase or increase below 20.

Anion	**35**	**36**	**37**	**38**
Benzoate	↑	↑	—	↑
Sulphate	↑	—	—	—
Monohydrogen phosphate	↑	—	—	—
Hydrogen sulphate	—	—	—	↑
Chloride	—	—	—	—

7.2. NMR

7.2.1. NMR Characterisation

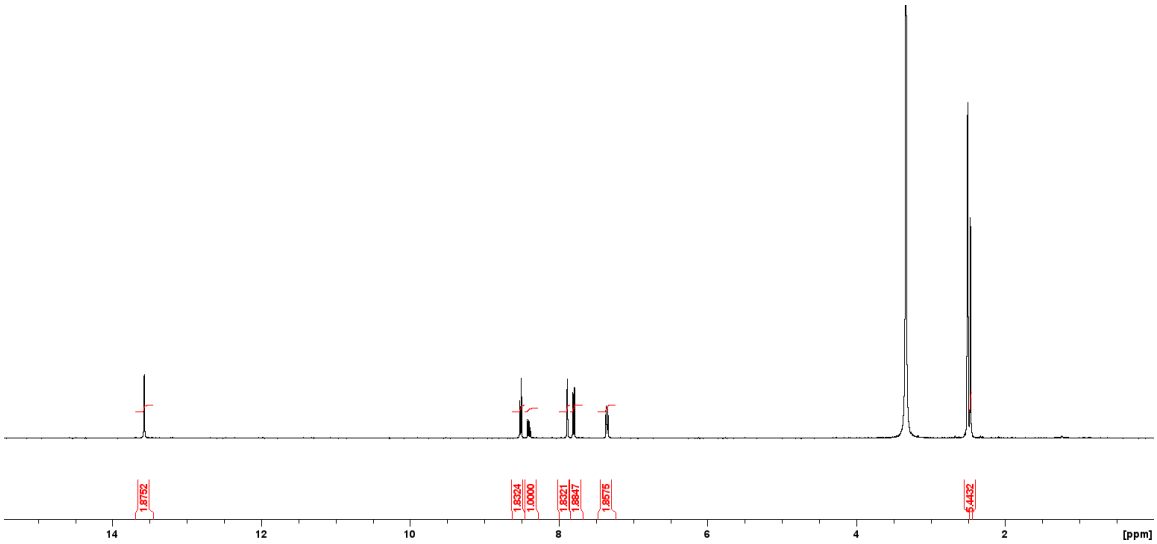

Figure S1 - ^{1}H NMR spectra of compound **35** in DMSO-d_6 conducted at 298 K.

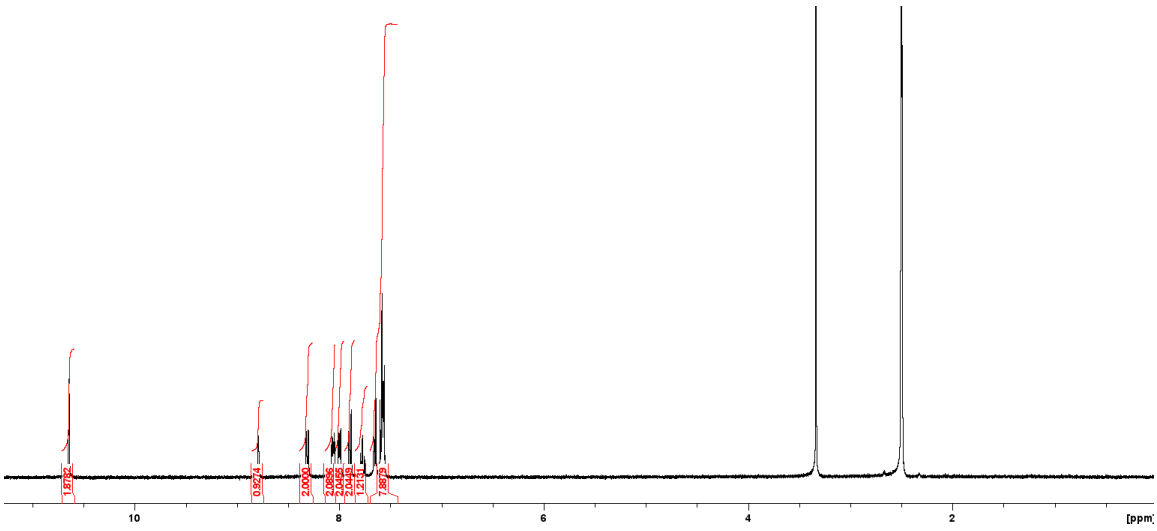

Figure S2 - ^{1}H NMR spectra of compound **36** in DMSO-d_6 conducted at 298 K.

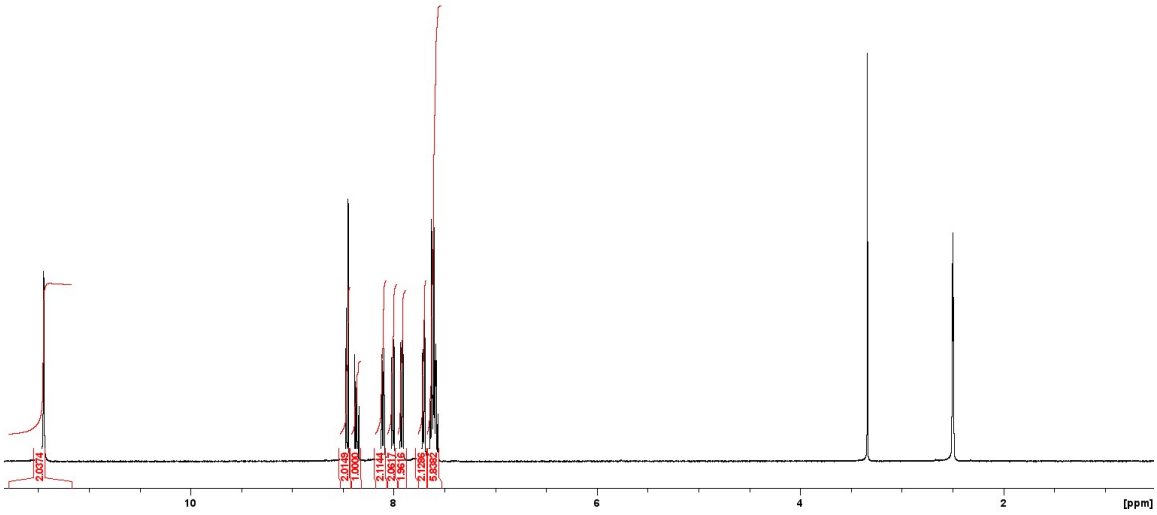

Figure S3 - ^{1}H NMR spectra of compound **36** in DMSO-d_6 conducted at 298 K.

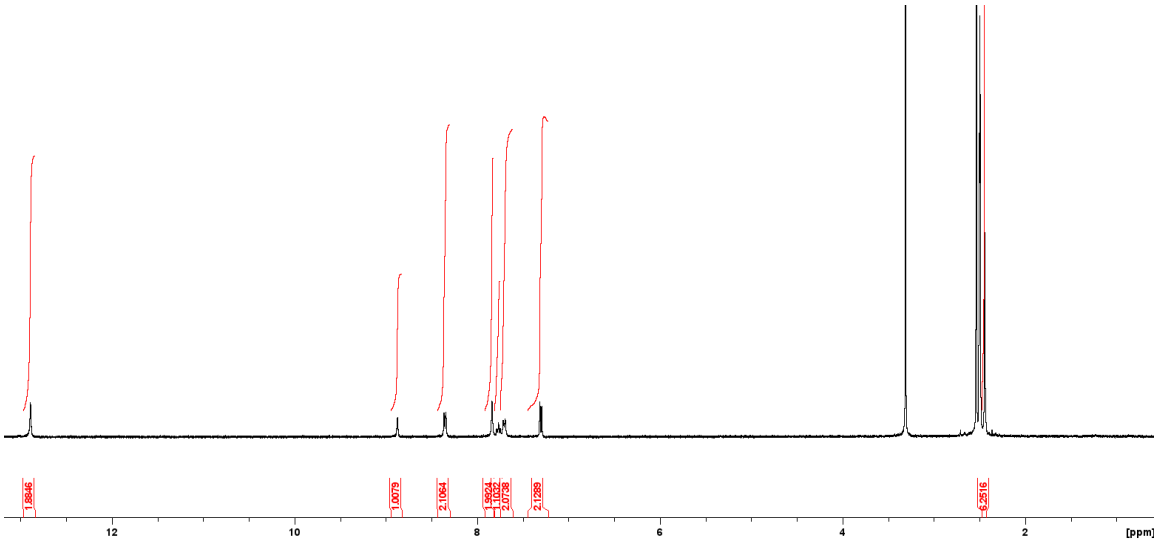

Figure S4 - ^{1}H NMR spectra of compound **37** in DMSO-d_6 conducted at 298 K.

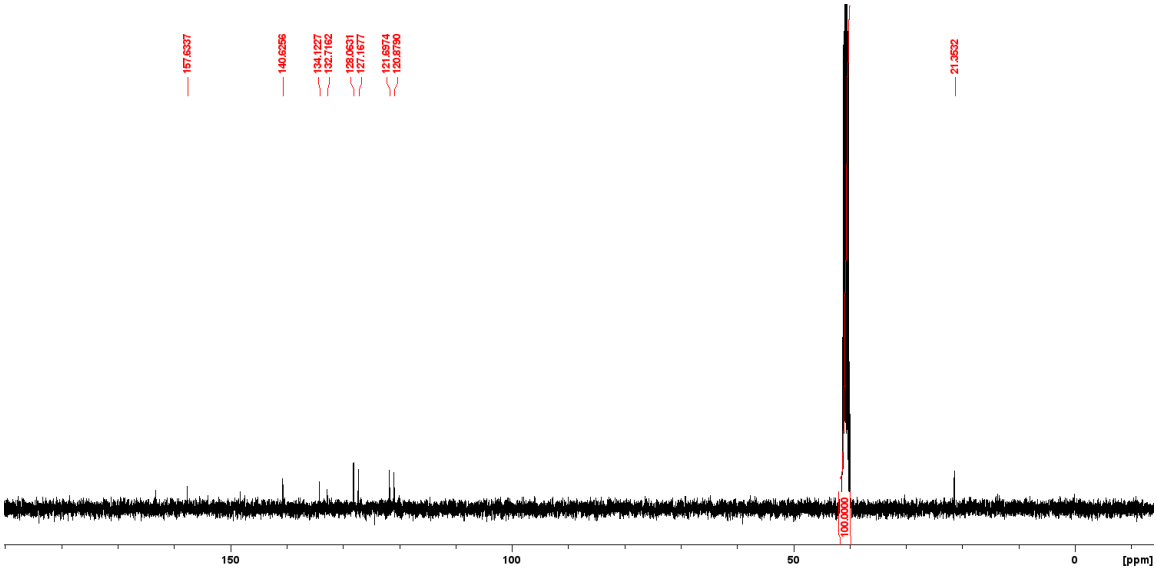

Figure S5 - $^{13}C\{H^1\}$ NMR spectra of compound **35** in DMSO-d_6 conducted at 298 K.

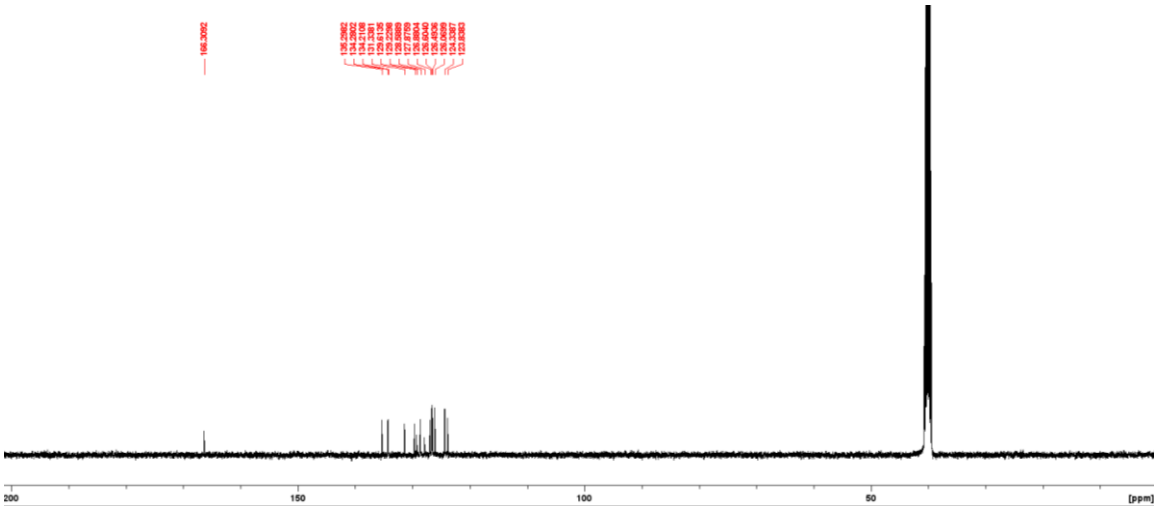

Figure S6 - $^{13}C\{H^1\}$ NMR spectra of compound **36** in DMSO-d_6 conducted at 333 K.

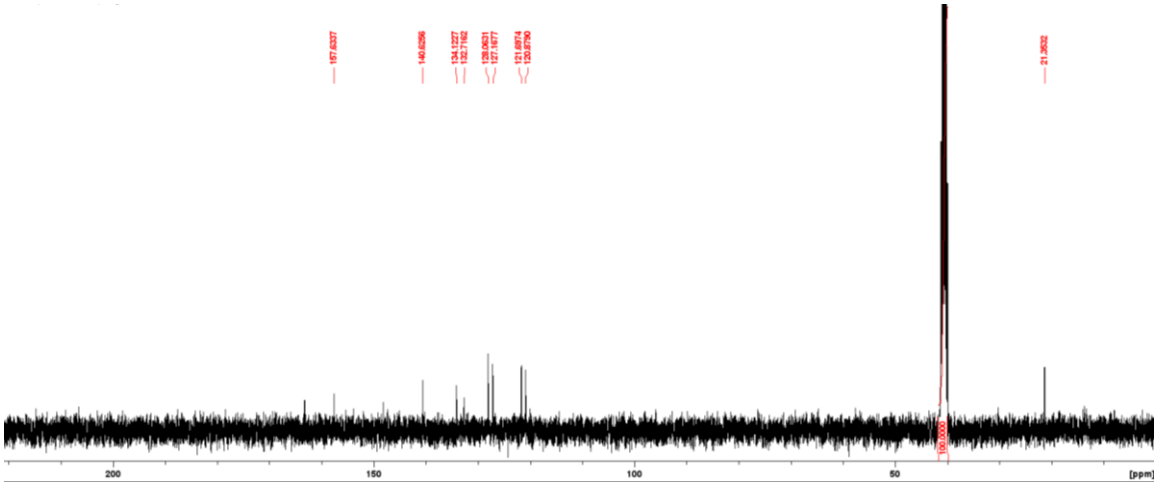

Figure S7 - $^{13}C\{H^1\}$ NMR spectra of compound **38** in DMSO-d_6 conducted at 298 K.

7.2.2. NMR titration studies

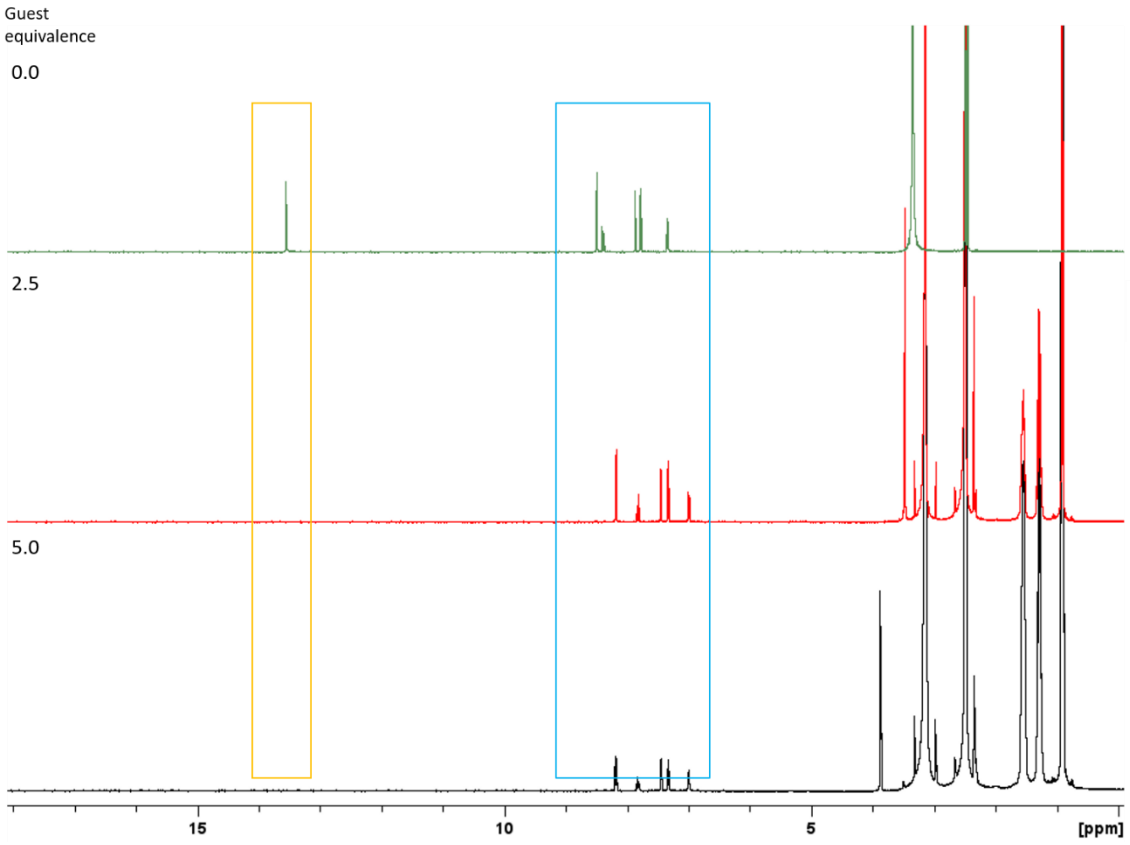

Figure S8- Enlarged ^1H NMR stack plot of compound **35** in a DMSO-d_6 0.5 % H_2O solution. TBA OH^- in MeOH solution was titrated in, guest equivalences stated on the left. NH region is highlighted in yellow, and the aromatic region is highlighted in blue.

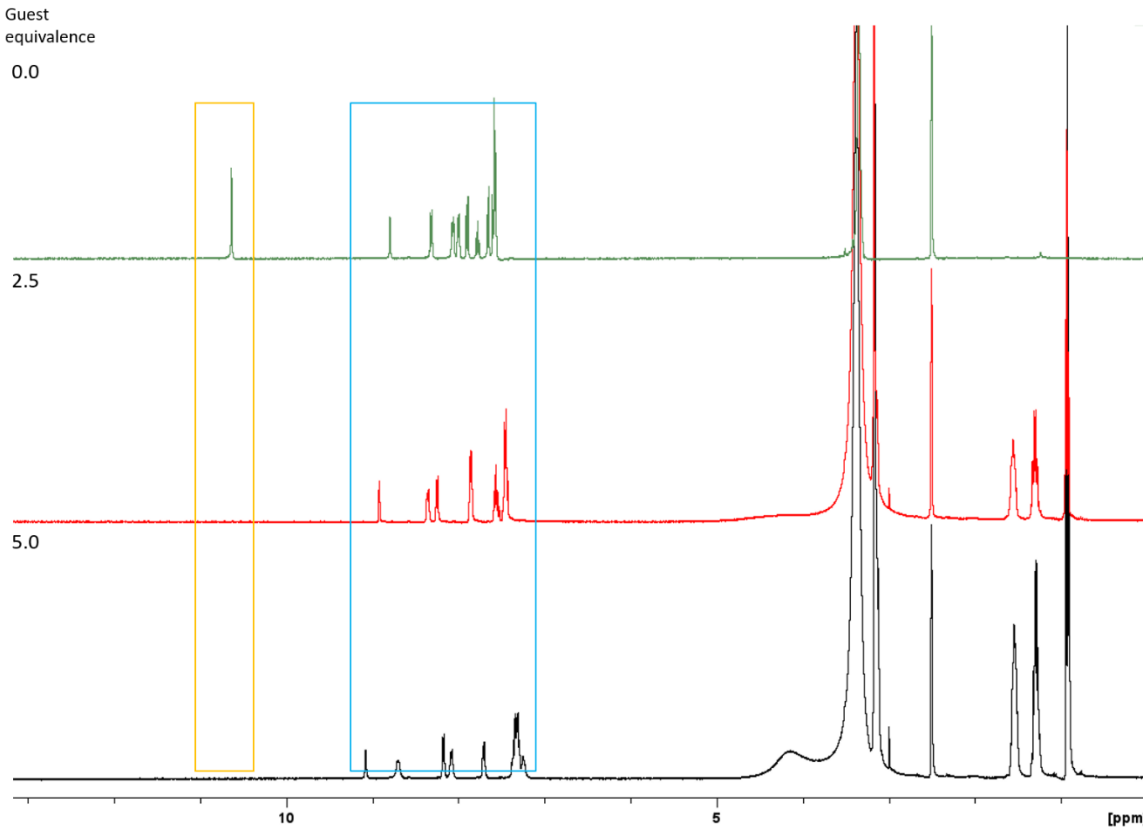

Figure S9 - Enlarged ^{1}H NMR stack plot of compound **36** in a DMSO-d_6 0.5 % H_2O solution. TBA OH^- in MeOH solution was titrated in, guest equivalences stated on the left. NH region is highlighted in yellow, and the aromatic region is highlighted in blue.

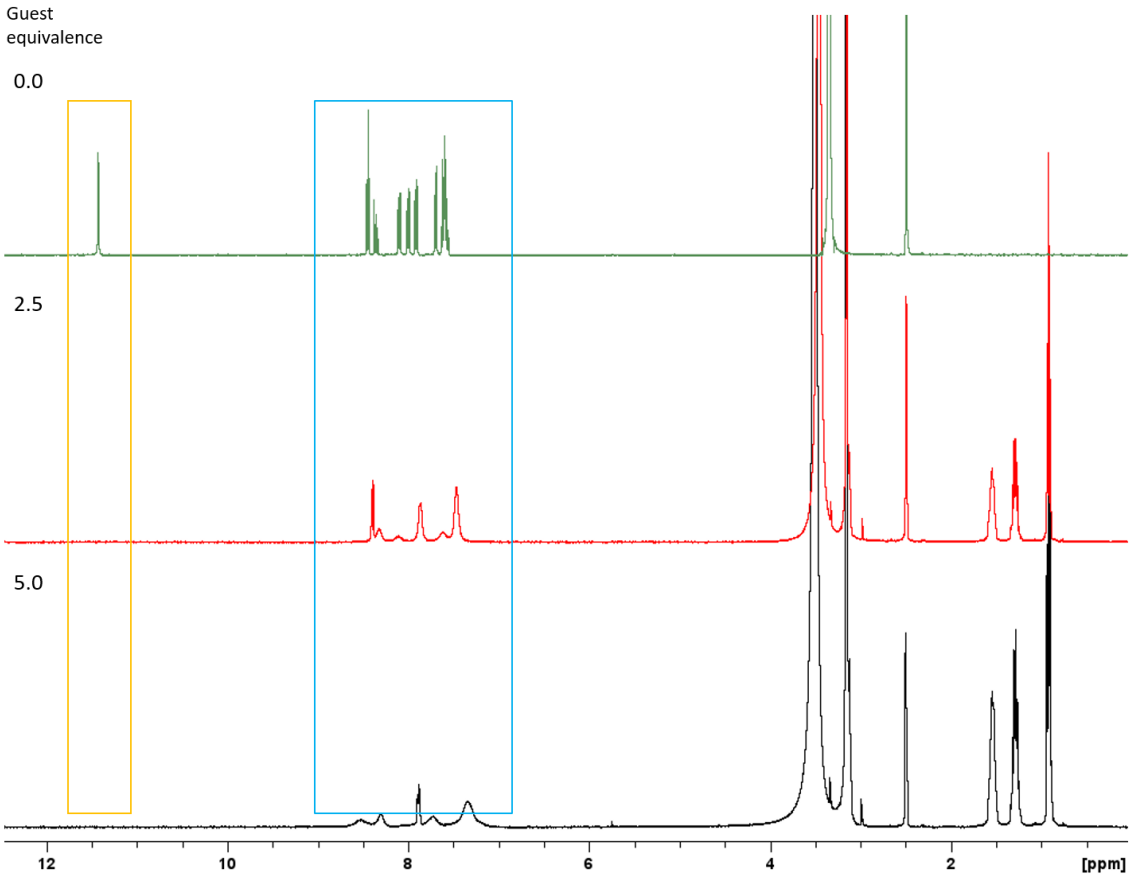

Figure S10 - Enlarged ^{1}H NMR stack plot of compound **37** in a DMSO-*d*$_6$ 0.5 % H_2O solution. TBA OH^- in MeOH solution was titrated in, guest equivalences stated on the left. NH region is highlighted in yellow, and the aromatic region is highlighted in blue.

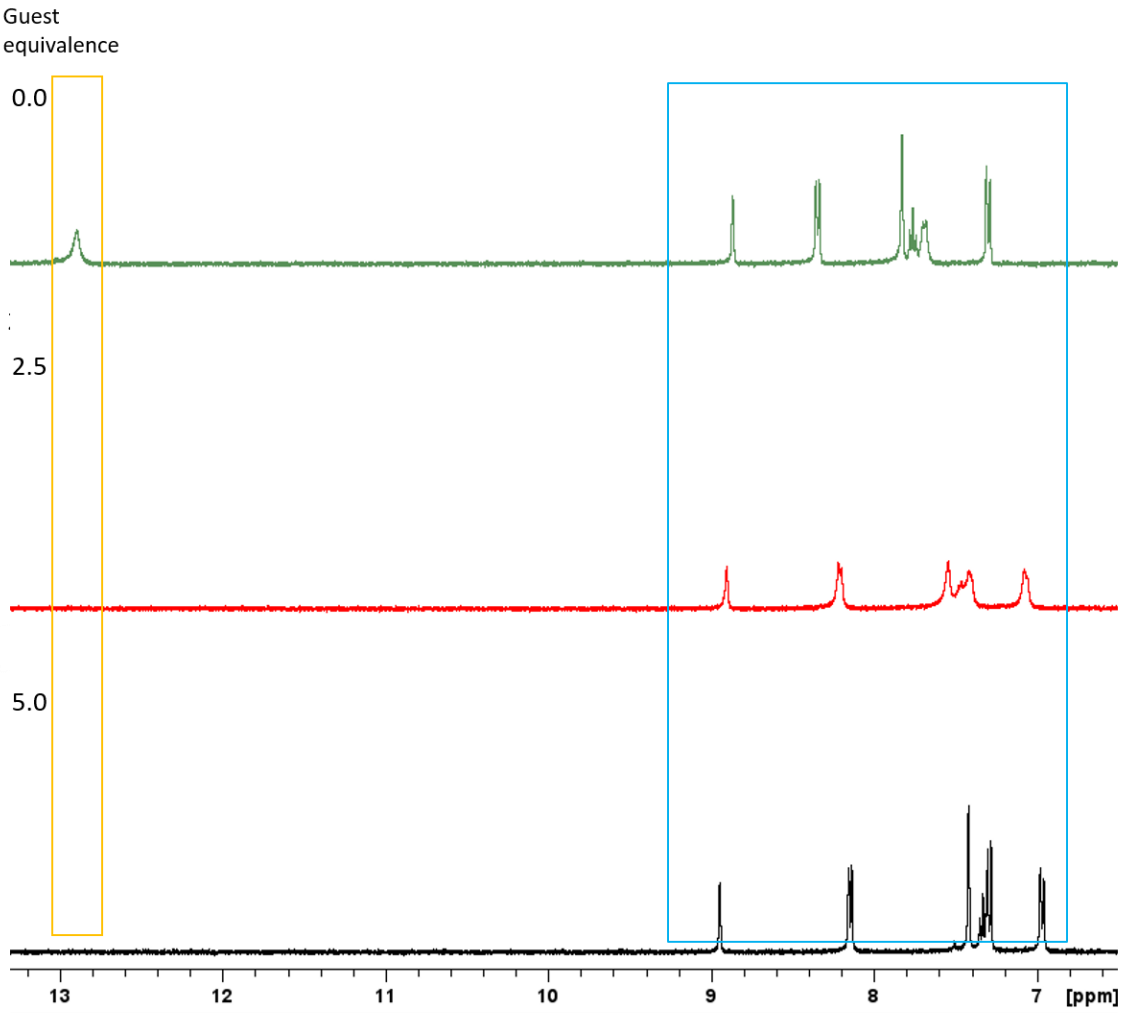

Figure S11 - Enlarged ^{1}H NMR stack plot of compound **38** in a DMSO-d_6/0.5 % H_2O solution. TBA OH^- in MeOH solution was titrated in, guest equivalences stated on the left. NH region is highlighted in yellow, and the aromatic region is highlighted in blue.

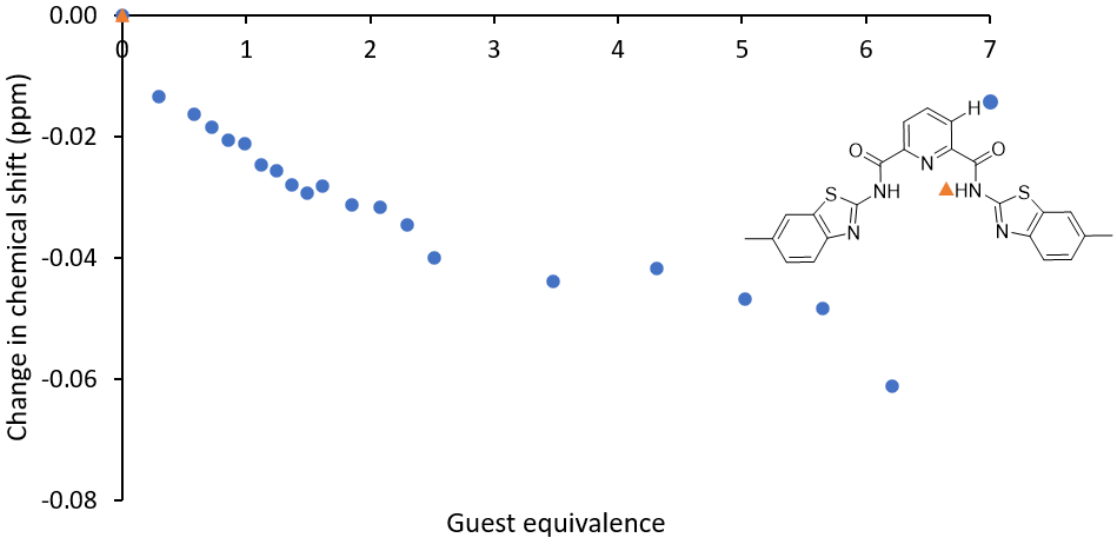

Figure S12 - Change in chemical shift for the NH and CH resonances of **35** (host) upon the addition of TBA OBz (guest) in DMSO-d_6/0.5 % H_2O at 298 K. The 1:1 association constant derived from the ArH change in chemical shift, K_{ass} = 149.59 M^{-1} ± 14.17 %. Due to peak broadening, the chemical shift for the NH resonance could not be followed accurately. 1:1 Bindfit link: http://app.supramolecular.org/bindfit/view/661aa10a-09ae-47c7-9016-535ca371c33a

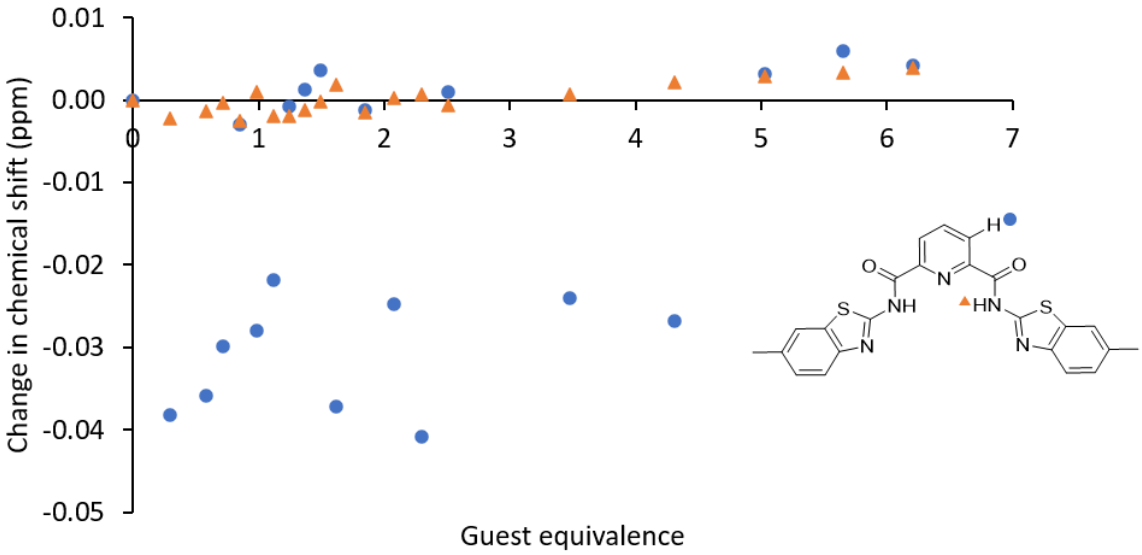

Figure S13 - Change in chemical shift for the NH and CH resonances of **35** (host) upon the addition of TBA sulphate (guest) in DMSO-d_6/0.5 % H_2O at 298 K. This data could not be fitted to a 1:1, 2:1 or 1:2 binding isotherm.

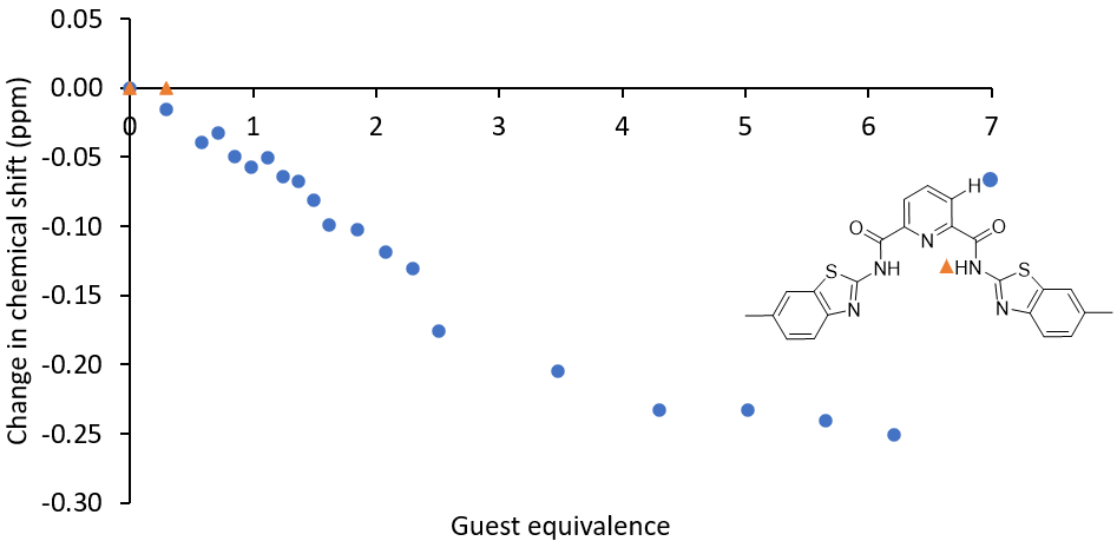

Figure S14 - Change in chemical shift for the NH and CH resonances of **35** (host) upon the addition of TBA phosphate (guest) in DMSO-d_6/0.5 % H_2O at 298 K. The 1:1 binding association derived from the ArH change in chemical shift, K_{ass} = 23.74 M^{-1} ± 7.94 %. Due to peak broadening, the chemical shift for the NH resonance could not be followed accurately. 1:1 Bindfit link: http://app.supramolecular.org/bindfit/view/f0cf7558-d023-4a7b-a5e3-81dd443cde86

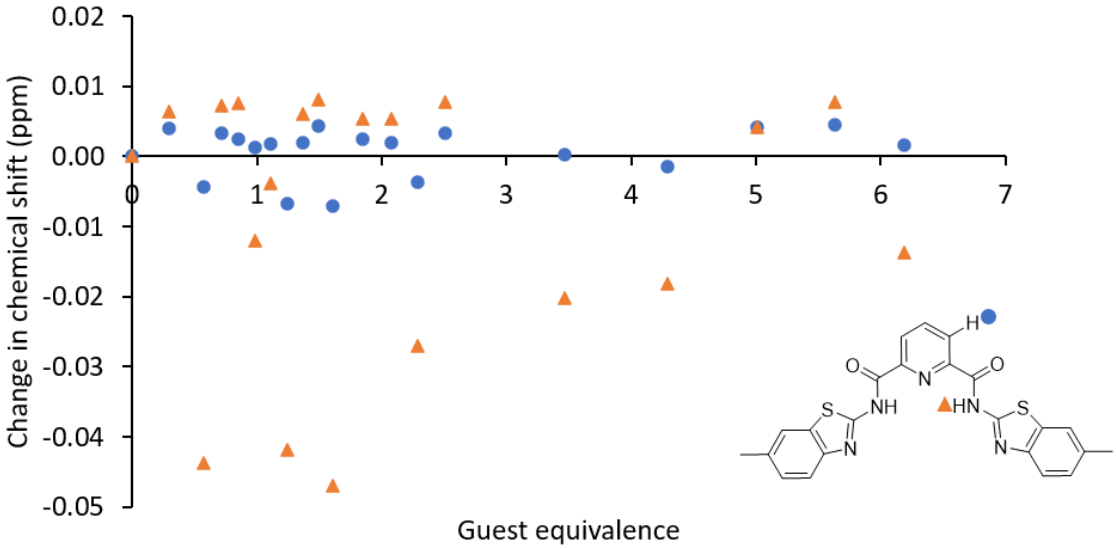

Figure S15 - Change in chemical shift for the NH and CH resonances of **35** (host) upon the addition of TBA hydrogen sulphate (guest) in DMSO-d_6/0.5 % H_2O at 298 K. This data could not be fitted to a 1:1, 2:1 or 1:2 binding isotherm.

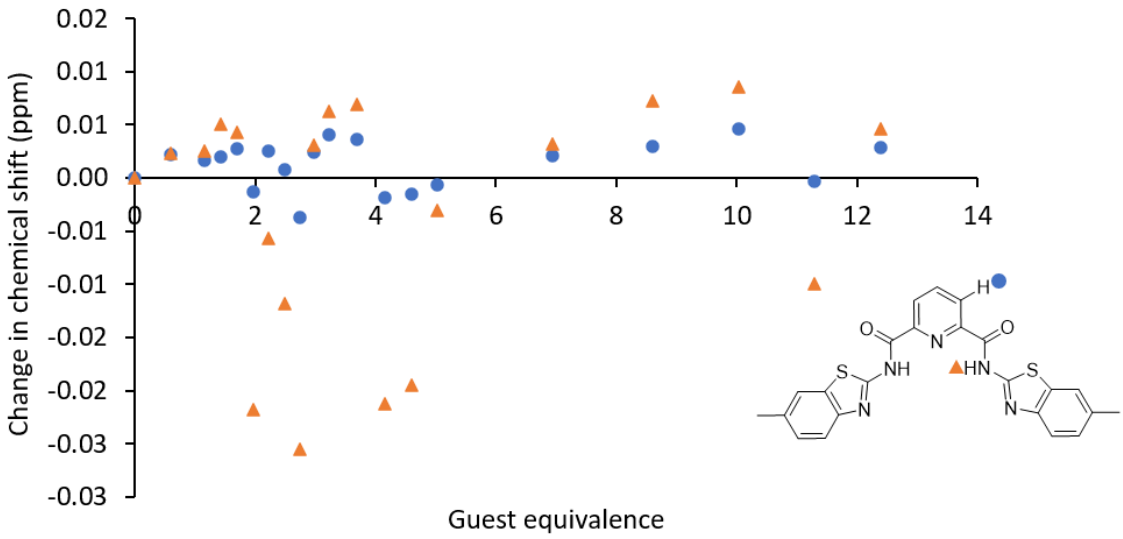

Figure S16 - Change in chemical shift for the NH and CH resonances of **35** (host) upon the addition of TBA chloride (guest) in DMSO-d_6/0.5 % H_2O at 298 K. This data could not be fitted to a 1:1, 2:1 or 1:2 binding isotherm.

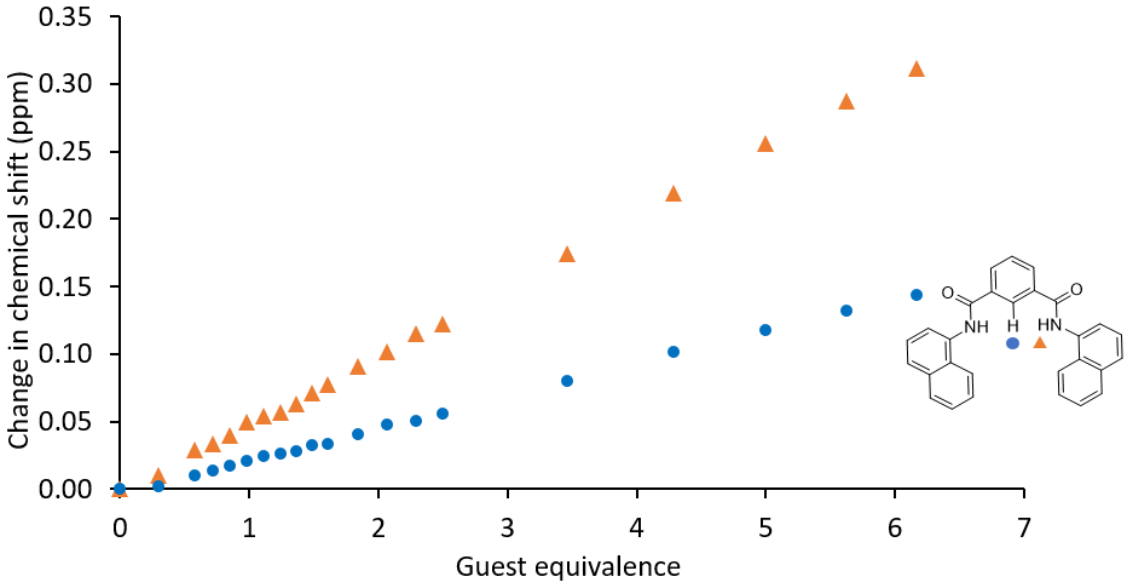

Figure S17 - Change in chemical shift for the NH and CH resonances of **36** (host) upon the addition of TBA OBz (guest) in DMSO-d_6/0.5 % H_2O at 298 K. This data could not be fitted to a 1:1, 2:1 or 1:2 binding isotherm.

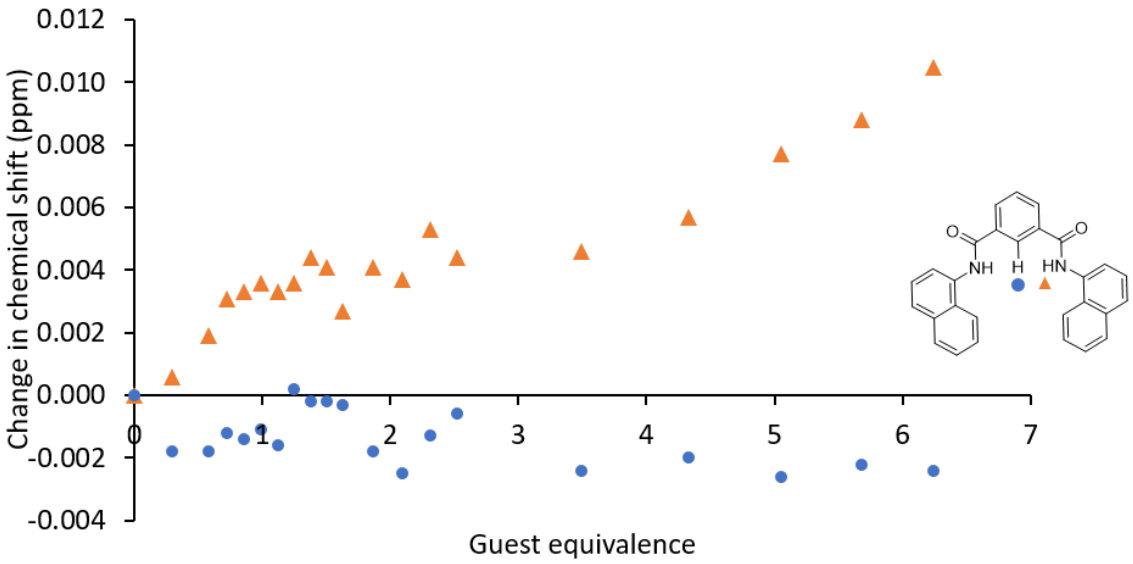

Figure S18 - Change in chemical shift for the NH and CH resonances of **36** (host) upon the addition of TBA sulphate (guest) in DMSO-d_6/0.5 % H_2O at 298 K. This data could not be fitted to a 1:1, 2:1 or 1:2 binding isotherm.

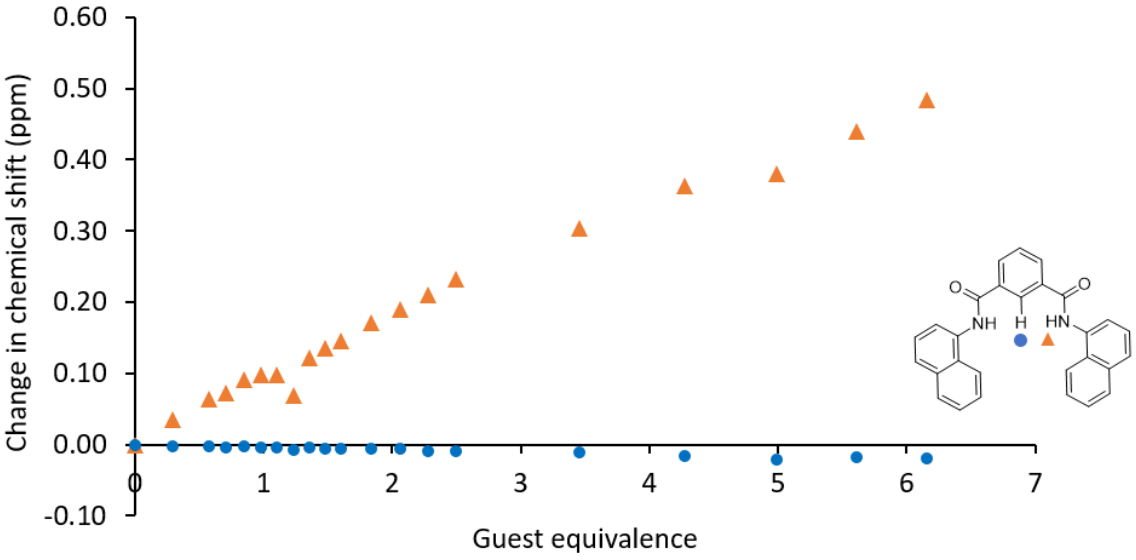

Figure S19 - Change in chemical shift for the NH and CH resonances of **36** (host) upon the addition of TBA dihydrogen phosphate (guest) in DMSO-d_6/0.5 % H_2O at 298 K. The 1:1 association constants derived from the NH change in chemical shift, K_{ass} = 9.58 M^{-1} ± 3.56 %, and the ArH change in chemical shift K_{ass} = 9.22 M^{-1} ± 9.31 %. 1:1 Bindfit link: http://app.supramolecular.org/bindfit/view/d84fa003-ac14-4904-bc78-c748d9145f40 1:1 Bindfit link: http://app.supramolecular.org/bindfit/view/8017babb-c157-4d25-b885-36aa79ebe023

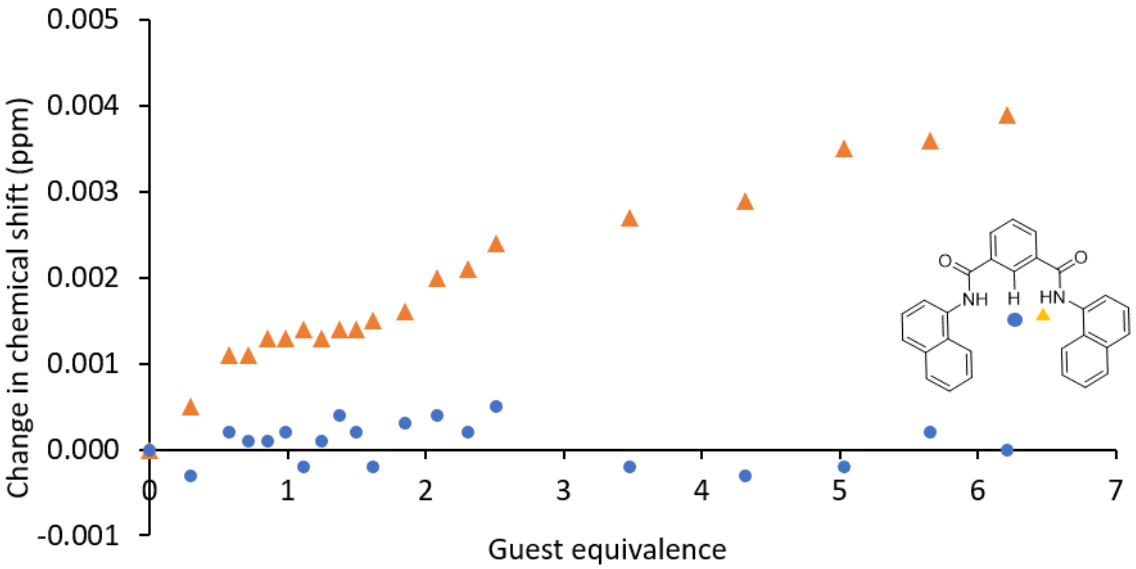

Figure S20 - Change in chemical shift for the NH and CH resonances of **36** (host) upon the addition of TBA hydrogen sulphate (guest) in DMSO-d_6/0.5 % H_2O at 298 K. This data could not be fitted to a 1:1, 2:1 or 1:2 binding isotherm due to change in chemical shift lying within the limitations of the NMR machine.

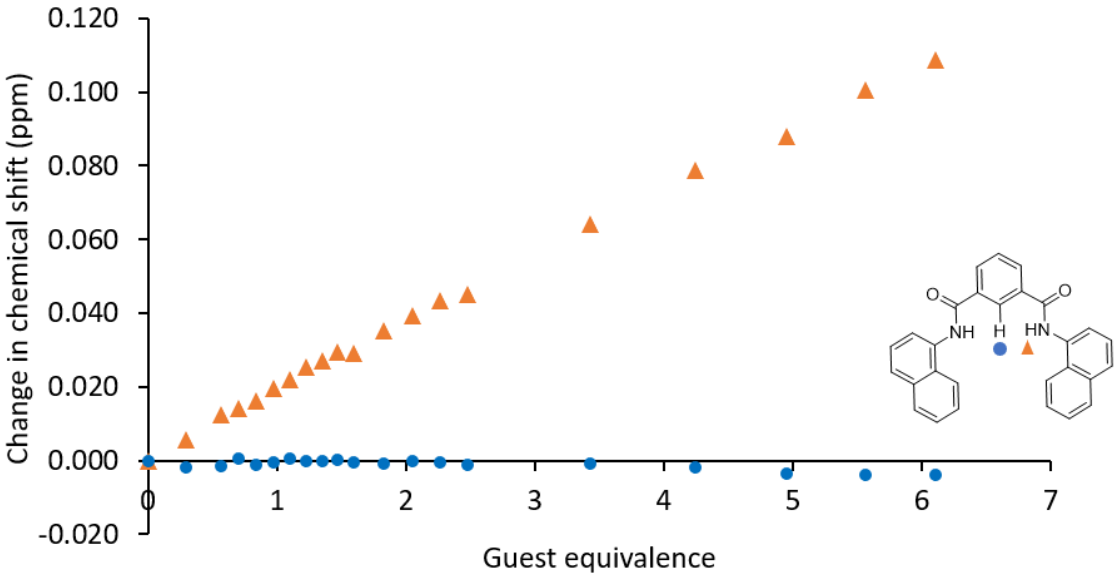

Figure S21 - Change in chemical shift for the NH and CH resonances of **36** (host) upon the addition of TBA chloride (guest) in DMSO-d_6/0.5 % H_2O at 298 K. The 1:1 association constant derived from the NH change in chemical shift, K_{ass} = 4.42 M^{-1} ± 0.99 %. 1:1 Bindfit link: http://app.supramolecular.org/bindfit/view/82167ece-f99f-457e-a64c-522d191d5ac2

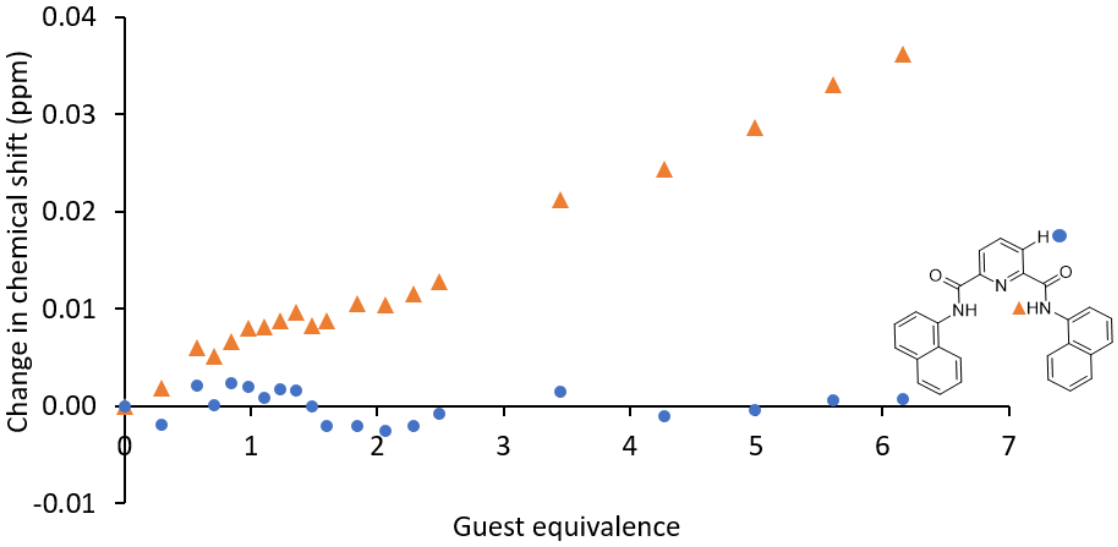

Figure S22 - Change in chemical shift for the NH and CH resonances of **37** (host) upon the addition of TBA benzoate (guest) in DMSO-d_6/0.5 % H_2O at 298 K. This data could not be fitted to a 1:1, 2:1 or 1:2 binding isotherm due to change in chemical shift lying within the limitations of the NMR machine.

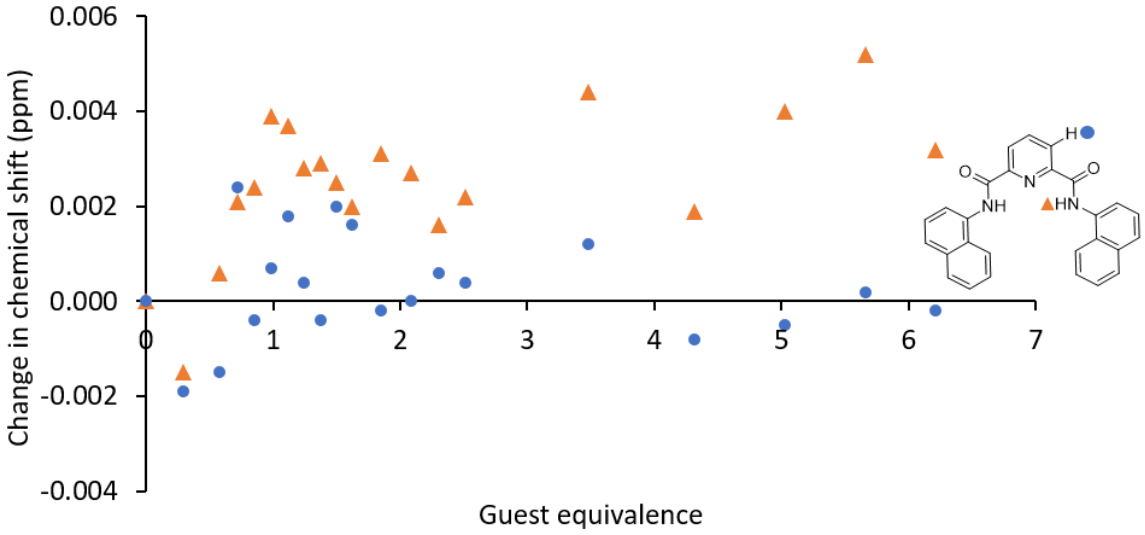

Figure S23 - Change in chemical shift for the NH and CH resonances of **37** (host) upon the addition of TBA sulphate (guest) in DMSO-d_6/0.5 % H_2O at 298 K. This data could not be fitted to a 1:1, 2:1 or 1:2 binding isotherm due to change in chemical shift lying within the limitations of the NMR machine.

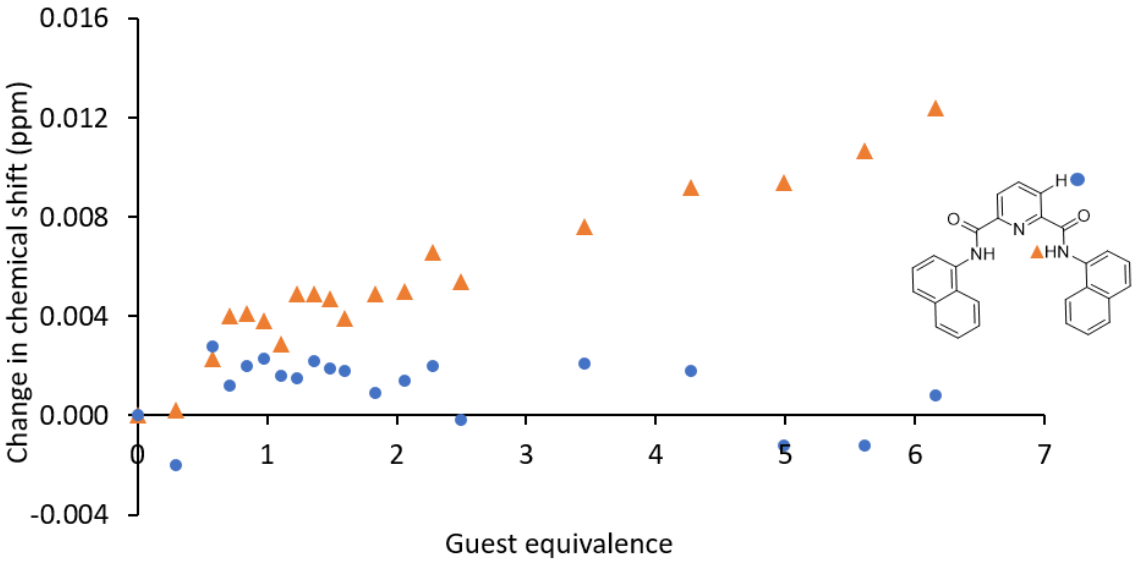

Figure S24 - Change in chemical shift for NH and CH resonances of **37** (host) upon the addition of TBA dihydrogen phosphate (guest) in DMSO-d_6/0.5 % H_2O at 298 K. This data could not be fitted to a 1:1, 2:1 or 1:2 binding isotherm due to change in chemical shift lying within the limitations of the NMR machine.

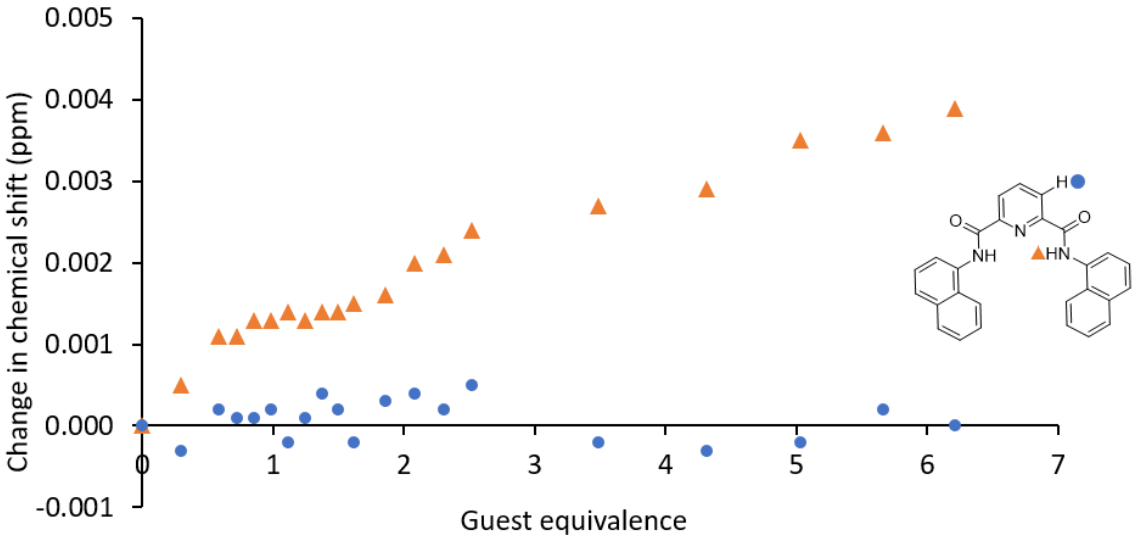

Figure S25 - Change in chemical shift for the NH and CH resonances of **37** (host) upon the addition of TBA hydrogen sulphate (guest) in DMSO-d_6/0.5 % H_2O at 298 K. The 1:1 binding association constant derived from the NH change in chemical shift, K_{ass} = 56.75 M^{-1} ± 8.68 %. 1:1 Bindfit link: http://app.supramolecular.org/bindfit/view/16da2f6b-5ef0-4e8f-afe6-581caaa49923

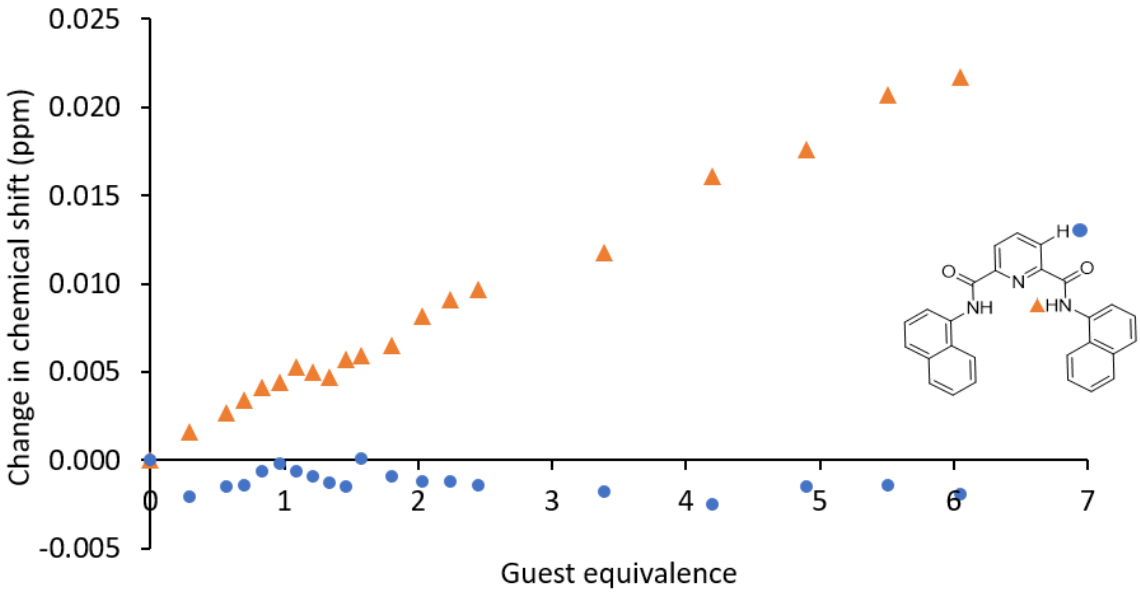

Figure S26 - Change in chemical shift for the NH and CH resonances of **37** (host) upon the addition of TBA chloride (guest) in DMSO-d_6/0.5 % H_2O at 298 K. The 1:1 binding association derived from the NH change in chemical shift, K_{ass} = 5.37 M^{-1} ± 2.98 %. 1:1 Bindfit link: http://app.supramolecular.org/bindfit/view/c67d5d70-0b81-4e76-aa0a-8dc7a464c375

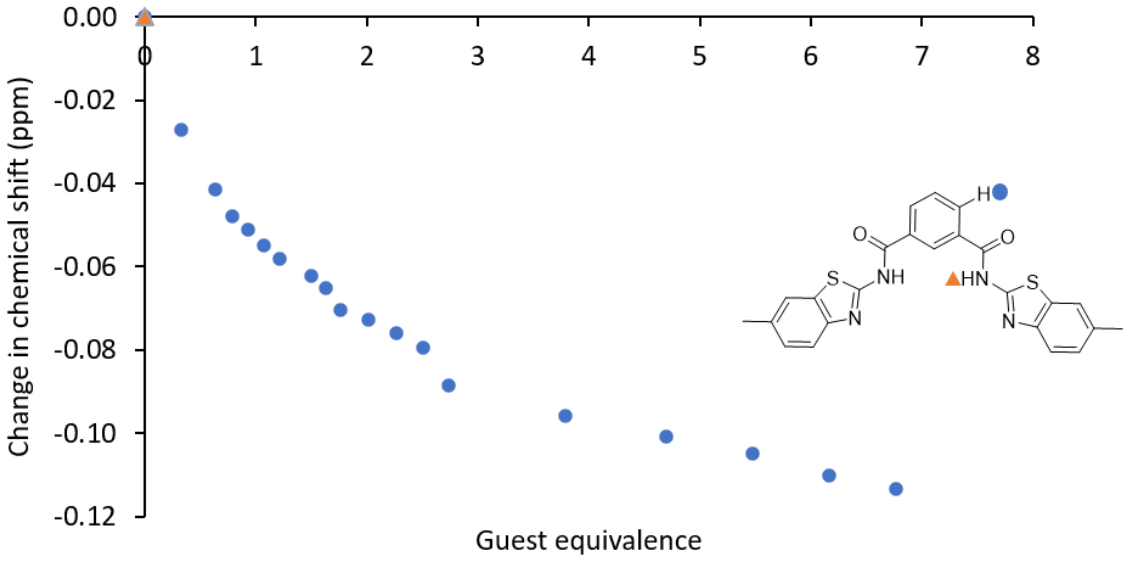

Figure S27 - Change in chemical shift for the NH and CH resonances of **38** (host) upon the addition of TBA OBz (guest) in DMSO-d_6/0.5 % H_2O at 298 K. Due to peak broadening, the chemical shift for the NH resonance could not be followed accurately. The 1:1 binding association derived from the ArH change in chemical shift, K_{ass} = 206.53 M^{-1} ± 8.41 %. 1:1 Bindfit link: http://app.supramolecular.org/bindfit/view/4966edf2-85b1-4e4f-ae30-d5e1077a7357

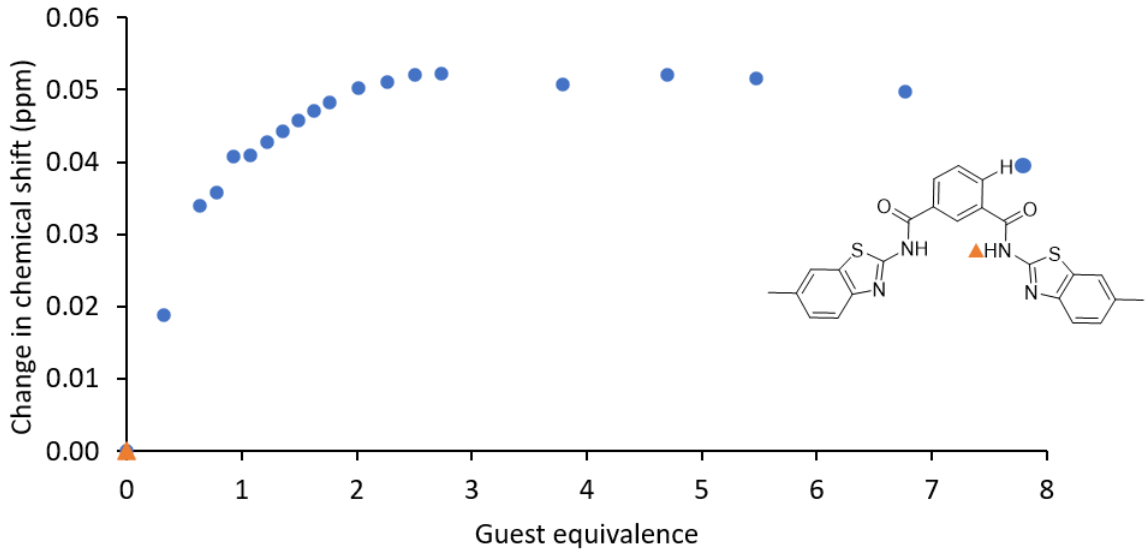

Figure S28 - Change in chemical shift for the NH and CH resonances of **38** (host) upon the addition of TBA sulphate (guest) in DMSO-d_6/0.5 % H_2O at 298 K. Due to peak broadening, the chemical shift for the NH resonance could not be followed accurately. The 2:1 (H:G) binding association derived from the ArH change in chemical shift, K_{11} = 107.37 M^{-1} ± 9.18 %, and K_{21} = 217.23 M^{-1} ± 3.57 %. 2:1 Bindfit link: http://app.supramolecular.org/bindfit/view/6eb56f84-7ca7-4b29-9b33-95ca2542c907

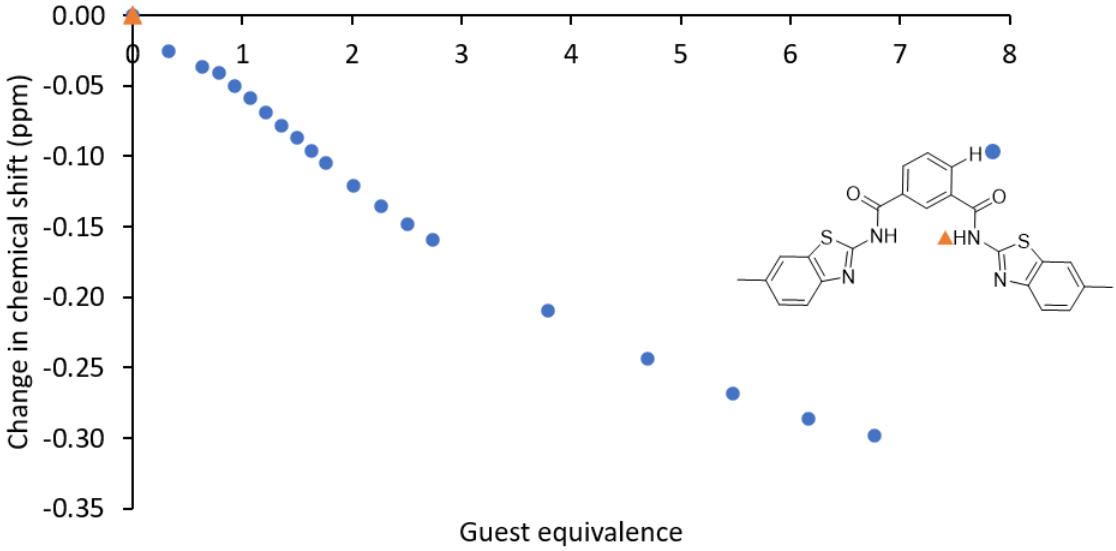

Figure S29 - Change in chemical shift for the NH and CH resonances of **38** (host) upon the addition of TBA dihydrogen phosphate (guest) in DMSO-d_6/0.5 % H_2O at 298 K. Due to peak broadening, the chemical shift for the NH resonance could not be followed accurately. The 1:1 binding association derived from the ArH change in chemical shift, K_{ass} = 17.75 M^{-1} ± 2.59 %. 1:1 Bindfit link: http://app.supramolecular.org/bindfit/view/3e23872c-6607-407e-b19b-7dc76222b34f

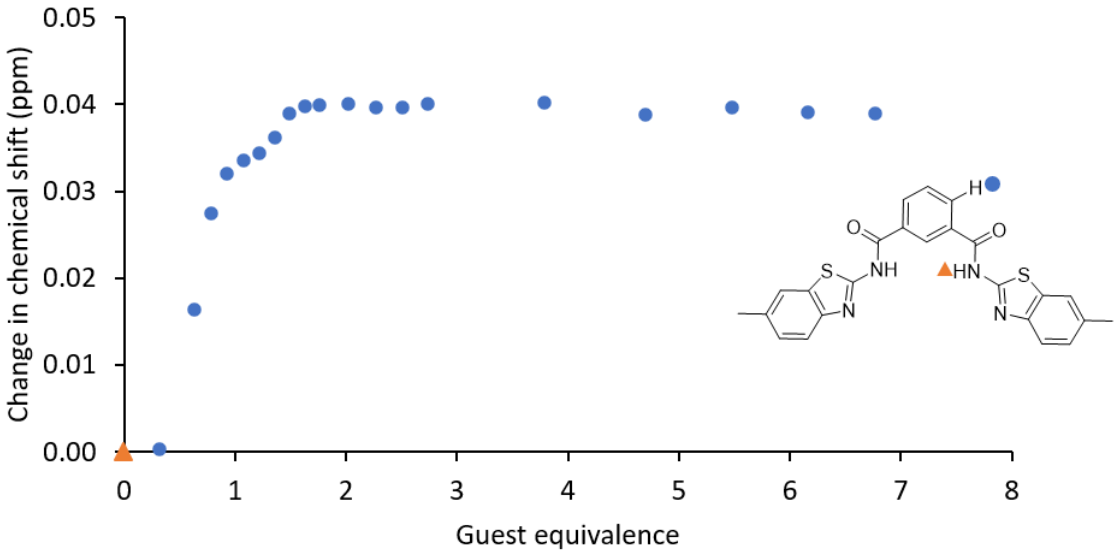

Figure S30 - Change in chemical shift for the NH and CH resonances of **38** (host) upon the addition of TBA hydrogen sulphate (guest) in DMSO-d_6/0.5 % H_2O at 298 K. Due to peak broadening, the chemical shift for the NH resonance could not be followed accurately. This data could not be fitted to a 1:1, 2:1 or 1:2 binding isotherm.

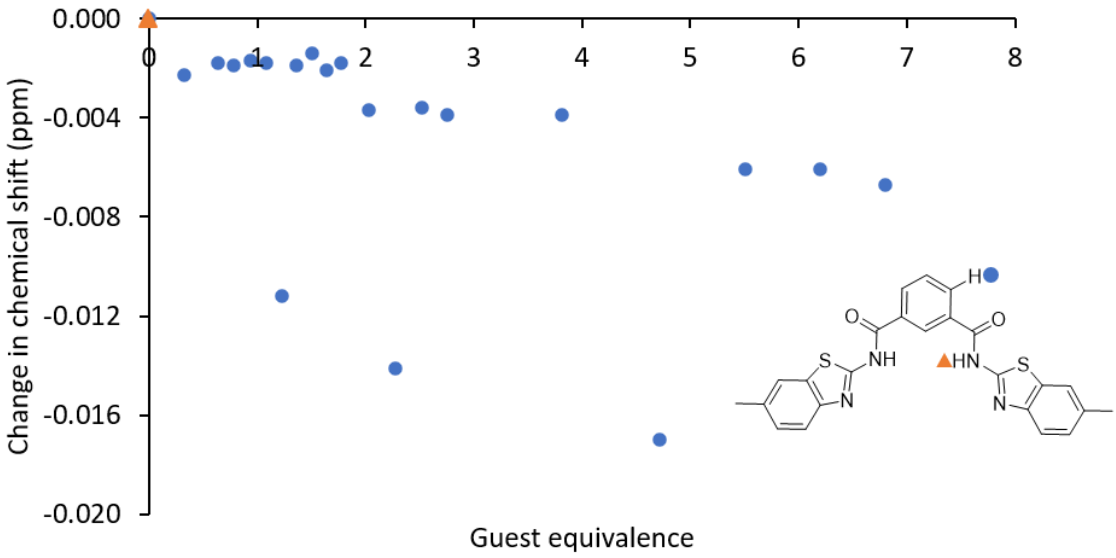

Figure S31 - in chemical shift for the NH and CH resonances of **38** (host) upon the addition of TBA chloride (guest) in DMSO-d_6/0.5 % H_2O at 298 K. Due to peak broadening, the chemical shift for the NH resonance could not be followed accurately. This data could not be fitted to a 1:1, 2:1 or 1:2 binding isotherm.

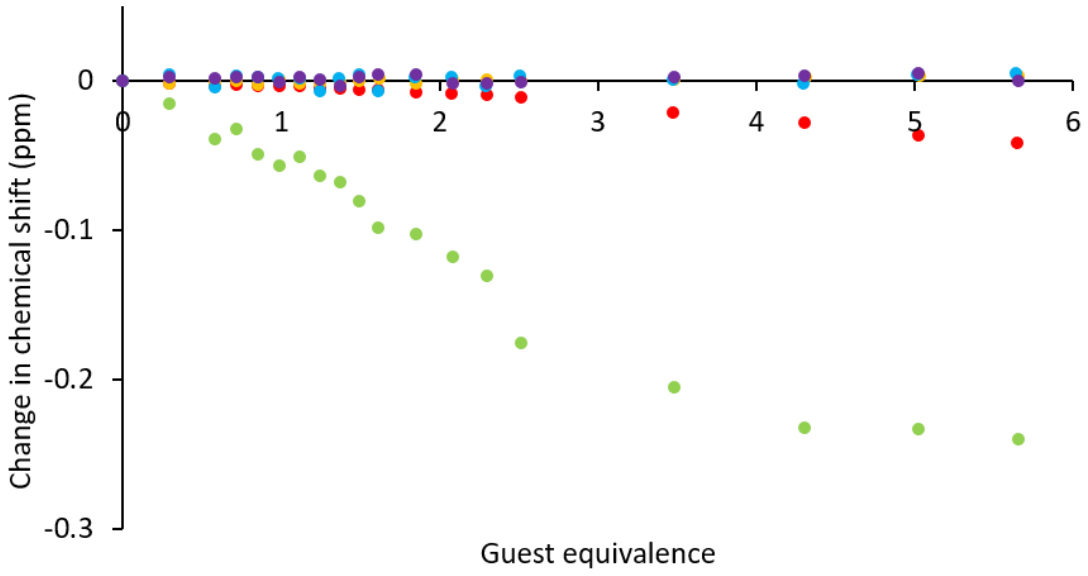

Figure S32 - Change in chemical shift for the CH resonances of **35** (host) upon the addition of listed guests; TBA OBz (red), TBA sulphate (orange), TBA dihydrogen phosphate (green), TBA hydrogen sulphate (blue), TBA chloride (purple) in DMSO-d_6/0.5 % H_2O at 298 K.

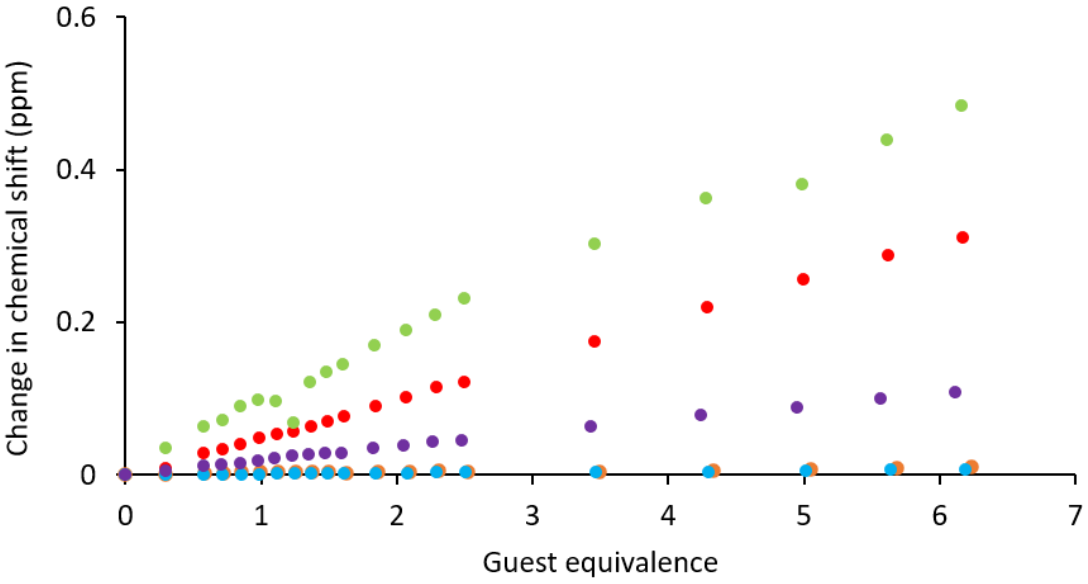

Figure S33 - Change in chemical shift for the CH resonances of **36** (host) upon the addition of listed guests; TBA OBz (red), TBA sulphate (orange), TBA dihydrogen phosphate (green), TBA hydrogen sulphate (blue), TBA chloride (purple) in DMSO-d_6/0.5 % H_2O at 298 K.

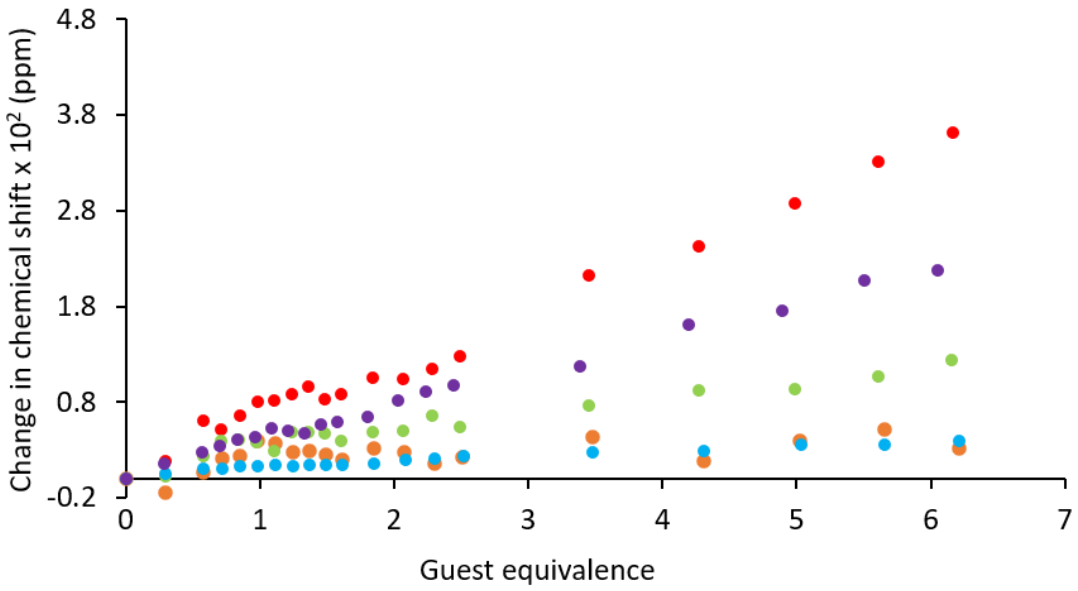

Figure S34 - Change in chemical shift for the CH resonances of **37** (host) upon the addition of listed guests; TBA OBz (red), TBA sulphate (orange), TBA dihydrogen phosphate (green), TBA hydrogen sulphate (blue), TBA chloride (purple) in DMSO-d_6/0.5 % H_2O at 298 K.

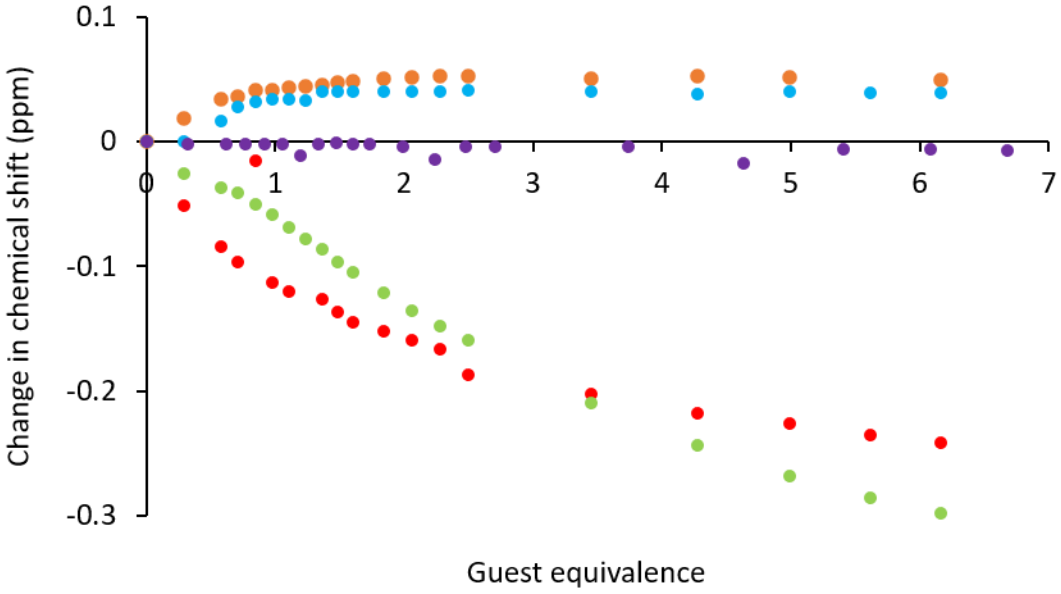

Figure S35 - Change in chemical shift for the CH resonances of **38** (host) upon the addition of listed guests; TBA OBz (red), TBA sulphate (orange), TBA dihydrogen phosphate (green), TBA hydrogen sulphate (blue), TBA chloride (purple) in DMSO-d_6/0.5 % H_2O at 298 K.

7.3. Fluorimeter titrations

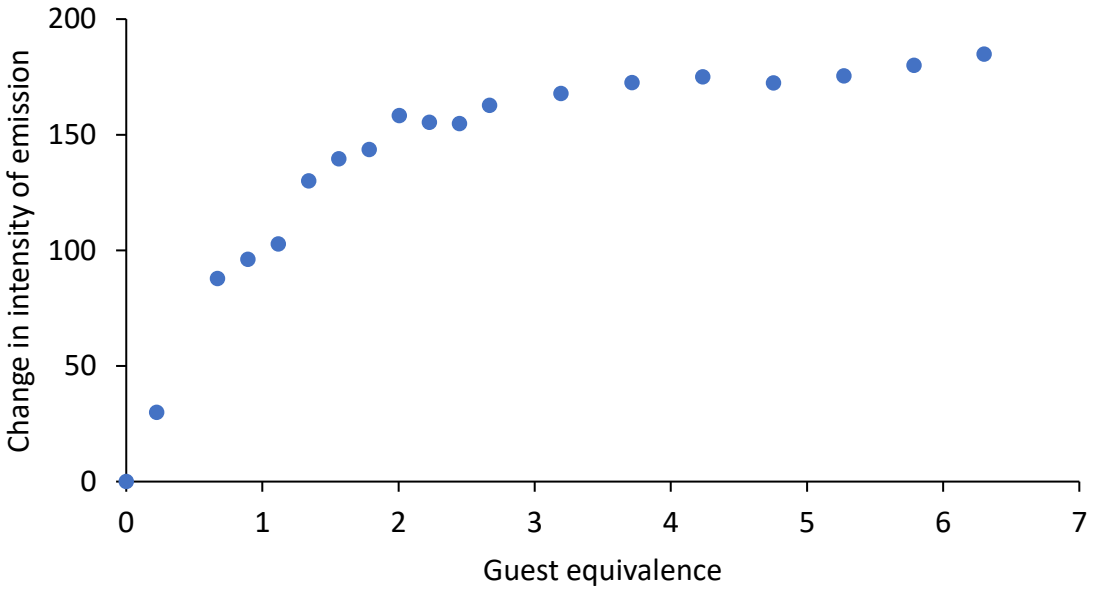

Figure S36 - Change in emission intensity at 400 nm of **35** (host) upon the addition of TBA benzoate (guest) in DMSO/0.5 % H_2O at 298 K. The 1:1 binding association derived from the change in intensity of emission at 400 nm, K_{ass} = 1958476.59 M^{-1} ± 13.75 %. 1:1 Bindfit link http://app.supramolecular.org/bindfit/view/3cec7447-3e31-41fe-b020-f0dac46e877b

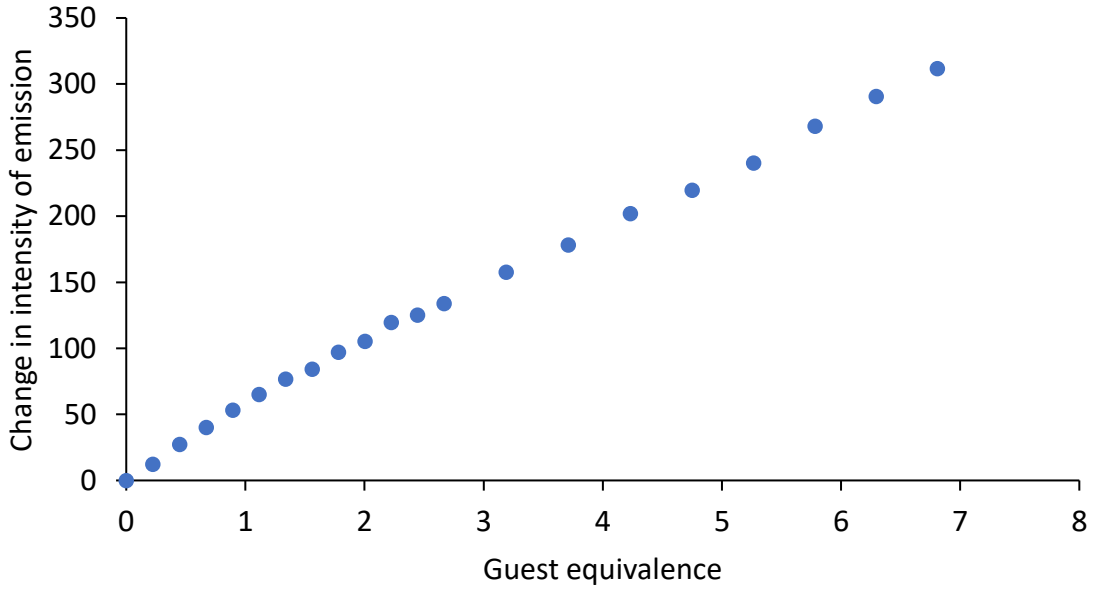

Figure S37 - Change in intensity of emission at 400 nm of **35** (host) upon the addition of TBA sulphate (guest) in DMSO/0.5 % H_2O at 298 K. The 1:1 binding association derived from the change in intensity of emission at 400 nm, K_{ass} = 45836.02 M^{-1} ± 1.51 %. 1:1 Bindfit link http://app.supramolecular.org/bindfit/view/1014a2ff-3bbf-458d-9a11-0d11b6aff1bc

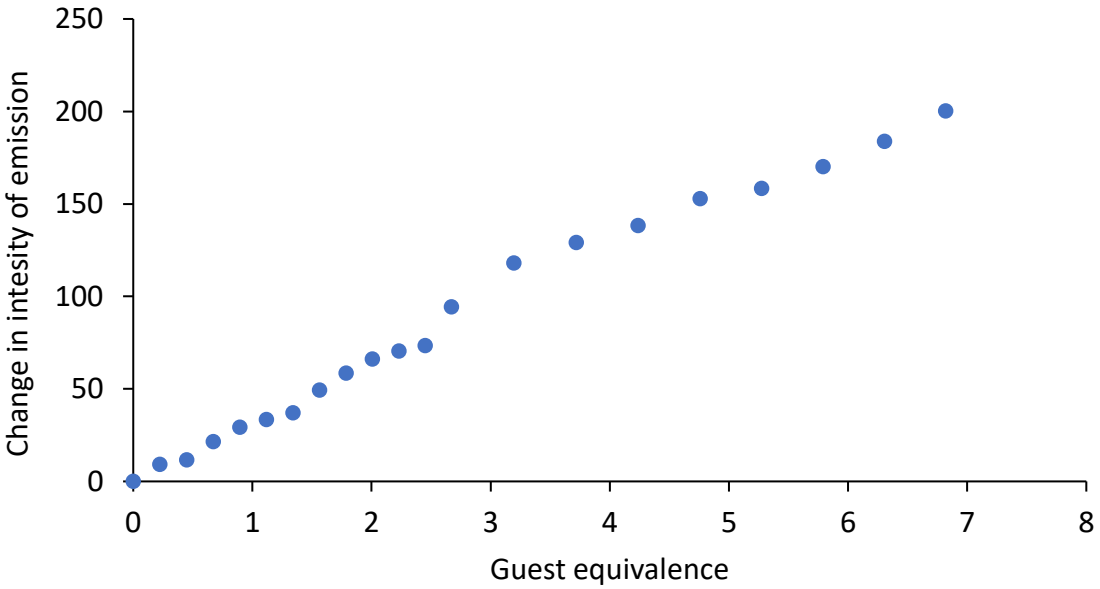

Figure S38 - Change in intensity of emission at 400 nm of **35** (host) upon the addition of TBA dihydrogen phosphate (guest) in DMSO at 298 K. The 1:1 binding association derived from the change in intensity of emission at 400 nm, K_{ass} = 35670.05 M^{-1} ± 3.58 %. 1:1 Bindfit link http://app.supramolecular.org/bindfit/view/db53ec46-21e7-4a0b-9dcf-0caa32530dbd

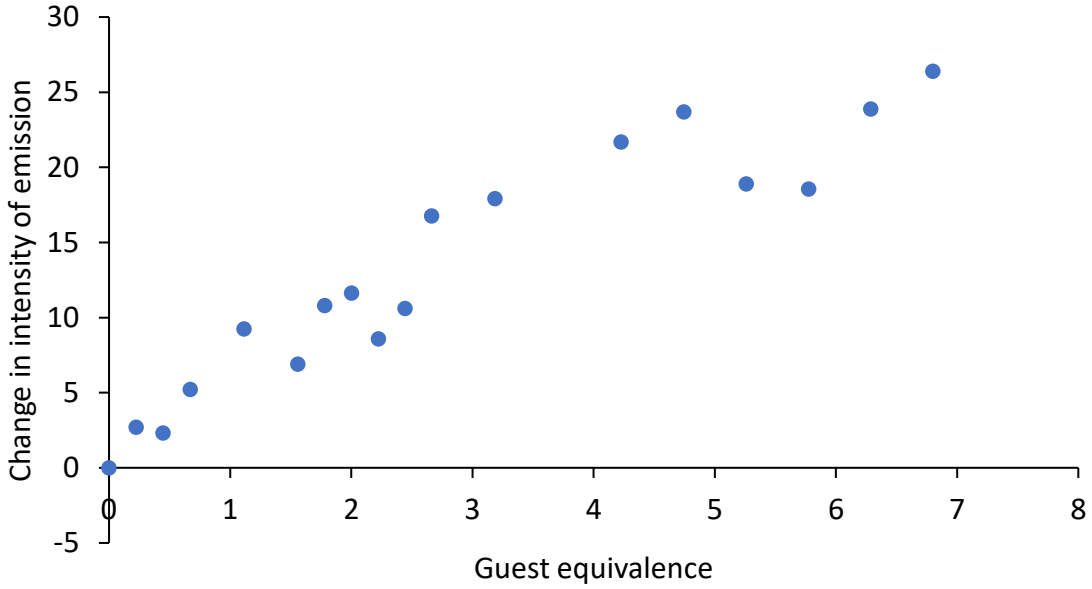

Figure S39 - Change in intensity of emission at 400 nm of **35** (host) upon the addition of TBA hydrogen sulphate (guest) in DMSO at 298 K. This data could not be fitted to a 1:1, 2:1 or 1:2 binding isotherm.

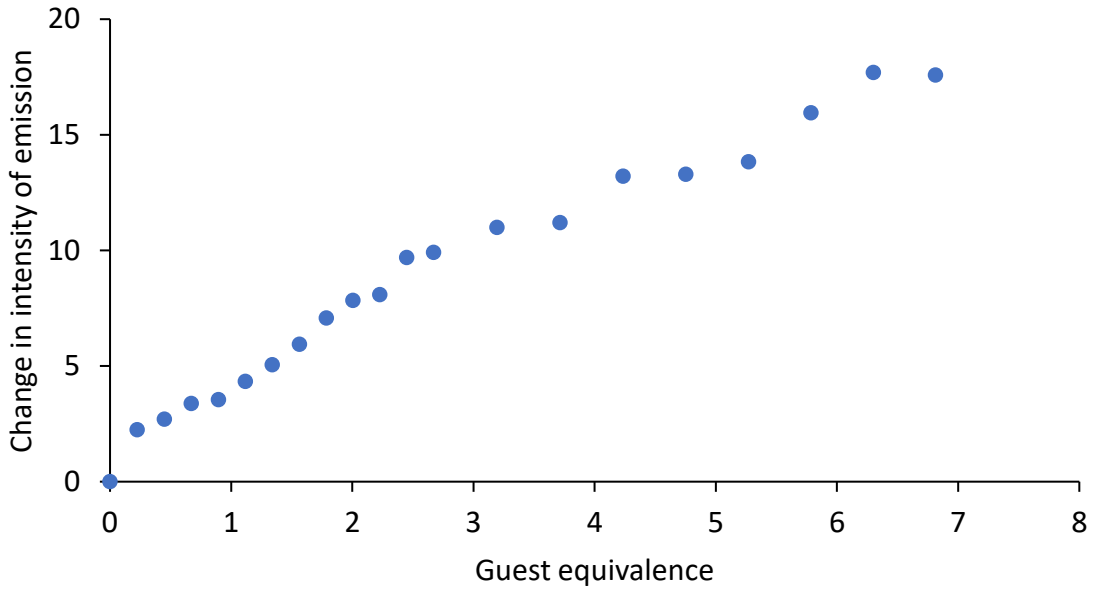

Figure S40 - Change in emission at 400 nm of **35** (host) upon the addition of TBA chloride (guest) in DMSO/0.5 % H_2O at 298 K. This data could not be fitted to a 1:1, 2:1 or 1:2 binding isotherm.

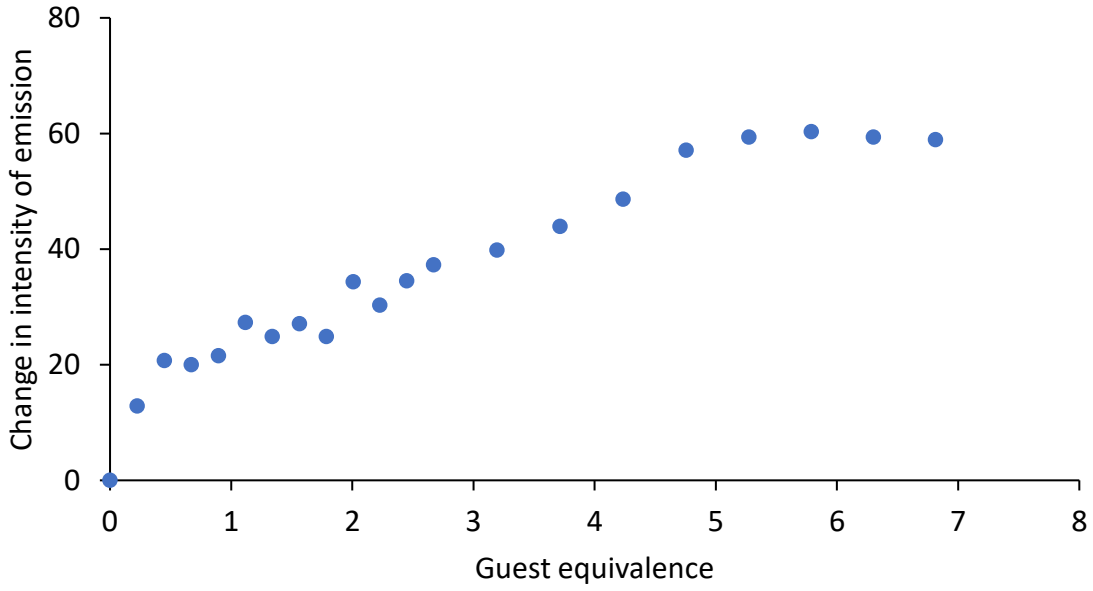

Figure S41 - Change in emission at 340 nm of **36** (host) upon the addition of TBA OBz (guest) in DMSO/0.5 % H_2O at 298 K. This data could not be fitted to a 1:1, 2:1 or 1:2 binding isotherm with a reliable percentage error (however, a 1:1 binding association of 366945.27 M^{-1} was obtained with an error of ± 14 %, Bindfit link http://app.supramolecular.org/bindfit/view/71838d15-834b-422c-ba08-93b075eaaaf2)

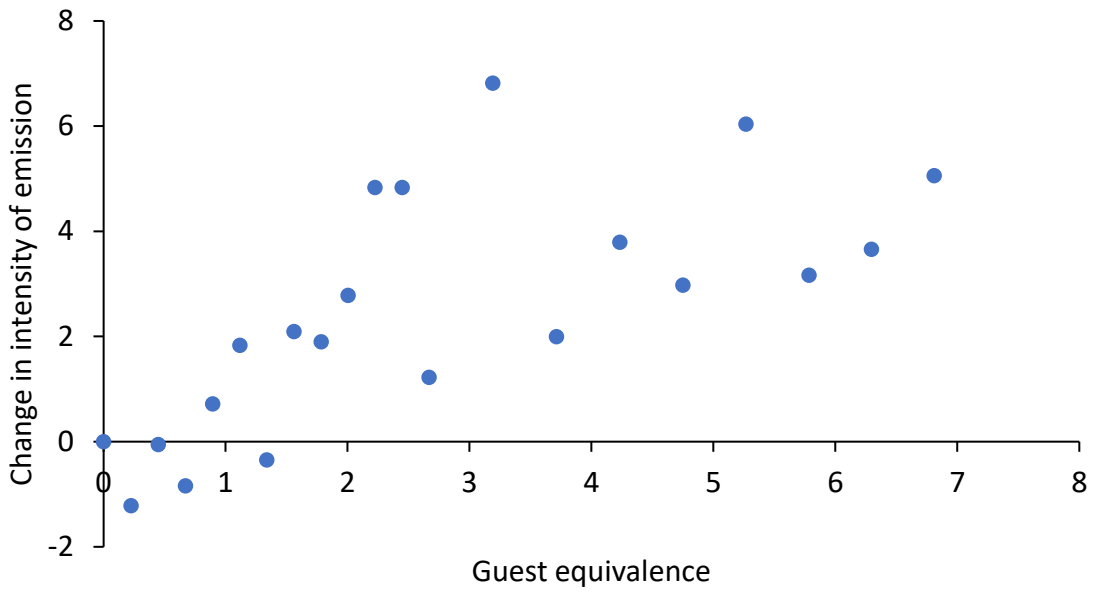

Figure S42 - Change in emission at 340 nm of **36** (host) upon the addition of TBA sulphate (guest) in DMSO/0.5 % H_2O at 298 K. This data could not be fitted to a 1:1, 2:1 or 1:2 binding isotherm.

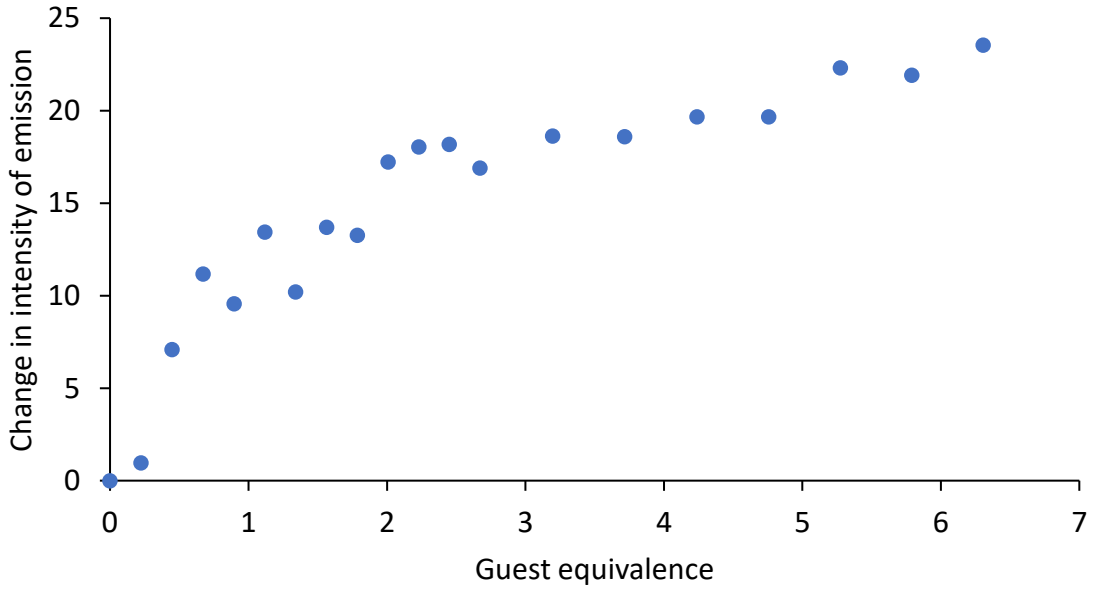

Figure S43 - Change in emission at 340 nm of **36** (host) upon the addition of guest TBA dihydrogen phosphate (guest) in DMSO/0.5 % H_2O at 298 K. This data could not be fitted to a 1:1, 2:1 or 1:2 binding isotherm.

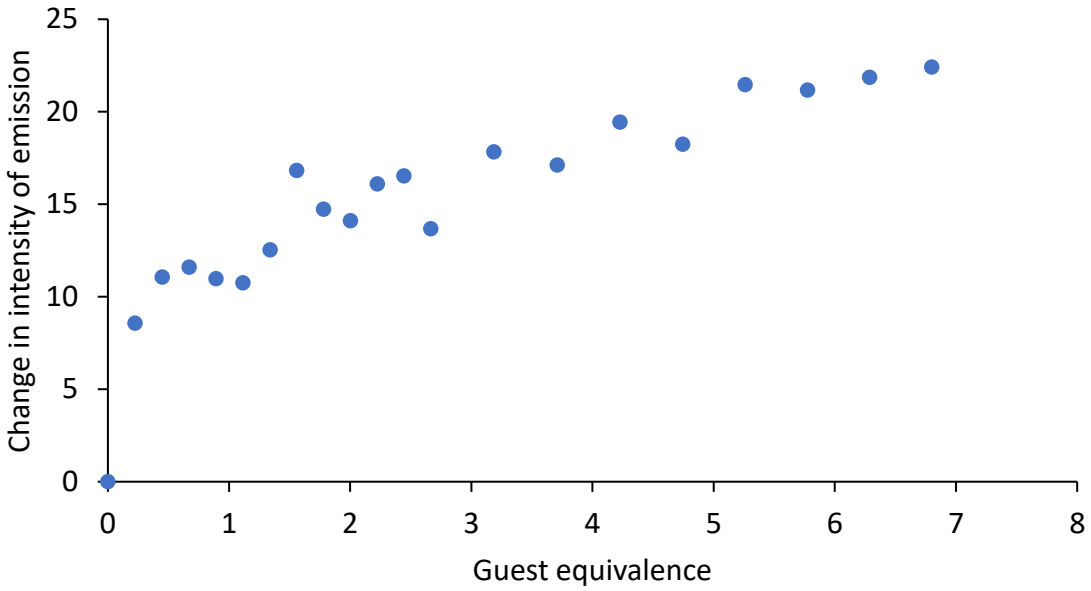

Figure S44 - Change in emission at 340 nm of **36** (host) upon the addition of TBA hydrogen sulphate (guest) in DMSO/0.5 % H_2O at 298 K. This data could not be fitted to a 1:1, 2:1 or 1:2 binding isotherm.

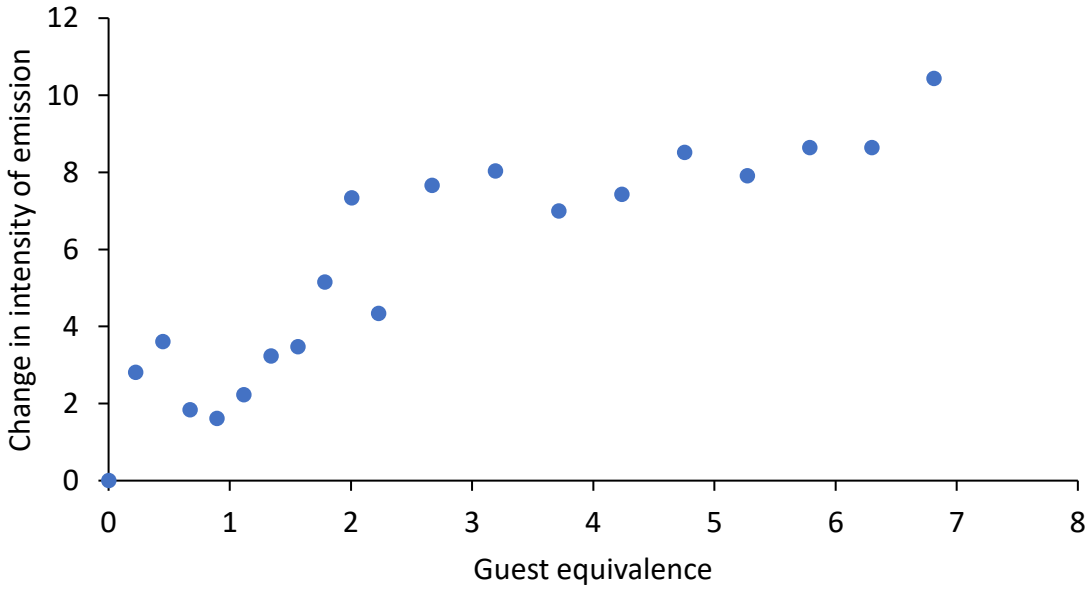

Figure S45 - Change in emission at 340 nm of **36** (host) upon the addition of TBA chloride (guest) in DMSO/0.5 % H_2O at 298 K. This data could not be fitted to a 1:1, 2:1 or 1:2 binding isotherm.

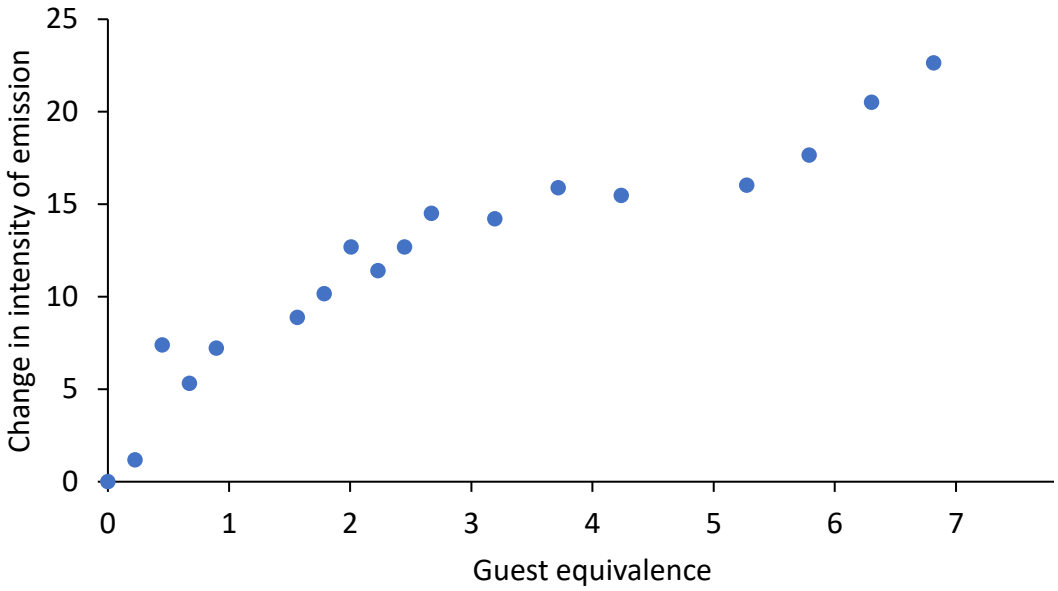

Figure S46 - Change in emission at 330 nm of **37** (host) upon the addition of TBA OBz (guest) in DMSO/0.5 % H_2O at 298 K. This data could not be fitted to a 1:1, 2:1 or 1:2 binding isotherm.

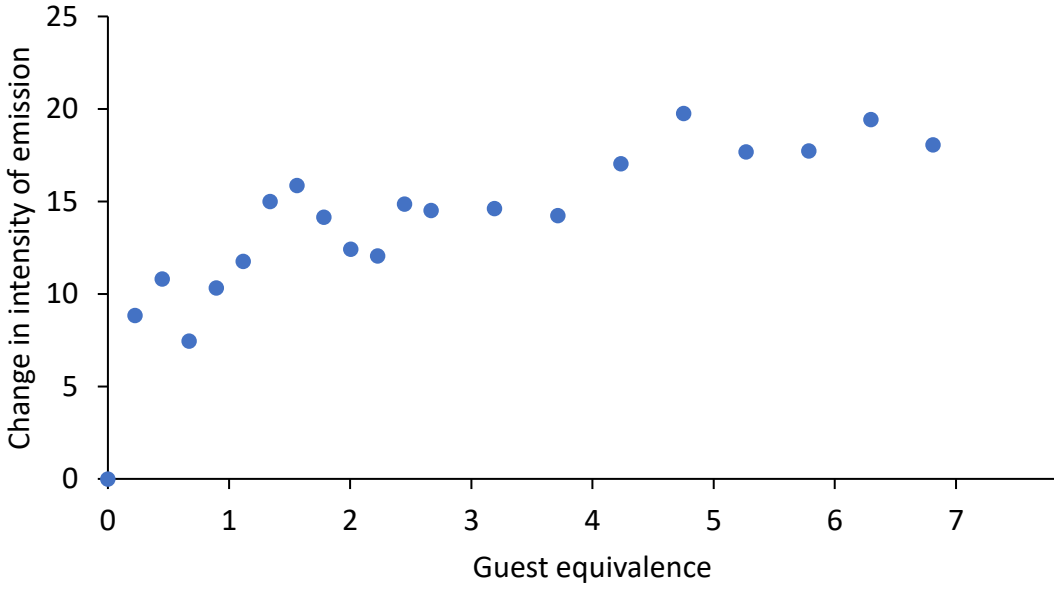

Figure S47 - Change in emission at 330 nm of **37** (host) upon the addition of TBA sulphate (guest) in DMSO/0.5 % H_2O at 298 K. This data could not be fitted to a 1:1, 2:1 or 1:2 binding isotherm.

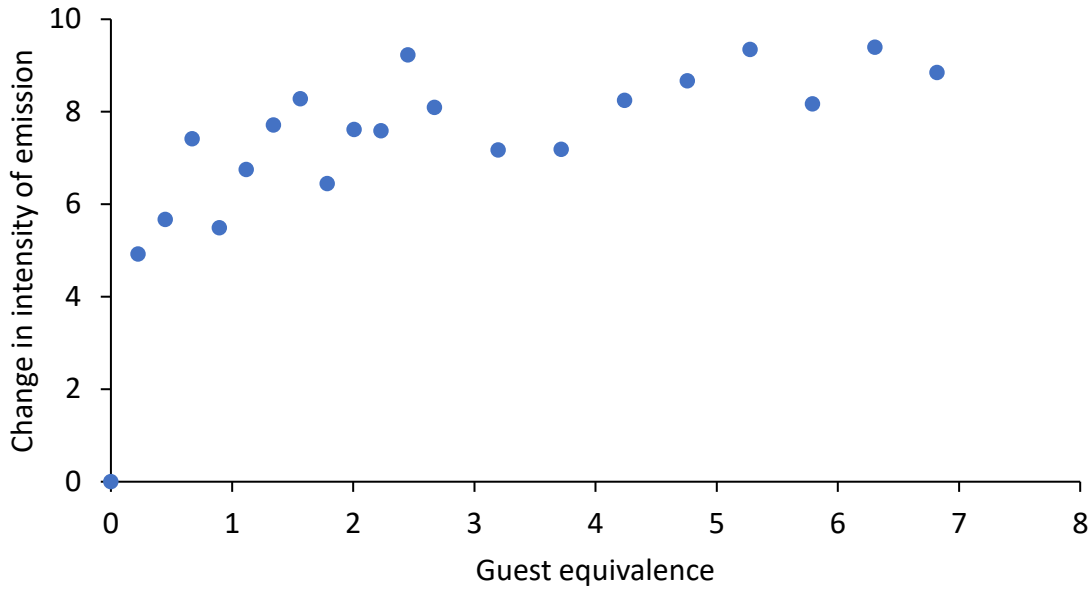

Figure S48 - Change in emission at 330 nm of **37** (host) upon the addition of TBA dihydrogen phosphate (guest) in DMSO/0.5 % H_2O at 298 K. This data could not be fitted to a 1:1, 2:1 or 1:2 binding isotherm.

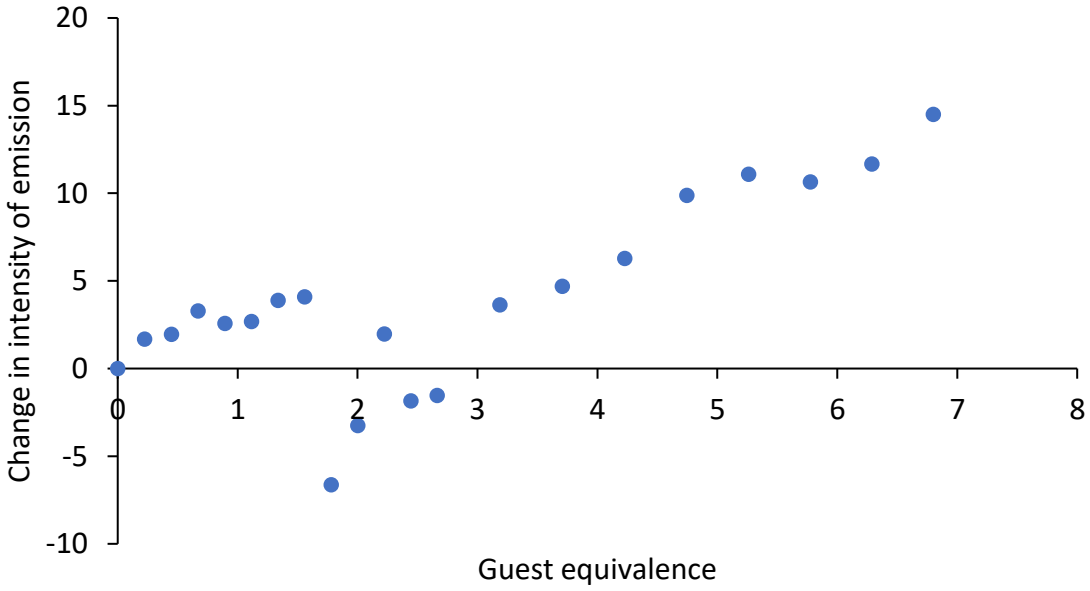

Figure S49 - Change in emission at 330 nm of **37** (host) upon the addition of TBA hydrogen sulphate (guest) in DMSO/0.5 % H_2O at 298 K. This data could not be fitted to a 1:1, 2:1 or 1:2 binding isotherm.

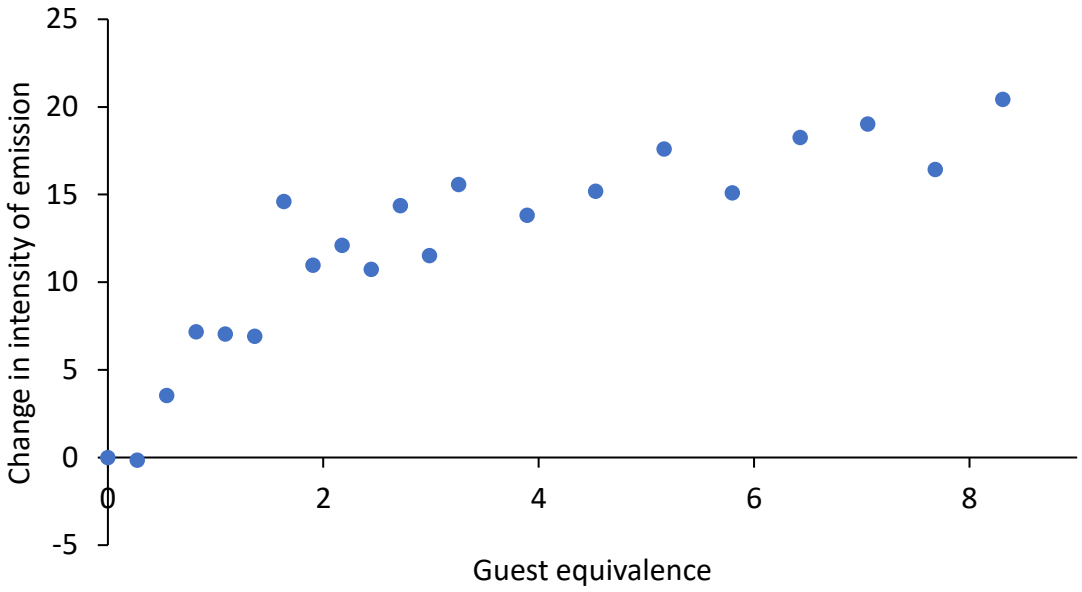

Figure S50 - Change in emission at 330 nm of **37** (host) upon the addition of TBA chloride (guest) in DMSO/0.5 % H_2O at 298 K. This data could not be fitted to a 1:1, 2:1 or 1:2 binding isotherm.

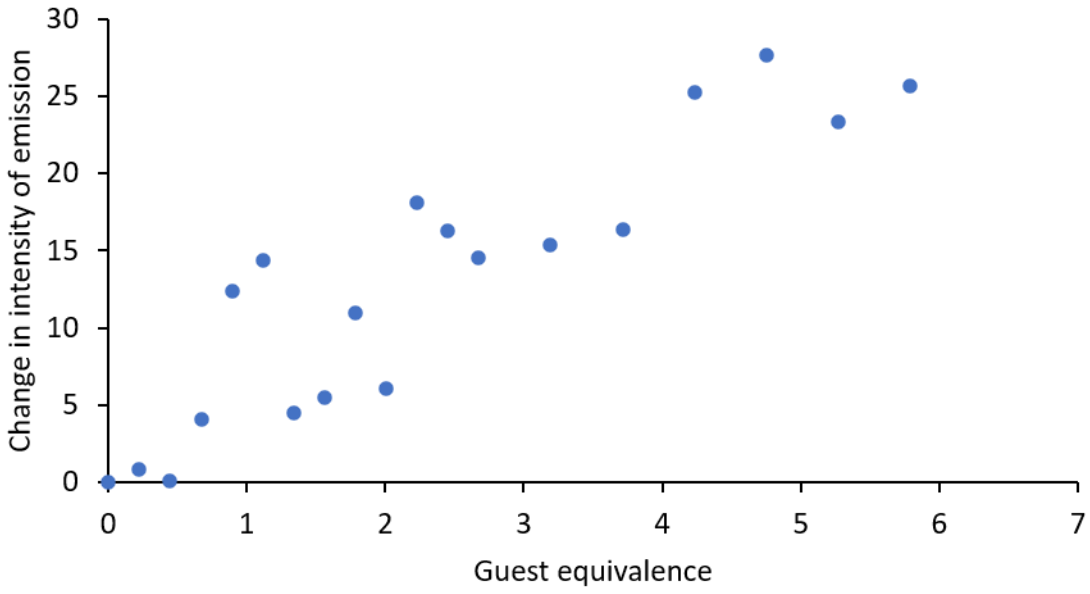

Figure S51 - Change in emission at 346 nm of **38** (host) upon the addition of TBA OBz (guest) in DMSO/0.5 % H_2O at 298 K. This data could not be fitted to a 1:1, 2:1 or 1:2 binding isotherm with a reliable percentage error (however, a 1:1 binding association of 89089.29M^{-1} was obtained with an error of ± 19.73 %. http://app.supramolecular.org/bindfit/view/71e68442-afe6-4e8d-9ba0-fa3d71073b49)

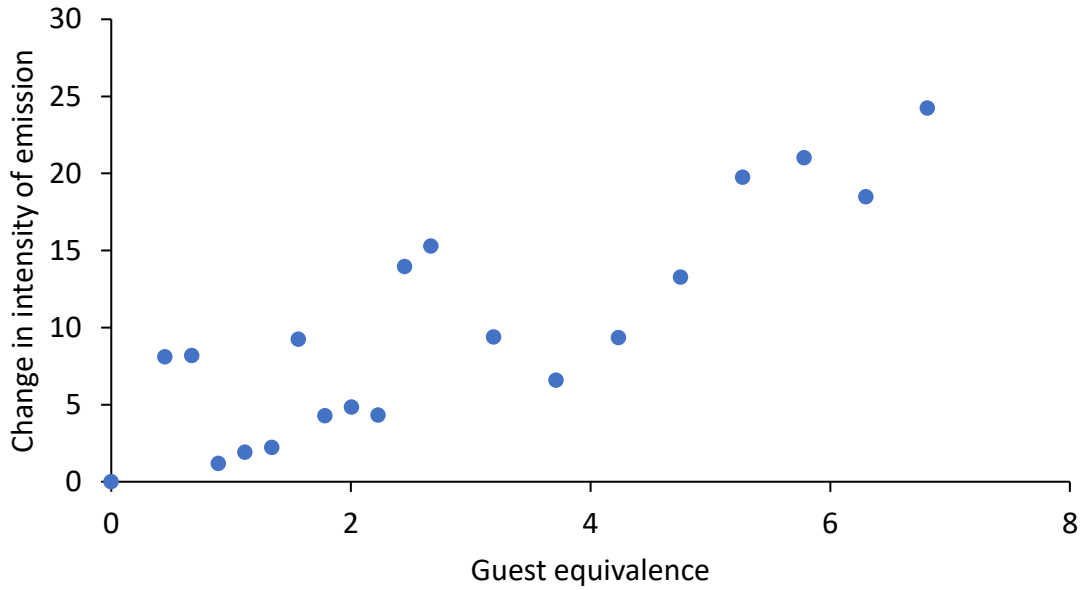

Figure S52 - Change in emission at 346 nm of **38** (host) upon the addition of TBA sulphate (guest) in DMSO/0.5 % H_2O at 298 K. This data could not be fitted to a 1:1, 2:1 or 1:2 binding isotherm.

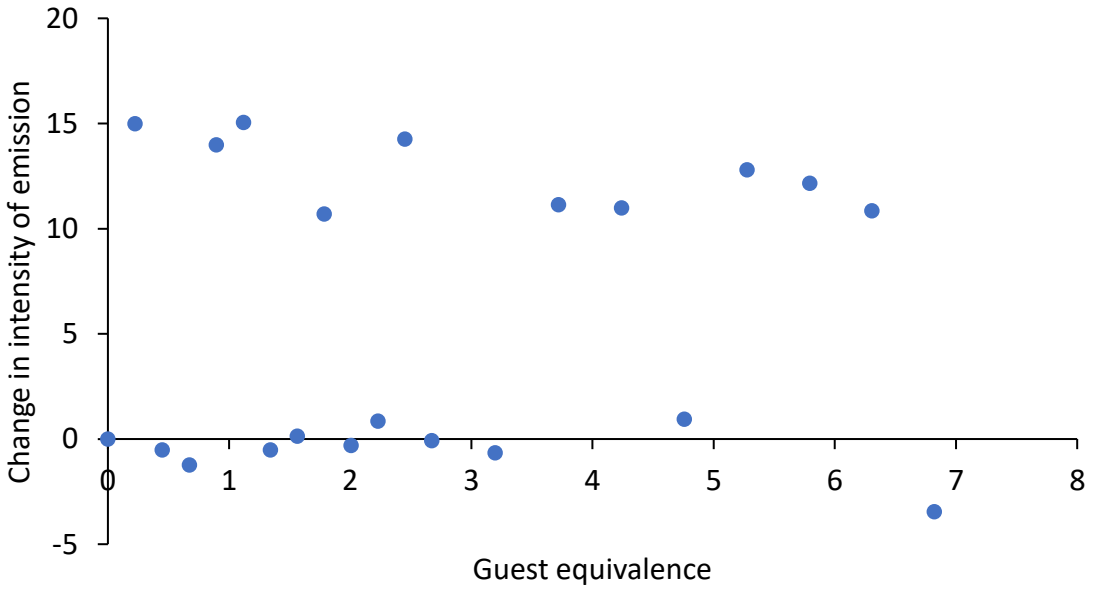

Figure S53 - Change in emission at 346 nm of **38** (host) upon the addition of TBA dihydrogen phosphate (guest) in DMSO/0.5 % H_2O at 298 K. This data could not be fitted to a 1:1, 2:1 or 1:2 binding isotherm.

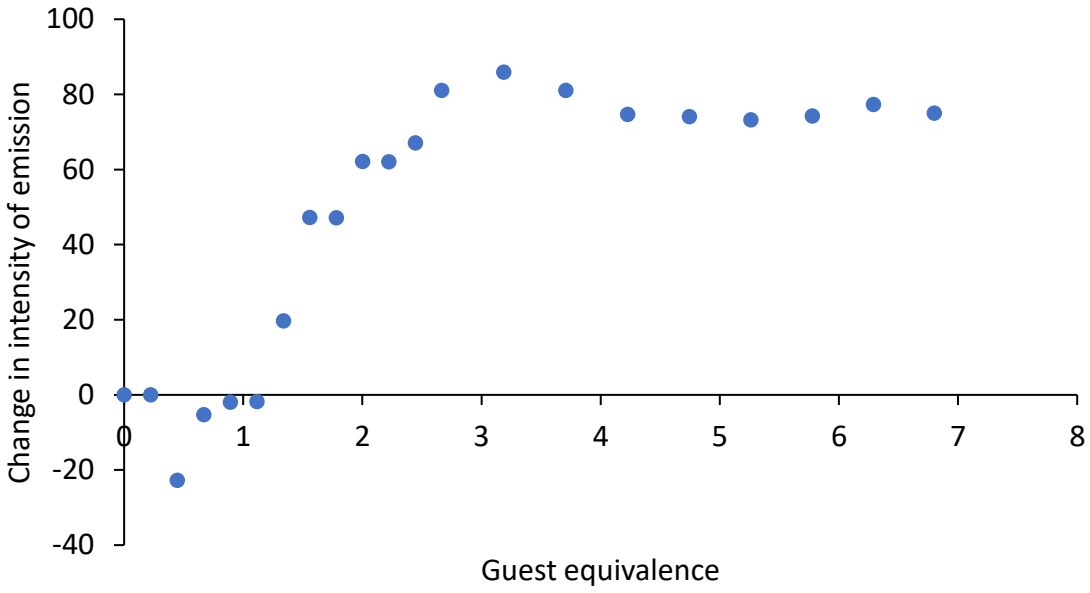

Figure S54 - Change in emission at 346 nm of **38** (host) upon the addition of TBA hydrogen sulphate (guest) in DMSO/0.5 % H_2O at 298 K. This data could not be fitted to a 1:1, 2:1 or 1:2 binding isotherm.

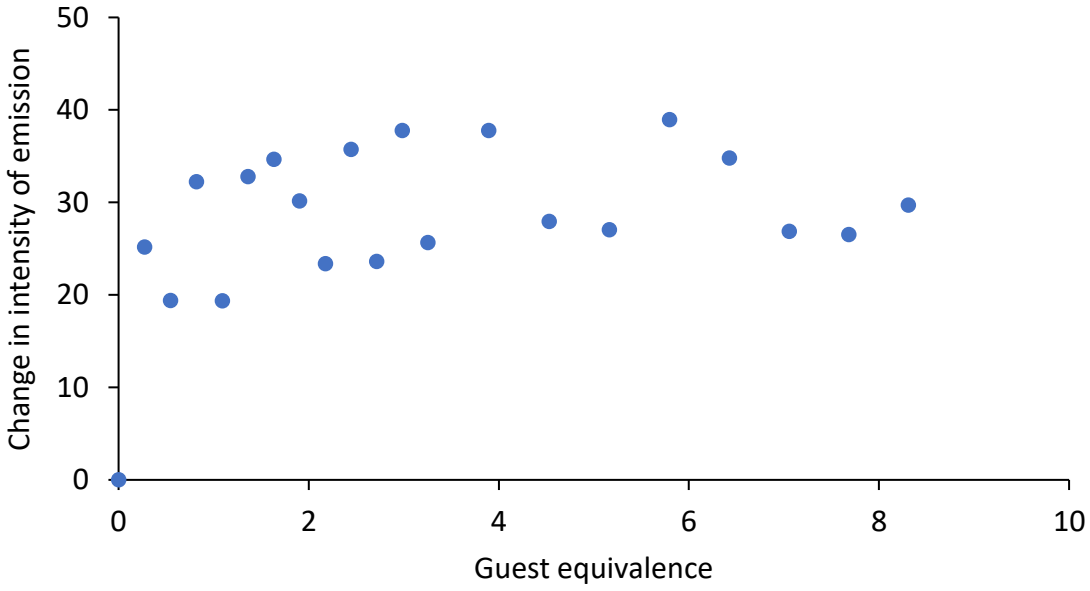

Figure S55 - Change in emission at 346 nm of **38** (host) upon the addition of TBA chloride (guest) in DMSO/0.5 % H_2O at 298 K. This data could not be fitted to a 1:1, 2:1 or 1:2 binding isotherm.

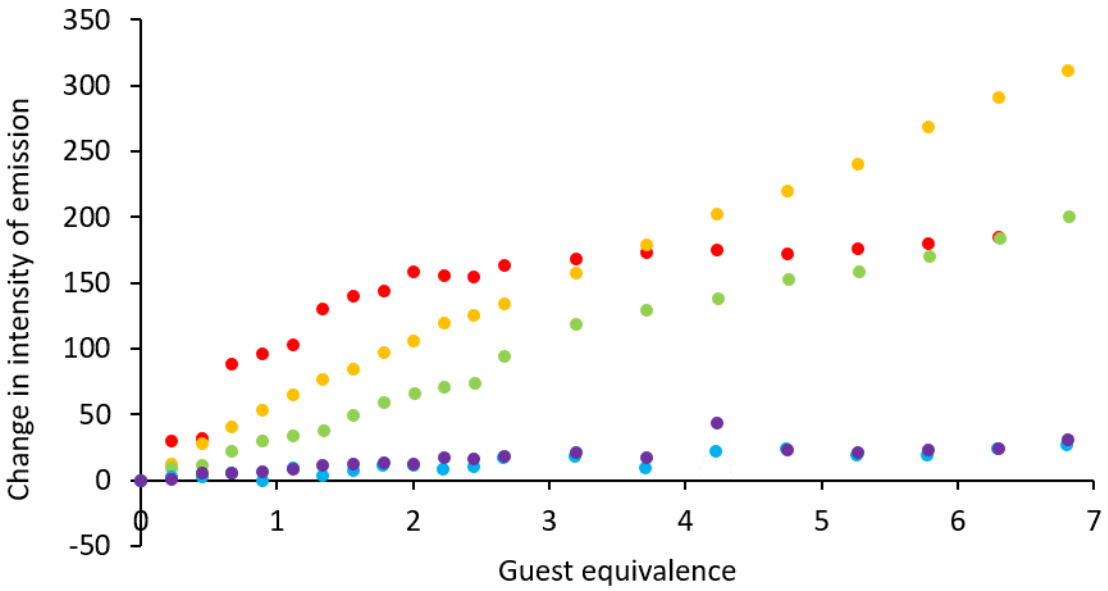

Figure S56 - Change in intensity of emission of **35** (host) at 400 nm of upon the addition of listed guests; TBA OBz (red), TBA sulphate (orange), TBA dihydrogen phosphate (green), TBA hydrogen sulphate (blue), TBA chloride (purple) in DMSO/0.5 % H_2O at 298 K.

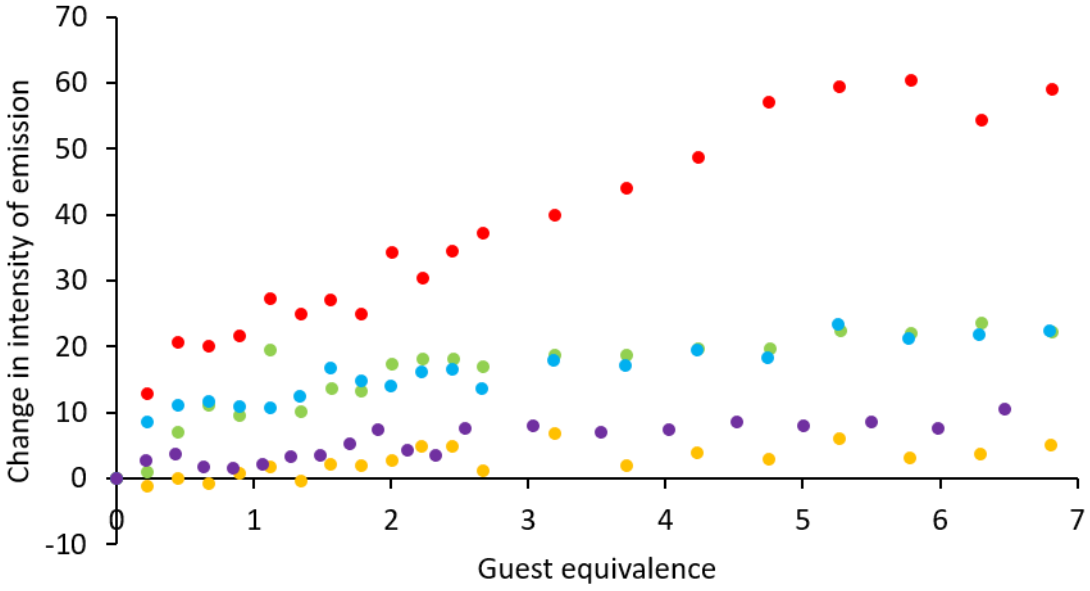

Figure S57 - Change in intensity of emission of **36** (host) at 340 nm upon the addition of listed guests; TBA OBz (red), TBA sulphate (orange), TBA dihydrogen phosphate (green), TBA hydrogen sulphate (blue), TBA chloride (purple) in DMSO/0.5 % H_2O at 298 K.

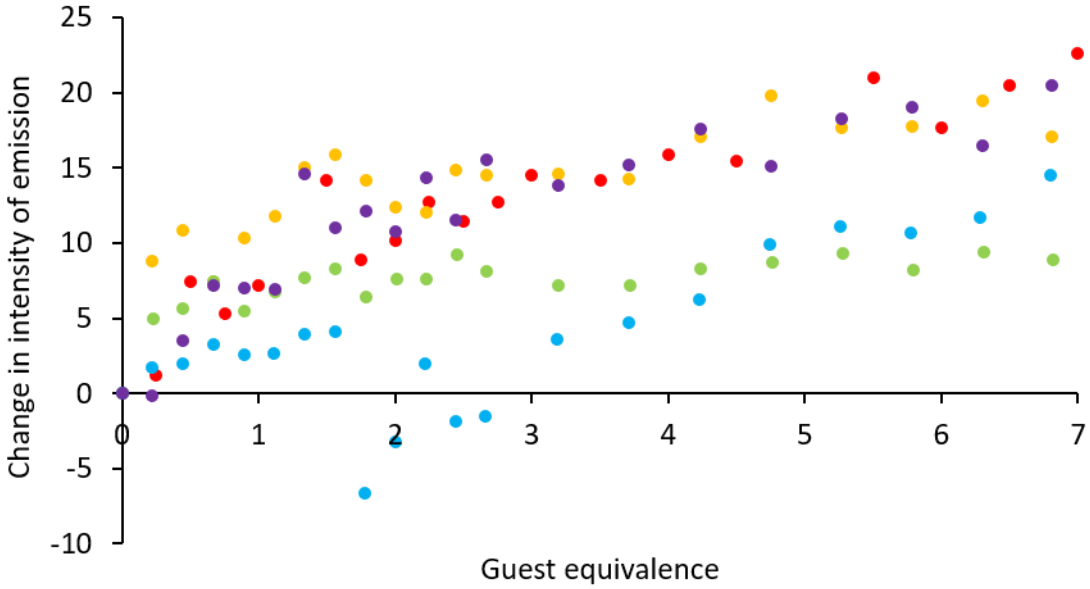

Figure S58 - Change in intensity of emission of **37** (host) at 330 nm upon the addition of listed guests; TBA OBz (red), TBA sulphate (orange), TBA dihydrogen phosphate (green), TBA hydrogen sulphate (blue), TBA chloride (purple) in DMSO/0.5 % H_2O at 298 K.

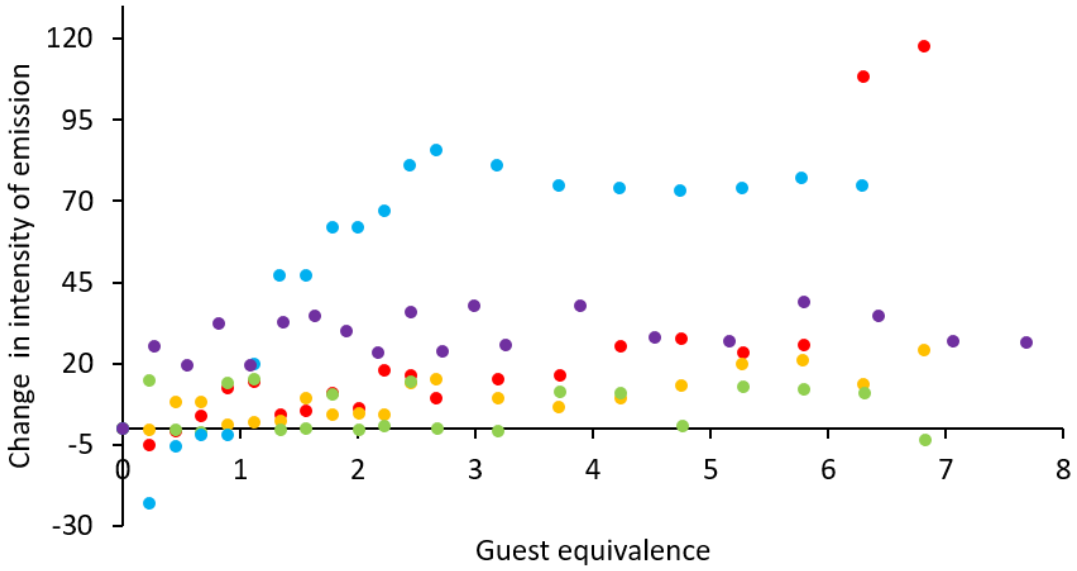

Figure S59 - Change in intensity of emission of **38** (host) at 346 nm upon the addition of listed guests; TBA OBz (red), TBA sulphate (orange), TBA dihydrogen phosphate (green), TBA hydrogen sulphate (blue), TBA chloride (purple) in DMSO/0.5 % H_2O at 298 K.

7.4. Mass spectrum data

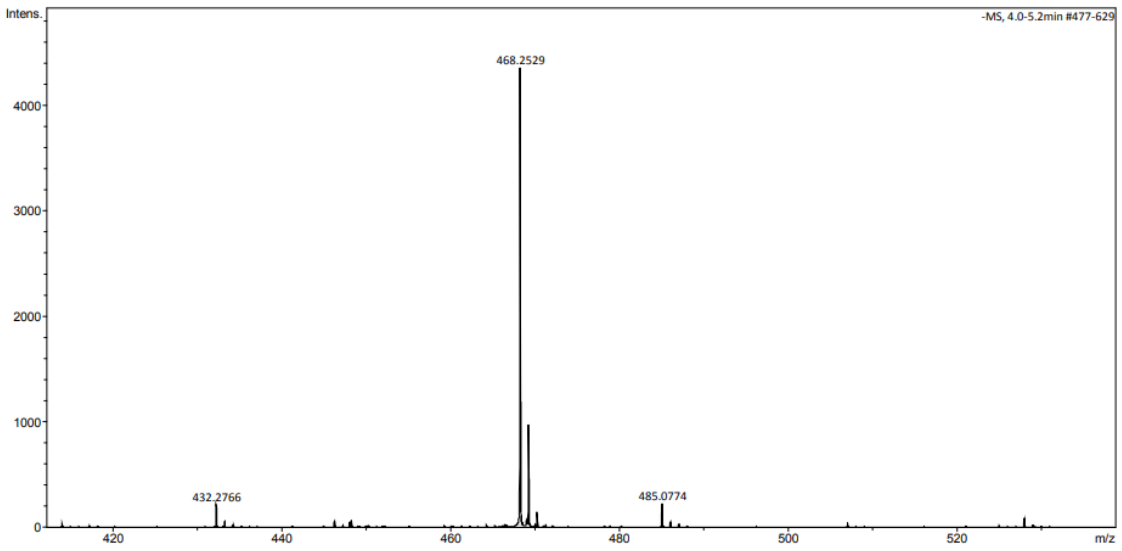

Figure S60 - A high-resolution mass spectrum (ESI^-) obtained for compound **35** in methanol, *m/z* [M].

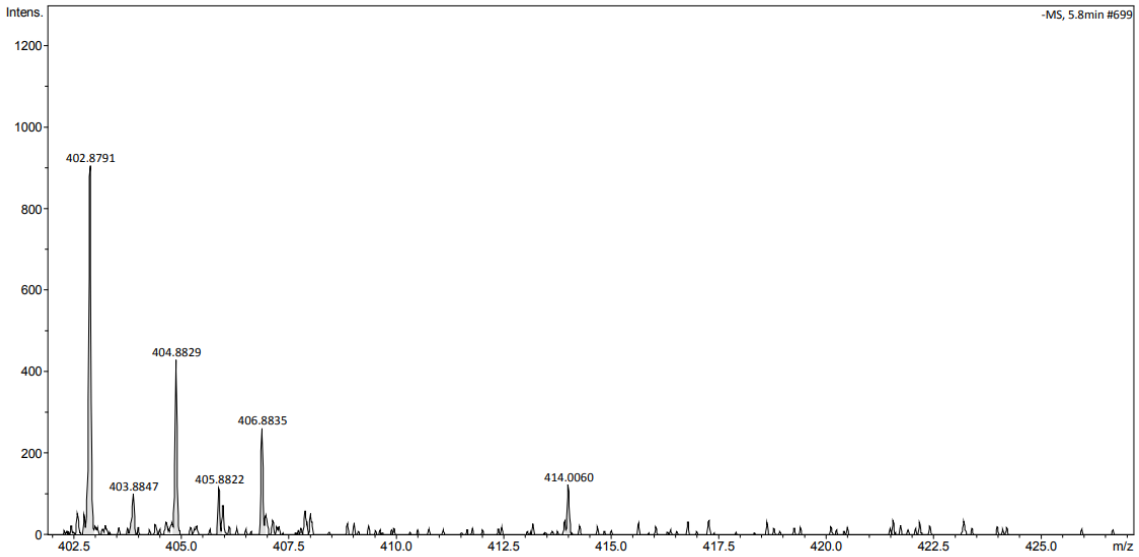

Figure S61 - A high-resolution mass spectrum (ESI^-) obtained for compound **36** in methanol, *m/z* [M].

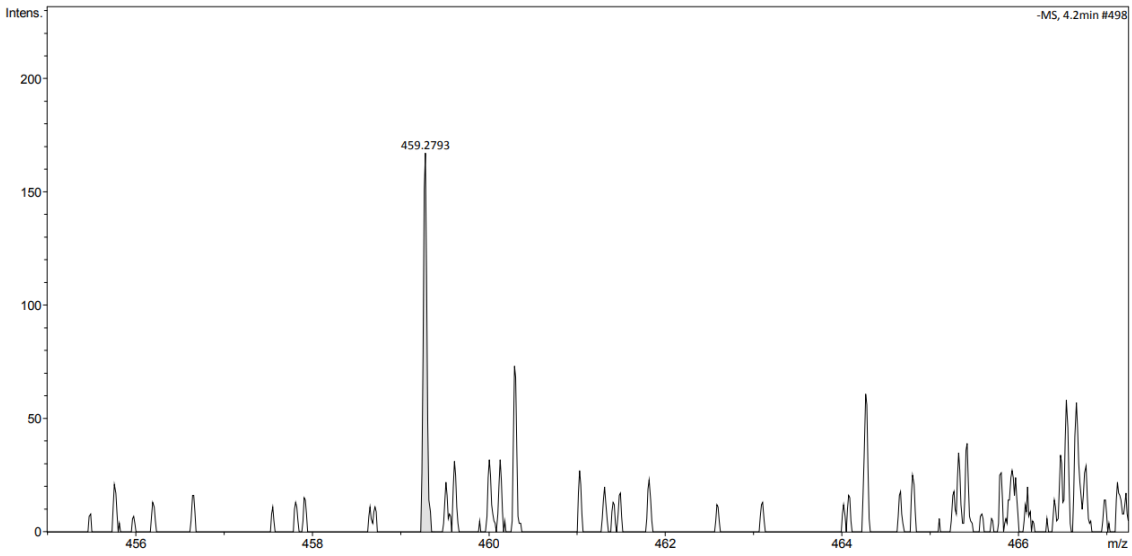

Figure S62 - A high-resolution mass spectrum (ESI^-) obtained for compound **38** in methanol, *m/z* [M].

8. Appendix *New class of SSAs*

8.1. Tables of data

Table S17 - Overview of ^{1}H qNMR study results, values given in % represent the component of the compound that has become NMR silent. SSAs were at concentrations of 112 mM in DMSO-d_6, and 11.2 in D_2O, with the exceptions of **39** (0.55 mM) and **42** (0.43 mM) due to solubility issues.

Compound	DMSO-d_6 1% DCM (%)			D_2O 5 % EtOH (%)		
	Neutral	**Anionic**	**Cationic**	**Neutral**	**Anionic**	**Cationic**
39	0.4	-	-	0.0	-	-
40	-	4.0	2.0	-	0.0	0.0
41	25.5	-	-	*a*	-	-
42	-	0.0	0.0	-	60.0	30.1

'a' indicates that the experiment was not conducted, and the dashes represent the data not being applicable due to the neutral or anionic nature of the compound.

Table S18 - An overview of the hydrodynamic diameters (nm), d_H, calculated for **39** – **42** in DMSO-d_6/0.5 % H_2O at 298 K.

Compound	d_H (nm)		
	Neutral	**Anionic**	**Cationic**
39	1.05	-	-
40	-	*1.46*	*1.24*
41	*d*	-	-
42	-	1.46	1.23

'a' indicates that the experiment was not conducted, and the dashes represent the data not being applicable due to the neutral or anionic nature of the compound.

Table S19 – Overview of self-association constants (M^{-1}) calculated for **39** – **42**, in DMSO-d_6 0.5 % H_2O solution at 298 K. Constants were obtained for EK and CoEK models using Bindfit v0.5.[225] through the input of ^{1}H NMR dilution study data following NH resonances.

Compound	EK model (M^{-1})		CoEK model (M^{-1})		
	K_e	K_{dim}	K_e	K_{dim}	ρ
39	0.61 (± 8 %)	0.30 (± 4 %)	10.13 (± 24 %)	5.06 (± 12 %)	0.26 (± 71 %)
40	4.91 (± 1 %)	2.45 (± 1 %)	15.63 (± 2 %)	7.81 (± 1 %)	0.39 (± 7 %)
41	*a*	*a*	*a*	*a*	*a*
42	2.34 (± 2 %)	1.17 (± 1 %)	9.31 (± 5 %)	4.66 (± 2 %)	0.42 (± 12 %)

Where 'a' represents the experiment not being completed as a loss of compound was observed in the qNMR.

Table S20 - An overview of CMC calculations for **39** – **42** in an EtOH:H_2O 1:19 mixture at 298 K.

Compound	CMC / mM	Surface tension/ mNm^{-1}
39	*a*	*a*
40	27.96	43.86
41	*a*	*a*
42	*a*	*a*

'a' indicates that a CMC value was not found, suggesting the absence of surfactant-like properties for the structure.

Table S21 – Overview of DLS data for **39**-**42** in DMSO at 111.12 mM, where average intensity of particle size distribution is calculated from 10 DLS runs. Samples were prepared by heating to 40 °C and cooling to 25 °C. Error = standard error of the mean and given to 1 dp.

Compound	PDI (%)	Peak maxima (nm)
39	34.42 (± 1 %)	3216.95 (± 1633)
40	*a*	*a*
41	374.19 (± 171 %)	719.70 (± 33)
42[b]	27.35 (± 1 %)	1351.90 (± 35)

Where 'a' represents the experiment not being able to be completed, and 'b' represents a sample which did not require a DLS study due to 0 % 'loss' of signal in DMSO-d_6 during the ^{1}H qNMR studies.

8.2. NMR

8.2.1. qNMR

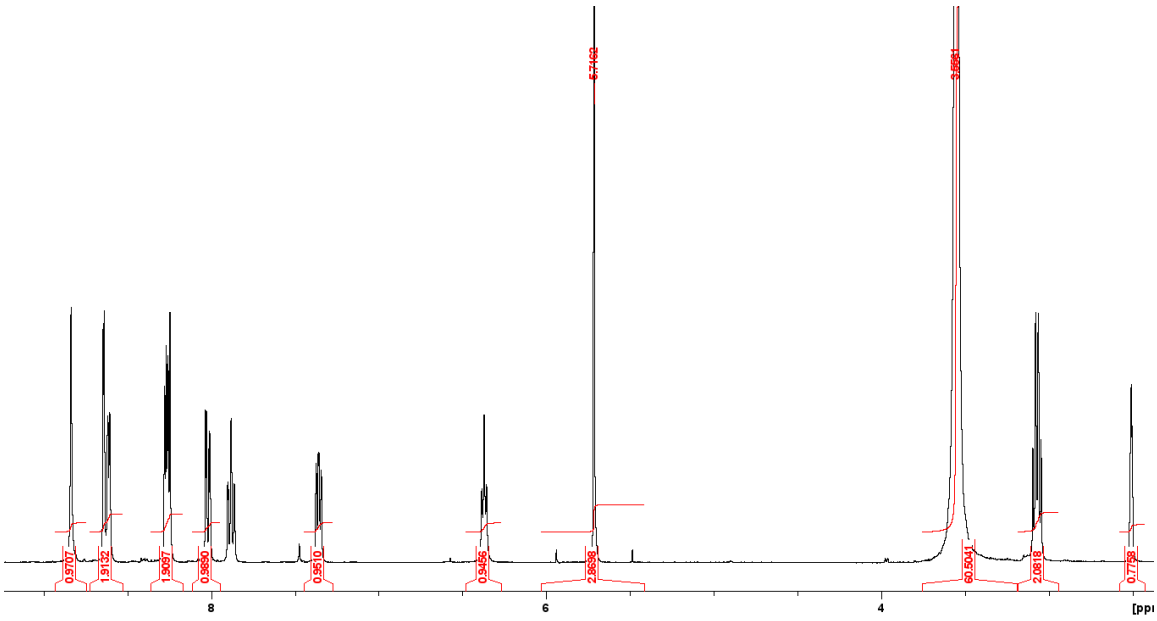

Figure S63 - ^{1}H NMR spectrum (d_1 = 60 s) of compound **39** (112 mM) in DMSO-d_6/1.0 % DCM. Comparative integration indicates 0.35 % of **39** has become NMR silent.

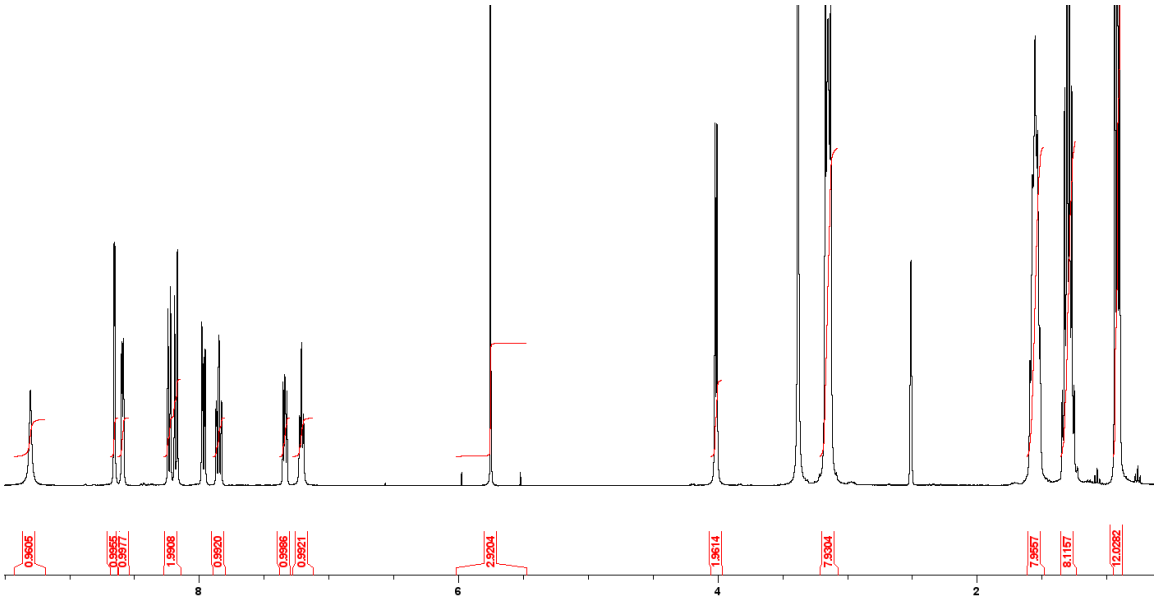

Figure S64 - ^{1}H NMR spectrum (d_1 = 60 s) of compound **40** (112 mM) in DMSO-d_6/1.0 % DCM. Comparative integration indicates 3.95 % of the anionic component, and 2.0 % of the cationic component **40** has become NMR silent.

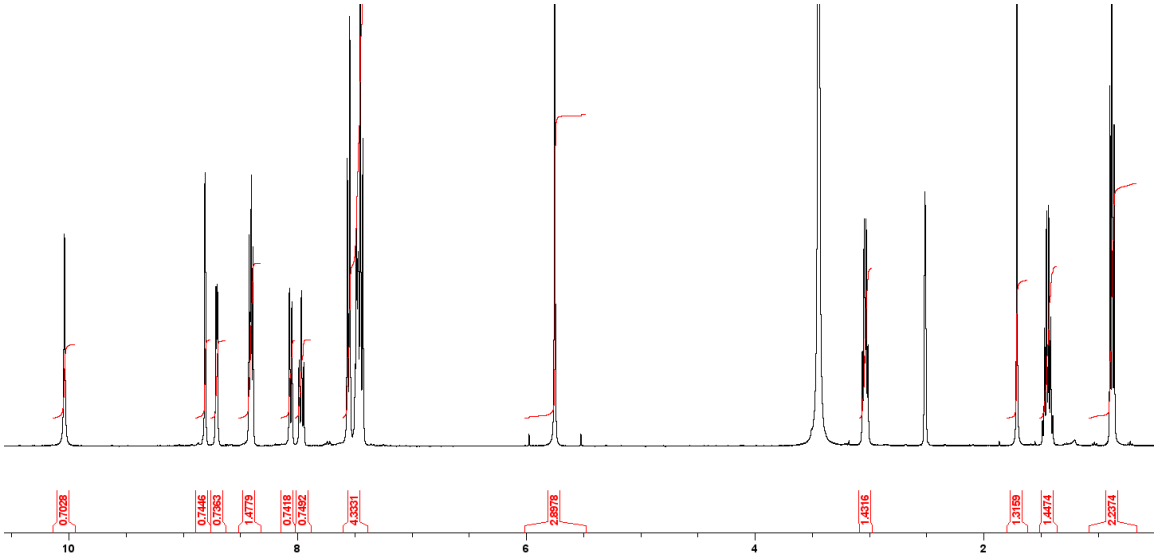

Figure S65 - ^{1}H NMR spectrum (d_1 = 60 s) of compound **41** (112 mM) in DMSO-d_6/1.0 % DCM. Comparative integration indicates 24.5 % of **41** has become NMR silent.

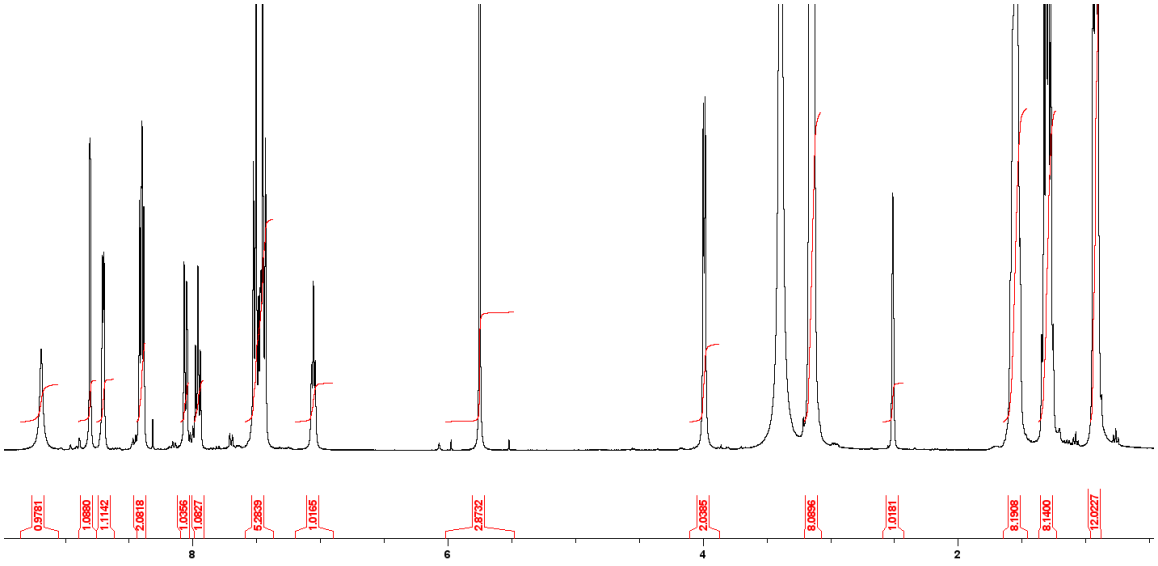

Figure S66 - ^{1}H NMR spectrum (d_1 = 60 s) of compound **42** (112 mM) in DMSO-d_6/1.0 % DCM. Comparative integration indicates none of the anionic component or cationic component of **42** has become NMR silent.

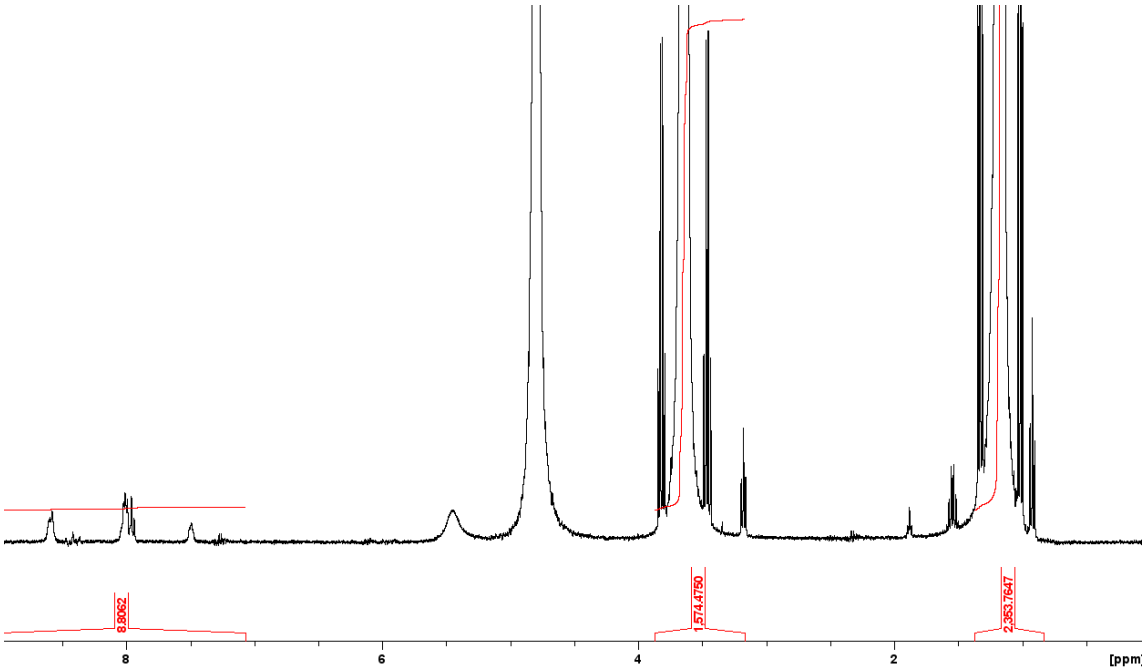

Figure S67 - ^{1}H NMR spectrum (d_1 = 60 s) of compound **39** (0.55 mM) in D_2O/5.0 % EtOH. Comparative integration indicates none of **39** has become NMR silent.

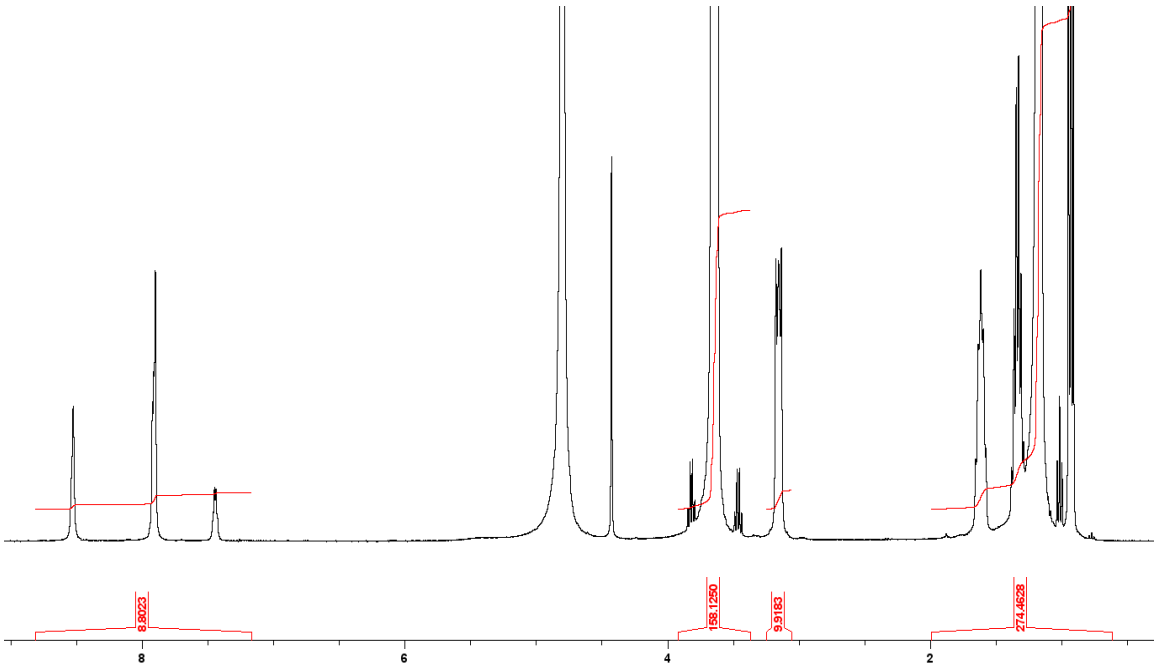

Figure S68 - ^{1}H NMR spectrum (d_1 = 60 s) of compound **40** (5.44 mM) in D_2O/5.0 % EtOH. Comparative integration indicates none of the anionic component of **40** has become NMR silent.

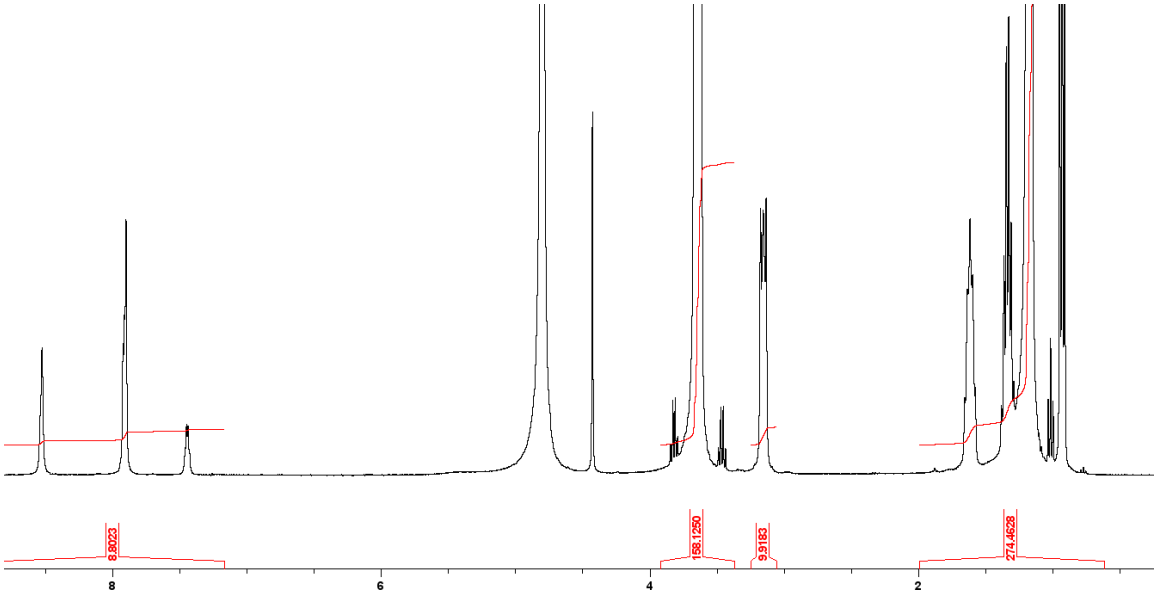

Figure S69 – ^{1}H NMR spectrum (d_1 = 60 s) of compound **42** (0.43 mM) in D_2O/5.0 % EtOH. Comparative integration indicates 59.6 % of the anionic component and 30.1 % of the cationic component of **42** has become NMR silent.

8.2.2. ^{1}H DOSY studies

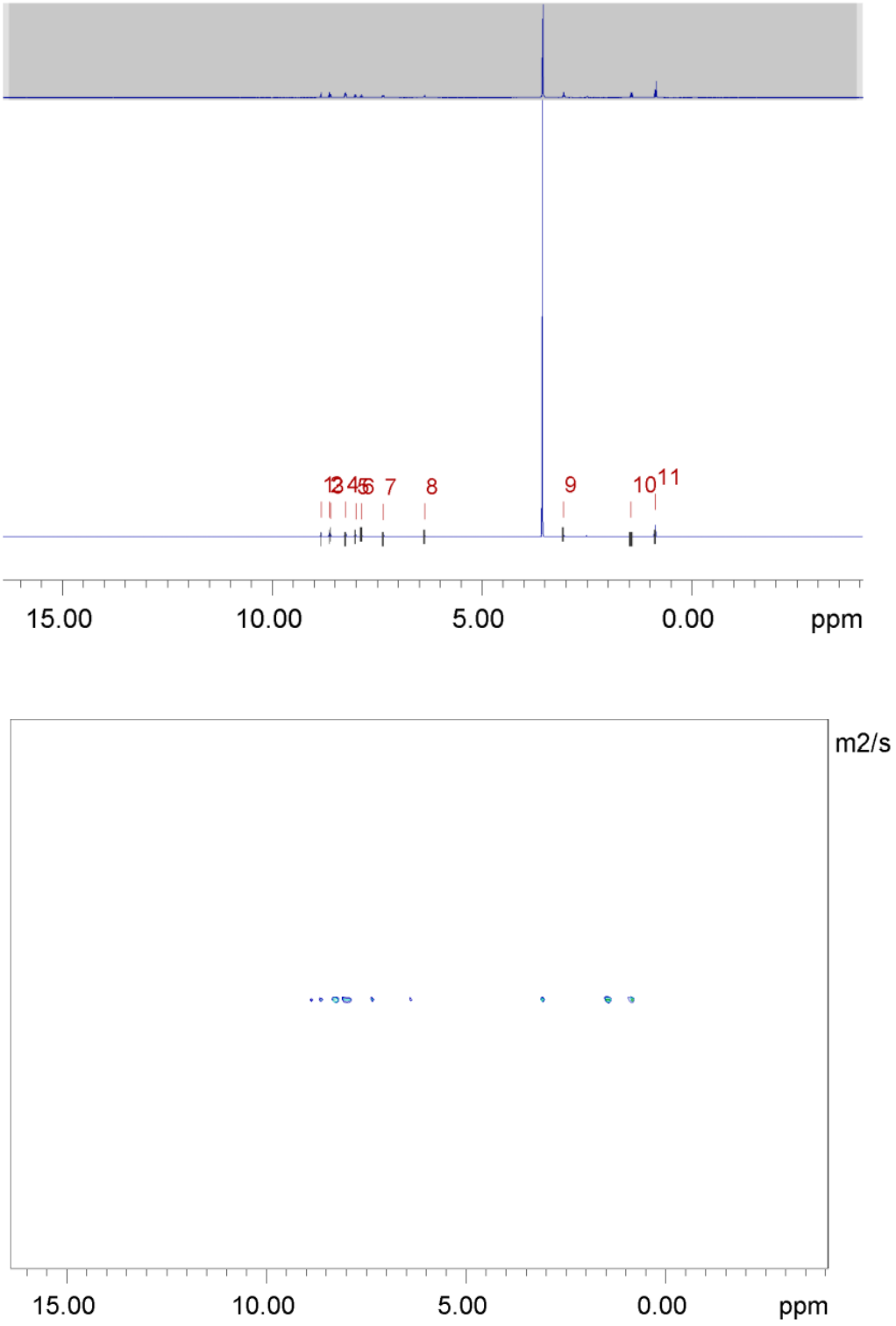

Figure S70 - ^{1}H DOSY NMR of compound **39** (111.2 mM) in DMSO-d_6 conducted at 298 K.

Peak name	F2 [ppm]	Io	error	D [m2/s]	error
1	8.838	9.45e+07	3147	2.09e-10	1.530e-14
2	8.639	1.10e+08	2784	2.08e-10	1.161e-14
3	8.610	1.14e+08	3499	2.09e-10	1.414e-14
4	8.258	2.49e+08	4768	2.09e-10	8.833e-15
5	8.017	1.28e+08	4602	2.09e-10	1.656e-14
6	7.879	1.31e+08	5434	2.09e-10	1.903e-14
7	7.357	1.27e+08	4829	2.09e-10	1.756e-14
8	6.372	1.04e+08	4622	2.09e-10	2.038e-14
9	3.069	2.62e+08	5829	2.09e-10	1.025e-14
10	1.454	2.75e+08	7742	2.08e-10	1.291e-14
11	0.873	3.91e+08	5232	2.09e-10	6.141e-15

Table S22 - ^{1}H DOSY NMR spectrum of the compound **39** (111.2 mM) in DMSO-d_6 at 298 K and a table reporting the diffusion constants calculated for each peak used to determine the solvation sphere diameter (d_H = 1.05 nm).

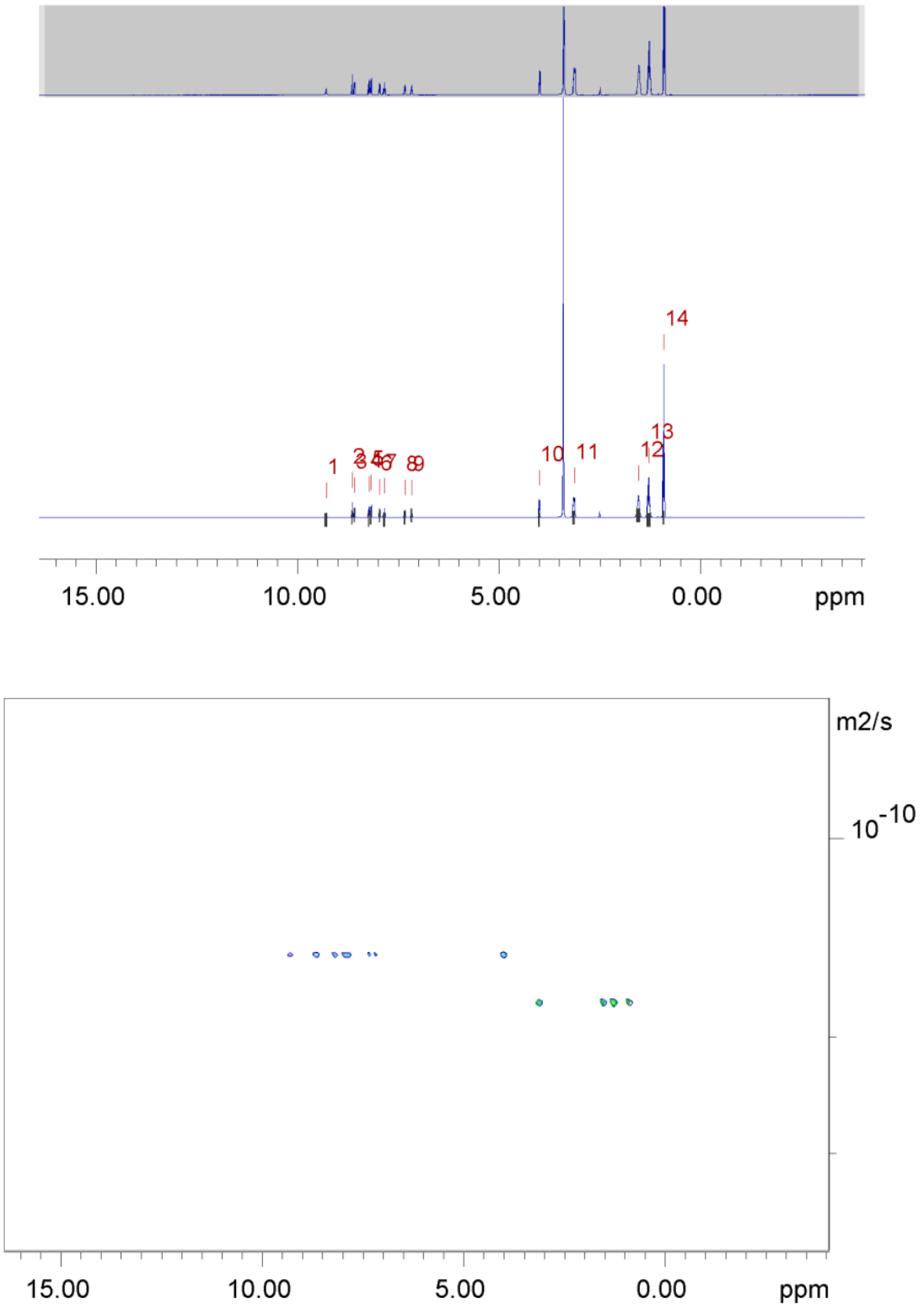

Figure S71 - ^{1}H DOSY NMR of compound **40** (112 mM) in DMSO-d_6 conducted at 298 K. Anionic component is highlighted in blue, TBA counter cation highlighted in green.

Peak name	F2 [ppm]	Io	error	D [m2/s]	error
1	9.293	4.40e+08	4.132e+04	1.50e-10	3.042e-14
2	8.649	6.75e+08	2.828e+04	1.50e-10	1.354e-14
3	8.591	6.44e+08	2.684e+04	1.50e-10	1.346e-14
4	8.230	6.27e+08	2.683e+04	1.50e-10	1.382e-14
5	8.180	6.32e+08	2.774e+04	1.51e-10	1.426e-14
6	7.964	6.36e+08	2.829e+04	1.50e-10	1.438e-14
7	7.849	6.50e+08	3.344e+04	1.50e-10	1.664e-14
8	7.340	6.64e+08	3.171e+04	1.50e-10	1.546e-14
9	7.172	5.16e+08	3.182e+04	1.50e-10	1.995e-14
10	4.007	1.12e+09	2.784e+04	1.50e-10	8.056e-15
11	3.146	3.05e+09	3.718e+04	1.77e-10	4.597e-15
12	1.549	3.77e+09	4.707e+04	1.78e-10	4.722e-15
13	1.293	4.90e+09	4.791e+04	1.78e-10	3.698e-15
14	0.916	7.93e+09	3.437e+04	1.78e-10	1.642e-15

Table S23 - ^{1}H DOSY NMR spectrum of the compound **40** (112 mM) in DMSO-d_6 at 298 K and a table reporting the diffusion constants calculated for each peak used to determine the solvation sphere diameter of the anionic component of **40** (d_H = 1.46 nm), and of the cationic component of **40** (d_H = 1.23) nm Peaks 1 - 10 correspond to the anionic component of **40** while peaks 11 - 14 correspond to the cationic component of **40**.

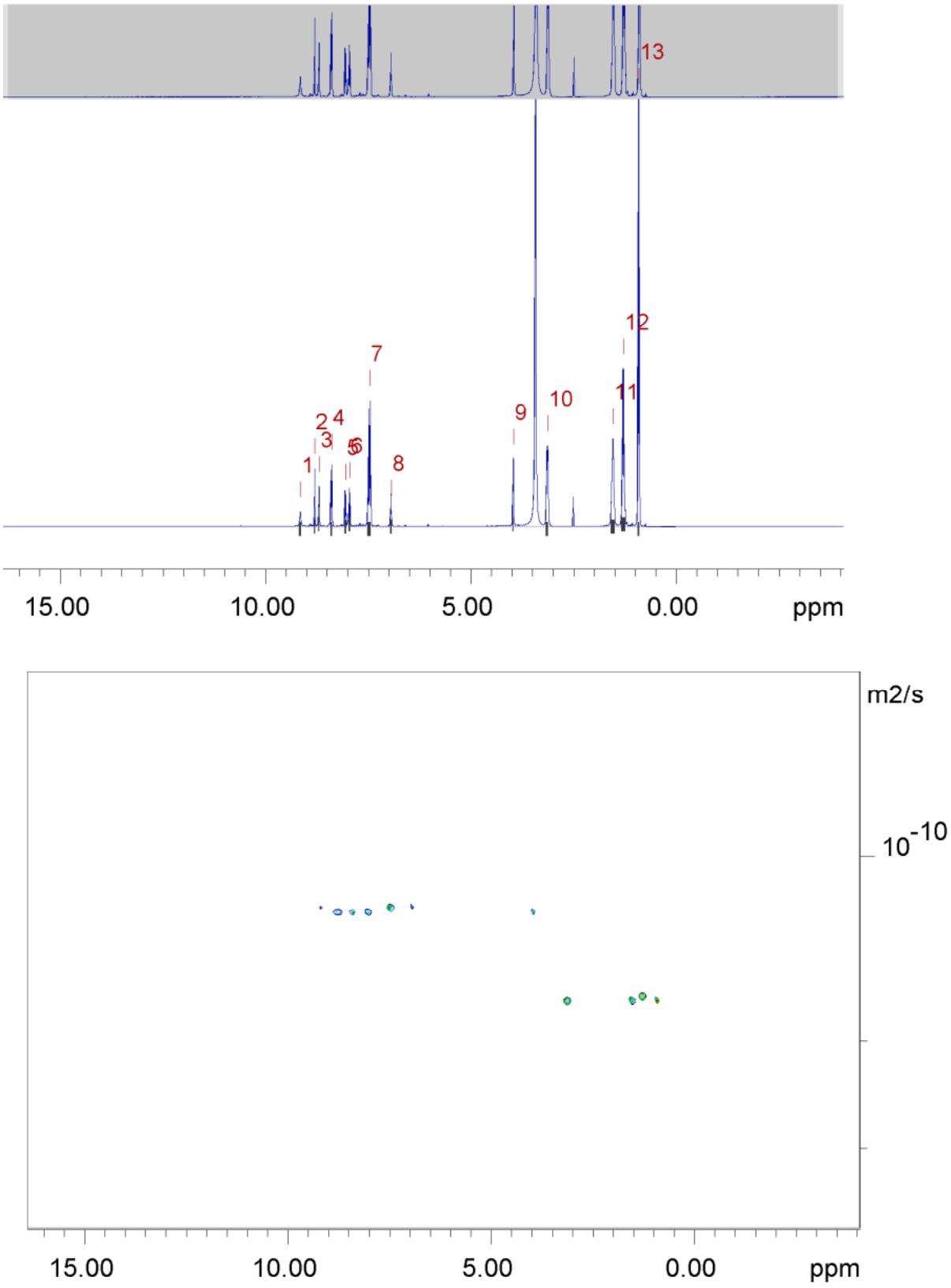

Figure S72 - ^{1}H DOSY NMR of compound **42** (112 mM) in DMSO-d_6 conducted at 298 K. Anionic component is highlighted in blue, TBA counter cation highlighted in green.

Peak name	F2 [ppm]	Io	error	D [m2/s]	error
1	9.158	5.42e+08	6.174e+04	1.22e-10	3.026e-14
2	8.805	8.17e+08	3.776e+04	1.23e-10	1.237e-14
3	8.700	9.93e+08	4.529e+04	1.23e-10	1.221e-14
4	8.397	2.07e+09	6.183e+04	1.23e-10	7.989e-15
5	8.060	9.75e+08	5.474e+04	1.23e-10	1.498e-14
6	7.959	1.11e+09	6.332e+04	1.24e-10	1.530e-14
7	7.473	5.38e+09	8.222e+04	1.23e-10	4.070e-15
8	6.951	8.11e+08	5.776e+04	1.22e-10	1.891e-14
9	3.972	1.54e+09	4.531e+04	1.24e-10	7.860e-15
10	3.142	4.66e+09	7.477e+04	1.71e-10	5.813e-15
11	1.549	5.89e+09	9.450e+04	1.71e-10	5.800e-15
12	1.296	7.85e+09	9.836e+04	1.70e-10	4.523e-15
13	0.919	1.26e+10	6.844e+04	1.71e-10	1.963e-15

Table S24 - ^{1}H DOSY NMR spectrum of the compound **42** (112 mM) in DMSO-d_6 at 298 K and a table reporting the diffusion constants calculated for each peak used to determine the solvation sphere diameter of the anionic component of **41** (d_H = 1.78 nm), and of the cationic component of **8** (d_H = 1.28) nm Peaks 1 - 9 correspond to the anionic component of **42** while peaks 10 - 13 correspond to the cationic component of **42**.

8.2.3. ^{1}H self-association studies

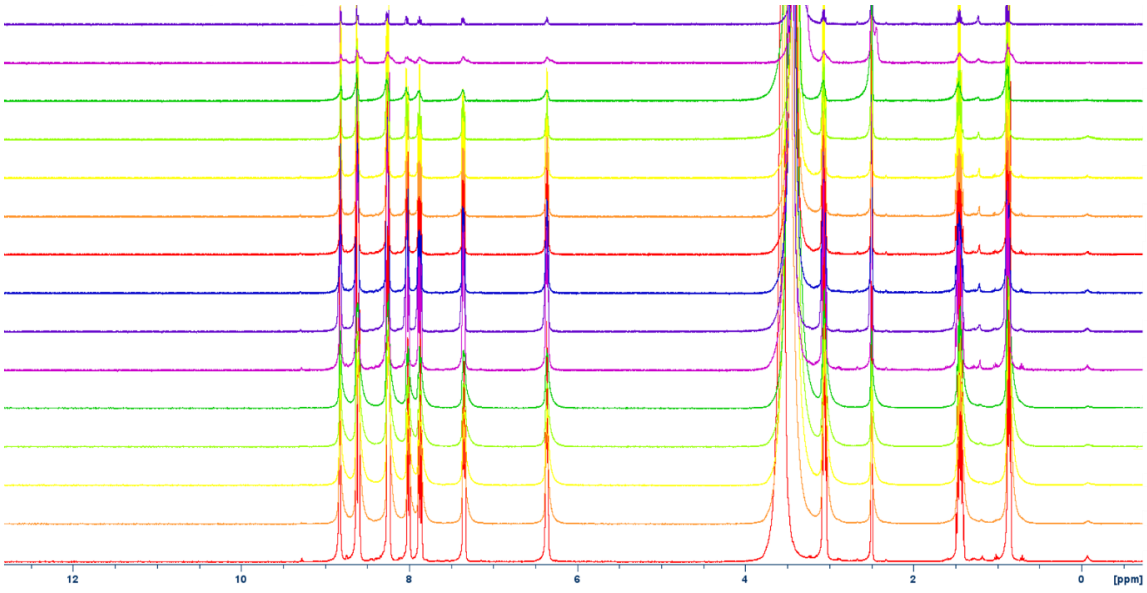

Figure S73- ^{1}H NMR stack plot of compound **39** in a DMSO-d_6/0.5 % H_2O solution. Samples were prepared in series with an aliquot of the most concentrated solution undergoing serial dilution.

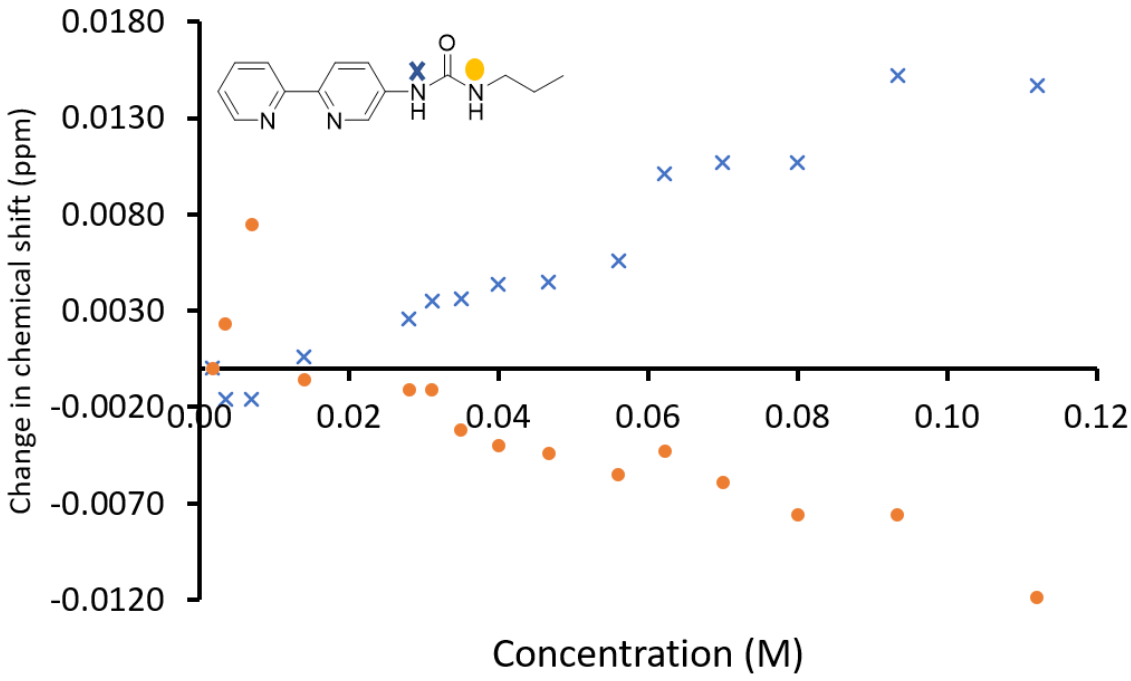

Figure S74 - Graph illustrating the ^{1}H NMR change in chemical shift of urea NH resonances with increasing concentrations of compound **39** in DMSO-d_6/0.5 % H_2O solution (298 K).

Compound **39** – Dilution study in DMSO-d_6 0.5 % H_2O. Values calculated from data gathered from both NH 1 and 2.

Equal K/Dimerization model

K_e = 0.61 M^{-1} ± 8.43 % K_{dim} = 0.30 M^{-1} ± 4.21 %

http://app.supramolecular.org/bindfit/view/171971ff-a2dc-4fec-9c93-4d2091d6701d

CoEK model

K_e = 10.13 M^{-1} ± 23.80 % K_{dim} = 5.06 M^{-1} ± 11.90 % ρ = 0.26 ± 70.54 %

http://app.supramolecular.org/bindfit/view/d2d28faf-af49-4bea-8f31-ab4f161d0a09

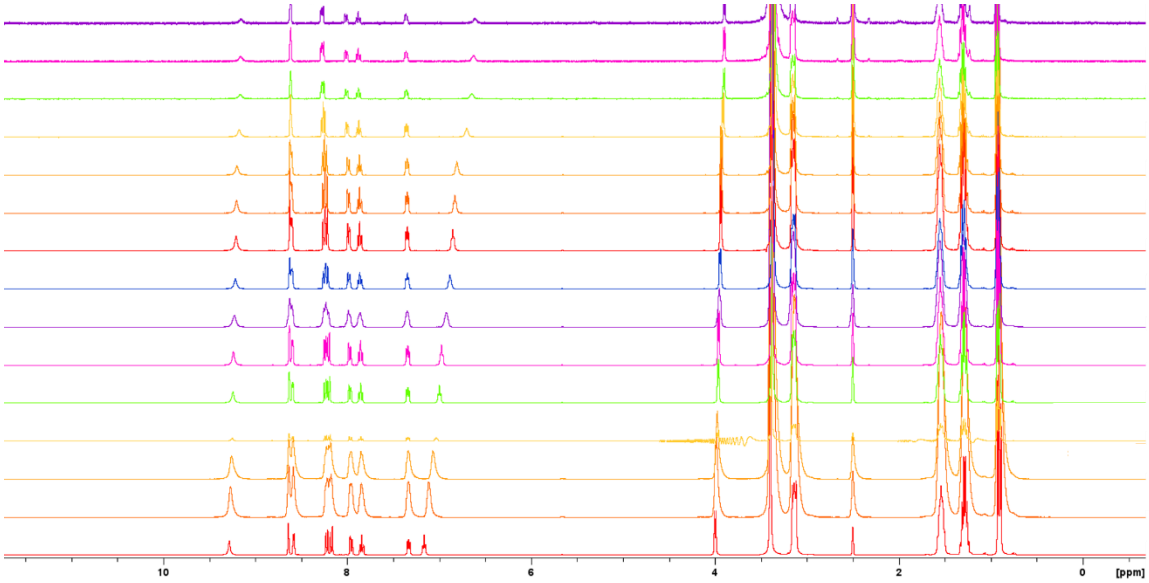

Figure S75- ^{1}H NMR stack plot of compound **40** in a DMSO-d_6/0.5 % H_2O solution. Samples were prepared in series with an aliquot of the most concentrated solution undergoing serial dilution.

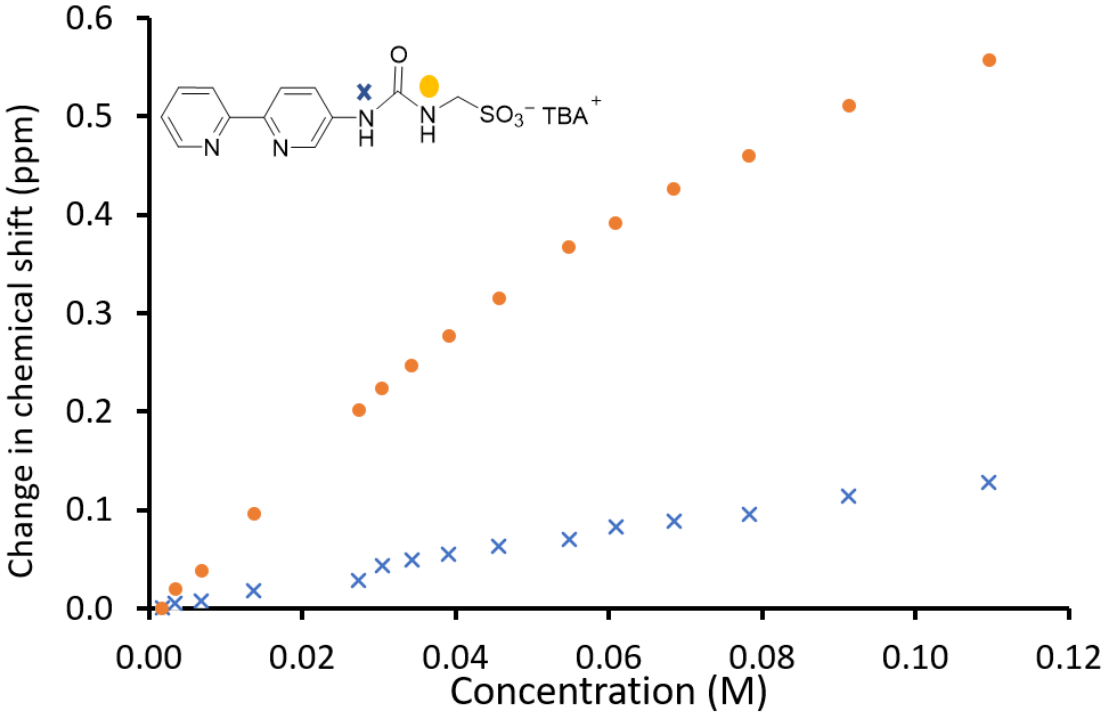

Figure S76 - Graph illustrating the ^{1}H NMR change in chemical shift of urea NH resonances with increasing concentrations of compound **40** in DMSO-d_6/0.5 % H_2O solution (298 K).

Compound **40** – Dilution study in DMSO-d_6 0.5 % H_2O. Values calculated from data gathered from both NH 1 and 2.

Equal K/Dimerization model

K_e = 4.91 M^{-1} ± 1.30 % K_{dim} = 2.45 M^{-1} ± 0.65 %

http://app.supramolecular.org/bindfit/view/6fe8f81f-acac-4ad7-a200-15825780a2d9

CoEK model

K_e = 15.63 M^{-1} ± 2.06 % K_{dim} = 7.81 M^{-1} ± 1.03 % ρ = 0.39 ± 7.18 %

http://app.supramolecular.org/bindfit/view/b7451867-e63f-4fd0-82db-aa738b07544d

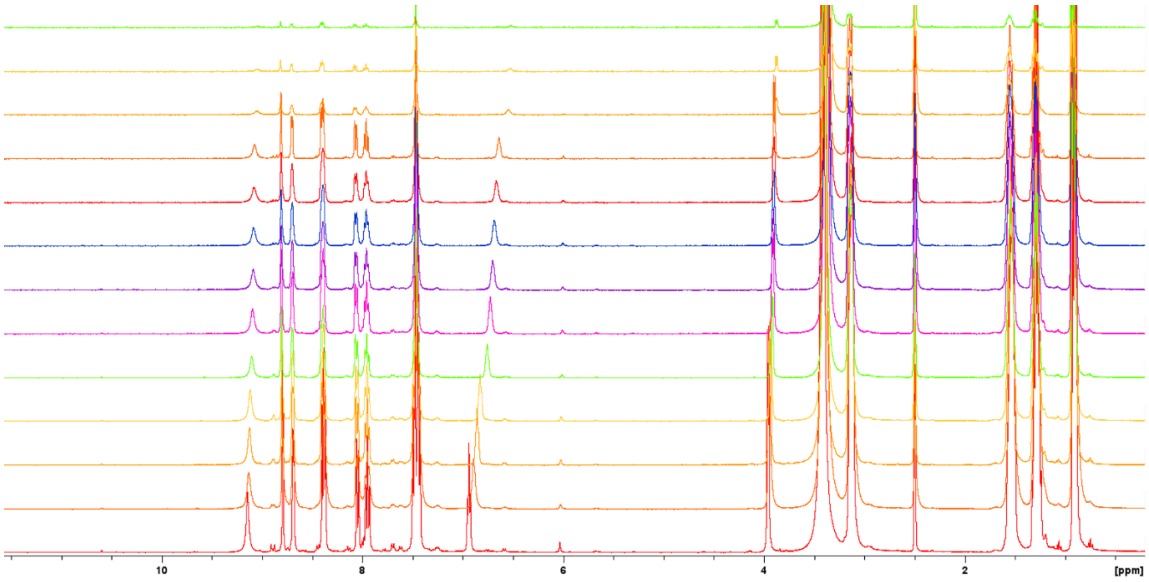

Figure S77- ^{1}H NMR stack plot of compound **42** in a DMSO-d_6/0.5 % H_2O solution. Samples were prepared in series with an aliquot of the most concentrated solution undergoing serial dilution.

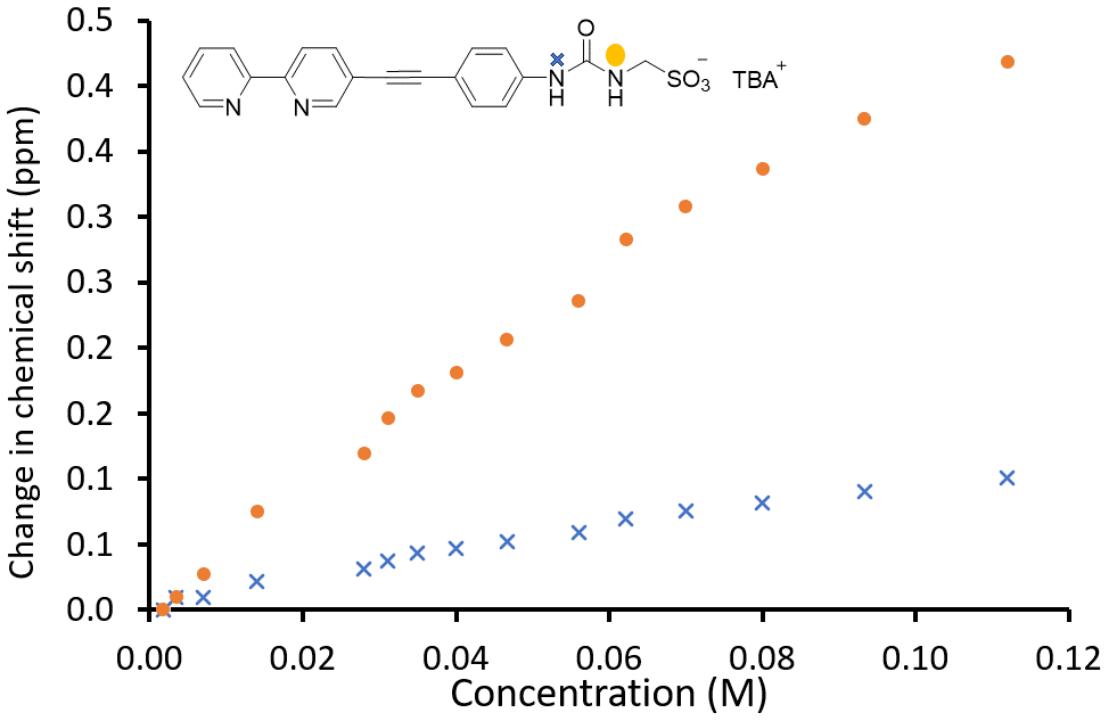

Figure S78 - Graph illustrating the ^{1}H NMR down-field change in chemical shift of urea NH resonances with increasing concentrations of compound **42** in DMSO-d_6/0.5 % H_2O solution (298 K).

Compound **42** – Dilution study in DMSO-d_6 0.5 % H_2O. Values calculated from data gathered from both NH 1 and 2.

Equal K/Dimerization model

K_e = 2.34 M^{-1} ± 1.66 % K_{dim} = 1.17 M^{-1} ± 0.83 %

http://app.supramolecular.org/bindfit/view/0c1e8fb1-1a68-4d74-a385-c4f5ac275328

CoEK model

K_e = 9.31 M^{-1} ± 4.80 % K_{dim} = 4.66 M^{-1} ± 2.40 % ρ = 0.42 ± 12.09 %

http://app.supramolecular.org/bindfit/view/2d4122e8-7049-46e7-bdf9-e371a1498811

8.3. Surface tension and CMC

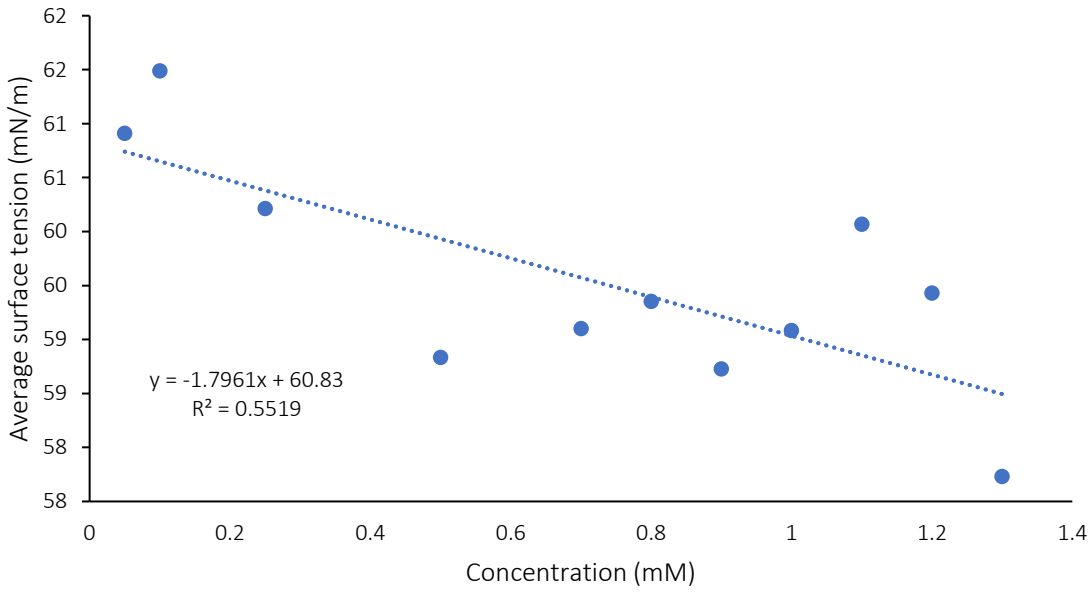

Figure S79- Calculation of CMC for compound **39** in an EtOH:H_2O 1:19 mixture using surface tension measurements, here this shows no CMC value could be attained, suggesting no surfactant properties for this structure.

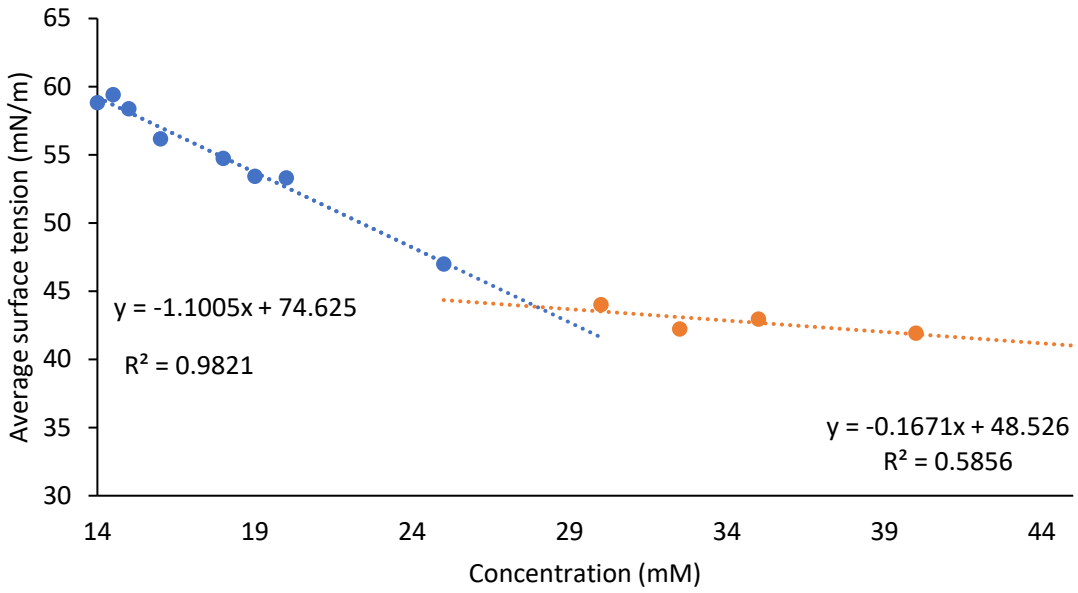

Figure S80 - Calculation of CMC (27.96 mM at 43.86 mNm-1) for compound **40** in an EtOH:H2O 1:19 mixture using surface tension measurements, suggesting surfactant properties for this structure.

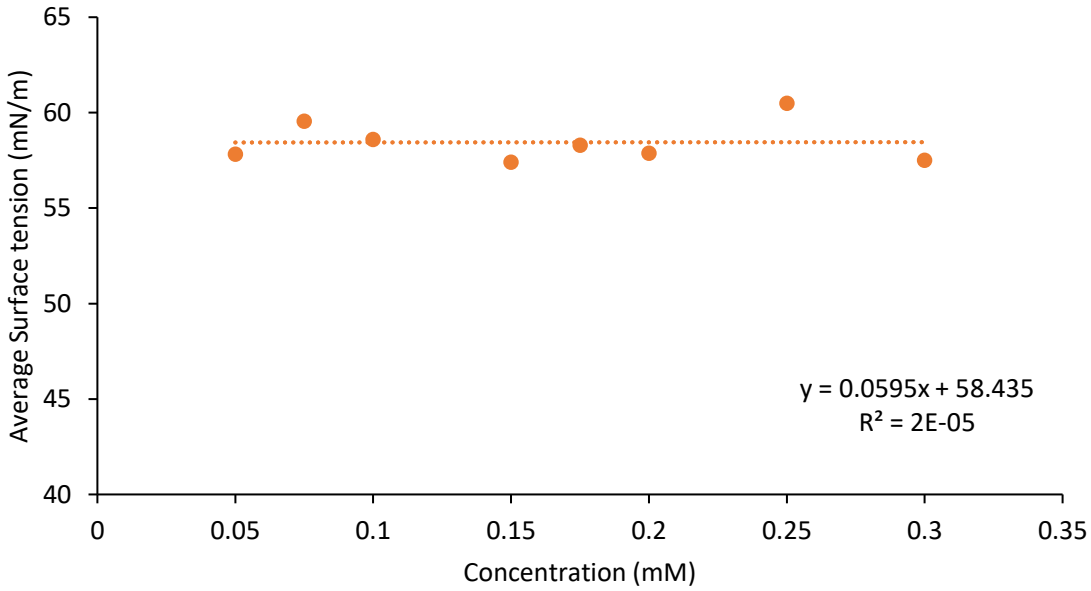

Figure S81 - Calculation of CMC for compound **41** in an EtOH:H_2O 1:19 mixture using surface tension measurements, here this shows no CMC value could be attained, suggesting no surfactant properties for this structure.

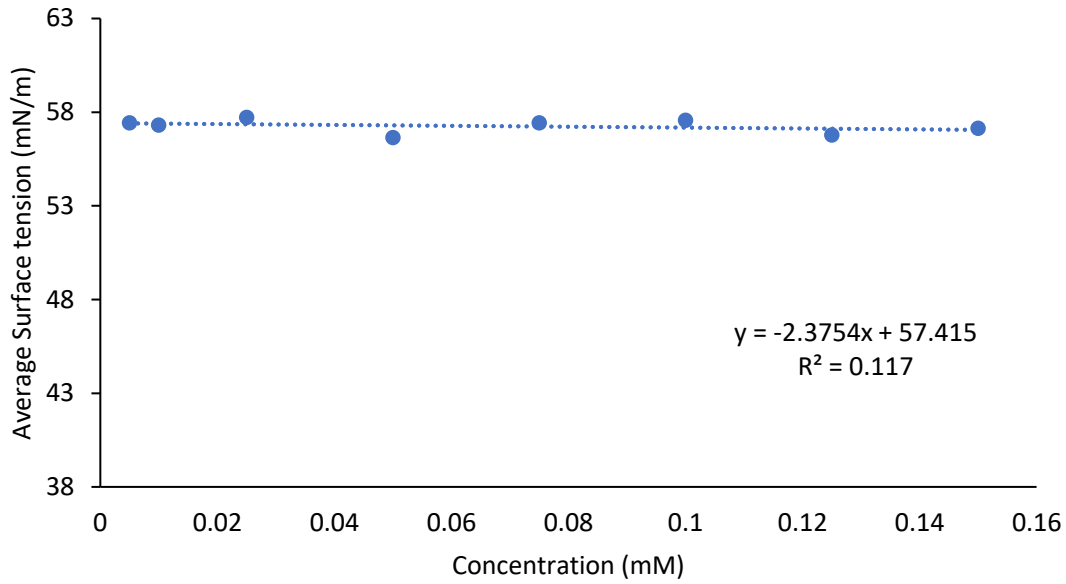

Figure S82- Calculation of CMC for compound **42** in an EtOH:H_2O 1:19 mixture using surface tension measurements, here this shows no CMC value could be attained, suggesting no surfactant properties for this structure.

8.4. DLS data

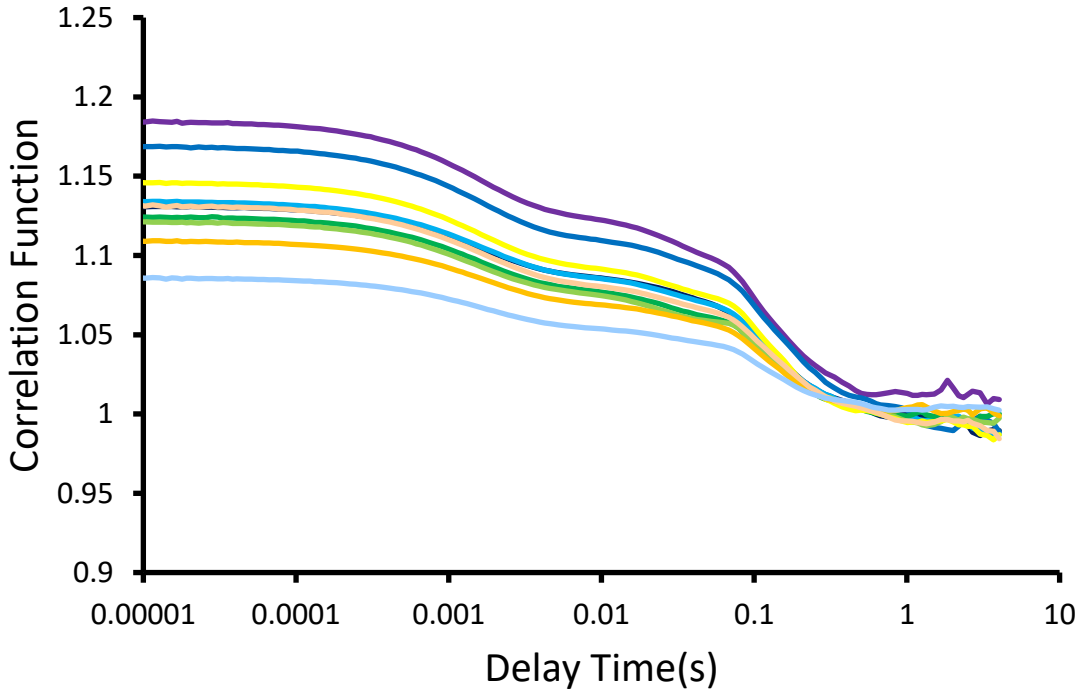

Figure S83 - Correlation function data for 10 DLS runs of compound **39** (111.2 mM) in a DMSO/0.5 % H_2O solution at 298 K.

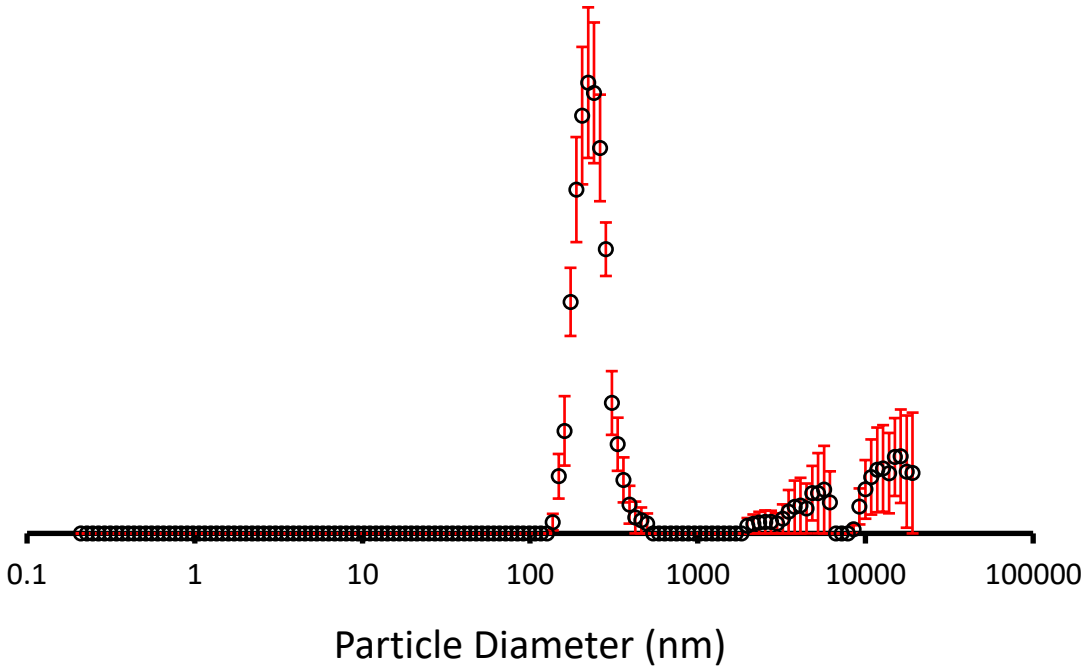

Figure S84 - The average intensity particle size distribution calculated (3216 nm) using 10 DLS runs for compound **39** (111.2 mM) in DMSO/0.5 % H_2O solution at 298 K.

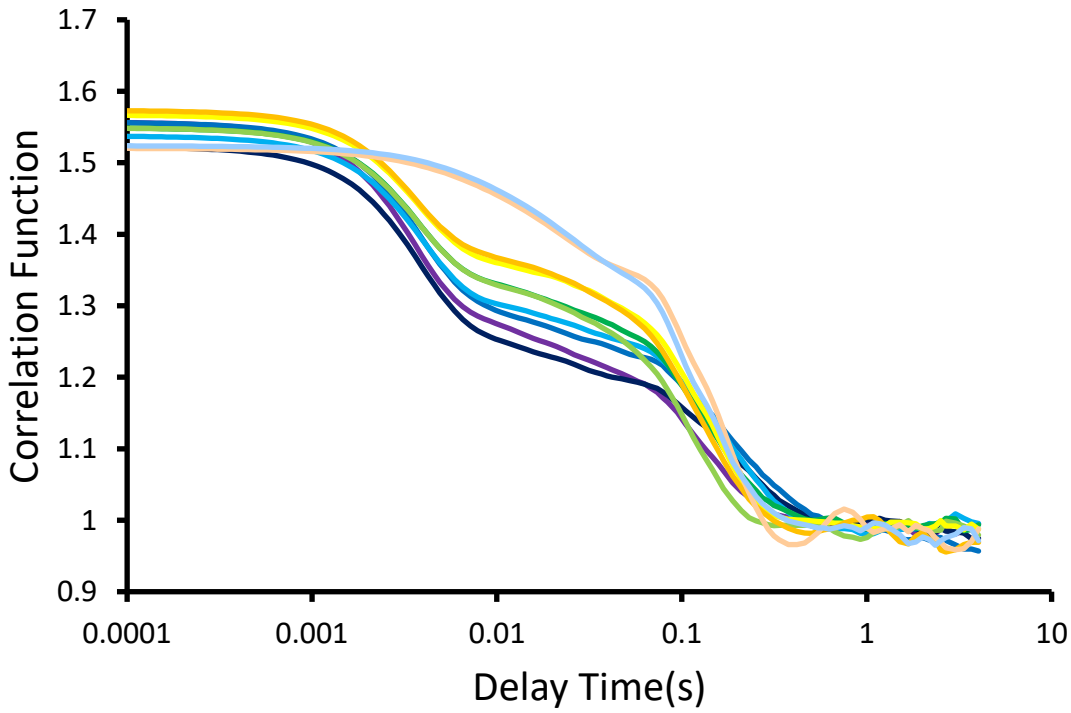

Figure S85 - Correlation function data for 10 DLS runs of compound **41** (111.2 mM) in a DMSO/0.5 % H_2O solution at 298 K.

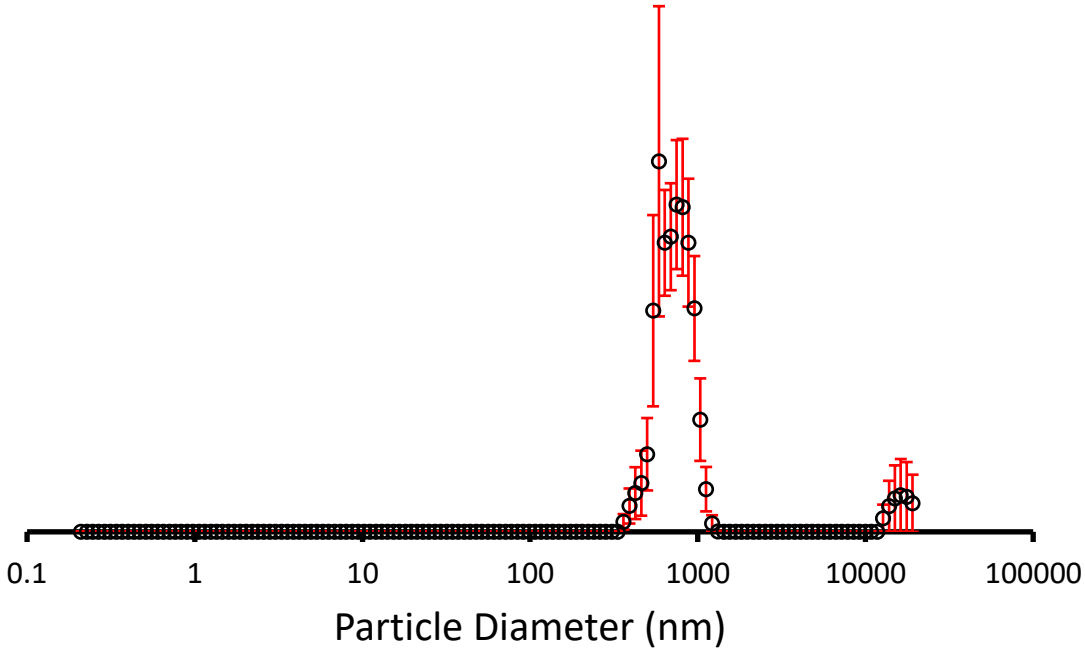

Figure S86 - The average intensity particle size distribution calculated (720 nm) using 10 DLS runs for compound **41** (111.2 mM) in DMSO/0.5 % H_2O solution at 298 K.

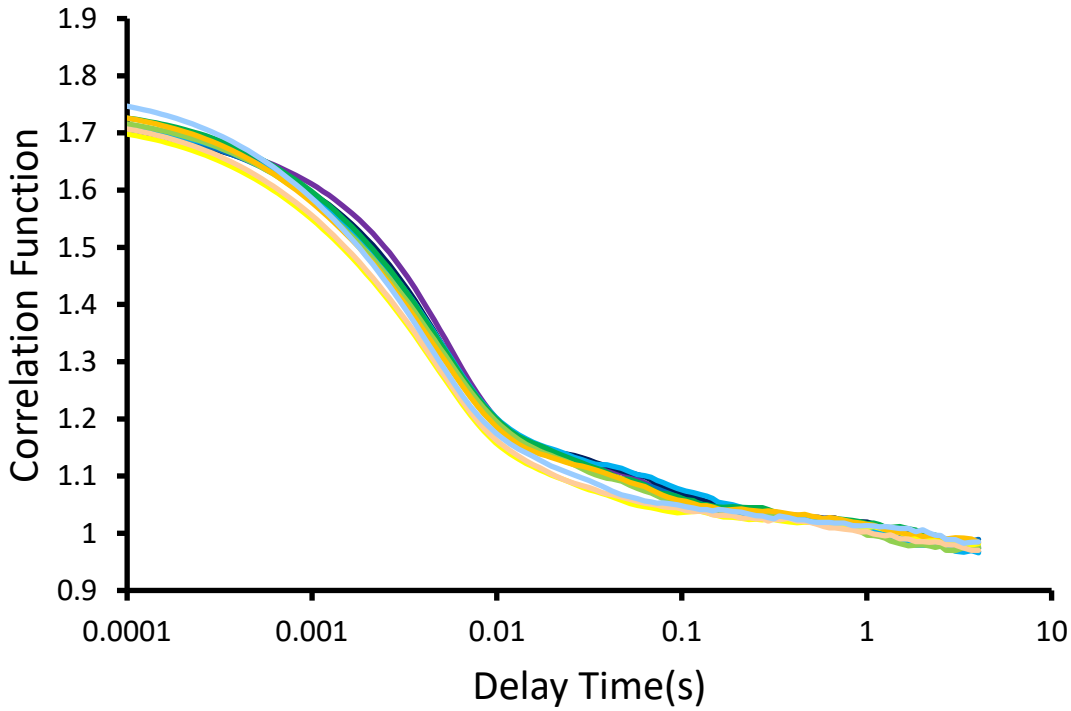

Figure S87 - Correlation function data for 10 DLS runs of compound **42** (111.2 mM) in a DMSO/0.5 % H_2O solution at 298 K.

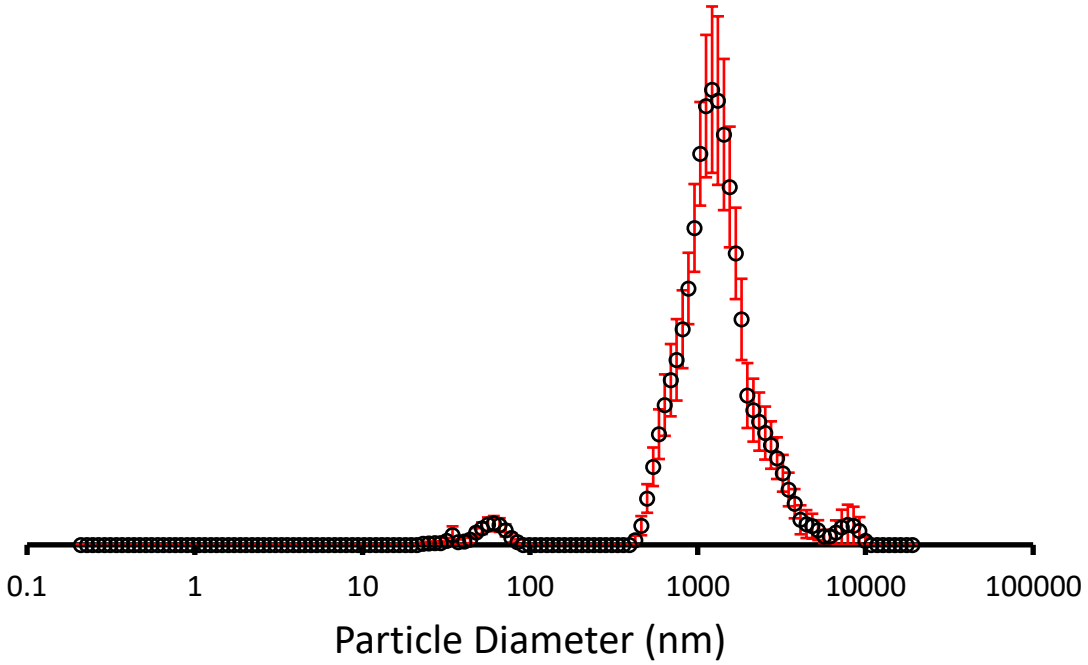

Figure S88 - The average intensity particle size distribution calculated (1351 nm) using 10 DLS runs for compound **42** (111.2 mM) in DMSO/0.5 % H_2O solution at 298 K.

8.5. Zeta potential

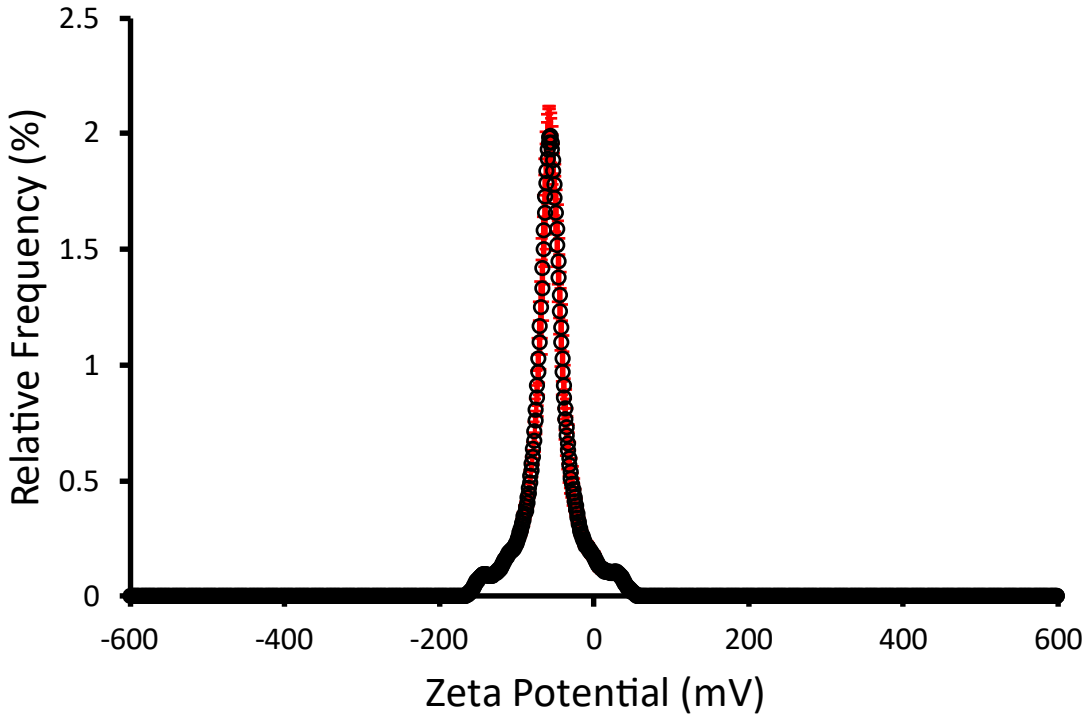

Figure S89 - The average zeta potential distribution calculated using 10 runs for compound **42** (0.56 mM) in EtOH:H_2O (1:19) solution at 298 K. Average measurement value - 56.95 mV.